

Diffusion MRI tractography for oncological neurosurgery planning

Citation for published version (APA):

Krahulec, D. (2023). *Diffusion MRI tractography for oncological neurosurgery planning: Clinical research prototype*. [Phd Thesis 1 (Research TU/e / Graduation TU/e), Biomedical Engineering]. Eindhoven University of Technology.

Document status and date:

Published: 04/04/2023

Document Version:

Publisher's PDF, also known as Version of Record (includes final page, issue and volume numbers)

Please check the document version of this publication:

- A submitted manuscript is the version of the article upon submission and before peer-review. There can be important differences between the submitted version and the official published version of record. People interested in the research are advised to contact the author for the final version of the publication, or visit the DOI to the publisher's website.
- The final author version and the galley proof are versions of the publication after peer review.
- The final published version features the final layout of the paper including the volume, issue and page numbers.

[Link to publication](#)

General rights

Copyright and moral rights for the publications made accessible in the public portal are retained by the authors and/or other copyright owners and it is a condition of accessing publications that users recognise and abide by the legal requirements associated with these rights.

- Users may download and print one copy of any publication from the public portal for the purpose of private study or research.
- You may not further distribute the material or use it for any profit-making activity or commercial gain
- You may freely distribute the URL identifying the publication in the public portal.

If the publication is distributed under the terms of Article 25fa of the Dutch Copyright Act, indicated by the "Taverne" license above, please follow below link for the End User Agreement:

www.tue.nl/taverne

Take down policy

If you believe that this document breaches copyright please contact us at:

openaccess@tue.nl

providing details and we will investigate your claim.

Diffusion MRI tractography for oncological neurosurgery planning

CLINICAL RESEARCH PROTOTYPE

PhD thesis. Department of Biomedical Engineering, Eindhoven University of Technology.
A catalog record is available from the Eindhoven University of Technology Library.

ISBN: 978-90-386-5655-7

This project has received funding from the European Union's Horizon 2020 research and innovation program under the Marie Skłodowska-Curie grant agreement No. 765148.

Financial support for the cover design and printing of this thesis was provided by the Department of Biomedical Engineering, Eindhoven University of Technology.

This thesis was typeset by the author using L^AT_EX.

Cover design and layout by Grefo Prepress.

Cover art "*Glioblastoma Brain Tumour, DTI MRI scan*" by Sherbrooke Connectivity Imaging Lab, Canada.

Printed by ADC Dereumaux Nederland B.V.

Copyright © 2023 Daniel Krahulec. All rights reserved. No part of this publication may be reproduced, stored in a retrieval system, or transmitted in any form or by any means, electronic, mechanical, photocopying, recording, or otherwise, without written permission of the copyright owner.

Diffusion MRI tractography for oncological neurosurgery planning

CLINICAL RESEARCH PROTOTYPE

PROEFONTWERP

ter verkrijging van de graad van doctor aan de Technische Universiteit
Eindhoven, op gezag van de rector magnificus prof.dr.ir. F.P.T. Baaijens,
voor een commissie aangewezen door het College voor Promoties, in het
openbaar te verdedigen op dinsdag 4 april 2023 om 13:30 uur

door

Daniel Krahulec

geboren te Ostrava, Tsjechië

De documentatie van het proefontwerp is goedgekeurd door de promotoren en de samenstelling van de promotiecommissie is als volgt:

voorzitter:	Prof.dr. Maarten Merkx
1e promotor:	Prof.dr.ir. Marcel Breeuwer
2e promotor:	Prof.dr. Josien Pluim
leden:	Prof.dr.ir. Anna Vilanova Prof.dr. Stefan Sunaert (Universitair Ziekenhuis Leuven) Prof.dr. Koen van Leemput (Technical University of Denmark)
adviseurs:	Dr. Geert-Jan Rutten (Elisabeth-TweeSteden Ziekenhuis Tilburg) Dr. Maarten Versluis (Philips Healthcare, MR Clinical Science)

Het ontwerp dat in dit proefontwerp wordt beschreven is uitgevoerd in overeenstemming met de TU/e Gedragscode Wetenschapsbeoefening.

*Not everything that can be counted counts,
and not everything that counts can be counted.*

Albert Einstein

Abstract

Diffusion MRI tractography (fiber tracking) is an exquisite noninvasive technique to investigate structural brain connectivity and neuronal pathway integrity both in health and disease. In brain tumor surgery planning, fiber tracking is infrequently used due to multifactorial impediments: cumbersome workflow, absence of advanced tractography techniques in commercial neurosurgical navigation software, clinically incompatible medical image processing timelines, and nontrivial interpretation of fiber tracking results in brains occupied by large lesions that require urgent surgical attention. Based on identified unmet clinical user requirements, sophisticated image processing tools available both open-source and in commercial research were exploited to design and implement a novel software solution that enables an optimized (accelerated and fully automated) image processing workflow, thereby facilitating the translation of advanced diffusion MRI tractography to daily clinical practice. Reconstructions of brain nerve fiber bundles generated by the herein realized application, FT4Onco, were clinically assessed by medical doctors in a qualitative evaluation, and quantitatively cross-validated with results obtained from another semi-automated research software that is routinely utilized in single-center neurosurgery planning. Despite non-negligible differences in methodology and architecture between the two compared image processing pipelines, it was possible to achieve comparable performance in a fully automated fashion. With further refinement and integration into the hospital infrastructure, FT4Onco may conceivably serve as a useful means of brain tumor resection planning.

Summary

Diffusion MRI tractography for oncological neurosurgery planning

This dissertation describes design-oriented research that is performed to optimize (accelerate and automate) diffusion MRI data processing and nerve fiber tracking workflow to aid brain tumor surgery planning. As introduced in Chapter 1, special attention is paid to the surgical resection of highly aggressive, fast-growing glial tumors, called *glioblastoma*, which is a devastating type of brain cancer that may result in early death in about six months or less if untreated. Glioblastomas pose miscellaneous treatment challenges because of resistance to conventional therapy, location in the brain, peritumoral edema, and intracranial hypertension. Often, patients with these tumors present with acute neurological decompensation and herniation due to tumor mass effect, which warrants a pressing need for immediate surgery for tumor resection. Oncological neurosurgery remains the mainstay of treatment for glioblastomas.

Diffusion magnetic resonance imaging (dMRI) has been imperative in presurgical brain mapping. Supported by background information in Chapter 2, the main topic of this work concerns the clinical translation of advanced diffusion-informed nerve fiber tracking techniques to daily neurosurgical practice in order to reliably localize eloquent white matter (WM) nerve fibers affected by glioblastomas, thereby assisting neurosurgeons in intervention planning. For the past 24 years, poor fiber tracking models have remained prevalent in clinical research and commercial neurosurgical navigation software (Chapter 3), inaccurately and unreliably detecting the main orientation of nerve fiber architecture based on oncological dMRI data. Nevertheless, the neurosurgical community has been globally unaccustomed to the use of advanced tractography methods in preoperative planning due to a user-dependent, time-consuming MR image processing workflow and challenging interpretation of fiber tracking results intraoperatively.

To enable faster, more reliable, and fully automated workflow, a clinical research tool, named FT4Onco (Fiber Tracking for Oncology) was designed and a prototype thereof was realized. The solution was engineered in accordance with a software development process outlined by the V-model. Starting from a blank canvas, interviews were held with the main stakeholders for this piece of software, neurosurgeons and neuroradiologists, to identify contemporary challenges and collect unmet needs in tractography-guided brain tumor resection planning (Chapter 4). Besides requirements modeling, this thesis describes design

considerations, design boundaries, and software architecture (Chapter 5). Moreover, the integration of various open-source as well as vendor-supplied image processing tools is explained, and potential limitations of selected functionalities are presented. Given that the development of FT4Onco was conducted in an industrial environment under the auspices of Philips Healthcare, the demonstrator comprises solely neuroimage processing tools with licenses permitting their utilization in commercial research.

In Chapter 6, FT4Onco was first evaluated on routine clinical data with initially interviewed end-users at Klinikum rechts der Isar der Technischen Universität München in Germany. This clinical evaluation proved that the utilized software packages facilitate the optimization of daily presurgical workflow through complete automation and significant acceleration of the fiber tracking process. Moreover, despite the low spatial and angular resolution of routinely acquired datasets at this clinical center, advanced tractography with the constrained spherical deconvolution model succeeded in the reconstruction of three eminently important eloquent WM tracts affected by large glial tumors. Outcomes of user evaluation were used for further improvement of the prototype.

The final version of FT4Onco underwent a technical cross-validation (Chapter 7), conducted in cooperation with the Department of Imaging and Pathology, Translational MRI, Katholieke Universiteit Leuven (KUL) in Belgium. Owing to the absence of ground truth in single-subject in vivo tractography and lack of validation consensus, the cross-validation protocol involved defining silver standards, against which voxel-wise volumetric comparisons were made. In two sets of pairwise agreement tests, the FT4Onco output of eight reconstructed WM tracts in glioblastoma patient datasets was compared with tractographical reconstructions generated with the KUL NeuroImaging Suite (KUL_NIS) and anatomical models available from the HCP842 tractography atlas. As discussed in Chapter 8, the highest achieved average bundle similarities of 0.59 (FT4Onco vs. KUL_NIS) and 0.42 (FT4Onco vs. HCP842), measured by the weighted Dice coefficient, indicated the future need for more extensive clinical validation studies and reliability tests as well as the verification of FT4Onco-based anatomical localization by intraoperative functional direct electrical stimulation.

Assuming clinicians' awareness of both the limitations in the MR neuroimaging domain as well as the real capabilities and bottlenecks of advanced fiber tracking methods, significant enhancement of preoperative planning by FT4Onco is deemed feasible.

Contents

Abstract	1
Summary	3
Contents	5
Nomenclature	9
1 Introduction	13
1.1 Problem statement & objectives	14
1.2 V-model design	16
1.3 Thesis scope	17
1.4 Added value to clinical research	18
1.5 Thesis outline	19
2 Clinical & technological background	21
2.1 Neuroanatomy overview	21
2.1.1 Cerebral anatomy and function	21
2.1.2 White matter fiber tracts	23
2.2 Neurosurgical oncology	25
2.2.1 Classification of brain neoplasms	25
2.2.2 Glioblastomas	26
2.2.3 Neurosurgical workflow	27
2.3 Diffusion magnetic resonance imaging (dMRI)	29
2.3.1 Physics of diffusion in biological tissue	29
2.3.2 Diffusion weighted imaging (DWI)	30
2.3.3 Diffusion tensor imaging (DTI)	32
2.3.4 High angular resolution diffusion imaging (HARDI)	34
2.4 Diffusion MRI-based tractography	37
2.4.1 Deterministic vs. probabilistic tractography	37
2.4.2 Diffusion tensor tractography	38
2.4.3 Constrained spherical deconvolution	39
2.4.4 Whole brain tractography	40
2.4.5 Anatomically constrained tractography	41
2.4.6 Atlas-based tractography	42

3	Review of the state of the art	45
3.1	Commercial solutions	45
3.2	Open-source tools	45
4	Requirements specification	51
4.1	Clinical perspective	51
4.2	Current challenges and unmet user requirements	51
4.3	Functional & non-functional requirements	57
5	Design description	59
5.1	Design considerations	59
5.1.1	FT4Onco as a Philips IntelliSpace Discovery plugin	59
5.1.2	FT4Onco as a command-line tool	62
5.2	Workflow optimization	65
5.2.1	Pipeline architecture	65
5.2.2	Handling data input and output	67
5.3	Anatomical MRI data processing chain	69
5.3.1	Brain segmentation and cortical parcellation	69
5.3.2	Tumor segmentation	70
5.3.3	T1 and T2 brain extraction	72
5.4	Diffusion MRI data processing chain	73
5.4.1	Diffusion data quality inspection	73
5.4.2	Denoising	74
5.4.3	Gibbs ringing correction	75
5.4.4	Motion correction with outlier detection	76
5.4.5	B_1 inhomogeneity correction	79
5.4.6	DMRI-T1 co-registration, brain extraction, distortion correction . . .	80
5.5	Tractography chain	82
5.5.1	Response function estimation	82
5.5.2	Estimation of fiber orientation distribution	83
5.5.3	Whole brain tractography	85
5.5.4	Bundle recognition	87
5.5.5	Spurious fiber filtering	88
5.6	Visualization & viewing	92
5.6.1	Formatting image processing output	92
5.6.2	Tumor-tract relationships	93
5.6.3	Visualization of fiber tracking uncertainty	94
5.6.4	Selective viewing	96
6	Verification, evaluation & sensitivity analysis	99
6.1	Software verification	99
6.2	Clinical evaluation	100
6.2.1	Assumptions for successful evaluation	101
6.2.2	MRI data selection	102

6.2.3	Hardware setup and pipeline configuration	103
6.2.4	Experimental design	105
6.2.5	Evaluation outcomes	106
6.2.6	Clinical implications	109
6.3	Sensitivity analysis	113
7	Technical cross-validation	119
7.1	Hurdles in tractography validation	119
7.2	Experimental setup	120
7.3	Non-negligible pipeline differences	123
7.4	Bundle comparison and analysis	124
7.5	Cross-validation outcomes	125
8	Discussion, recommendations & conclusions	131
8.1	User needs fulfillment	131
8.2	Architecture and site-specific workflow optimization	135
8.3	Repeatability, replicability, reproducibility, reliability & robustness	136
8.4	Future development of FT4Onco	138
8.5	Concluding remarks	139
	Appendices	141
A	Technical specification of FT4Onco	141
B	Functionality comparison across pipelines	144
C	Clinical evaluation questionnaire	146
D	Technical cross-validation results	147
	List of publications	149
	Acknowledgements	151
	Curriculum Vitae	153
	Bibliography	155

Nomenclature

Symbols and units

Δ	time between two diffusion-sensitizing gradient pulses	s
δ	duration of a diffusion-sensitizing gradient pulse	s
ℓ_{\max}	highest spherical harmonics order	
η	medium viscosity	$\text{N} \cdot \text{s}/\text{m}^2$
λ	isotropic Laplacian convolution filter	
\mathcal{X}	reconstructed bundle X in cross-validation comparison	
\mathcal{Y}	reference bundle Y in cross-validation comparison	
μ	mean	
∇	vector differential operator	
ρ	Pearson product-moment correlation coefficient	
σ	standard deviation	
τ	relative fiber-to-bundle coherence threshold	
\mathbf{r}	vector determining particle position	
θ	angular threshold for fiber tracking	$^\circ$
ζ	derivative filter for convolution stabilization along a slice profile	
b	diffusion weighting factor	s/mm^2
B_0	main magnetic field intensity	T
B_1	radiofrequency field	MHz/T
C	particle concentration	
D	diffusion coefficient	m^2/s
J	particle flux	
r	particle radius	μm
T	thermodynamic temperature	K

Abbreviations

2D, 3D, ...	#-Dimensional
5TT	five-Tissue-Type image volume for anatomically constrained tractography
ACT	Anatomically Constrained Tractography
AD	Axial Diffusivity
ADC	Apparent Diffusion Coefficient
AF	Arcuate Fasciculus
AFD	Apparent Fiber Density
AFQ	Automatic Fiber Quantification
API	Application Programming Interface
ASL	Arterial Spin Labeling
BA	Bundle Adjacency
BBB	Blood-Brain Barrier
BIDS	Brain Imaging Data Structure

BOL	Bundle OverLap
BOR	Bundle OverReach
C	Cingulum
CE	Contrast-Enhanced
CFR	Code of Federal Regulations
CG	Conjugate Gradient
CN	Computation Node
CNN	Convolutional Neural Network
CNS	Central Nervous System
CPU	Central Processing Unit
CSD	Constrained Spherical Deconvolution
CSF	CerebroSpinal Fluid
CST	CorticoSpinal Tract
CT	Computed Tomography
DBS	Deep Brain Stimulation
DCS	Direct Cortical Stimulation
DES	Direct Electrical Stimulation (electrocorticography)
DG	Diffusion-sensitizing Gradient
DICOM	Digital Imaging and COmmunications in Medicine
DKT	Desikan-Killiany-Tourville atlas
DL	Deep Learning
dMRI	diffusion Magnetic Resonance Imaging
dODF	diffusion Orientation Distribution Function
DSC	Sørensen-Dice Similarity Coefficient
DSI	Diffusion Spectrum Imaging
DTI	Diffusion Tensor Imaging
DWI	Diffusion Weighted Imaging
EPI	Echo-Planar Imaging
FA	Fractional Anisotropy
FACT	Fiber Assignment by Continuous Tracking
FBC	Fiber-to-Bundle Coherence
FDA	Food and Drug Administration
FLAIR	FLuid-Attenuated Inversion Recovery (anatomical MR image)
FOD	Fiber Orientation Density
fODF	fiber Orientation Distribution Function
FRT	Funk-Radon Transform
FT	Fiber Tracking
FT4Onco	Fiber Tracking for Oncology
GBM	GlioBlastoma Multiforme
GM	Grey Matter
GPU	Graphics Processing Unit
HARDI	High Angular Resolution Diffusion Imaging
HCP842	Human Connectome Project (population-averaged tractography atlas)
HGG	High-Grade Glioma
HTTP	HyperText Transfer Protocol

ICAP	Imaging Clinical Applications and Platforms (Philips division)
IDH	Isocitrate DeHydrogenase
IFOF	Inferior Fronto-Occipital Fasciculus
ILF	Inferior Longitudinal Fasciculus
ISD	Philips IntelliSpace Discovery research platform
ISO	International Organization for Standardization
IST	Interpolated Streamline Tractography
KUL_NIS	Katholieke Universiteit Leuven NeuroImaging Suite
LGG	Low-Grade Glioma
MD	Mean Diffusivity
MDF	Minimum average Direct-Flip (distance metric)
MdLF	Middle Longitudinal Fasciculus
MEG	MagnetoEncephaloGraphy
MERC	Medical Ethics Review Committee
MNI	Montreal Neurological Institute and Hospital coordinate system
MRI	Magnetic Resonance Imaging
NIFTI	Neuroimaging Informatics Technology Initiative
NOS	Not Otherwise Specified
OR	Optic Radiation
PDF	Probability Density Function
PGSE	Pulsed Gradient Spin Echo
QSI	Q -Sampling Imaging
RA	Radial Anisotropy
REST	REpresentational State Transfer
RF	RadioFrequency
ROI	Region of Interest
rs-fMRI	resting-state functional MRI
SC	SubCortical grey matter
SDF	Spin Distribution Function
SDM	Signal Decay Metric
SE	Spin Echo
SH	Spherical Harmonics
SIFT	Spherical-Deconvolution Informed Filtering
SLF	Superior Longitudinal Fasciculus
SLR	StreamLine-based Registration
SNR	Signal-to-Noise Ratio
SVD	Singular Value Decomposition
T1	anatomical MR image weighted by spin-lattice relaxation times
T1C	contrast-enhanced anatomical MR T1-weighted image
T2	anatomical MR image weighted by spin-spin relaxation times
tb-fMRI	task-based functional MRI
TDI	Track Density Image
TMS	Transcranial Magnetic Stimulation
TRF	Tissue Response Function
UID	Unique Identifier

URI	Uniform Resource Identifier
VOI	Volume of Interest
WBT	Whole Brain Tractography
WHO	World Health Organization
WM	White Matter

Physics constants

π	the ratio of a circle's circumference to its diameter	3.14159265359
k	Boltzmann constant	$1.380649 \times 10^{-23} \text{ m}^2 \text{ kg s}^{-2} \text{ K}^{-1}$

1 Introduction

Neurosurgery planning is an indispensable prerequisite for effective brain tumor resection. Medical image processing platforms with automated software have a high potential to support neurosurgeons in preoperative decision-making by deriving pivotal information from routine imaging data. This thesis describes a clinical research software, named FT4Onco (Fiber Tracking for Oncology), that has been designed to address unmet needs in clinical presurgical workflow. This introductory chapter presents the primary topical subjects of focus in this work with its objectives, important thematic constraints, and the design approach. The last two sections discuss the added value of the prototype to clinical research, outline each chapter, and summarize all contents.

Clinical neuro-oncology is the study of neoplastic lesions in the central nervous system (CNS, the brain and spinal cord), many of which demand rapid application of curative procedures in order for affected individuals to survive. The World Health Organization (WHO) groups CNS neoplasms according to their histological characteristics into various families, providing neuro-oncologists with a widely accepted reference for classification [1]. Brain diseases can be examined by neuroimaging, which encompasses a set of tools to directly or indirectly draw inference about structural and functional properties of the human CNS. In neuro-oncology, it provides considerable assistance when performing radiographic evaluation of brain tumors based on diverse imaging biomarkers [2]. Clinical practice nowadays utilizes two standardized imaging techniques involving computed tomography (CT), and magnetic resonance imaging (MRI). Both these imaging modalities are mechanically noninvasive, unless contrast-enhancing media are administrated to aid tissue type differentiation.

In general, CT imaging is conveniently fast and less sensitive to motion effects than MRI. From the application perspective, CT is an excellent method for bone imaging and discovering areas of hemorrhage, while soft-tissue imaging with CT provides limited detail. Conversely, MRI has the ability to differentiate soft-tissue (e.g. fat, water, muscle) better than CT without exposing the examined subject to ionizing radiation. Brain MRI utilizes tissue magnetization properties to localize neuroanatomy and neurovasculature (anatomical MRI, angiography, venography), detect consumption levels of blood oxygenation to infer about function (functional MRI), quantify blood volume by sampling blood flow (perfusion MRI, arterial spin labeling – ASL), measure metabolite concentrations within tissues (MR spectroscopy), and most eminently for this work, help delineate white matter (WM) nerve fibers by tracing the orientation of water diffusion (diffusion MRI).

In addition to the diagnostic power of the mentioned neuroimaging modalities, they also help estimate patient prognosis (lesion progression, neurological deficits, recurrence likelihood, etc.), and select the most appropriate treatment approach. The choice of brain tumor therapy is vastly influenced by numerous lesion characteristics, such as size, type, and location as well as patient's overall health and preferences. Therapeutic strategies may involve watchful waiting, supervised medication, chemotherapy, radiation therapy, neurosurgical interventions, or the combination of radiation and chemotherapy with or without surgery [3]. For many decades, the three main cornerstones of brain tumor treatment have remained the same: maximum surgical removal followed by external beam radiation therapy and chemotherapy.

1.1 Problem statement & objectives

This thesis is entirely focused on clinical workflow in the planning stage of oncological neurosurgery. Special attention herein is paid to surgery planning for high-grade tumors, particularly glioblastomas, because of their rapid and aggressive growth, infiltrating adjacent healthy WM structures, and a very poor prognosis. Aiming for maximized safe lesion removal, brain tumor surgery planning typically relies on soft-tissue contrast provided by anatomical MRI scans to localize pathology, and diffusion MRI (dMRI) scans to characterize relationships between tumor tissue and surrounding structures (nerve fibers) as well as to define resection margins. Standard clinical dMRI protocols for tumor mapping have used diffusion tensor imaging (DTI) along 6–32 directions with a diffusion weighting factor (b -value) of 1000 s/mm^2 . A DTI acquisition is relatively fast (whole brain coverage within ~ 5 minutes) and available on most clinical systems [4]. DTI-based tractography methods facilitate noninvasive reconstruction and visualization of nerve fibers by modeling physiological water directionality and motion based on dMRI data [5, 6]. Despite the growing usage of advanced tractography algorithms in clinical research, presurgical fiber tracking applications predominantly incorporate the deterministic DTI-FACT algorithm (Fiber Assignment by Continuous Tracking) [7]. This most widespread implementation has yet proven inappropriate in multiple aspects [8].

The diffusion tensor model inherently assumes a unique orientation of nerve fibers in each image voxel that can be represented by the tensor’s principal eigenvector [9]. However, it has been stated that the proportion of WM voxels containing crossing fibers (multiple fiber populations propagating in various orientations within a brain region) reaches up to 90 % [10]. Besides crossing, WM fibers may bend, fan or diverge at intra-voxel level [11], rendering the tensor model assumptions on water diffusion invalid. For instance, the most frequently scrutinized bundle (a set of WM fibers) in neurosurgery, the pyramidal tract, can only be partially detected because of the improper resolution of fiber propagation in its intersection with the superior longitudinal fasciculus [12], leading to a surgically evoked loss of motor function [13]. In addition, DTI-FACT algorithms have shown inability to detect fibers in edematous zones around brain tumors [14].

Fiber tracking has been infrequently utilized in neurosurgery planning owing to the prevalence of the DTI-FACT model in clinical neuronavigation software [15]. Maximized identification of individual WM bundles requires more sophisticated models that estimate a voxel-wise distribution of fiber orientations. However, the uptake of advanced models by neurosurgical practice is impeded due to multiple factors [16, 17]: (1) lack of awareness or misconception of technical nuances that underpin the reconstructed nerve fiber bundles, (2) unfamiliarity with the real capabilities of advanced techniques; (3) long acquisition or processing times incompatible with acute neurosurgical scenarios, such as immediate need for tumor debulk in high-grade glioma cases; and (4) perceiving advanced fiber tracking approaches as too complex. An approach capable of resolving crossing fibers and even peritumoral propagation is realized in the constrained spherical deconvolution (CSD) model [18, 19] that relies on high angular resolution diffusion imaging (HARDI) data (at least 60 diffusion directions weighted at $b = 1000\text{--}4500 \text{ s/mm}^2$) [20]. Higher bundle reconstruction feasibility with CSD compared to DTI-FACT in the context of tumor resection planning has been reported in several studies [21, 22, 23].

In order to fully exploit the benefits of the CSD model to create high-quality bundle reconstructions, dMRI data need to undergo a sequence of advisable preprocessing steps (ca. 20–25) to compensate for artifacts such as image noise, geometric distortions, slice/volume misalignment or motion [24]. Such image corrections demand substantial technical and image processing knowledge that may be lacked by medically trained clinical staff. Custom-made data processing pipelines containing a mixture of open-source and, if available, the clinic’s proprietary algorithms are often assembled to optimize site-specific presurgical workflow. Nevertheless, these workflows reach beyond clinically applicable timelines, require a couple of manual data handling and formatting steps, work on data acquired with inflexible dMRI acquisition protocols, and produce inconsistent results. Moreover, the integration of tractography output (reconstructed bundles) into intraoperative neuronavigation systems is often nearly impossible, and final visualizations only give limited surgically relevant information. Finally, advanced tractography techniques were typically developed by imaging scientists, mathematicians, or MR physicists with little input from medical experts or neuroanatomists as well as limited consideration to clinical use.

As reported by neuroradiologists and neurosurgeons, these issues collectively lead to a suboptimal workflow hampering the preparation for semi-urgent or elective surgeries as well as reluctance to use advanced tractography methods in acute cases. Hence, there is a clear need for optimized and user-independent solutions. In this thesis, the overall aim was to design and develop fully automated clinical research software to assist tumor resection planning, incorporating the best-performing open-source tools for dMRI data processing and advanced fiber tracking. Achieving this goal required the following major steps:

- ▶ Identify unmet needs in the presurgical workflow of oncological neurosurgery by interviewing neuroradiologists and neurosurgeons.
- ▶ Optimize (accelerate and automate) the preoperative workflow of diffusion and anatomical MRI data processing on routine clinical data.
- ▶ Improve the quality and accuracy of dMRI-based tractography output using the CSD model, and probabilistic tractography algorithms to overcome DTI-FACT limitations.
- ▶ Represent fiber tracts and tumors in a more informative three-dimensional multiparametric fashion via indication of fiber tracking confidence and relationships between tumor and healthy tissue.
- ▶ Deploy the finalized application at clinical sites to evaluate and validate its output quality and performance with potential end-users.

1.2 V-model design

Envisioning and engineering a software solution demands a well-structured approach to ensure all user requirements are met. As opposed to semi-automated or user-centered software designs, FT4Onco (Fiber Tracking for Oncology) was meant to become a data processing application with a fully automated workflow, for which the design process is best defined by a flow chart outlining sequential events. Therefore, the so-called V-model (Figure 1.1), a.k.a. V-shaped model, was selected as the ideal software development process representation [25].

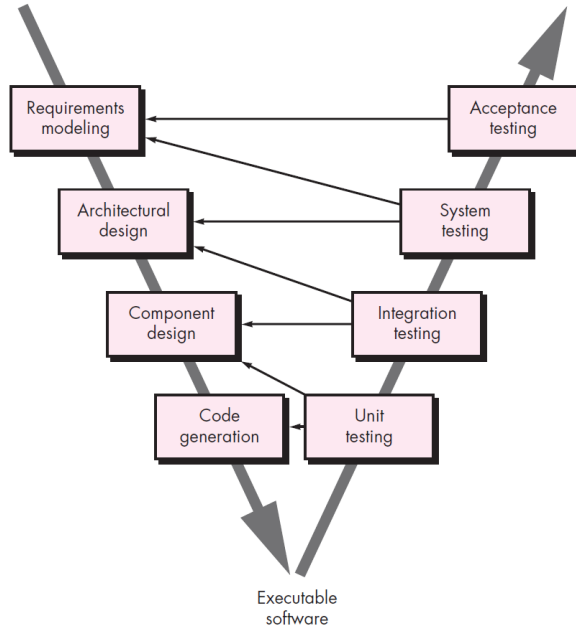


Figure 1.1: V-model diagram in software development. Moving down the left side of the V, top-level requirements are progressively broken down into more detailed functional and technical requirements. Moving up the right side of the V after code generation, the quality of conformance and quality of design are validated against defined requirements (arrows) to ensure that a “good enough” software tool is developed [26]. In this thesis, the descending stages of the V-model are described in Chapters 4 and 5, and the ascending stages are addressed in Chapters 6 and 7. Section 8.1 discusses acceptance testing based on identified user requirements.

The V-model is a variation of a more generic waterfall model, and its use is considered advantageous in multiple ways. Consecutive design phases are completed one at a time in a hierarchical perspective from high-level to low-level design. Such partitioning permits incremental development at each iteration to predict the impact of intermittent changes. Finalized steps are retrospectively correlated with assigned requirements, which is a validation method commonly known as cross-referencing. Also, given the clearly defined and fixed requirements for this thesis, it is a suitable model focusing on verification and validation in early stages of the development cycle, thereby increasing the likelihood of building an error-free and high-quality solution.

The descending part of the V-model is typically understood as defining problems and proposing solutions. Requirements identification is followed by architectural system design, which conveys information on system elements (hardware, software), and relationships among those elements. Next, individual modules (functionalities) are derived from the system design, and data handling between these modules (or remote systems) is specified. Eventually, each module is described with respect to its underlying structure, which is commonly known as low-level design.

Once the code implementation has been finalized, the ascending phase (a series of quality assurance actions) of the V-model commences. Debugging operations and solitary module executions are performed to eliminate errors and inconsistencies at unit level (unit testing). Thereafter, modules are integrated and tested together to ensure smooth intermodular compatibility. The last step before presenting the solution to end-users is system testing, which examines the interdependency and communication among functionalities across the entire application. Both functional and non-functional requirements (e.g. performance) are verified at this stage.

In the final phase, the resulting software is delivered to the intended real-world environment, where user acceptance testing happens. At this point, end-users validate the developed application for adherence to their requirements and compliance with all criteria. Essentially, the system undergoes final verification before transformation into a (research) product. Multiple instances of user acceptance testing may be conducted [26].

1.3 Thesis scope

The presented thesis reports research and design activities conducted within the European TRABIT consortium (TRAnslational Brain Imaging Training, www.trabit.eu). Oncological neurosurgeons and neuroradiologists are defined as the main clinical end-users of the herein developed research application. The goal is to offer this piece of software to clinical researchers investigating the utilization of advanced dMRI tractography methods in a neurosurgical workflow.

Initial requirements engineering involved direct communication with customers to understand their expectations. For this purpose, clinical staff (neuroradiologists, neurosurgeons) was interviewed at several European institutions, some of which are Philips customers or TRABIT partners (Table 1.1). Furthermore, conference material and proceedings were screened for further details about user requirements at other sites.

The development of FT4Onco had numerous intentionally defined boundaries explained in Chapter 5. These limitations are related to the use of selected presurgical brain MR imaging contrasts for brain segmentation, tumor localization, and WM bundle reconstruction. Further restrictions include the exploitation of commercially adoptable image processing functionalities coming from open-source distributions, and aiming for wide compatibility on Philips MRI data.

Testing whether the final solution fulfils its intended purpose and meets all identified requirements was done via in-house verification, clinical evaluation, and cross-validation with another clinical application used at University Hospital in Leuven (Belgium). A complete clinical validation study to assess the ultimate impact of FT4Onco-based surgery planning on intraoperative workflow and postoperative outcomes was out of scope.

Institution	Location
Leuven University Hospital	Leuven, Belgium
Elisabeth Tweesteden Ziekenhuis	Tilburg, The Netherlands
Erasmus University Medical Center	Rotterdam, The Netherlands
Klinikum rechts der Isar	Munich, Germany
Amsterdam Universitair Medische Centra	Amsterdam, The Netherlands
Carlo Besta Neurological Institute	Milan, Italy
Akademiska Sjukhuset	Uppsala, Sweden
Haukeland University Hospital	Bergen, Norway
Sainte-Anne Hospital	Paris, France

Table 1.1: List of European medical centers approached during requirements collection.

1.4 Added value to clinical research

This thesis presents the unmet requirements, user-centered design, clinical evaluation, and technical cross-validation of a research software application for neurosurgery planning with advanced dMRI-based fiber tracking. To our knowledge, the developed research prototype and its architecture do not represent a clone, copy or recipe compilation of any other publicly available image processing pipeline. The hereinafter presented solution brings an added value to the clinical research community in multiple aspects.

Firstly, the orchestration and arrangement of all functional components within the pipeline is unique, and has never been reported in literature as a whole. Clinical workflow is enhanced through a series of 24 sequentially executed processing tasks with fully automated workflow. Changing the order of image processing steps within FT4Onco may result in unforeseen glitches at successive tasks, leading either to hampered inference about tractography output or obtaining no meaningful results.

Secondly, all processes on anatomical and diffusion MRI data are configured to reliably analyze two types of clinical patient datasets, which are acquired using standardized MRI protocols in the routine clinical workflow of two sites: University Hospital in Leuven (Belgium) and Klinikum rechts der Isar in Munich (Germany). Related optimization of image processing parameters for these data required extensive empirical testing, literature screening, expert consultations, and experimental setup.

Thirdly, the vast majority of freely available software packages are published to support a limited area of application. Usually, these tools were developed ad hoc, and their adoption as building blocks in a completely new configuration, aiming at addressing unmet user needs in a new area, demands substantial data adjustments to fit input constraints (format, encoding, compression, size, etc.) as well as fine-tuning of algorithmic parameters. The output constructed by these tools thus has to be carefully checked prior to forwarding it as a source for the next consecutive step in the pipeline. In the pursuit of robustness to new datasets, the functionally most efficient placement of employed tools in the pipeline was determined by numerous optimization tests and verification on selected datasets.

In addition, the concept of FT4Onco attempts to reflect the latest research insights, and is therefore a product of applied science. The adoption of toolkits that are distributed under licenses not permitting commercial research use was avoided by design. Consequently, workaround strategies had to be implemented to account for artifacts in diffusion MRI data, such as motion correction (Section 5.4.4), susceptibility-induced distortion correction, or the co-registration of diffusion MRI-derived parametric maps with the T1 image (Section 5.4.6).

Finally, the scientifically most relevant outcomes of this work are presented in Chapters 6 and 7. Chapter 6 presents observations from the qualitative evaluation of image processing outcomes by clinical experts, investigates the sensitivity of output bundle quality to varying initialization of tractography parameters, and suggests a suitable parametric setup that enables reconstructing the most anatomically plausible bundle representations (with respect to atlas models). This setup is later applied in the cross-validation experiment reported in Chapter 7, where nerve fiber bundle reconstructions from FT4Onco are quantitatively compared with outcomes from another regularly utilized software to judge the applicability of FT4Onco in daily clinical research.

1.5 Thesis outline

Chapter 2 concisely reviews human brain anatomy and explains brain tumor classification with particular focus on glioblastomas and their typical manifestation in clinical neuroimaging. Thereafter, an insight into the procedural stages of clinical neurosurgery workflow (pre-, intra-, and postoperative) is given. The next sections deal with the basic principles of DTI and HARDI to support the understanding of the design choices presented later. The last part explains the reconstruction of WM nerve fibers from diffusion MR images using both deterministic and probabilistic tractography approaches.

Chapter 3 consists of a review of prior art, providing an overview of commercially available software and open-source freeware for diffusion MRI data processing and tractography. A comparison of open-source packages is reported to understand the complexity of available dMRI data processing pipelines, and their maturity to address the main topic of this thesis.

Chapter 4 summarizes all clinical needs and user requirements in presurgical workflow as presented by clinicians at visited centers. Further sections present the decomposition of corresponding user requirements into functional, and non-functional requirements as prescribed by the descending part of the V-model.

Chapter 5 is dedicated to the design description discussing particular choices in hardware and software, and the description of system architecture. Apart from these topics, this chapter deals with the cause and mitigation of artifacts in diffusion MR images, justifying the reasons for integrating individual software modules.

Chapter 6 reports relevant software assessment steps to test whether the designed application meets the initially defined requirements. Following the ascending blocks of the V-model, the implementation is retrospectively verified by a set of compliance tests at multiple levels. Eventually, the clinical evaluation of the designed solution at Klinikum rechts der Isar in Munich (Germany) is reported, where neuroradiologists and neurosurgeons interacted with FT4Onco and shared their opinions on applicability in clinical practice with comments on further improvements. The last part delivers results of a sensitivity analysis investigating the impact of changes in input tractography parameters on a given set of bundle features.

Chapter 7 presents the setup and outcomes of a quantitative technical cross-validation study performed in collaboration with University Hospital in Leuven (Belgium). In addition, this chapter shows results obtained from the cross-validation of FT4Onco output with model bundles from a tractography atlas.

Chapter 8 discusses the entire design, and presents concluding remarks on the future outlook and suggestions for improvement in terms of code structure, modularity, system architecture, and the presentation of data processing output to oncological neurosurgeons. Recommendations for deployment on premise and an optimal image acquisition protocol are proposed as well, supplemented with future research prospects.

2 Clinical & technological background

The following sections aim to describe the major central nervous system (CNS) structures and introduce key anatomical terminology associated with white matter nerve fibers. Functional importance of white matter pathways for oncological neurosurgery is also explained with deficits related to tumor-induced effects, and perioperative fiber interruption. Subsequent sections present the basic principles of diffusion MRI and tractography.

2.1 Neuroanatomy overview

Neurosurgeons' efforts in the preservation and recuperation of the human brain (cerebrum) are driven by deep knowledge of neuroanatomy. The first observations about brain anatomy were already documented by ancient Egyptians [27]. For centuries, the field has been progressively extended by expertise about the coarse brain structure and its intricate networks. This section describes the arrangement of cerebral anatomy with commonly used orientation labels. To help readers pinpoint individual anatomical landmarks, Figure 2.1 illustrates how to navigate in the brain.

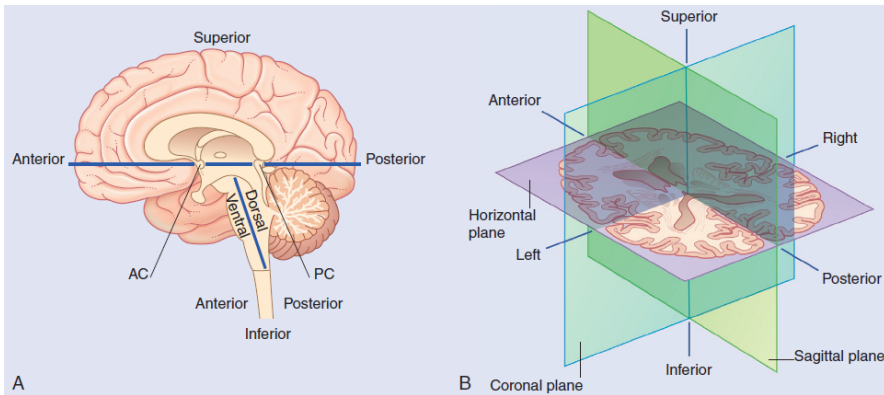


Figure 2.1: (A) Planes of reference with orientation labels for the CNS. Due to its obliquity, the brainstem is an exception to the overall standard. In some literature, the terms ventral/dorsal are used to refer to the anterior/posterior aspects with respect to the spinal cord. Similarly, the terms rostral/caudal describe the superior/inferior orientation in the brain. The blue horizontal line represents the bicommissural plane (AC = anterior commissure, PC = posterior commissure). In MRI, the horizontal plane is typically called *axial* plane. (B) Cross-section of the brain in the bicommissural plane [28].

2.1.1 Cerebral anatomy and function

The CNS is covered by three protective layers: dura mater, arachnoid mater and pia mater. The brain communicates with the entire body through the spinal cord, to which it is connected via the brainstem. At the back of the brain in the posterior cranial fossa, the center for coordination and balance is located, the cerebellum. Both the brain and spinal cord are circulated by the

cerebrospinal fluid (CSF) flowing in a set of four interconnected cavities called ventricles.

The brain accommodates approximately 86 billion neuronal cells (neurons) transmitting signals (action potentials) through a complex network of axonal connections (white matter). Neuronal bodies integrate and evaluate transferred information in different regions of the cortex (grey matter). Neurons are supported and nourished by 10–50 times more abundant glial cells (astrocytes, oligodendroglia, ependymal cells, microglia).

Continuous supply of oxygenated blood is essential for the proper functioning of the brain, and is regulated by exquisitely sophisticated control systems in the medulla oblongata. The CNS is separated from the blood by the blood-brain barrier (BBB) which is a border system of endothelial cells serving multiple functions. The BBB selectively modulates both inward and outward flow of vital metabolic nutrients (e.g. glucose) into the brain's extracellular fluid, where neurons reside. Also, the BBB is responsible for sodium-potassium (Na^+ - K^+) ion exchange, and protection from toxins or pathogens that may cause CNS infections. Especially in the presence of infiltrative tumors, fluid leakage through a disrupted BBB consequently causes the development of vasogenic peritumoral edema [29].

The folded appearance of the brain is created by gyri (ridges) and sulci (fissures, grooves) that cover the two cerebral hemispheres. The sulci patterns vary per individual, yet some are constant enough for general description. The two deepest sulci (central sulcus or Rolandic fissure, and lateral sulcus or Sylvian fissure) help divide the brain into four distinct lobes (with lobules as subunits) and the limbic system, which is also referred to as the fifth lobe (Figure 2.2). In neuroscience, brain gyri are typically assigned descriptive names explaining their primary cognitive or control function.

The *frontal lobe* is generally responsible for higher cognitive functions (e.g. concentration or emotional expression) and is divided into superior, middle and inferior parts. Medially, the anterior portion of the cingulate gyrus (center for hunger and pain) is found. The inferior frontal gyrus terminates with the olfactory bulb, which is the center for smell. Posterior segments of the frontal lobe complete the precentral gyrus, where voluntary movements are initiated. Although the precise anatomical definition is inconsistent, a part of the inferior frontal gyrus also represents the Broca's area responsible for speech production.

The *parietal lobe* is the center for motion and somatosensory functions (sensation and proprioception). The anterior lobule is marked by the postcentral gyrus, where somatic sensations from the body including touch, pressure, temperature, and pain are perceived. Commonly known as the somatosensory association area (e.g. object recognition according to weight), the supramarginal and angular gyri can be found in the posterior parietal lobe. Medially, the precuneus is covered behind the paracentral lobule.

The *occipital lobe* conducts visual information processing (sight, image recognition and perception). Its lateral surface is marked by lateral occipital gyri. Medially, the occipital lobe is bordered by the parieto-occipital sulcus and the calcarine sulcus (the seat of the primary visual cortex).

The *temporal lobe* is laterally separated into superior, middle and inferior temporal gyri, where the primary auditory cortex can be found. Auditory signals as well as short-term memory and emotions are processed in this area. Depending on the dominant hemisphere, the lateral superior portion of the temporal lobe embodies the Wernicke's area known as the center for written and spoken language comprehension.

The *limbic lobe* is concerned with mechanisms of attack and defense, creativity and feeding. The main constituents of the limbic lobe are the cingulate and parahippocampal gyri. More often, this area is referred to as the limbic system comprising the hippocampi (memory), fornix, amygdalae (emotional reactions), and hypothalamus (autonomic system control).

Deep brain anatomy is not described here in detail due to its high complexity, and less frequent occurrence of aggressive gliomas in deep subcortical regions. Functionally prominent deep brain structures include the thalamus (attention, alertness), pituitary and pineal glands (endocrine system and circadian rhythm regulation), basal ganglia (coordination of fine movements), internal capsule, a part of the limbic system, and the ventricular system.

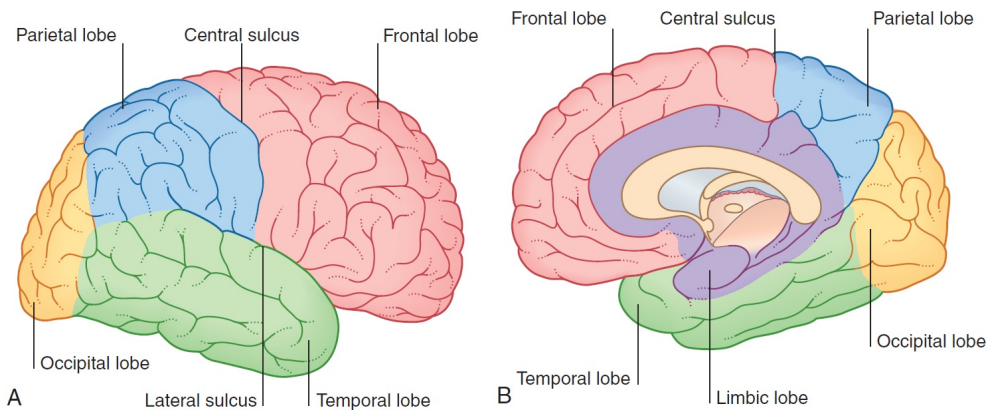


Figure 2.2: Lateral (A) and midsagittal (B) views of the five brain lobes [28].

2.1.2 White matter fiber tracts

A fiber tract (also called fascicle) is a bundle of nerve fibers carrying a common function. Cerebral white matter pathways are typically divided according to propagation direction into three categories: *projection* fibers propagating from the distant inferior brain areas to the cortex; *association* fibers connecting two regions in the same hemisphere; and *commissural* fibers bridging the two brain hemispheres. The description of all WM bundles in the brain is beyond the scope of this work. Instead, attention is paid to selected fiber bundles (listed in Table 2.1) that can be collectively found in diverse regions of the human brain, and that simultaneously play a major role in surgical neuro-oncology. Detailed connectional anatomy, functional relevance, and consequences of bundle damage are summarized in extensive reviews, e.g. [30].

In neurosurgery, the corticospinal tract (CST) is perceived as the most important projection bundle of the CNS. Damage to this pathway leads to the impairment of voluntary movements, either manifested as motor paresis (weakness) or paralysis (loss). Moreover, the CST is vulnerable to disease given its vast extent along the entire vertical length of the CNS. The majority of the CST fibers originate from the precentral gyrus (primary motor cortex), the postcentral gyrus (primary sensorimotor cortex), the parietal association cortex, and descend via the internal capsule to the spinal cord.

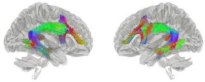
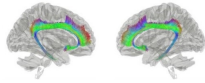
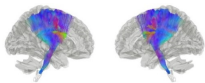
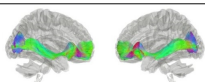
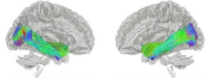
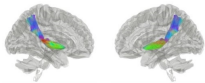
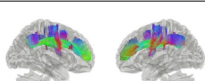

Fiber tract	Location (R-L)	Pathway	Main function
Arcuate fasciculus (AF) [31]		From the posterior temporal region to the frontal lobe, connects Broca's and Wernicke's areas	Language
Cingulum (C) [32]		From the cingulate gyrus to the entorhinal cortex	Communication among components of the limbic system
Corticospinal tract (CST) [33]		From the primary motor and sensorimotor cortices via internal capsule to spinal cord	Voluntary motion
Inferior fronto-occipital fasciculus (IFOF) [34]		From frontal to occipital lobes	Semantic language processing, goal-oriented behavior
Inferior longitudinal fasciculus (ILF) [35]		From temporal to occipital lobes	Visual processing and language comprehension
Middle longitudinal fasciculus (MdLF) [36]		From the superior temporal gyrus to the parietal and occipital lobe	High-order acoustic information processing
Superior longitudinal fasciculus (SLF) [37]		From the parietal to frontal lobe (dorsal SLF I, middle SLF II, ventral SLF III)	Visuo-spatial
Optic radiation (OR) [38]		From the lateral geniculate nucleus to the primary visual cortex	Vision

Table 2.1: Nomenclature and macroscopic description of WM fiber bundles targeted for tractography in this thesis. Locations of particular bundles in the right and left hemisphere (R-L) are shown with reference to the HCP842 tractography atlas in the MNI152 coordinate space [39].

Another projection fiber, the geniculocalcarine tract or optic radiation (OR), links the thalamus with the calcarine sulcus, and its preservation is important to minimize postoperative visual deficits.

Short association fibers connect brain gyri within a lobe while long association fibers link one lobe with another. In neurosurgery, special care is taken when operating around the arcuate fasciculus (AF, sometimes described as SLF IV) since an interruption to this pathway leads to the inability to produce an answer to a comprehended language input. Other crucial association fibers include the superior longitudinal fasciculus (SLF) linking the occipital and frontal lobes, the inferior fronto-occipital fasciculus (IFOF) linking the frontal lobe with the occipital lobe, and the cingulum (C) linking the cingulate gyrus with the parahippocampal gyri.

The largest commissural fiber bundle is the corpus callosum that consists of about 200–300 mill. axons connecting the two cerebral hemispheres. Damage to callosal fibers may cause impaired verbal and visual information processing. The next two functionally important commissural bundles are the anterior and posterior commissures.

2.2 Neurosurgical oncology

Surgical neuro-oncology is a field specializing in the treatment of brain, spinal cord, and peripheral nerve lesions, many of which pose life-threatening risks to the patients. Every pathological finding is reviewed by multidisciplinary teams (typically referred to as *tumor board*), consisting of neurological surgeons, neurologists, radiologists, physiatrists, psychiatrists, endocrinologists, and radiation oncologists. This section aims to give insights into brain tumor classification and describe essential parts of a standard neurosurgical workflow.

2.2.1 Classification of brain neoplasms

Brain tumors are subcategorized into primary brain tumors and metastatic tumors. According to their growth speed and aggressiveness to their surrounding tissue, diffuse, nondiffuse, and mixed-type tumors are recognized. Pathology examination based on medical images helps determine whether a lesion is benign (noncancerous) or malignant (cancerous). Lesions are stratified depending on their originating cellular constituents (glia, astrocytes, ependymal, mesenchymal cells, etc.), anatomical location (e.g. tumors of the pineal region), and macromolecular biomarkers (e.g. oligodendroglioma IDH-mutant) into several pathologic grades (WHO grade I–IV) [40].

Cerebral tumors may originate either externally (extra-axial tumors) from structures surrounding the brain (e.g. skull or meninges), or from the cerebral mass and its cells (intra-axial tumors) [41, 42]. Intra-axial tumors are further grouped according to their location into supratentorial (found in the cerebrum and diencephalon) and infratentorial lesions (located in the cerebellum, fourth ventricle and brainstem). The term “tentorium” refers to a fold of dura mater separating the cerebrum from the cerebellum and lower brainstem portions.

Diffuse astrocytic and oligodendroglial tumors belong to the most common primary intra-axial brain tumors. A simplified classification of this tumor group is schematically illustrated in Figure 2.3. Out of these tumors, gliomas are recognized as low-grade (slowly growing, median survival rate ranges from as little as 2 up to a dozen years) or high-grade (growing fast). In its frequent usage, the term “glioma” designates only astrocytic tumors, although it could be ascribed to other tumors of glial origin (ependymal, microglial lesions, etc.) as well. General clinical aspects of gliomas include progressive neurologic deficits, such as motor weakness (45 %), headaches (54 %) or seizures (26 %). Depending on tumor location, focal neurologic deficits may occur in the frontal lobe (personality changes), temporal lobe (hallucinations, memory impairment), parietal lobe (contralateral motor or sensory impairment), occipital lobe (contralateral visual deficits, alexia), and posterior fossa (cranial nerve deficits) [43].

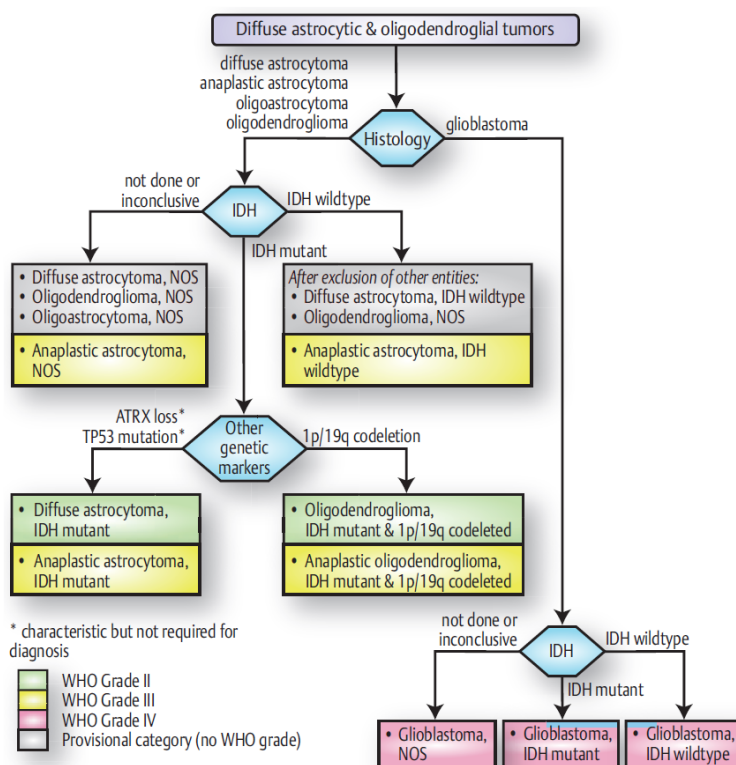


Figure 2.3: Adapted classification scheme of primary intra-axial diffuse astrocytic and oligodendroglial tumors [43]. Findings from histological examination determine first-stage diagnosis, and further mutation status assigns respective classification. Molecular genetic signatures and mutation markers (isocitrate dehydrogenase (IDH), chromosome arm deletion (1p/19q), and TP53 gene mutation) are used to differentiate among various subtypes of these tumors.

2.2.2 Glioblastomas

A glioblastoma (GBM) is not only the most common, malignant and lethal type of astrocytic tumors, but also frequently recurrent. Three subtypes are typically recognized: IDH-wildtype (primary GBM), IDH-mutant (secondary GBM) and NOS (not otherwise specified). Examples of patients with GBM are shown in Figure 2.4. A primary GBM may grow in any part of the brain, mainly in the temporal and parietal lobes, while a secondary GBM grows predominantly in the frontal lobe. Standard medication usually fails to treat GBM patients because of multiple cell types and focal necroses present in these tumors. Individuals with GBM typically experience the poorest median survival rates of 16–18 months [44, 45]. Similar to other high-grade gliomas (HGG, type III and IV), the surgical treatment of glioblastomas aims for cytoreduction to relieve mass effect (compression of adjacent brain tissue leading to displacement), and to obtain adequate tissue samples for histological analysis.

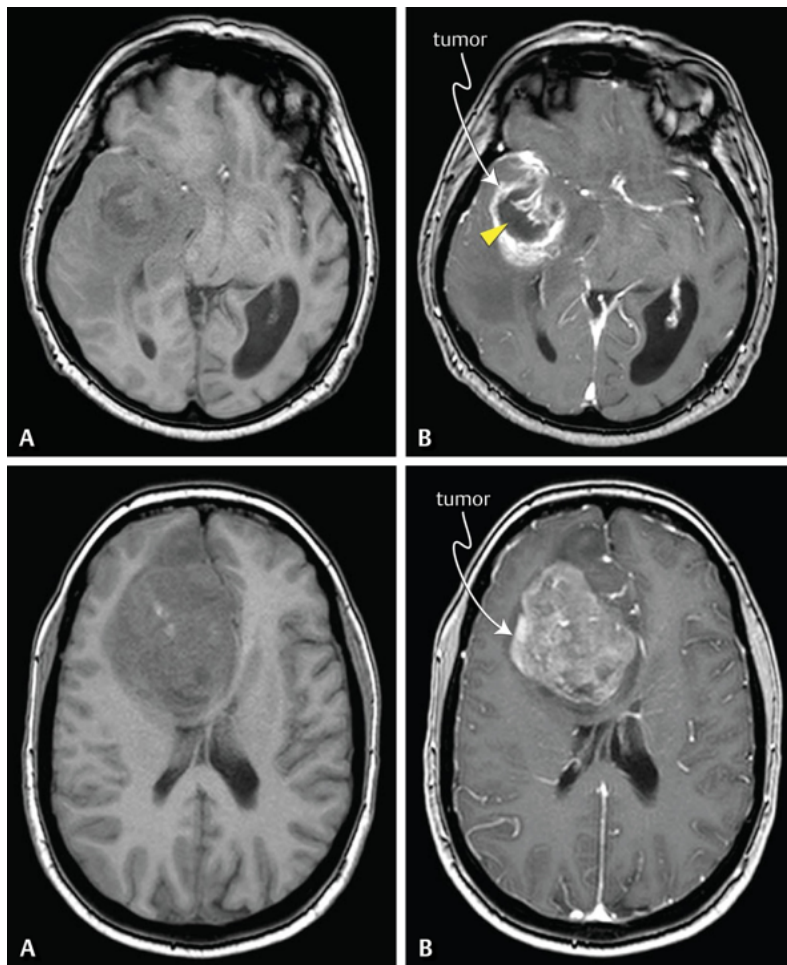


Figure 2.4: Axial glioblastoma T1 (A) and T1C (B) MR scans [43]. *Upper row:* Primary GBM with molecular signature IDH-wildtype (95 % of cases). Most often found in the temporal lobe, these tumors are characterized by extensive edema with a central necrosis (yellow arrowhead) and hyperintensities on the contrast-enhanced T1-weighted image (right). *Lower row:* Secondary GBM of type IDH-mutant without dark necrotic area.

2.2.3 Neurosurgical workflow

Prior to surgery, the identification of tumor mass and its nearby environment is done both visually and through semi-automated image analysis. HGG and particularly glioblastoma MR imaging techniques utilized in clinical practice over the past two decades are summarized in comprehensive reviews, e.g. [46, 47]. Preoperative HGG mapping (Figure 2.5) involves the acquisition of anatomical MR scans to localize the lesion (T1-weighted images), highlight areas of BBB breakdown and delineate tumor extent (contrast-enhanced T1-weighted images), find hyperintense areas representing edematous zones (T2-weighted FLAIR scans), and determine increased vascularization (perfusion weighted MRI). Functional imaging typically

aims to localize cortical areas involved in motor and language functions (functional MRI, magnetoencephalography – MEG, transcranial magnetic stimulation – TMS), and delineate subcortical white matter (diffusion MRI).

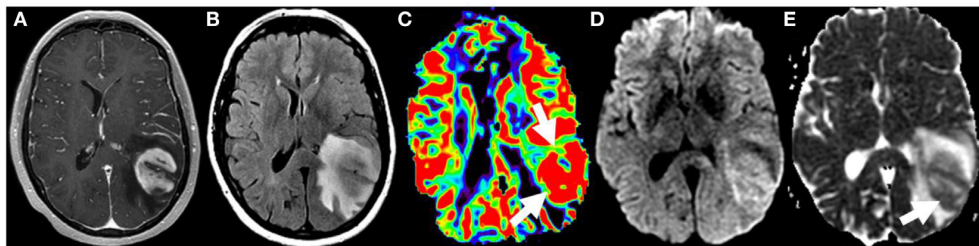


Figure 2.5: Preoperative GBM imaging. Axial contrast-enhanced T1 (A), and T2 FLAIR (B) scans show a heterogeneously enhancing tumor mass in the left parietal lobe with extensive edema. Elevated relative cerebral blood flow (white arrows) on the perfusion weighted image (C) indicates higher vascular density. Diffusion MRI maps (D, E) reveal hypercellular areas of restricted water diffusion [48].

There is a myriad of neurosurgical approaches, and selecting the optimal one is determined by tumor location, size, and urgency (growth speed). Should the path to access the lesion be too complicated via body cavities (endonasally, transsphenoidally, etc.), open-skull surgery is needed. The location of presurgically visualized white matter fascicles is validated by direct cortical (DCS) and deep brain stimulation (DBS). Awake craniotomy with intraoperative functional mapping has been reported to further improve the localization of functionally eloquent areas [49]. In highly aggressive tumors causing white matter fiber infiltration, surgeons are sometimes permitted no other choice than to mechanically invade and remove parts of healthy fibers. Whenever possible, the main objective is to maximize the extent of resection with the preservation of eloquent and other critical structures. As confirmed both by retrospective and prospective studies [50, 51], partial (incomplete) GBM resection poses risks of postoperative complications (hemorrhage, edema, herniation), and increases the likelihood of tumor regrowth. Gross total resection is therefore considered to increase the number of survival benefits [52]. Intraoperatively, neurosurgeons must also cope with the unavoidable brain shift (deformation ranging from a couple of millimeters up to several centimeters). The causes of intraoperative brain shift are multifactorial, including CSF loss, gravity or even medication. The presurgical estimation of this event is difficult, and an intraoperative update of imaging data on neuronavigation systems (e.g. with intraoperative MRI) helps overcome the problem [53].

Surgical outcomes are assessed within 48–72 hours after intervention. Resection is considered the most effective if the entire contrast-enhancing tumor portion has been removed. Early postoperative MRI scans are acquired to evaluate the extent of resection, quantify the amount of tumor residual and essentially, distinguish surgically evoked damage (manifested by hemorrhage) from tumor recurrence on contrast-enhanced structural MRI scans. Recently, the amount of tumor remnants has been reported to correlate with overall survival in GBM patients [54]. Follow-up scans are performed every three months to monitor the long-term surgical consequences, and clarify indications for repeated surgery.

2.3 Diffusion magnetic resonance imaging (dMRI)

Diffusion MRI is an MR imaging modality trying to infer features of tissue composition and microstructure without the utilization of exogenous contrast agents. The measured signal contains contributions from the displacement of water molecules that undergo diffusion in a complex set of tissue microenvironments. This section introduces the physical underpinnings of diffusion and its relation to diffusion signal weighting, explains the core physics behind a diffusion MRI sequence, and presents methods for diffusion modeling via different dMRI acquisition schemes. The principles of magnetic resonance image acquisition and diffusion MRI are extensively reviewed in relevant books [55, 56], and therefore not repeated here.

2.3.1 Physics of diffusion in biological tissue

Diffusion is a physical phenomenon manifested by random, spontaneous, microscopic movement of molecules due to thermal agitation (Brownian motion, Figure 2.6). Dating back to the mid-19th century, German physicist Adolf Fick showed that diffusion occurs along a concentration gradient. Fick introduced the diffusion coefficient (D) and defined flux (J) of a particle with concentration (C) through a surface: $J = -D\nabla C$. The negative sign in this equation embodies the notion that particles move from regions with high concentration to those with lower concentration. Later in 1905, Albert Einstein presented his “random walk” theorem, where he incorporated Fick’s laws of diffusion together with George Stokes’ principle of fluid friction [57]. This foundation yielded the Stokes-Einstein equation:

$$D = \frac{kT}{6\pi r\eta} \text{ [mm}^2/\text{s]} ,$$

where T is the thermodynamic temperature, k the Boltzmann constant, r the particle radius, and η the medium viscosity. For biological tissues at body temperature, the diffusion constant is equal to approximately $1.0 \times 10^{-3} \text{ mm}^2/\text{s}$.

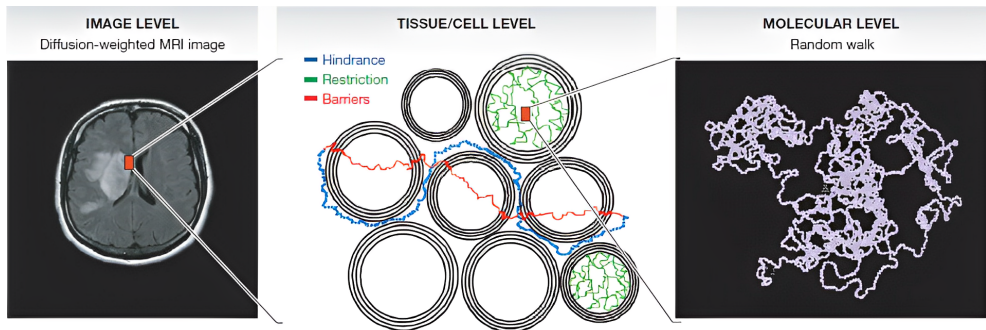


Figure 2.6: The diffusion-weighted image contrast (*right*) reflects the diffusion behavior of free water in a tissue, which is hindered (blue lines) or completely restricted (green lines) in the inter-/intracellular space (*middle*) due to the presence of multiple macromolecules and cytoskeleton. Molecules may also encounter barriers (cell walls), indicated here with red lines. *Left:* Demonstration of the incessant Brownian motion at molecular level [58].

The probability distribution function of such free particle motion $p(\mathbf{r}, t)$ (also known as the diffusion propagator, which is modeled to estimate the principal diffusion orientation along nerve fibers in tractography applications) starting from an origin and observed at position $\mathbf{r} = (x, y, z)$ after a time t is Gaussian:

$$p(\mathbf{r}, t) = \frac{1}{\sqrt{(4\pi t)^3 D}} \exp\left(-\frac{\mathbf{r}^T \mathbf{r}}{4tD}\right).$$

Water molecules diffuse between the intra- and extracellular compartments at various proportions depending on the organ of interest. In brain tissue, particles can either diffuse freely in all directions with no motion-restricting materials in their proximity (unhindered isotropic diffusion, e.g. in ventricular cerebrospinal fluid), encountering some barriers (restricted or hindered isotropic diffusion, e.g. in peritumoral edema), or move unequally (anisotropic diffusion, typically seen in crossing fiber compartments). Intravoxel WM fiber arrangement is an important determinant of diffusion anisotropy.

2.3.2 Diffusion weighted imaging (DWI)

Diffusion weighted MRI (DWI) utilizes an MRI sequence with gradients to detect the diffusion of water molecules in the human body. DWI output maps are principally measures of diffusive attenuation. The origin of DWI dates back to the mid-20th century, when Edward Stejskal and John Tanner showed the diagram of a pulsed gradient spin echo (PGSE) sequence (Figure 2.7). Nuclear spins represent magnetic properties (intrinsic angular momentum) of atomic and subatomic particles (in DWI, hydrogen protons in water molecules). In accordance with the spin-echo (SE) technique discovered by Erwin Hahn earlier in 1949, a 90° radiofrequency (RF) spin excitation pulse is triggered, followed by a 180° refocusing RF pulse and echo collection. On either side of the 180° pulse, a strong diffusion-sensitizing gradient (DG) is applied to sensitize signal from diffusing spins that flow into different locations within the excited volume in between of the two diffusion gradients. Stationary spins remain unaffected by the DGs.

After the second DG, the image acquisition module is applied, commonly employing the echo-planar (EPI) sequence. This technique applies rapidly switching phase and frequency encoding gradients to acquire multiple gradient echoes in one acquisition. In modern commercial DWI schemes, the core PGSE sequence is retained with enhancements for chemical shift artifact suppression, fat saturation, or minimizing the effects of eddy currents or spatial distortions.

The attenuation of the diffusion signal is governed by two principal factors, namely diffusion orientation, and the degree of diffusion weighting, represented by the b -value [s/mm^2]. The b -value depends on the DG amplitude, duration and time spacing between paired gradients. In general, the more an imaged structure is aligned with the measured diffusion orientation, the more signal attenuation is observed. As demonstrated in Figure 2.8, it generally applies that the higher the b -value, the longer the water molecules dephase, which results in a decrease in the signal-to-noise ratio (SNR). Although DWI probes diffusion that occurs on the order of microns, microstructural information is averaged over the relatively large size of the image voxel.

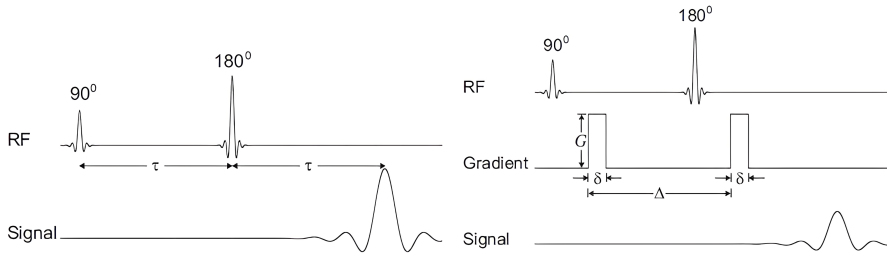


Figure 2.7: *Left:* In the SE method, signal loss due to spin dephasing caused by microscopic magnetic field inhomogeneities can be reversed by another 180° RF pulse. An echo is generated at echo time (TE) equal to twice the time between two consecutive RF pulses (τ). *Right:* Diagram of the Stejskal-Tanner PGSE sequence. Δ expresses the time between two gradient pulses that typically varies between 10 and a couple of hundreds of milliseconds. The gradient pulse duration (δ) may be as short as a few milliseconds and as long as the total Δ [59].

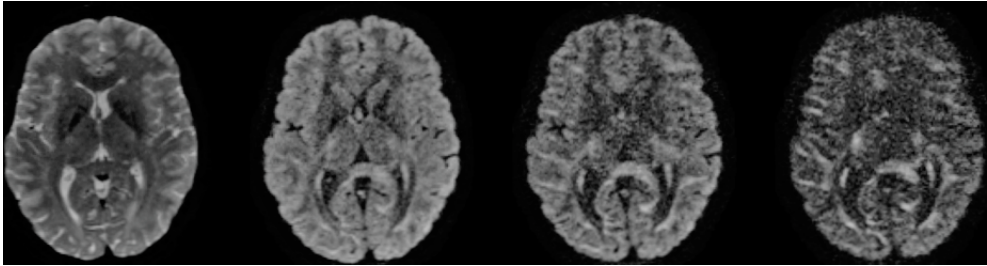


Figure 2.8: Demonstration of signal attenuation as a function of b -value. From left to right: $b=0, 1000, 2000, 3000 \text{ s/mm}^2$. The b -value depends on the strength, duration, and temporal spacing of diffusion gradients. Data were provided by the Human Connectome Project [60].

During a clinical diffusion MR image acquisition, DWI scans and their derived maps are obtained in a cascade of steps:

1. The first instance of the DWI pulse sequence incorporates either no DG or one set to a very low b -value, generating a series of T2-weighted b_0 images.
2. The second step involves DGs with varying strength that are run either individually or combined to sensitize diffusion at multiple diffusion orientations, producing diffusion-weighted source images.
3. For clinical diagnostic purposes, the DW source images are used to create a trace DW image. To assess abnormalities on these trace images, the ADC (apparent diffusion coefficient) map is calculated from the source DW images and the b_0 scans.

Local WM fiber orientations are assessed per voxel by measuring the dMRI signal along a number of different orientations. In the absence of pathology, water molecules are less hindered in motion along nerve fibers than perpendicularly to fiber propagation. The less diffusion occurs in a particular brain region, the brighter signal appears on DW images (Figure 2.9). Therefore, free water molecules will appear dark (signal loss caused by unhindered diffusion), while highly cellular tumorous tissue causes reduction of diffusion times, rendering abnormal DW image areas bright [61].

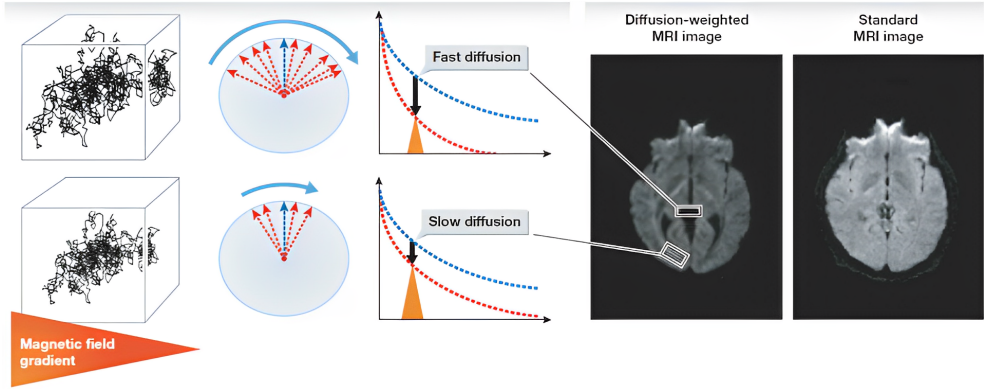


Figure 2.9: Diffusion-sensitizing magnetic field gradients cause water molecule hydrogen atoms to dephase. The magnitude of dephasing is directly proportional to the displacement occurring during the measurement. The bulk dephasing effect leads either to a reduction in MRI signal amplitudes (fast diffusion in CSF) or an increase in the MR signal intensity (slow diffusion in WM fibers) [58].

2.3.3 Diffusion tensor imaging (DTI)

In white matter, diffusion is highly anisotropic due to the parallel orientation of nerve fibers. While the diffusion coefficient for isotropic tissues can be expressed as a single number, diffusivity in anisotropic materials is described by a *tensor* of a particular rank n (number of basis vectors to fully specify a tensor component) and m^n components, where m is a scalar expressing the dimensional space.

Amongst other representations, an adequate coordinate system for viewing the diffusion tensor is referred to as *diffusion ellipsoid* (Figure 2.10) whose principal axis is parallel to the main intra-voxel white matter fiber propagation. The primary advantage of modeling diffusion tensor with an ellipsoid instead of Cartesian coordinate system is that the off-diagonal components disappear. The model thus only consists of three unit vectors (eigenvectors ϵ_1 , ϵ_2 , and ϵ_3) with corresponding lengths (eigenvalues λ_1 , λ_2 , and λ_3).

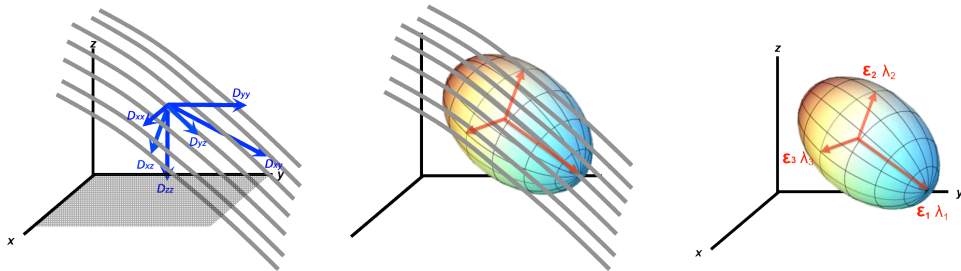


Figure 2.10: *Left:* Six unique directional elements of the diffusion tensor in the Cartesian coordinate system describe diffusion along a set of fiber tracts. Off-diagonal components depend on the frame of reference. *Center:* In each voxel, the center of the reference frame is situated tangentially to the fiber orientation. *Right:* Eigenvectors and eigenvalues of the diffusion ellipsoid. If diffusion is perfectly isotropic, the ellipsoid becomes a sphere with $\lambda_1 = \lambda_2 = \lambda_3$ [62].

A tensor is an object that is invariant under a change of coordinate systems, with components that change according to certain transformation laws (mathematical formulae). A 2-rank tensor is a linear map from two vector spaces, and can therefore be represented by a matrix:

$$D = \begin{bmatrix} D_{xx} & D_{xy} & D_{xz} \\ D_{yx} & D_{yy} & D_{yz} \\ D_{zx} & D_{zy} & D_{zz} \end{bmatrix} ,$$

where diffusion coefficients along the matrix diagonal denote diffusion measured in the laboratory frame of reference (x, y, z), and the six off-diagonal elements correlate diffusion between each pair of principal directions. While a matrix is a collection of numbers, the tensor representation requires a specification of the coordinate system, components, and basis vectors ($\hat{i}, \hat{j}, \hat{k}$) that each of the components corresponds to.

During image reconstruction, each tensor component is mathematically estimated using multivariate linear regression of signal intensities. The value of each component is strictly dependent on the frame of reference in which it is measured. Though variations exist, the clinical MRI frame of reference is often aligned with the orientation of the main magnetic field (B_0) and the patient's body. To find all six tensor elements, a minimum of seven diffusion-weighted images are required (one b_0 and six high- b -value images).

Several parameters (Figure 2.11) can be extracted from the diffusion tensor, its eigenvectors and eigenvalues to create quantitative maps of diffusion magnitude in tissues (apparent diffusion coefficient – ADC), assess the degree of diffusion anisotropy and find areas with restricted diffusion (fractional anisotropy – FA, radial anisotropy – RA, mean diffusivity – MD, axial diffusivity – AD), or extract combined diffusion anisotropy with fiber orientation in one image (directionally encoded FA maps). To avoid confusion, DTI is not synonymous with DWI as it only represents one of the many local diffusion MRI modeling methods.

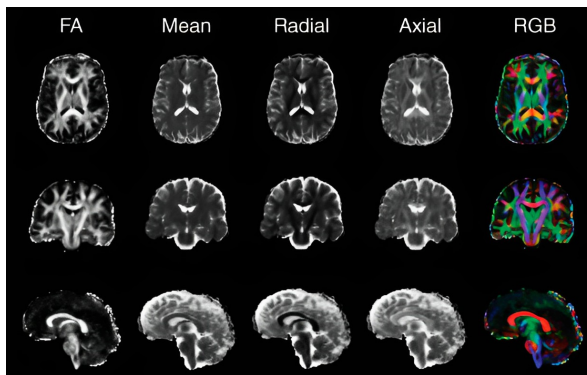


Figure 2.11: Axial, coronal and sagittal maps of various tensor-derived metrics, commonly used in literature as well as the clinical setting. By convention, diffusion is color-coded in FA maps to show directionality from left to right (red), front to back (green), and top to bottom (blue), and intermediate colors for oblique orientations [20].

2.3.4 High angular resolution diffusion imaging (HARDI)

As described above, the diffusion tensor model can only represent a single fiber population per voxel, expressed by the diffusion ellipsoid's main eigenvector. Subsequent analysis of the primary diffusion orientation therefore fails to resolve more complex WM architectures. High angular resolution diffusion imaging (HARDI) was originally developed to mitigate the well-known crossing fibers problem, improve fiber tracking robustness by estimating angular distributions, and offer new measures of tissue diffusivity beyond the DTI-derived FA. Extraction of multiple fiber populations per voxel requires the acquisition of more dMRI data. HARDI samples significantly more diffusion directions than DTI, and acquires images with stronger b -values (ranging from $b = 1000$ to 4500 s/mm^2). Also, HARDI is accompanied by non-DTI reconstruction techniques which are often tailored to particular sampling and acquisition schemes.

In HARDI, along each gradient direction, a diffusion signal \mathbf{S} is measured with discrete sampling of the unit sphere along N points in each imaging voxel. The HARDI diffusion signal \mathbf{S} is most often mathematically represented via a spherical harmonics (SH) transform [63], which is equivalent to the in-plane Fourier transform, but on a sphere. A sum of spherical harmonics coefficients of order l and phase m , Y_l^m , can be used to represent a spherical function (Figure 2.12), just like cosines and sines are used to decompose an image with Fourier transform. Usually, the HARDI-measured signal is estimated by a series of truncated spherical harmonics of order l_{\max} , which has $R = (l_{\max} + 1)(l_{\max} + 2)/2$ terms. For instance, an order of $l_{\max} = 2, 4, 6$ will have 6, 15, and 28 SH coefficients, respectively.

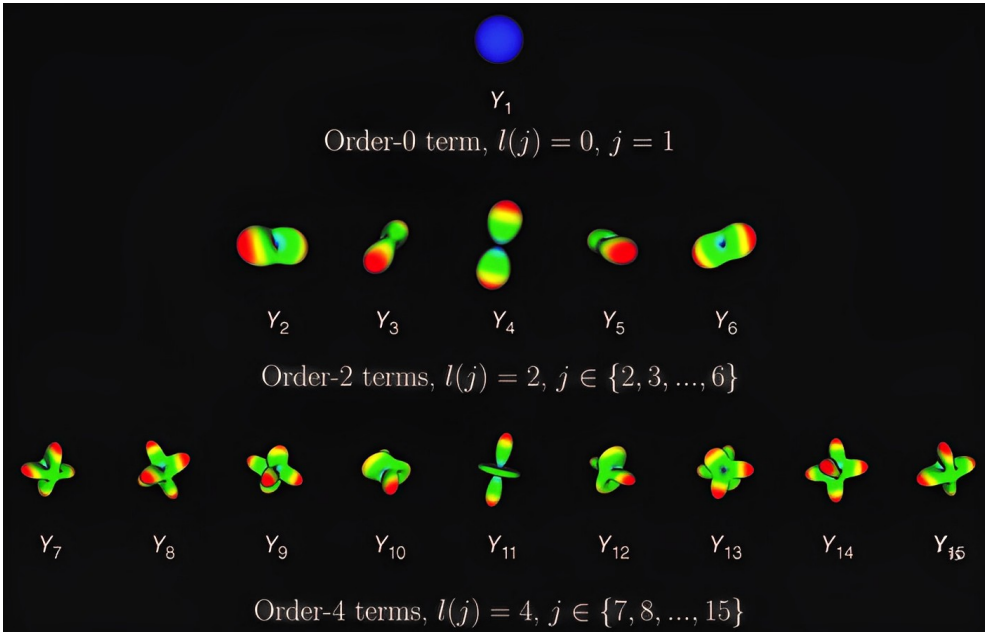


Figure 2.12: Example decomposition of the HARDI signal into the first 15 elements of the spherical harmonics basis. Figure taken from [20].

A Funk-Radon transform is often employed on HARDI-derived data to form diffusion shapes called Q-balls, which are models of diffusion density at multiple orientations. To indicate fiber presence, peaks of these Q-balls are interpreted. The Funk-Radon transform essentially sets each point on a Q-ball proportional to all of the signal values equatorial to that point. The overall shape of the Q-Ball is then fairly resilient to noise as each point on it is determined through many individual measurements, however, the same feature causes the Q-ball to be artificially smooth and inflated.

Creating fiber orientation estimates requires a response function that defines an ideal representation of the diffusion density when a voxel contains one coherent bundle. Nevertheless, diffusion signals in brain tissue also originate from extra-cellular water motion besides that along axons. Each voxel of brain tissue also accommodates other structures, such as glial cell bodies, which contain water with limited diffusion and may contribute to the net signal. Using only a single response function, poor fiber orientation density estimates may be made. These observations can be addressed by exploiting e.g. compartmentalization models.

Intrinsically, it is assumed that every voxel's orientation diffusion density comprises one or more fiber tracts at different orientations and scales. Combining the response function in a variety of angles and fractions yields the diffusion orientation distribution function Ψ (dODF), defined as the radial integral of the diffusion propagator in spherical coordinates:

$$\Psi(\theta, \phi) = \int_0^\infty p(r, \theta, \phi) r^2 dr,$$

where $\theta \in [0, \pi]$, $\phi \in [0, 2\pi]$, and p is the probability density function of any 3D displacement r of water molecules during diffusion time t , also noted as $p(\mathbf{r}, t)$. The ODF is represented as an either simple or complex set of spherical functions on a unit sphere, and is most commonly visualized in the form of glyphs on a spherical mesh. Diffusion ODF profiles are directly related to the displacement of water molecules, and are therefore model-independent.

Inflated fiber orientation models are inherently poor at distinguishing fiber orientation at closer angles. Therefore, to improve erroneous situations where two separate fiber tracts are estimated as a single bundle, one can model the actual fiber orientation density instead of the diffusion orientation density. The fiber ODF (fODF) typically yields much sharper diffusion profiles owing to its ability to directly recover underlying fiber orientations. The amplitude of each fODF lobe can provide useful tract-specific information about the approximate microstructural diffusion properties of distinct fiber orientations per voxel, such as apparent fiber density (AFD) [64], angular fiber density, fiber spread [65] or hindrance modulated orientational anisotropy (HMOA) [66].

Several HARDI acquisition methods exist to obtain the ODF, generally called q -sampling imaging (QSI) [67]. QSI can be utilized through random sampling; diffusion spectrum imaging (DSI) [68] that measures diffusion in the entire q -space (a 3D space with coordinates q_x , q_y and q_z defined by the diffusion-encoding gradients G_x , G_y and G_z) along a Cartesian grid; and sampling across a shell (a spherical shape in q -space) or a combination thereof, commonly known as single-shell HARDI or multi-shell HARDI, depending on the number of b -values [69]. Standard clinical single-shell HARDI acquisition schemes measure diffusion along ~ 60 directions with a b -value of 1000 s/mm^2 at an approximate time of 5–20 minutes.

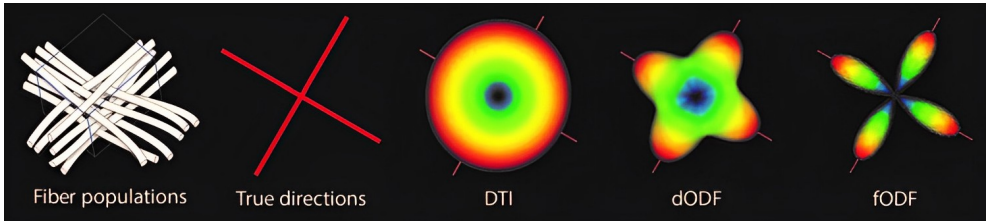


Figure 2.13: In an environment with a complex WM architecture, multiple peaks along each fiber population should be seen in the diffusion propagator. While tensors are flat, angular profiles capturing crossing fibers can be constructed using an orientation density function and a fiber ODF. Figure adapted from [20].

By only measuring a single b -value, different spin populations can hardly be distinguished, and it is instead assumed that all spins experience the same type of diffusion, averaging them homogeneously when calculating the diffusion coefficient. Increasing the b -value shows that the estimates do not match the actual measurement because they did not account for spin subpopulations, which ultimately leads to higher signal contributions than what was predicted. To account for the various spin subpopulations, multiple b -values have to be acquired.

The main benefits of acquiring multi-shell HARDI data for tractography applications are the improvement of fiber orientation estimation despite partial volume effects, and the separation of other components unrelated to fiber bundle orientation. In normal white matter, a single-shell HARDI acquisition can provide a sufficiently accurate estimate of the principal fiber orientation, such as free water. However, in the presence of edema, it is typically beneficial to acquire multi-shell data to enable tractography in a complex set of tissue microenvironments. Besides brain tumor imaging, the relative contributions of these compartments can also be used as additional measures in the early diagnosis of WM degeneration.

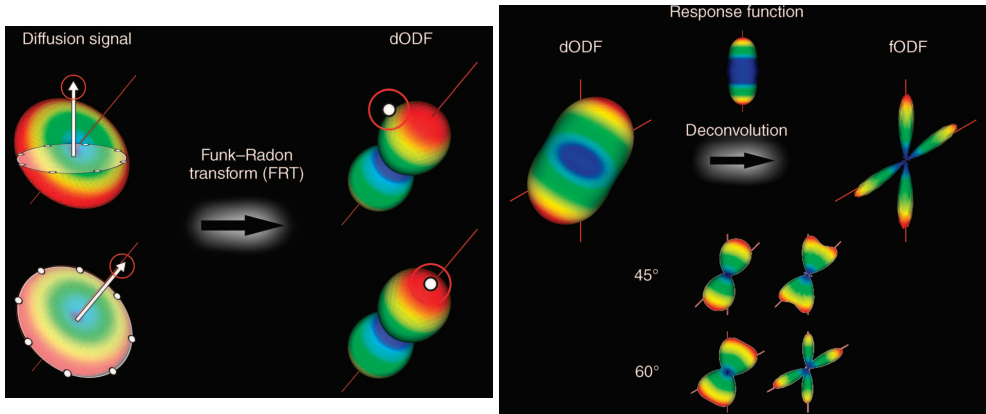


Figure 2.14: Left: Application of the Funk-Radon transform in Q-ball imaging. Integrating over the diffusion signal circles yields the dODF. Right: Spherical deconvolution applied on a dODF to improve angular resolution (here shown for 45° and 60°), sharpen the ODF, and better capture the underlying fiber populations. Figures taken from [20].

2.4 Diffusion MRI-based tractography

Diffusion MRI enables encoding the 3D profile of water molecule displacement, thereby capturing the orientation of tissue microstructure in space. Tractography (or fiber tracking, FT) is the process of integrating voxel-wise fiber orientations to infer connection pathways in the brain. In neuroscience, tractography facilitates the estimation of long-range connectivity as well as division of grey matter into subregions. This section describes the process of image-based fiber bundle reconstruction starting from diffusion orientation modeling per voxel via fiber trajectory integration up to the generation of whole brain tractography maps and bundle segmentation.

To avoid confusion, readers should note that the expression *track* refers to the output of tractography algorithms, while a *tract* denotes a white matter fiber bundle. Hereinafter, attention is paid to selected tractography methods only. For further methods, readers are encouraged to study relevant reviews, e.g. [70].

2.4.1 Deterministic vs. probabilistic tractography

In deterministic tractography [71], the primary assumption is that the first eigenvector of the diffusion propagator is tangential to the underlying white matter trajectory, thereby providing the best estimate of axonal fiber existence. Starting from a seed (initial location in a voxel), the trajectory is reconstructed by propagating a three-dimensional curve representing the white-matter pathway. Once the tracking process has been initiated, there is a need to control for the propagation direction, and to include stopping criteria to govern the propagator's termination. The most commonly set stopping criteria aim to avoid tracking in regions with the CSF and GM, or outside of the brain. Ensuring full WM fiber tracking coverage, a structural WM mask is typically added to the tracking algorithm, and an additional angular (curvature) threshold is set to intentionally target specific fiber bundles with predicted shapes, and to restrict the propagator's turning angle. The angular threshold is nonetheless dependent on the used algorithm as well as the resolution of the dataset. Another approach is to set an anisotropy threshold, where the tracking process is terminated if a certain FA value has been exceeded. Results from deterministic FT do not show all possible connections, and are therefore prone to a higher false negative rate and lower sensitivity.

Higher-order probabilistic FT models [72] primarily address uncertainty originating from ambiguous WM fiber arrangements in the data. Uncertainty increases also due to the presence of noise, motion and distortion artifacts, and the fact that many algorithms assume well-defined orientations despite an intrinsic orientation dispersion of the underlying WM axons. Hence, the tracking process is blurry due to limited measurable angular resolution, and all these major sources of uncertainty are inherently ignored by deterministic tractography algorithms.

Many probabilistic FT approaches have been developed over the past two decades, employing front evolution strategies [73], path optimization [74], or probabilistic streamlines. Unlike deterministic FT, probabilistic algorithms start seeding in a complete WM region of interest (ROI), from where a representative sample of possible fiber orientations is followed using statistical sampling from a probability density function (PDF) of the nerve fiber orientation. The majority of algorithms apply WM ROIs either as termination zones (cortical areas), waypoints (specific white matter regions, through which streamlines are supposed to

project) or volumetric landmarks (in case of U-shaped fiber bundles) to represent fiber tracts strictly within a specific WM volume. The selection of representative samples is repeated at consecutive points in space, which ultimately evolves into a streamline. The streamline propagation process is then repeated from the initial seeding point, which yields a set of streamlines carrying a certain confidence interval for tractography. The PDF can be estimated using heuristic approaches [75], bootstrapping techniques [76], Bayesian Markov chain Monte Carlo sampling methods [72], or by sampling directly from the fiber ODFs using e.g. spherical deconvolution methods [18].

Since probabilistic FT samples across all possible orientation estimates, it is essential to impose an angular constraint to obtain only the most probable candidates. The more pathways emanate from a seed ROI, the lower the probabilities of particular streamlines. Probabilistic FT does not quantify probability that a connection exists or how strong connections are; these methods rather aim to depict a set of streamlines that represent the range of connections consistent with the data. Results from probabilistic FT approaches typically suffer from a high false positive rate and lower specificity.

The tradeoff between specificity and sensitivity of tractography algorithms is highly application-dependent. In presurgical planning for intracranial tumors, higher sensitivity is in general preferred to ensure that critical pathways are not missed during surgery preparation, especially in cases with extensive edema.

2.4.2 Diffusion tensor tractography

To date, DTI-based tractography has been the most widely applied methodology both in clinical and scientific research applications to determine inter-voxel connectivity according to diffusion anisotropy. As explained earlier, tensor-based tractography assumes the dominant orientation of axonal pathways to be parallel to the primary eigenvector of the diffusion tensor. Diffusion fiber trajectories (streamlines) are then reconstructed by following the principal direction of the diffusion propagator in each image voxel (Figure 2.15).

Since its introduction in 1999, the most widely used deterministic tensor-based algorithm in clinical practice has been known as fiber assignment by continuous tracking (FACT) [7]. This algorithm initiates streamlines from user-defined seeds (ROIs), and follows the primary eigenvector in each voxel to reconstruct axonal connections in 3D while changing direction of the diffusion propagator at a variable step size (length between two consecutive voxels) to match the primary eigenvector of the consecutive voxel. Additional thresholds can be applied, such as the maximum turning angle or the highest voxel FA value to constrain fiber tracking only to brain regions where WM pathways can realistically be found. As observed in Figure 2.15, several initial expert-defined ROIs improve the anatomical specificity of results produced by FACT, which aids in the delineation of desired fiber bundles. This technique is commonly known as *virtual dissection*.

However, FACT cannot cope with abrupt directional changes in inter-voxel primary diffusivity, which leads to sudden interruptions of the tracking process, manifested by missing cortical connections in three-dimensional representations. A much smoother representation of white matter fibers is usually obtained using IST (Interpolated Streamline Tractography) [78], involving a family of various numerical approaches, e.g. Eurler, Runge-Kutta or Midpoint, to name some.

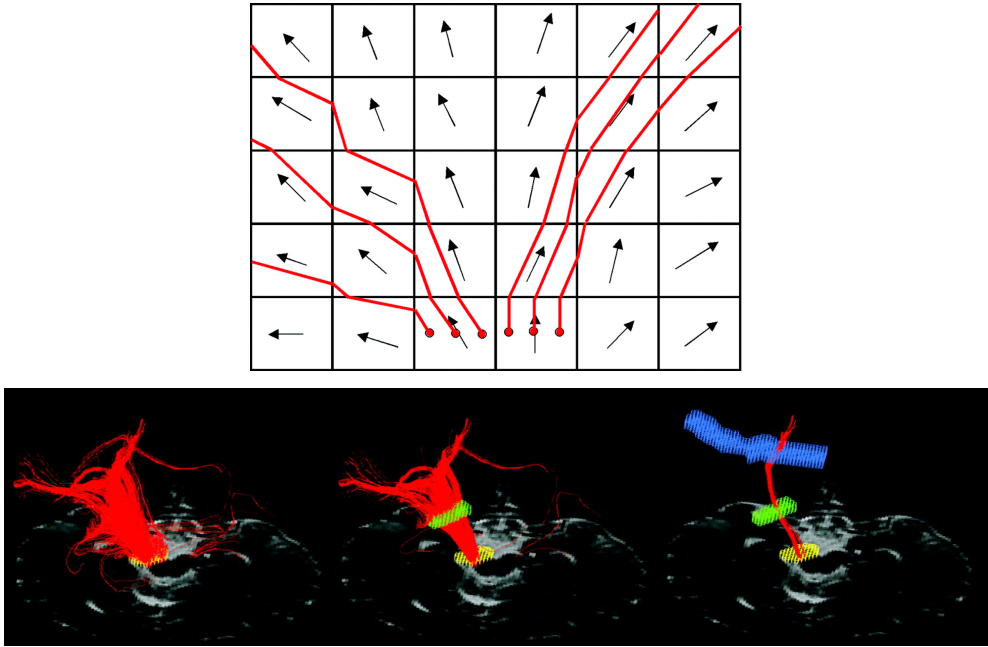


Figure 2.15: Upper: Schematic explanation of the FACT algorithm. Red lines represent generated streamlines. Black arrows show the principal eigenvector per voxel [77]. **Lower:** Multiple user-defined ROIs to isolate only tracks belonging to the CST bundle. *Left:* Streamlines (red) are generated from the cerebral peduncle (yellow voxels). *Middle:* Fiber trajectories propagate through an ROI drawn in the posterior limb of the internal capsule (green voxels). *Right:* The retained set of streamlines passes through the ROI at the centrum semiovale (blue) besides the internal capsule and cerebral peduncle regions [77].

As opposed to FACT, IST algorithms make use of a fixed, controlled step size that is smaller than the voxel dimensions of data at hand.

Deterministic tensor tractography is also susceptible to artifacts resulting in uncertainties in the orientation of the diffusion ellipsoid in each voxel. Probabilistic tensor tractography algorithms incorporate expected uncertainties, and as explained before, these methods aim at reconstructing a greater portion of targeted WM bundles through streamline dispersion. Nevertheless, probabilistic DTI only performs within the fundamental limits of the tensor model as well as limits posed by the reconstruction of the PDF. The deterministic FACT has also prevailed in clinical settings due to the relatively higher computational demands of probabilistic DTI algorithms [77].

2.4.3 Constrained spherical deconvolution

As explained in Section 2.3.4, the process used to combine the response function with the fiber orientation density (FOD) is referred to as convolution over spherical coordinates. Nevertheless, scanner measurements first only enable deriving the ODF while the FOD remains unknown. Spherical deconvolution [18] is the inverse operation that estimates a WM FOD based on an estimate of the signal expected for a single-fiber white matter population within each voxel.

However, spherical deconvolution is an ill-posed problem since there are likely several FODs that can be convolved with the response function to produce the same diffusion orientation density. Therefore, the term constrained spherical deconvolution (CSD) came to existence when accounting for the high sensitivity of deconvolution methods to noise effects by imposing non-negativity and sparsity constraints [19].

A minimum requirement for CSD approaches is that DWI data are sampled shell-wise since the response function signal is estimated using spherical basis functions, disregarding radial components. The CSD method has been reported to provide robust estimations of fiber orientations within clinically acceptable timelines [8], and its superiority over DTI in tractography applications has been demonstrated in the context of neurosurgery planning. Figure 2.16 illustrates a clinical example, where the CSD method overperforms DTI-based tractography in the delineation of anatomically known pathways adjacent to a brain lesion, thereby enabling the determination of safer resection margins.

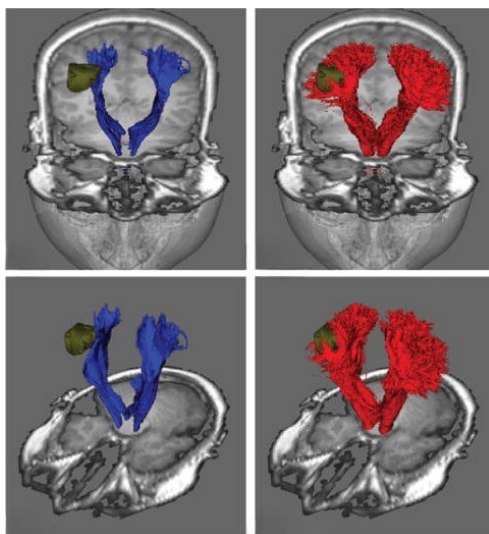


Figure 2.16: Fiber bundle reconstructions from DTI-based (blue) and CSD-based (red) tractography algorithms in the same patient dataset. Bundles are overlaid on coronal T1-weighted images with a right cortical lesion (green). CSD tractography reveals more lesion-surrounding corticospinal fibers than the DTI-based reconstruction. Figure adapted from [8].

2.4.4 Whole brain tractography

Groups of streamlines need to be virtually dissected to create ultimate bundle representations before further qualitative and quantitative analyses. A necessary step preceding such virtual dissection is to find ROIs for different bundles. In seed-based tractography, the positioning of seeding ROIs is essential and determines the quality of output bundles. However, regardless of the tractography algorithm, complex WM architectures may be incompletely captured by seed-based approaches, which is why it has become more common to first generate global tractograms with whole brain tractography (WBT, a.k.a. global tractography), where ROIs are

only reference landmarks and do not fractionate output tractograms.

WBT aims to construct a full-brain fiber configuration that best explains the dMRI data. This approach builds on the assumption that axons extend in organized fascicles, and accounts for ambiguous intra-voxel configurations by examining estimated orientations in neighboring voxels. Seeding most often relies either on complete WM masks or WM-GM interface masks. The selection of one of these global seeding approaches is a matter of compromise. Using the whole WM mask may cause excessive seeding from one parcellated subregion of the mask in the case of long bundles, while seeding from the WM-GM interface may lead to the omission of certain WM tracts due to the low dMRI data resolution. As opposed to streamline methods, WBT is more resilient to changes in noise, and the density of the output tractogram directly corresponds to available data. However, whole brain tracking algorithms have relatively high computational demands due to whole brain coverage and typically require sophisticated microstructural models with firmly set parameters that are not adjustable for other datasets [79]. Mitigating partial volume effects and improving the number of valid connections for whole brain fiber tracking has been addressed by incorporating a multi-shell multi-tissue model based on spherical deconvolution into the WBT framework [80].

2.4.5 Anatomically constrained tractography

Efficient use of biologically sound information can further make dMRI streamlines tractography and virtual bundle dissection more realistic through the provision of relevant anatomical ROIs commonly known as inclusion (logical *and* and *or*) and exclusion (logical *not*) criteria [81]. If the inclusion/exclusion ROIs are known for a particular fiber bundle, they may serve as highly reliable start/end areas for bundle dissection from diffusion data. Biological plausibility therefore further influences the desired termination of fiber tracking, and eventually introduces a new acceptance/rejection criterion for tractography-generated streamlines. This framework is commonly referred to as anatomically constrained tractography (ACT).

Neuroanatomically, it is well known that neuronal axons never enter the CSF-filled regions of the brain, and most of their terminations occur in the cortical and subcortical grey matter or the spinal column. Whether a streamline is accepted or rejected by the ACT framework is defined as follows (simplified explanation visually represented in Figure 2.17; for details, see [82]):

1. Streamline is considered to have reached an acceptable termination point once it has entered the cortical GM.
2. Streamline is rejected if leaving the WM mask and entering a CSF-filled region.
3. Streamline is accepted even if leaving the provided WM brain mask to enable tracking within the spinal WM column.
4. Streamline can be terminated by an FA threshold (for tensor-based tracking), FOD amplitude threshold (for spherical-deconvolution based methods), or excessive angular deviation. However, if, besides these thresholds, a streamline is not terminated according to criteria (1) and (3), it is deemed unacceptable.
5. Streamlines that enter the subcortical structures, but are terminated by thresholds described in criterion (4), are accepted.

6. Streamlines crossing through subcortical structure boundaries (as defined by subcortical GM masks) are truncated and accepted.

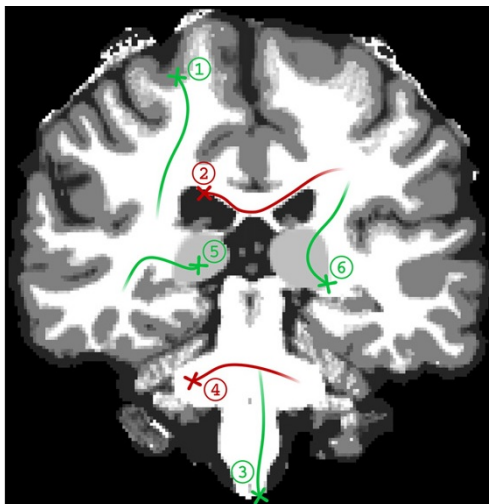


Figure 2.17: Demonstration of the application of anatomical priors in the ACT framework. Streamlines originating out of the displayed slice are presented by fading shades. Streamline termination points are marked by crosses. Accepted (*green*) and rejected streamlines (*red*) either meet or violate the six assigned criteria [82].

Groups of cortical/subcortical GM parcellations together with WM region subsegmentations as streamline propagation masks are typically added to the ACT algorithm to guarantee homogeneous white matter seeding, and utilize expert-defined anatomical priors. Another approach is to use the WM-GM interface and start unidirectional tracking from seeds generated in the cortical or WM-GM region or bidirectional tracking from seeds initiated in subcortical WM-GM areas. In the event of a poor streamline termination, backtracking enables the truncation of that streamline and retracking to find a more suitable termination endpoint. Finally, a commonly imposed constraint for ACT tracking is the minimum/maximum fiber length, which essentially acts as a filter to rule out spurious and under-represented tracks in the DWI data.

2.4.6 Atlas-based tractography

In the presence of brain lesions, various tissue displacements or distortions may lead to incomplete or poor WM segmentation, which subsequently hampers bundle reconstruction using the ACT framework. Besides the use of cortical or subcortical anatomical constraints to guide fiber tracking algorithms, the location of neuronal pathways and morphological characteristics of individual bundles can further be captured by the registration of templates [83] or atlas-based models [84] into the subject space and direct segmentation of bundles based on these reference shapes. Derived entirely from diffusion MRI data, high-resolution fiber bundle template maps can augment the performance of virtual bundle dissection, capitalizing on prior knowledge from neuroanatomists who have labeled each bundle based on previous experience from cadaveric and comparative tractography studies.

The biggest advantage of using template-space WM pathway identification with population-averaged atlases in single-subject analyses lies in the improved taxonomical and topological precision. However, atlas-based approaches typically rely on thorough registration, are prone to registration errors, and outcome dissections have to be carefully checked if anatomically plausible. A population-averaged WM bundle atlas used in this work was constructed from 842 subjects' dMRI data in the Human Connectome Project. All MRI data for the atlas construction were acquired using a multi-shell dMRI sequence (b -values: 1000, 2000, and 3000 s/mm²). The atlas consists of 80 bundles (Figure 2.18) reconstructed in the MNI space using q-space diffeomorphic reconstruction to obtain the spin distribution function (SDF, an orientation distribution function that quantifies the density of diffusing spins) which was averaged across all 842 subjects [39, 85].

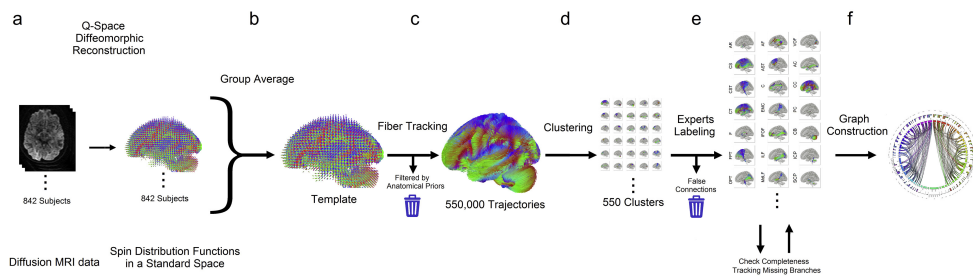


Figure 2.18: Illustration of constructing the HCP842 population-averaged structural connectome. (a) The SDFs of 842 subjects' diffusion volumes were reconstructed in the MNI space. (b) A group average was created from the SDFs of all subjects. (c) The template was applied in the fiber tracking process to generate 550 000 trajectories. (d) Fiber bundles were created through automatic track clustering. (e) Neuroanatomists manually labeled each cluster and identified false trajectories according to their expertise. Checked clusters were grouped to compose the structural connectome atlas. (f) A connectogram was derived from the atlas to graphically indicate connections among brain regions. Figure adapted from [39].

A common method applied in many implementations of atlas-based dissection is track clustering, which employs feature space or distance metrics to infer about WM connections [86]. Recent research has focused on developing fully automated deep learning (DL) algorithms for WM dissection [87], aiming to train networks that recover the shape of a bundle based on an input tractogram.

In conclusion, the presented topics discussed foundations of human brain anatomy, the basics of neurosurgical oncology, and fundamentals of diffusion magnetic resonance imaging along with dMRI-based tractography. The background information is intentionally limited to cover only the most essential concepts and technical nomenclature used hereinafter. Readers of further chapters are expected to understand associations and relationships across the related fields. Moving towards the design of FT4Onco, the next chapter offers a comprehensive review of commercial and open-source dMRI data processing and fiber tracking tools.

3 Review of the state of the art

The field of diffusion MRI-based tractography for oncological neurosurgery covers a wide range of technological progress over the past decades. This chapter provides an overview of prior art in the field, targeting commercial and open-source software tools for neurosurgery planning with dMRI-based tractography. All hereinafter presented information corresponds to the best knowledge at the time of thesis completion, based on inspection of company websites, publications in online databases (PubMed), video tutorials, and user documentation.

3.1 Commercial solutions

Companies developing diffusion MRI-based fiber tracking applications typically incorporate their image processing software into proprietary server- or cloud-based platforms. As learned during interviews with neurosurgeons and neuroradiologists, some centers even send raw MR datasets to companies, where these data are processed, tractographical reconstructions created, and output delivered in a form tailored to customer needs.

While commercial platforms may support a range of image processing tasks besides fiber tracking, their architecture may only enable processing a restricted variety of patient datasets, imposing constraints on image quality and providing semi-automated workflows. Moreover, commercial neuronavigation systems are known to fall behind research advancement when it comes to the integration of tractography models that may more accurately replicate the underlying patient anatomy. An overview of available commercial solutions on the market is provided in Table 3.1.

3.2 Open-source tools

In recent years, publicly available dMRI processing tools have significantly mushroomed. Freeware solutions (see Table 3.2) are stored in open-source repositories (GitHub, Bitbucket), and are typically developed for a specific purpose to support certain research groups or a community of experts who may adopt them in the attempt to create an automated data processing framework. The majority of these tools are not intended for clinical or diagnostic use at all. A software package suitable for oncological neurosurgery planning should ideally offer tools and algorithms for tumor segmentation, anatomical data processing, diffusion data processing, fiber tracking, and visualization in a viewer, all in one suite.

Nevertheless, such a rich collection of tools from one distribution is rarely discoverable, and tools from multiple different software packages need to be combined to construct an image processing chain complex enough for a dedicated purpose. While open-source pipelines wrapping up a number of functionalities and dependencies from different software packages are freely accessible, the level of automation in these pipelines varies enormously. Currently, none of them provide an image processing chain capable of delivering output that is desired by oncological neurosurgeons for brain tumor resection planning, i.e. 3D visualization of multi-compartment tumor segmentation with anatomically informed fiber bundle reconstructions.

When judging the quality of open-source pipelines, another crucial aspect is their architecture. Many tools come as collections of scripts (written in Python, Bash or MATLAB, such as DESIGNER [88], PreQual [89], MRtrix3_connectome or KUL_NIS). These script files are quite easily created, but difficult to maintain, and many hurdles may arise in the event of unexpected interruptions during image processing. Besides command-line callable scripts, several pipeline tools exist enabling the orchestration of various functionalities into processing chains. However, it is often complicated to add and curate software versions in these tools, e.g. Snakemake [90] or Nipype [91]. Recently, Nextflow [92] and Singularity [93] have been proposed for higher reproducibility and easier software package maintenance in the Tractoflow pipeline [24]. Further frameworks have also adopted containerization to fix the versions of dependencies, e.g. QSIprep [94].

Several (commercially) available cloud-based solutions, such as Flywheel [95], O8T [96], BrainLife [97], QuNex or QMENTA, enable the configuration of multiple tools under a common interface, where datasets are either uploaded to a cloud environment via web interfaces or processed directly on premise. These approaches aim at providing automated and reproducible frameworks by reducing data-management overhead.

In the development of FT4Onco, two software packages (MRtrix [98] and DIPY [99]) were utilized for the majority of diffusion MRI processing and fiber tracking steps. As the most comprehensive state-of-the-art toolkits, MRtrix and DIPY were preferred over other tools since they address essential tasks in diffusion MRI data processing and analysis, support flexible integration into image processing pipelines, and are well-suited to commercial research applications. To determine the adequate ordering of image processing steps, inspiration was found in the Tractoflow pipeline that usefully fits the design concept of FT4Onco described in Chapter 5.

The following chapter specifies user needs and defines functional requirements, based on which further Philips-proprietary and open-source tools were selected and integrated into FT4Onco.

Product name	Company	Website	FT methods	Automation
Syngo MR Tractography	Siemens Healthineers	www.siemens-healthineers.com	DTI	Semi
FiberTrak	Philips Healthcare	www.philips.com	DTI	Semi
BRAIN View	GE Healthcare	www.gehealthcare.com	DTI	Semi
Sphere	Olea Medical (Canon Group)	www.olea-medical.com	DTI-FACT	Semi
Brain Voyager	Brain Innovation	www.brainvoyager.com	DTI	Semi
QMENTA cloud platform	QMENTA	www.qmenta.com	DTI, CSD	Fully
Neuroimaging Software Solutions	Mevis	www.mevis.fraunhofer.de	DTI	Manual
BrainMagix	Imagilys	www.imagilys.com	DTI, CSD	Semi
Ziostation2	Ziosoft	www.zio.co.jp/en	DTI	Semi
nordicTRACT	NordicImagingLab	www.nordicimaginglab.com	DTI, CSD	Semi
Quicktome	Omniscient Neurotechnology	www.o8t.com	DTI, CSD	Fully
iPlan Fibertracking	Brainlab	www.brainlab.com	DTI	Semi
StealthDTI	Medtronic	www.medtronic.com	DTI	Semi
BrightMatter Plan	Synaptive Medical	www.synaptivemedical.com	DTI	Fully
ImFusion DTI	ImFusion	www.imfusion.com	DTI	Fully
Advantis Brain	Advantis	www.advantis.io	DTI	Fully

Table 3.1: List of commercial solutions for diffusion MRI tractography. Despite ca. 24 years of algorithmic advancement, most companies seem to still utilize fiber tracking (FT) methods that are notoriously known for limitations in resolving complex nerve fiber architecture and in the estimation of principal fiber orientation based on dMRI data. DTI = Diffusion Tensor Imaging, CSD = Constrained Spherical Deconvolution.

SW package	Tumor seg- mentation	Anatomical processes	Diffusion processes	FT methods	FT models	UI/Viewer	Automation	License	Commercial use
3D Slicer	✓	✓	✓	D, P	DTL multi-fiber unaccented Kalman filter (UKF), NODDI, tensor with free water	✓	Semi	BSD	Yes
AFNI	N/A	N/A	✓	D, P	DTI	✓	Semi	GNU General Public Licence	Yes
ANIMA	N/A	N/A	✓	D, P	DTL ODF, multi-compartment models (MCM)	N/A	Semi	GNU Affero General Public Licence	Yes
BrainVISA- Diffuse	N/A	N/A	✓	D, P	DTL CSD, particle filtering (PFT)	N/A	Semi	CeCILL	Yes
Camino	N/A	N/A	✓	D, P	DTL multi-fiber HARDI	N/A	Semi	Artistic License 2.0	Yes
DIPY	N/A	✓	✓	D	particle filtering (PFT), tensor with free water, DTL, DKI, CSD (only single-sided), CQI, Ball & Stick, constant solid angle (CSA), sparseness, fascicle model (SFM)	✓	Semi, command- line tools for automatic bundle detection	BSD	Yes
DoDTI	N/A	✓	✓	D	DTI	✓	Fully	Matlab license	No
DSI Studio	N/A	✓	✓	D	DTI generalized q-sampling imaging (GQI), q-space diffomorphic reconstruction (QSDR)	✓	Semi (few clicks)	International License (CC BY-NC-SA 4.0)	No, license must be negotiated

Table 3.2: List of open-source freeware for diffusion MRI tractography. This overview of prior art has recently been published in extensive reviews [100, 101]. The majority of listed packages offer image processing modules rather than complete workflows. Abbreviations: D = deterministic, P = probabilistic.

SW package	Tumor seg- mentation	Anatomical processes	Diffusion processes	FT methods	FT models	UI/Viewer	Automation	License	Commercial use
DTIStudio	N/A	N/A	✓	D	DTI	✓	Semi (few clicks)	not found	not found
ExploreDTI	N/A	✓	✓	D, P	DTI	✓	Semi	Matlab license	No, permission required
FSL	✓	✓	✓	P	DTI	✓	Semi, command- line tools for automatic bundle detection	FMRIB Software Library	No, license must be negotiated
MRIToolkit	N/A	✓	✓	D	DTI, DKI, CSD (single-, multi-shell), generalized/damped Richardson-Lucy (DGR-L)	✓	Semi	GNU Lesser General Public License v3	Yes
MRtrix	N/A	N/A	✓	D, P	CSD (single- and multi-shell), DTI, DTI-FACT, NulDISI, SD-STREAM	✓	Semi, command- line workflows	Mozilla Public License 2.0	Yes
SATURN	N/A	N/A	N/A	D	DTI, 4th order Runge-Kutta	✓	Semi	not found	not found
TrackVis	N/A	N/A	✓	D	DTI	✓	Semi	Mass General Hospital CSRL License	No

Table 3.2-continued.

4 Requirements specification

Translating advanced nerve fiber tracking methods into clinical practice requires deep understanding of clinical needs in the neurosurgical workflow. The design of FT4Onco was governed by clinical user needs for surgery planning, which were collected through direct interviews with medical doctors specialized in neurosurgery and neuroradiology at several clinical sites (see Table 1.1 for details). This chapter provides an overview of the current standard and challenges in the use of fiber tracking in preoperative neurosurgical workflow. Clinical needs are explained, and unmet user requirements for dMRI-based surgery planning are presented. Functional and non-functional (performance) requirements are discussed in the last part of this chapter.

4.1 Clinical perspective

Preoperative planning is clinically considered a vital prerequisite for success in surgical interventions. The main clinical need in brain tumor surgery is to maximize the extent of resection while minimizing inadvertent harm to healthy tissue. A reliable surgical plan must be created through risk identification and the estimation of potential functional deficits. The selection of neurosurgical approaches, i.e. from where to enter the cranial cavity, which vascular structures and white matter regions to avoid, and where to apply resection techniques, determines the amount of risk posed to the patient.

Although maximizing the extent of resection correlates with increased risks of cognitive impairment, a recent comparative assessment [51] has concluded that gross total resection, i.e. no visual evidence of contrast-enhancing tumor parts on postoperative MR images, seemed to be associated with better surgical outcomes and patient lifespan than subtotal resection. Another aspect in the preparation for tumor resections is adjusting presurgical plans according to the craniotomy-induced brain tissue displacement (also called *brain shift*). However, methods for the presurgical prediction and simulation of intraoperative brain displacement are out of scope for this work.

4.2 Current challenges and unmet user requirements

In oncological neurosurgery, presurgical brain mapping and intervention planning involve two groups of stakeholders: neuroradiologists and neurosurgeons. Hereinafter, the core unmet user needs are formulated concisely, followed by an expanded description of each requirement. Eventually, all identified user needs are linked to functional requirements for the FT4Onco software.

Aiming for the delineation of tumor boundaries and the estimation of surgical margins with diffusion MRI tractography, the MRI data processing workflow is perceived as suboptimal for several reasons:

- Lack of powerful methods for accurate segmentation of brain structures based on anatomical MRI data with large tumors.

- ▶ Complicated diffusion MRI data handling with various formats in the downstream steps of the fiber tracking analysis
- ▶ High demand on expertise in performing diffusion tractography and interpreting computer-generated reconstructions of nerve fiber bundles
- ▶ Necessity for frequent manual interaction in the currently available semi-automated MRI data processing pipelines
- ▶ Difficulties linking tractography results with intraoperative observations

Besides general data processing issues and interpretability in the intraoperative workflow, the application of vendor-supplied or open-source fiber tracking software solutions in clinical practice is infrequent due to the following caveats:

- ▶ Lack of methodological standard for fiber tracking (order of MRI data processing steps, parametric setup for tractography)
- ▶ Use of suboptimal fiber tracking methods incapable of disentangling complex subvoxel nerve fiber architecture
- ▶ Missing indication of uncertainty for tractography outcome interpretation
- ▶ Lack of high-resolution 3D visualization of reconstructed bundles with an indication of risk areas and surgical margins for neurosurgery
- ▶ Poor compatibility of tractography software with datasets across centers, scanners, and MR image acquisition protocols

The text below lists all identified unmet needs (UN) with contextual explanations of their relevance in the preoperative neurosurgery workflow. All UNs are also summarized with corresponding functional requirements in Table 4.1.

UN1: *Localize brain tumor and classify all its microenvironments (compartments)*

Accurate preoperative localization of brain tumors helps formulate the complete diagnosis, and enables tumor characterization according to its shape, dimensions, degree of malignancy [102] as well as the selection of appropriate neurosurgical approaches. Glioblastomas comprise multiple lesion compartments (contrast-enhancing portion, necrosis, surrounding edema) that can be classified based on anatomical T1, T2, FLAIR and contrast-enhanced T1 MR images. Especially in poorly differentiated tumors, finding precise tumor boundaries after entering the intracranial cavity can be extremely challenging, which is why image-based compartment detection provides valuable information to surgery. Moreover, although GBM neurosurgery aims at maximized resection, preoperative volumetric delineation of tumor compartments helps determine critical risk areas with closely located nerve fibers that must be treated conscientiously.

UN2: *Localize brain anatomy (cortical structures, white matter fibers, subcortical structures)*

During surgery, blood vessels and functionally eloquent areas must be minimally affected to ensure the best possible surgical outcomes and patient survival [103, 104]. While brain structure segmentation from pathological MRI data with massive tumors causing large-scale abnormalities in the neuroanatomy architecture remains burdensome, the delineation of nerve fiber bundles connecting eloquent cortical and subcortical regions is essential to minimize risks of postoperative neurological deficits.

UN3: *Recognize tumor mass effect and edematous infiltration of fiber tracts*

Damage to histologically normal nerve fiber tissue around tumors can either be induced due to a mass effect (surrounding tissue being pushed away or displaced) or tumor-associated edema (swelling caused by the disruption of the blood-brain barrier, allowing the capillary fluid to accumulate in the extracellular cerebral space). These secondary pathological effects significantly contribute to morbidity in patients with primary brain tumors. In neuroradiology, damage to adjacent fiber bundles is preferably estimated still in the proliferation stage of tumors [105]. The recognition of these tumor-tract relationships also helps neurosurgeons determine the least invasive entry zones.

UN4: *Mitigate problems with MRI data formatting and conversion*

The standard data archiving format for clinical (neuro)imaging datasets is DICOM (digital imaging and communications in medicine). Once acquired, medical images are usually stored in a hospital's picture archiving and communications system (PACS). To perform fiber tracking, numerous data handling and conversion steps need to be undertaken [106]. Software applications performing neuroimage analysis in clinical research typically rely on the NIfTI (neuroimaging informatics technology initiative) format. When input data are fed into a processing chain and converted from DICOM to NIfTI, multiple problems may arise:

- ▶ Export of incomplete image series from PACS due to more storage locations on the server
- ▶ Undesired DICOM header manipulation due to data anonymization or face removal
- ▶ Unexpected changes of image geometry after DICOM to NIfTI conversion
- ▶ Coordinate system mismatch caused by the use of inharmonious image manipulation by different algorithms
- ▶ Non-NIfTI formatting of diffusion streamlines (MIF, TCK, TRK, VTK, ...)

In recent years, the neuroimaging research community has strived to create an input data standard to ensure compatibility across all open-source tools and to unify the input data structure of complex datasets coming from various MRI acquisition protocols. These convention efforts have given birth to the Brain Imaging Data Structure (BIDS). Besides correct input data formatting, datasets must conform to international privacy standards and protection regulations, which requires (pseudo)anonymization or face removal methods to be applied.

While image conversion is predominantly a problem in neuroimaging research, daily clinical products would handle data processing directly in DICOM without additional anonymization or defacing.

UN5: *Create a fully automated and computationally efficient solution*

Image analysis with fiber tracking can become very challenging due to long computation times depending on the number of image processing steps, scheduling (sequential or parallel processing), hardware configuration, etc. Clinical sites do not always possess the most modern fast-computing facilities, which may lead to extra internal costs for more computationally powerful infrastructure. The involvement of multiple manual steps in the preoperative workflow at the neuroradiology department of University Hospital in Leuven (Belgium) is exemplified in Figure 4.1. The preparation of tractography output for neurosurgery also faces other problems with respect to inaccuracies in brain image segmentation, geometrical alignment of overlays, structural and diffusion image co-registration, etc. Moreover, at times when a processing tool does not converge at the last step, the source of failure may be almost untraceable [106]. Tractography output for neurosurgery is typically prepared by medical residents, neuroradiologists, MR physicists, doctoral students, or laboratory assistants, who are given specialized training to conduct image analysis at their clinical center. This extra manpower is often employed to complement the limited technical and MR image processing knowledge and experience in medical doctors. Anonymized datasets are sometimes sent to partnering commercial entities who deliver fiber tracking and data analysis reports according to the contractor's demands, which implies an expensive logistic burden [107].

UN6: *Generate fiber tracking results that can be easily interpreted in the intraoperative workflow*

In operating rooms, neurosurgeons receive real-time updates on the location and tumor distance through computer-assisted neuronavigation systems. During resections, surgeons prefer to rely more on their expertise and anatomical knowledge than tractography representations of nerve fiber bundles since anatomical information provides guidance for where to expect function. The verification of fiber tract location via (sub)cortical stimulation often results in different mapping outcomes compared to what is observed on fiber tracking platforms, which is why tractography mapping alone is perceived as unreliable [108]. Ultimately, it is essential for neurosurgeons to differentiate between functionally critical and supportive fiber tracts [109, 110]. Some users have reported tractography to be a useful means to localize where the core of a fiber bundle has been disrupted, i.e. where to expect risk areas [108, 109, 111]. At some sites, surgeons instead use intraoperative MRI scans to determine the extent of resection and remap adjacent white matter. Nevertheless, intraoperative MRI causes the total surgery time to elongate (patient preparation, check-listing, and MRI scan time) by up to 90 minutes, which results in higher costs, the need for additional monitoring, repeated anesthesia, and MR-compatible surgical instruments (clips, etc.) [112].

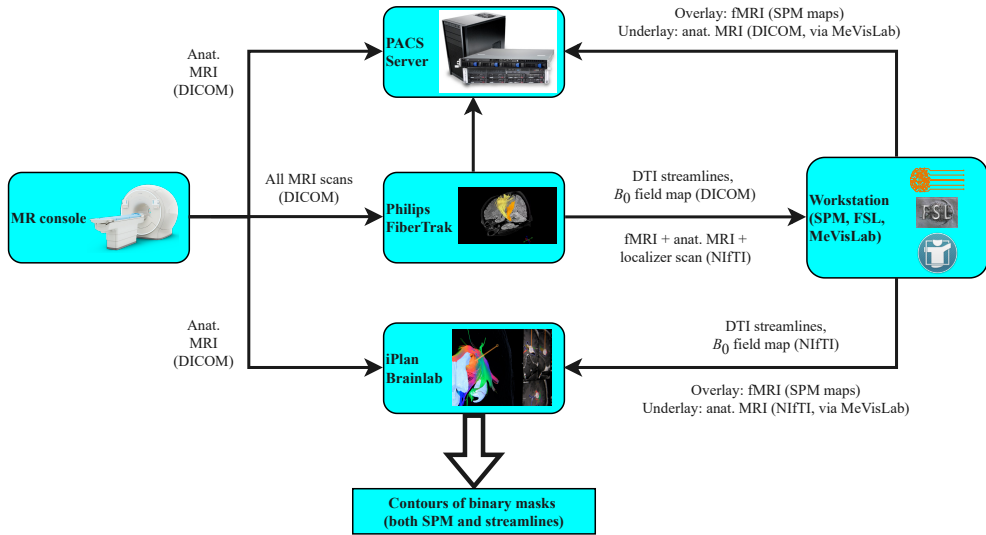


Figure 4.1: A diagram demonstrating the complexity of workflow in presurgical planning at University Hospital in Leuven (Belgium). After image acquisition, obtained MRI DICOM data (anatomical MRI, functional MRI, DTI, and B_0 field maps) are sent to a workstation, where nerve fiber tracks (diffusion streamlines) are semi-automatically generated via the Philips FiberTrak software. All other imaging data are stored in PACS. Reconstructed fiber bundles are then sent to the PACS as quick movies on B_0 field maps, and also to another workstation, where further image processing tasks (registration, segmentation) are performed using SPM, FSL and MeVisLab functionalities. Functional SPM maps are then stored as overlays on anatomical MRI images in PACS, and diffusion streamlines are sent in the NIfTI format together with DTI and anat. MRI data to the Brainlab’s surgery planning platform called iPlan. Here, neurosurgeons create their surgical plan based on prepared data in iPlan (contour overlays of binary masks with streamlines). This workflow was reported to consume up to 12 hours per single subject, posing high demands on radiologists’ mental skills [106].

Note: This workflow was present during clinical needs analysis in 2018 and it was adopted as inspirational groundwork for the design of FT4Onco. By now, the entire infrastructure has undergone significant rearrangement, updates and automation by technical experts at the clinical site.

UN7: Visualize all tissue types and bundles in a 3D fashion with options for selective viewing

Although vendors supply intraoperative neuronavigation systems with integrated fiber tracking tools, the quality of reconstructed bundles is usually suboptimal, and data export possibilities are very limited [107]. Neuronavigation systems show poorly informative bundle profiles with missing indication of tumor-tract distances, resection margins, false positives (non-existent brain fibers), and dynamic thresholding of individual streamlines is rarely available [109]. Streamlines are desired to be stored in a specific value range on structural T1-weighted or FLAIR images with the possibility to view them selectively depending on surgeons’ will, and they should fully substitute the current representation as static low-resolution block-sectioned lines.

UN8: *Use more advanced fiber tracking methods that can resolve crossing fibers and propagation through edema*

The omission of fiber tracking information in preoperative planning is attributed to the size mismatch between axon diameters (μm) and voxels (in mm), high (inter-subject) variability in tractography output (e.g. tract volume), and difficulties related to the determination of seeding points and termination zones for tracking individual bundles, which makes the selection of these regions greatly subjective and user-dependent [106]. Despite the wide availability of advanced fiber tracking models in (clinical) research, most clinically approved applications still employ the traditional deterministic tensor-based FACT algorithm [106, 107, 109, 112]. Deterministic tensor-based streamlines tractography algorithms cannot cope with complexities in the subvoxel fiber architecture (crossing, C-shaping, fanning or kissing), which leads to ambiguous estimates of fiber propagation and the generation of false negatives (missing true axonal connections) in bundle representations [109, 113]. A study investigating the prevalence of complex fiber configurations in WM tissue found that fiber crossing occurs in up to 90 % of brain regions [10]. Losing information about vitally important nerve fibers can have detrimental impact on surgical outcomes. Moreover, image noise in DTI data causes imprecise measurements of the diffusion tensor, error accumulation across consecutive data processing steps, and variance in the estimated fiber orientation.

UN9: *Indicate uncertainty in the presence of peritumoral bundles to aid result interpretation*

Despite the known limitations of the deterministic FACT algorithm, advanced (probabilistic) fiber tracking models have rarely been adopted in preoperative planning owing to poor credibility. Though increased fiber tracking sensitivity can be achieved through the use of more anatomically plausible diffusion models (such as a sphere), neurosurgeons reported that visualizations of denser bundle representations increase doubts whether or not to apply surgical techniques in peritumoral areas [107]. Owing to the probabilistic nature and low specificity (generation of multiple false positives, i.e. non-existent connections) as well as low confidence in reconstructed bundles, conclusions derived from advanced tracking may lead to overinterpretation. This problem becomes even more complex given that there is no ground-truth reference in single-subject tractography.

UN10: *Create a robust solution for datasets from different centers, scanners, and acquisition protocols*

In order to define relationships between a brain tumor and adjacent WM fiber bundles, relevant information from acquired MRI data can only be extracted after artifact correction, image segmentation, co-registration, and other steps. In practice, image processing and parameter setup tends to be optimized through consent paradigms among doctors at some clinical sites, and custom-made pipelines consisting of open-source or clinic-owned tools are constructed ad hoc, following little or no standards with inadequate and manually adjustable values (e.g. tracking step size and angular threshold) which leads to the generation of irreproducible results [114]. Often, these pipelines can only work on data acquired with specific MRI acquisition schemes on a “trusted” MR scanner.

Furthermore, storing image processing output (bundle reconstructions with parametric maps, reports, and anatomical underlays) into PACS servers for later inspection was claimed to be wearisome at times [115].

4.3 Functional & non-functional requirements

In order to meet the identified unmet user needs, functional and non-functional requirements were specified. Preoperative dMRI data processing lacks the *speed* to meet clinically acceptable timelines, the *automation* to substitute user interaction and avoid inadequate parametric setup, as well as the *optimization* of the fiber tracking process to create more reproducible bundle representations out of patient data.

In this work, functional requirements are understood as a set of specific end-user demands that constitute a great proportion of the basic facilities that an ideal solution should offer. All these functionalities are mandatory and need to be incorporated into the system to meet user needs. Collectively, these functionalities are related to the speed and automation of the image processing and fiber tracking workflow, better image quality enhancement methods, and outcome visualization with clinically relevant informative features (e.g. uncertainty in fiber tracking or indication of tumor-tract relationships, etc.). Top-level functional requirements are summarized in Table 4.1, and further described in detail in Chapter 5.

Apart from the desired functionalities, numerous non-functional requirements have been mentioned in conversations with stakeholders, referring to performance, portability, security, reliability, scalability, and flexibility. These requirements are perceived as quality constraints that are crucial for the final transfer of FT4Onco into clinical practice as a complete product. In this thesis, FT4Onco is designed as a clinical research prototype, which is why non-functional requirements are only marginally considered.

In non-functional terms, there is a high demand on rapid computing infrastructure with interactive viewing not only to achieve acceleration in image processing, but also more user comfort during outcome inspection. A clinically deployable fiber tracking application should be equipped with an interactive user interface capable of instantaneous responsiveness to every user-initiated action (mouse-click reaction speed, data file loading, instant viewing, etc.) and informative features (fiber bundle encyclopedia, user guide, descriptive pop-up windows, navigation buttons, etc.). As presented in later sections, a compact auxiliary user interface was implemented to simplify the in-house FT4Onco development and verification processes.

In addition, the interviewed clinical users unanimously raised the wish to be able to launch fully automated image processing through a single-button click on any dataset of choice. Although tumor resection rarely happens on the same day as preoperative mapping, the majority of interviewed clinical users stated that the total duration of image processing and fiber tracking should not exceed two hours. The fiber tracking pipeline should be integrable within the clinic's or department's software ecosystem, easily installable on hospital servers, and it should follow the most recent data security standards.

UN	Definition	Functional requirement
UN1 *◇	Localize brain pathology	Whole-tumor segmentation
UN1 ◇	Classify all lesion compartments	Lesion compartment classification
UN2 *◇	Segment white matter anatomy	Whole brain segmentation Segmentation of fiber bundles connecting eloquent areas
UN2 *	Localize all cortical and subcortical regions	Cortical parcellation
UN3 *◇	Recognize tumor-tract relationships (mass effect, infiltration)	Whole brain white matter tractography Detection of fiber tract displacement or edematous infiltration
UN4 *	Mitigate problems with MRI data formatting and conversion	Fully automated and orchestrated data flow with optimized conversion among multiple formats Export of outcomes in common data formats
UN5 *◇	Create a fully automated and computationally efficient solution	
UN6 ◇	Generate fiber tracking results that can be easily interpreted in the intraoperative workflow	Informative multi-parametric, color-coded 3D visualization of reconstructed bundles with segmented anatomical underlays Filtration of false positive streamlines
UN7 ◇	Visualize all tissue types and bundles in a 3D fashion with options for selective viewing	
UN8 *◇	Use more advanced fiber tracking methods that can resolve crossing fibers and propagation through edema	Advanced probabilistic tracking with more sophisticated diffusion models beyond tensor
UN9 ◇	Indicate uncertainty in the presence of peritumoral bundles to aid result interpretation	Indication of tracking uncertainty along bundle profiles
UN10 *◇	Create a robust solution for datasets from different centers, scanners, and acquisition protocols	Support for datasets coming from different sites, MRI scanners and acquisition protocols

Table 4.1: Specification of top-level functional requirements for FT4Onco. Relevance of individual requirements for particular user groups is indicated with a star (*) denoting neuroradiologists, and with a diamond (◇) referring to neurosurgeons. Further details on the selected functionalities and technical specification are elaborated in Chapter 5.

As described in the following chapter on the design of FT4Onco, the aim was to avoid reinventing already available processing pipelines, but to find efficient remedies for the weaknesses of the current clinical preoperative diffusion MRI-based fiber tracking workflow. In the design of FT4Onco, careful attention was paid to the choice of image correction and analysis tools with the intention to integrate well-tested widely-used functionalities that best match individual user requirements. The development of novel algorithms was not intended in this work.

5 Design description

In requirement-driven software development, user needs can be met through a well-elaborated design plan and the utilization of suitable functionalities. In this chapter, an overview of conceptual design considerations for FT4Onco is given and the complete implementation is discussed, providing rationale for the selection of particular anatomical and diffusion MR image processing as well as fiber tracking tools. Both system and software architectures are explained as outlined by the V-model. In addition, the integration of the image processing pipeline into a commercial research platform is presented here.

5.1 Design considerations

As briefly summarized in Section 1.3, several intentional limitations were imposed to constrain the focus of FT4Onco development. These constraints enabled a significantly faster development process and early acceptance testing with clinical end-users. Before designing the software, it was hence essential to define the complete system architecture with all subsystems and hardware. Two conceptual models of FT4Onco as a clinical research application were outlined upfront:

1. Philips IntelliSpace Discovery plugin
2. Standalone command-line tool

The following sections describe the structure and behavior of their components in detail.

5.1.1 FT4Onco as a Philips IntelliSpace Discovery plugin

The first concept was governed by the architecture of a commercial research platform called Philips IntelliSpace Discovery (ISD¹). Delivered as an integrated solution for medical research on a standalone server hosting a Windows operating system, ISD offers a client server architecture accessible via a web browser. It also comes with research application packages, such as the Research Oncology Suite (ROS) that provides tools for longitudinal lesion tracking and characterization as well as an API (Application Programming Interface) for integrating new algorithms (Figure 5.1). Software developers can utilize ISD for the integration and evaluation of analysis tools as plugins containing either a complete compiled software executable locally, or a configuration setup with a network reference to a remote machine where image processing happens.

Remote computing is facilitated by the so-called Computation Node (CN) framework, which provides the capability to execute arbitrary scripts or executables stored on distant servers connected to the same network. Figure 5.2 shows the ISD-based architecture with a remote CN subsystem. After launching a plugin on ISD, selected imaging datasets are converted from DICOM to the Philips-internal VSR format, and sent (together with CN configuration files) to a remote server, where image processing starts after the transfer has finished.

¹Hereinafter, ISD is defined as an ecosystem consisting of the physical system with its control software.

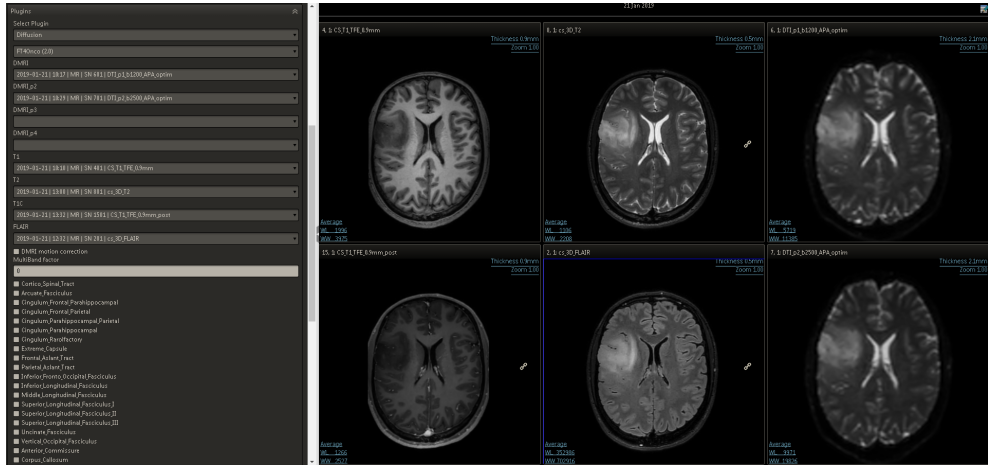


Figure 5.1: Web interface of the ISD Research Oncology Suite with a glioblastoma case opened for inspection. The application plugin window with its options is located in the left column. Plugin input data can either be filled out manually or specified in a configuration file to enable fully automated processing. Image courtesy: Philips ICAP Aachen, Germany.

To achieve optimal data transfer and processing speed, some minimum hardware requirements have to be met both on ISD and (remote) computation servers, summarized in Table 5.1. Besides these system specifications, a stable and fast network connection must be established to ensure flawless communication between the servers.

System info	CN server	ISD server
Type	virtual or physical machine	virtual or physical machine
Operating system	Linux 64-bit CentOS 8	Windows Server 2012 64-bit
Processor	8x Intel(R) Xeon(R) CPU E5-2620 v4, 2.10 GHz	4x Intel(R) Xeon(R) logical CPU E5-2620 v4, 2.10 GHz
RAM	64 GB	32 GB

Table 5.1: Minimum hardware requirements for the CN and ISD servers in the first conceptual design of FT4Onco.

After all data from a patient case have been transferred to the remote server, the main functionality, typically an application or a top-level script of a processing pipeline, is automatically triggered. Image processing automation can be achieved via Docker [116], which is an open-source platform enabling the combination of the source code, libraries and dependencies of image processing tools, and packaging them into standardized executable components under any environment (subsystems), deployed as containers on the computation server. In the ISD-based architecture, individual MR image processing steps are sequentially launched in an order prescribed by the top-level FT4Onco script. While the plugin is executed, ISD waits for completing all core tasks and generating results which are then collected and sent back to ISD.

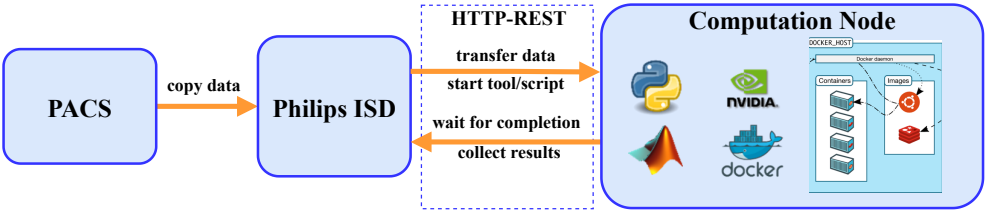


Figure 5.2: ISD-based workflow and system architecture of the first FT4Onco concept. Medical imaging data are migrated from PACS to ISD. The components of FT4Onco are stored on the remote server’s (CN) host system in Docker images, which are sequentially instantiated as containers at different image processing stages. The transfer of imaging data and configuration files from ISD to remote computing servers and reversely happens via a REST (representational state transfer) interface [117], where external systems with respect to ISD are seen as web resources identified by URIs (uniform resource identifiers, also abbreviated as UIDs). ISD communicates with external systems over HTTP (hypertext transfer protocol). Only image processing outcomes specified in the CN configuration files are sent back to the ISD server and automatically merged with corresponding patient data.

Even though ISD provides an environment for inspection of various image processing outcomes (Figure 5.3), and inherently also a full-fledged interactive user interface both for clinical research and practice, its capabilities of visualizing tractography results and compatibility with fiber tracking datatypes are limited. These observations were collected during the clinical evaluation of FT4Onco-v0.1, reported in Chapter 6. Moreover, owing to a substantial need for extensive training, and frequent external support with the integration of FT4Onco into ISD during clinical deployment, this architectural concept was later solely used for internal FT4Onco development, which is why further details are not provided.

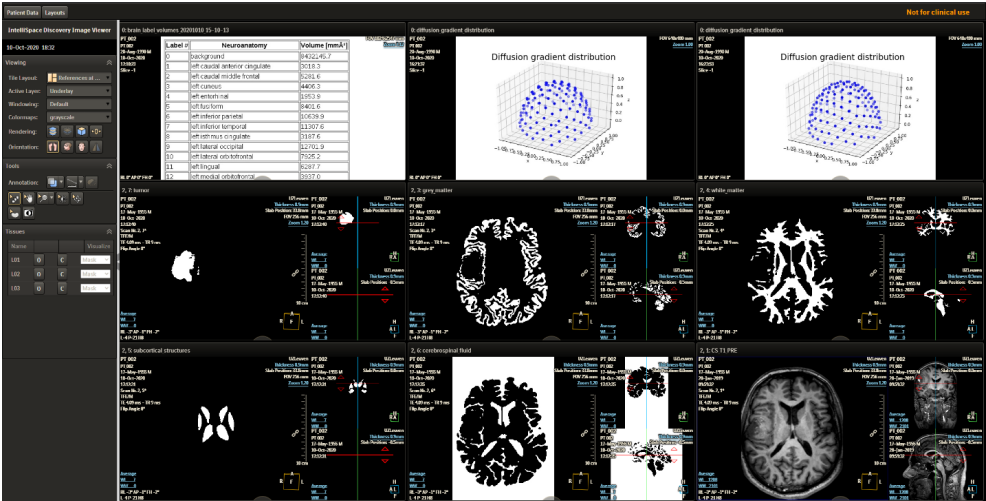


Figure 5.3: Outcomes from remote image processing returned to ISD over the computation node framework. This active view shows labels from the segmentation of the lesion and all brain structures, graphs of the diffusion MR imaging gradients in each HARDI acquisition to check for uniform distribution, and a report of brain region volumes for this patient case. Image courtesy: Philips ICAP Aachen, Germany.

5.1.2 FT4Onco as a command-line tool

As demonstrated in the previous system architecture, ISD provides a sophisticated display service and a channel for communication with externally located image processing tools. In FT4Onco, a strong emphasis was placed on the design and implementation of FT4Onco's data access layer, where image processing is conducted. Hence, the second concept presents a system design incorporating FT4Onco as a standalone command-line tool deployed on one server, which enables integrability at multiple sites both on physical servers as well as in a cloud environment.

Refraining completely from the ISD-driven concept, there are fewer hardware requirements for the deployment of the processing pipeline. The hardware specification (summarized in Table 5.2) takes into account the large variability of dMRI acquisition protocols across different clinical sites, and thus the varying size of diffusion MRI series to ensure the capability of processing both DTI (few megabytes) and HARDI (few gigabytes) MRI data. Given the limited availability of high-performance clusters with aggregated power or dedicated GPUs (Graphics Processing Unit) to optimize computing performance at most visited sites, the entire FT4Onco was engineered for machines operated by CPUs (Central Processing Unit).

System info	CN server
Type	virtual or physical machine
Operating system	Linux 64-bit CentOS 8
Processor	8x Intel(R) Xeon(R) CPU E5-2620 v4, 2.10 GHz
RAM	64 GB

Table 5.2: Minimum hardware requirements in the second conceptual design for FT4Onco. The CentOS 8 Linux operating system was chosen for system security reasons.

Before tractography, several image processing steps need to be taken as a prerequisite for fiber tracking inference since dMRI data suffer from a range of imaging artifacts that challenge the analysis of results and their interpretability when inappropriately accounted for. To date, the number, order and staging of the necessary image processing steps follow little or no standardization [5, 118], which is why the first complete blueprint of FT4Onco design was obtained by screening already existing diffusion MR image processing pipelines. The most comprehensive solution, comprising processing chains for anatomical, diffusion MRI data, and tractography, appeared to be Tractoflow [24].

Tractoflow (Figure 5.5) leverages two engines: Nextflow (pipelining SW that supports parallelization, [92]) and Singularity (containerization SW for running tools with restricted user access [93]). It offers a publicly available, fully automated diffusion MRI processing pipeline, requires almost no installation and complies with the BIDS standard for neuroimaging data [91].

Focusing primarily on coarse structural brain connectivity mapping, Tractoflow lacks modules for processing patient data with neoplastic lesions. Therefore, the development of FT4Onco was thoroughly consulted with collaborating neuroradiologists from University Hospital in Leuven (Belgium), where an automated BIDS-compliant CSD tractography pipeline [119] was constructed to automate the labor-intensive preoperative fiber tracking workflow for neurosurgery planning reported in Chapter 4. In agreement with the purpose of FT4Onco, this BIDS-CSD pipeline (Figure 5.4) utilizes state-of-the-art software tools to mitigate user bias and the requirement for manual interaction by experienced personnel. The BIDS-CSD pipeline is fully written in bash (a Unix shell command language). However, this pipeline lacks automation for brain tumor segmentation, as tumor labels are obtained by semi-automated annotation of the anatomical MR images in the ITKSnap tool [120]. An overview of software tools and functional methods for individual image processing steps in the Tractoflow and BIDS-CSD pipelines is provided in Appendix B Tables 5 and 6.

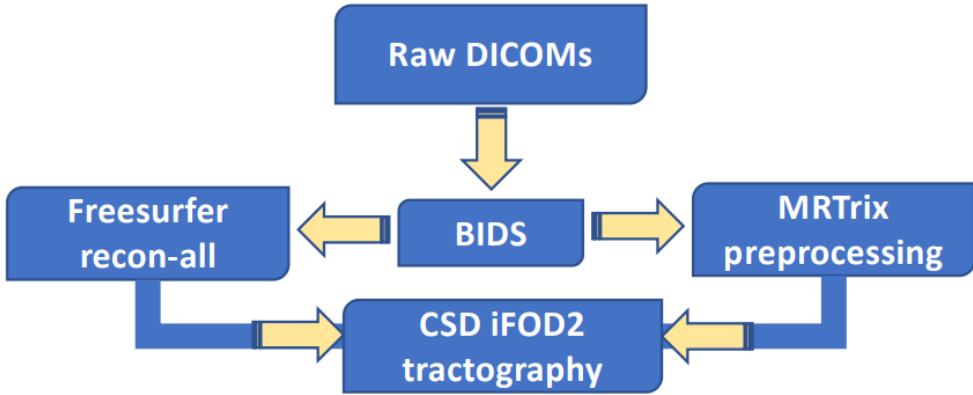


Figure 5.4: Coarse sketch of the BIDS-compliant CSD fiber tracking pipeline with automatic dMRI and anatomical MRI data processing designed to address the slow and labor-intensive preoperative workflow at University Hospital in Leuven (Belgium) [119]. After the conversion from DICOM to BIDS, anatomical data are processed in FreeSurfer [121] with the *recon-all* functionality for brain segmentation, and DWI data with image processing methods from MRtrix [98] and FSL [122]. Eventually, all image processing outcomes are used as input for the MRtrix-driven CSD tractography using a probabilistic algorithm based on second-order integration over fiber orientation densities (iFOD2) [123].

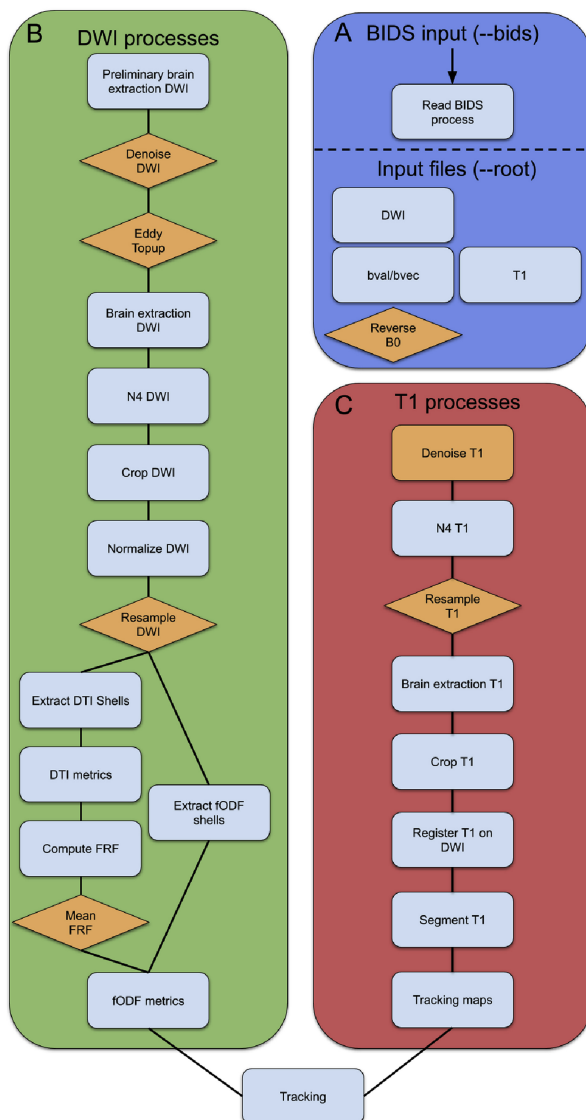


Figure 5.5: Graphical representation of the Tractoflow pipeline. (*A – blue*) BIDS-conformant input data files required to run the pipeline. (*B – green*) Diffusion processes that run on DWI data, the *b*-values, *b*-vectors and the blip-up/blip-down DW images. (*C – red*) Processes that run on the T1-weighted MR images. Orange elements are optional tasks. Figure adopted from [24].

5.2 Workflow optimization

In this section, the software architecture is explained, and a coarse overview of the entire image processing pipeline is provided. In addition, this section presents a recommended, minimum-quality input dataset, explains how imaging data are systematically treated along the pipeline, and defines further constraints imposed on FT4Onco development. Forthcoming sections then describe the methodological underpinnings of all employed image processing tools, and explain the importance of integrating each functional element into the pipeline, clarifying potential caveats. The verification of all functionalities at unit, integration and system levels is documented in Section 6.1.

5.2.1 Pipeline architecture

FT4Onco contains three core sets of necessary image processing steps for anatomical MRI data, diffusion MRI data, and fiber tracking analysis, all of which are connected by supervisory Python scripts. In total, FT4Onco was constructed from 24 functional elements enabling fully automated image processing. Functionalities were selected exclusively from Philips-proprietary tools and open-source packages. By design, preference was given to publicly available neuroimaging research methods distributed under licenses permitting adoption in commercial research. Consequently, the two most frequently utilized neuroimage analysis toolsets, FreeSurfer and FSL, were substituted with other functionalities since their licenses violate the condition of commercial utilization.

As schematically explained in Figure 5.6, initial data selection, and the viewing of image processing outcomes are not automated and require users to intervene. Although the importance of automating these steps is unequivocal, integrating automatic data preselection from external systems as well as the transfer of image processing outcomes to servers with deployed tools for medical image visualization is strongly affected by access restrictions within hospital file systems and on-site network configuration. Hence, creating a generic solution to automate these steps irrespective of premise is rather difficult, and not attempted here.

The goal of this work was not to create novel image processing algorithms. For some known imaging artifacts, a suitable open-source method was not identified, which is why these artifacts are not directly addressed in the pipeline. Examples include signal drift [124] (gradual signal decay across volumes in each series due to temporal MR scanner instabilities) or gradient nonlinearities (such as eddy current induced misalignments). It is assumed that initial intensity normalization (explained in Section 5.4.1) across all volumes and *b*-shells together with the utilization of rigid/affine slice-to-volume motion correction (see Section 5.4.4) would suffice to suppress these effects. Modern Philips MR scanners produce high-resolution and non-distorted anatomical MRI data, which is why neither bias field correction nor noise suppression methods are applied on these scans. While these effects should not be neglected, the cumulative influence of all disregarded artifacts on diffusion orientation estimation and fiber tracking inference has not been investigated in this work.

An optimal orchestration of all image processing steps is essential when aiming for a fast and fully automated workflow. Adopted from the ISD-based concept, image processing tools were deployed via Docker. While advanced techniques for parallel computing exist to simultaneously handle separate subprocesses, and more efficient scheduling could be achieved through multi-threading or deployment across multiple hosting systems, the FT4Onco pipeline was chained up as a cascade of Docker containers running in a single (virtual) machine.



Figure 5.6: Diagram demonstrating the sequence of 24 fully automated FT4Onco image processing steps (excluding two user-dependent tasks in blue). Automated MRI data manipulation with the generation of informative features for visualization are shown in yellow; green rectangles represent anatomical MRI data processes; diffusion processes are highlighted in red, and tractography processes have purple background.

5.2.2 Handling data input and output

Despite the fact that routine clinical preoperative brain MRI acquires multiple contrasts and preoperative imaging protocols significantly vary across sites, only selected anatomical (T1-weighted, T2-weighted, contrast-enhanced T1-weighted, FLAIR) and diffusion MR images are used to reconstruct WM fascicles in brains with neoplastic lesions. These imaging series compose the minimum input requirements for FT4Onco. Aiming for compatibility with Philips MR data, other vendors' preoperative MRI datasets were not considered in FT4Onco development.

Overcoming the drawbacks of tensor-based tractography by employing advanced probabilistic tracking algorithms, standard DTI acquisitions (b -values of ca. 1000 s/mm^2 , 6–32 directions) do not contain enough directional information to resolve subvoxel fiber configurations, let alone in the presence of large tumors. Ideally, a multi-shell HARDI dataset is used as input with a b -value of $1000\text{--}2500 \text{ s/mm}^2$ and more than 60 volumes, optionally containing field maps (diffusion MR images with opposing phase encoding direction) for susceptibility-induced distortion correction. Figure 5.7 shows an example dataset used in the description of individual processing tasks in subsequent sections. All datasets from University Hospital in Leuven (Belgium) were acquired according to a Medical Ethics Review Committee (MERC)-approved research protocol (S61759) with a corresponding patient informed consent attached.

For figure consistency, all MRI slices are flipped to match the radiology viewing convention, where the patient's left side is located on the right, as opposed to the neurology perspective. Unlike in literature, where b -values ≤ 50 are often considered to be without diffusion weighting, and b_0 volumes are not referred to as a separate “shell”, the hereinafter described image processing steps use the term “multi-shell” for DWI series containing at least one b_0 volume regardless of the number of non- b_0 shells.

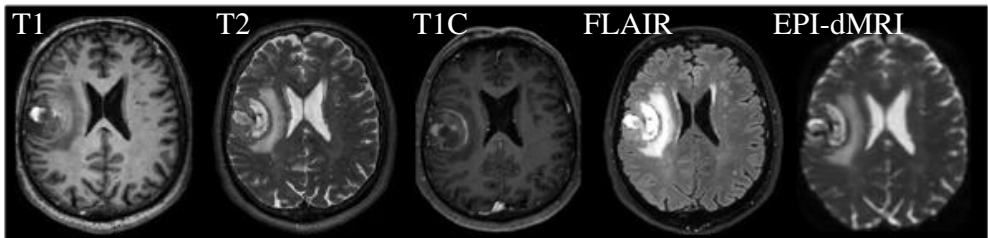


Figure 5.7: Example patient dataset used to demonstrate individual image processing steps. The case presents a right frontoparietal glioblastoma (WHO grade IV). This dataset consists of 3D T1-weighted (voxel size: 0.9 mm isotropic, $TE/TR = 4.05/9 \text{ ms}$), contrast-enhanced T1-weighted (T1C), T2-weighted, FLAIR volumes, and two separate EPI-dMRI series (258 volumes in total with b -values = $0/1200/2500 \text{ s/mm}^2$, $TE/TR = 85/4500 \text{ ms}$). Courtesy: University Hospital in Leuven (Belgium).

Neuroimage processing may generate complicated data structures, for which no official data arrangement consensus exists. Its lack results in irreconcilable opinions across researchers as to how the data should be organized on file systems. At the beginning of the FT4Onco pipeline, input datasets are converted into the brain imaging data structure [91] using the *dcm2bids* conversion tool encapsulated in a Docker image (Figure 5.9). Dcm2bids is a community-centered project provided under the GNU General Public License v3.0, and

maintained at UNF Montreal (Unité de neuroimagerie fonctionnelle). The project aims at facilitating an effortless BIDS conversion through automated and modifiable scripts, and actively reflects new features in the BIDS specification. Figure 5.8 shows a simplistic overview of the main data formats used in FT4Onco.

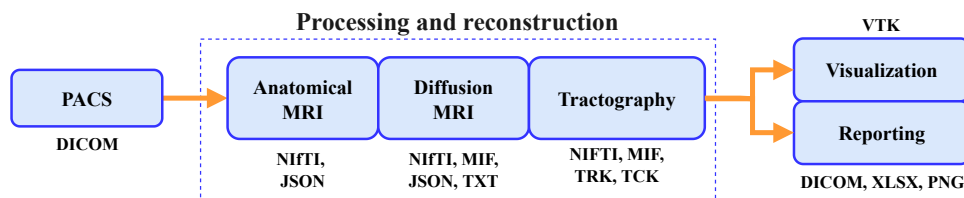


Figure 5.8: Input and output formats used in the processing pipeline. DICOM – standard format for storing medical imaging data in hospital systems; NIfTI – common neuroimaging data format; JSON – text-based structured format for storing DICOM header information; TXT – text files for storing values such as transformation matrices, b -values and b -vectors; MIF – MRtrix-specific image format; TRK – DIPY-specific tractography format; TCK – MRtrix-specific tractography format; VTK – visualization format both for tractography and segmentation output; XLSX – Microsoft Excel table; PNG – picture format for statistical output.

Apart from reconstructed bundles, parametric visualization features (tracking uncertainty, tumor-tract relationships), and co-registered anatomical underlays, FT4Onco produces an Excel sheet with an image processing report. Recorded are the duration of each subprocess, information about input data (number of dMRI series, volumes, b -values, image dimensions, voxel size), and parametric setup for tractography. Moreover, the report contains qualitative information about reconstructed bundles, such as fiber count, and average streamline length.

```

sub-PT_002/
├── anat
│   ├── sub-PT_002 FLAIR defaced.nii.gz
│   ├── sub-PT_002 FLAIR.json
│   ├── sub-PT_002 T1c defaced.nii.gz
│   ├── sub-PT_002 T1c.json
│   ├── sub-PT_002 T1w defaced.nii.gz
│   ├── sub-PT_002 T1w.json
│   ├── sub-PT_002 T2w defaced.nii.gz
│   └── sub-PT_002 T2w.json
├── dwi
│   ├── sub-PT_002_run-01 dwi.bval
│   ├── sub-PT_002_run-01 dwi.bvec
│   ├── sub-PT_002_run-01 dwi.json
│   ├── sub-PT_002_run-01 dwi.nii.gz
│   ├── sub-PT_002_run-02 dwi.bval
│   ├── sub-PT_002_run-02 dwi.bvec
│   ├── sub-PT_002_run-02 dwi.json
│   └── sub-PT_002_run-02 dwi.nii.gz

```

Figure 5.9: Example patient dataset converted from defaced DICOM data to the BIDS-NIfTI format. “Sub” – subject, “PT-002” – anonymized patient name, “run-XX” – image acquisition run. Structural JSON files contain information on b -vectors, b -values, and other DICOM-extracted metadata. Every name of an executed and finished process in the FT4Onco pipeline is attached to the end of the filename string in front of the file extension.

In the following explanation of the image processing pipeline, the technical specification of all pipeline blocks is presented with scientific background and rationale explaining why particular functionalities should be present in clinical research tractography trials. Details on the distribution and licensing of individual processing tools can be found in Appendix A.

5.3 Anatomical MRI data processing chain

Tractography outcomes are typically inspected by overlaying them on T1-weighted images. To find the location of WM fiber bundles, including fascicles affected by a tumor or edema, tractography uses output from segmentation algorithms capable of 3D identification of WM regions and cortical/subcortical areas as well as from tools for brain tumor delineation. Brain (mask) extraction methods are typically applied to aid the later co-registration of anatomical underlays with produced tractograms. Hereinafter, a summary of the main anatomical image processing steps is provided. More information on utilized algorithms and software packages can be found in Appendix A Table 2.

5.3.1 Brain segmentation and cortical parcellation

Accurate 3D segmentation of brain tissue along with parcellation of the cortex (lobes, gyri) is especially relevant for anatomically informed connectivity analysis. Standard open-source toolboxes, such as FreeSurfer, demand multiple hours to perform brain segmentation on a single T1-weighted MRI scan. FT4Onc makes use of the Philips-developed hybrid full brain segmentation (HBS, Figure 5.10) that combines deep learning classification and shape-constrained modeling. Cortical segmentation and WM tissue classification are achieved through a fully convolutional 3D neural network (F-Net CNN), while the identification of subcortical structures and hemispheres exploits shape-constrained deformable models [125]. HBS enables a fully automated brain tissue segmentation that needs ca. 2 minutes to converge on GPUs and ca. 10 minutes on CPUs.

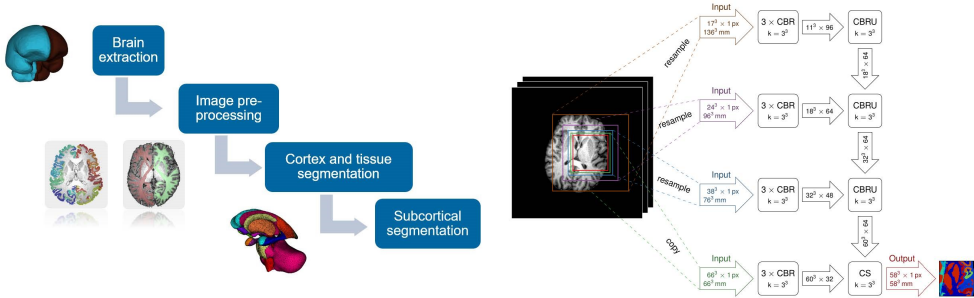


Figure 5.10: Illustration of the HBS processing pipeline (left) and the architecture of the F-Net CNN (right). Shape-constrained models are used for brain extraction and subcortical structure segmentation. Intensity normalization and volume reorientation are done before deep learning based voxel-wise cortical and white matter tissue classification. The F-Net consists of several blocks: a convolutional layer followed by batch normalization and the rectified linear activation transfer function (CBR), a CBR block with upsampling (CBRU), and a convolutional layer with a channel-wise softmax layer (CS). Arrow shapes represent data tensors with given voxels flowing through the network, and k indicates the convolution kernel size in some blocks. Whole 3D images are segmented by successively segmenting smaller nonoverlapping subvolumes, indicated by the red rectangle. For each of these subvolumes, larger overlapping patches at different scales (green, blue, purple, and brown rectangle) are used as input to the network. Using larger but fewer subregions leads to significantly reduced processing times at the cost of higher memory consumption, which is compensated by the reduced number of simultaneously processed voxels. In an experiment processing 101 T1 images, the HBS tool achieved the following average DSC (Dice Similarity Coefficient) scores: 0.80 (cortical regions), 0.92 (WM), 0.83 (GM), 0.81 (CSF), 0.95 (SC).

HBS takes a 3D NIfTI T1-weighted MRI scan of the brain as input, and performs brain extraction (isolation from non-brain structures) by employing a shape-constrained model of the hemispheres. Next, the extracted brain volume is normalized (shifting and scaling so that all pixels have a zero mean and unit variance) and reoriented, followed by deep learning based voxel-wise classification of cortical and WM areas, the cerebellum and the ventricular system. Finally, another shape-constrained model is applied to segment subcortical structures. Bihemispheric segmentation is achieved by deforming the Desikan-Killiany-Tourville (DKT) atlas divided into 62 regions. Eventually, the HBS tool yields a 3D NIfTI image with 63 brain labels (including a 0 for background). These labels are then automatically separated into four label masks to serve as input for anatomically informed whole brain tractography (Figure 5.11). Most importantly, the WM mask is added as input to the tracking algorithm to constrain tractography solely to cerebral areas with nerve fibers.

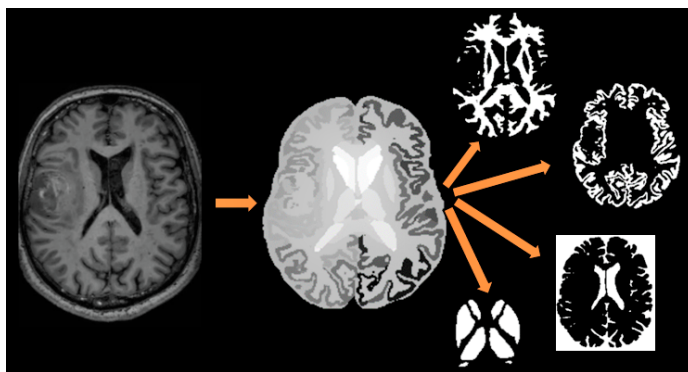


Figure 5.11: Output of the hybrid brain segmentation algorithm on the selected patient T1 volume. The label volume is separated into masks (WM, GM, CSF with background, SC) for tractography.

5.3.2 Tumor segmentation

In neurosurgery, the identification of tumor core and the boundaries of edema is needed for lesion characterization. The quality and behavior of tractography algorithms has been reported to improve with the use of masks representing different tumor compartments [126]. The above-described whole brain segmentation tool is not designed for multi-scale tissue segmentation on diseased brains with neoplastic lesions. Brain regions affected by tumors are erroneously classified by the HBS approach, which is why an additional solution for tumor segmentation is required. In FT4Onco, a Philips-developed method was integrated, comprising image preprocessing through the Statistical Parametric Mapping software package (SPM), followed by automatic glioblastoma segmentation (GBS) using a deep learning model based on DeepMedic, and postprocessing of the output volumes of interest (VOIs) [127]. The DeepMedic implementation consists of a multi-layer 3D CNN for the detection and segmentation of tumor compartments [128], and a 3D fully connected network to remove false positives.

The tumor segmentation workflow is illustrated in Figure 5.12. GBS requires four series (T1, T2, FLAIR, and T1C MR images) as input. Preprocessing involves bias field correction (to remove a very smooth signal caused by B_1 -field inhomogeneities), co-registration of the T1, T2 and FLAIR images with the T1C volume, brain extraction, normalization, and resampling (changing the resolution and dimensions of the image). Automatic tumor segmentation generates up to four output VOIs, representing the contrast-enhancing portion, necrosis, non-enhancing part and edema, depending on which compartments are detected. All segments are resampled to the original resolution of the T1C volume as the last step in the pipeline. In addition, all compartment labels are unified into a whole-tumor mask.

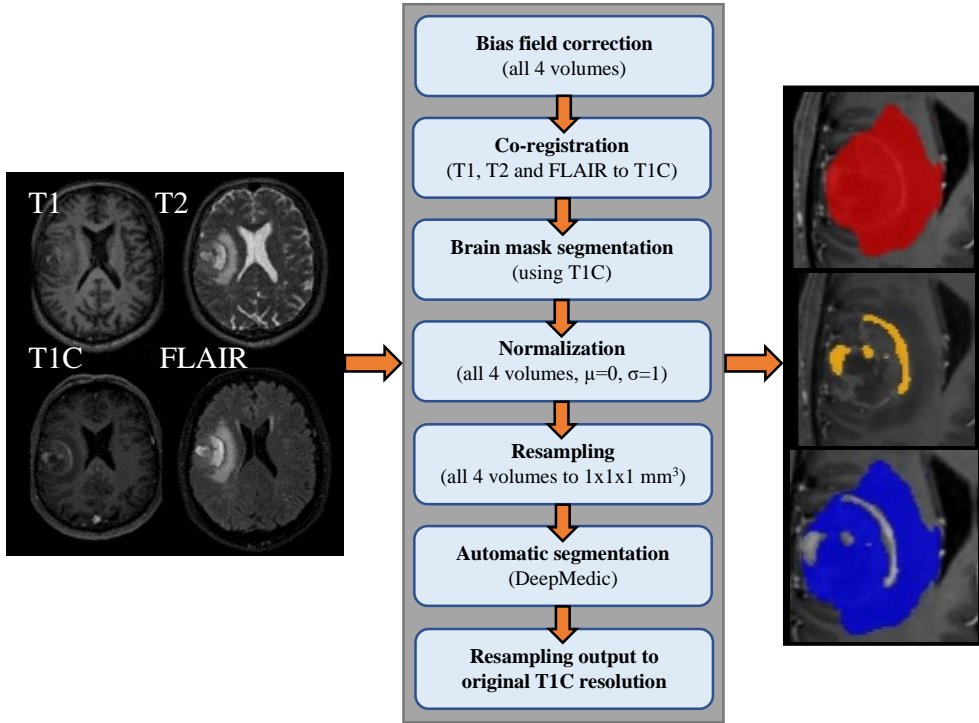


Figure 5.12: Overall workflow of the automatic brain tumor segmentation pipeline. After SPM preprocessing, the four co-registered imaging contrasts and the extracted brain mask are fed into an independently trained model based on DeepMedic. Output labels are classified 3D masks of whole tumor (red) as well as separate masks for edema (blue) and contrast-enhancing portion (yellow). The model was ranked as best performing in the BRATS 2015 challenge, and was trained on 220 GBM datasets with expert manual annotations. Details of the network architecture are not provided as they are well reported in [128].

To mitigate the lack of a joint segmentation strategy for simultaneous tumor and brain tissue segmentation, the output brain masks constructed by HBS are corrected by overwriting voxels, where the lesion is located, with voxels from the whole-tumor mask generated by GBS. As shown later, the WM segmentation mask is combined with the whole-tumor mask for WBT in order to detect fiber bundle propagation through tumors. The tumor segmentation tool is deployed in two separate containers, one containing the SPM tools and another with the DeepMedic software.

5.3.3 T1 and T2 brain extraction

Removing non-brain tissue parts of the entire volume later enables improving the registration accuracy between diffusion and anatomical data. Brain extraction (a.k.a. skull stripping) is an additional step in FT4Onco enabling fast and automatic brain tissue isolation. Using the affine registration algorithm from the ANTs (Advanced Normalization Tools) package [129], the T1 and T2 volumes are co-registered with the MNI152 T1 and T2 brain templates [130] as illustrated in Figure 5.13.

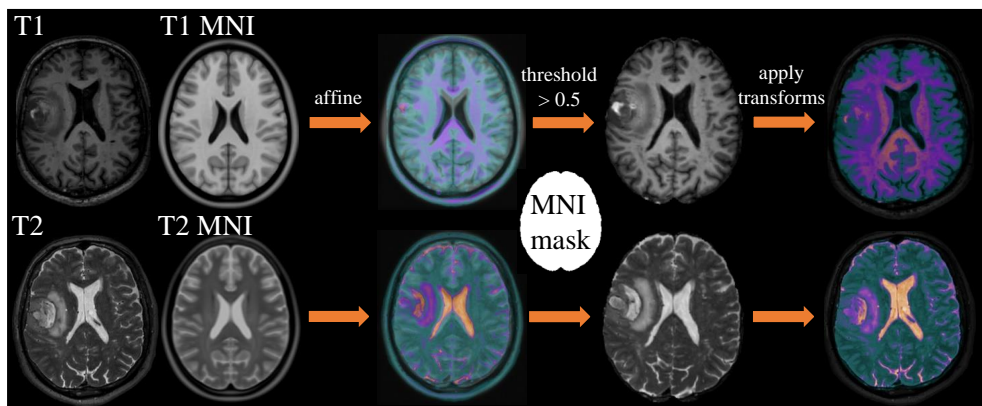


Figure 5.13: Demonstration of the brain extraction process both for T1 and T2 images using the MNI152 template volumes and the MNI brain mask. Firstly, each MRI volume is registered on the corresponding MNI template. Then, the affine-registered MRI data are thresholded with the MNI mask so that all voxels outside of the template mask (valued less than 0.5) are discarded. Finally, the registered and thresholded image volume is mapped back to the native space using the computed affine transforms from the initial registration.

5.4 Diffusion MRI data processing chain

Numerous MR imaging artifacts result in difficulties during fiber tracking, thereby hampering direct off-scanner diffusion analysis. Hence, a number of artifact compensation methods need to be applied on dMRI data before supplying them to tractography algorithms. The majority of these processes utilize compiled command-line tools from the MRtrix distribution [98], medical imaging libraries from ANTs [129], and generic methods from DIPY (Diffusion Imaging in Python) [99], see Appendix A Table 3 for more details. As input, these processing tools require a gradient table (a text file containing diffusion gradient vectors and b -values for each diffusion volume) with respective imaging series (4D NIfTI files), and optionally also diffusion B_0 field maps acquired with opposing phase encoding direction. The following sections describe the core diffusion image processing tasks in the FT4Onco pipeline.

5.4.1 Diffusion data quality inspection

The first step comprises several qualitative checks of the diffusion imaging series in terms of dimensional congruence across all volumes, intensity rescaling, presence of negative values, and concatenation when a dataset consists of multiple diffusion series.

Intensity correction accounts for differences in intensity scaling between two individually acquired series from one scanning session. Scaling correction is performed by first calculating the global mean intensity value of all b_0 volumes through all series. Then, the mean b_0 volume from each series is divided by the global mean value, and each diffusion series is multiplied by the outcome of this division. Essentially, intensity rescaling has to precede series concatenation.

Moreover, in the event of imperfectly converted gradient axis directions in the diffusion gradient table, some axes must be flipped. An MRtrix tool used in FT4Onco for the evaluation of the diffusion gradient b -matrix performs a short whole brain tracking experiment on the uncorrected diffusion series, and computes the average streamline length under various axis flips and permutations of the gradient table. Looping through all possible combinations, the tool checks whether the flips and permutations occur in scanner coordinate system (negating values in the first *column* of the gradient table) or in image coordinate system (negating values in the first *row* of the gradient table). If the header information is stored correctly, the tool will show that the gradient direction coordinate frame was in scanner space, which is by convention expected in MRtrix-based image processing.

Axis flipping may originate from improper header extraction when writing DICOM header information into gradient table files, however, extreme care needs to be taken when forcing axis flips. As shown in Figure 5.14, wrong axis orientation in the gradient table typically leads to false fiber orientation distribution estimates, and consequently incorrect bundle reconstructions.

In order to exploit the full potential of the CSD algorithm, and to estimate signal contributions per tissue type via spherical basis functions, the data must be acquired with shell-wise sampled, uniformly distributed diffusion weighting gradients.

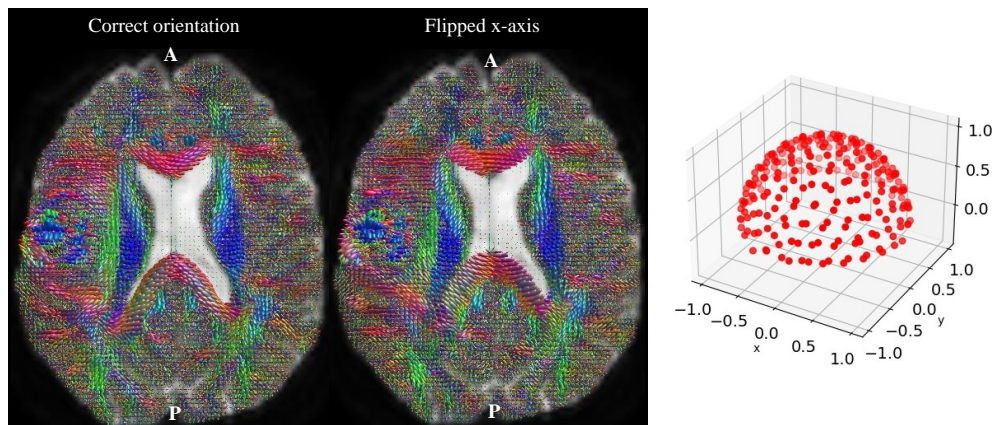


Figure 5.14: *Left:* Demonstration of the effect of flipped diffusion gradient axis on the FOD lobe orientation overlaid on a b_0 diffusion volume. The correct orientation of FOD lobes follows the anatomical curvature of the genu and splenium of the corpus callosum, while flipping the x-axis of the gradient vectors causes the FOD lobes to shift away from the nerve fiber orientation. Color-coding of FOD lobes: blue – inferior-superior, red – medial-lateral, green – anterior-posterior. *Right:* Example DWI data acquisition scheme with uniform distribution of diffusion gradients on half a sphere. Abbreviations: A = anterior, P = posterior.

5.4.2 Denoising

Diffusion MR images suffer from SNR decrease due to MR signal attenuation associated with motion of water molecules or thermal scanner fluctuations. Accumulated noise components may cause tractography algorithms to generate more spurious streamlines and visual clutter in reconstructed bundles.

Novel image acquisition schemes introduce new noise sources, such as acceleration factor-dependent noise in compressed sensing MRI, which are difficult to model and remove. Multiple techniques have been implemented for noise removal as extensions of 2D methods, e.g. non-local means, empirical Bayes or correlation-based joint filtering [131, 132, 133]. Other methods utilize the quality of 4D series that the same exact 3D volume is acquired multiple times at varying b -values and gradient directions, such as the Marchenko-Pastur Principal Component Analysis (MP-PCA) method based on random matrix theory [134]. All of these methods however require a well-calibrated noise model as they make assumptions about the signal (e.g. its distribution). In addition, noise removal with these methods must be performed in the beginning of the image processing pipeline since interpolation or smoothing applied in subsequent downstream tasks may change the noise characteristics, thereby violating signal assumptions in the underlying algorithms.

A recently proposed self-supervised denoising algorithm, integrated in the DIPY package and called Patch2Self [135], abandons the requirement for noise modeling, while assuming that noise aggregated at consecutive image acquisitions is statistically independent. Patch2Self can efficiently separate anatomical structures from noise components by learning a full-rank locally linear denoiser at each volume, while only relying on the randomness of noise in the acquired signal.

Patch2Self can be applied at any stage of an image processing pipeline, and it has shown to outperform the MP-PCA method in suppressing more noise components (even non-Gaussian) from images while preserving anatomical structures unaltered (Figure 5.15).

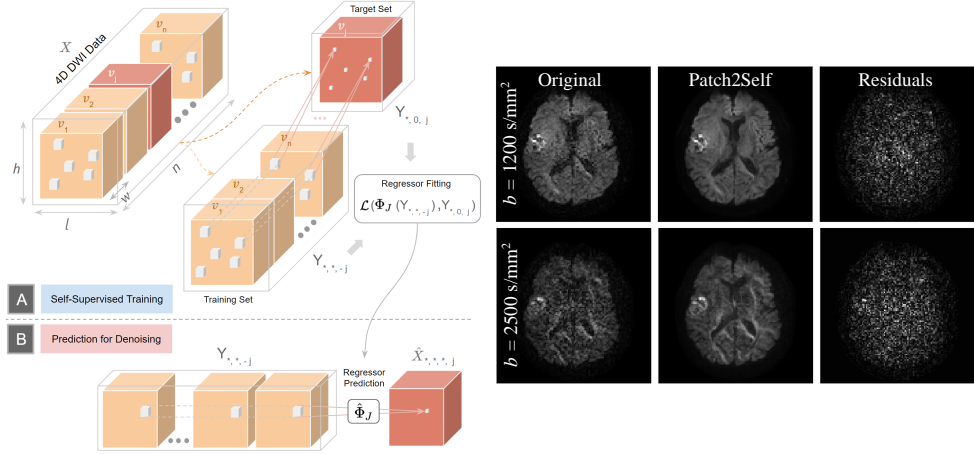


Figure 5.15: *Left:* Demonstration of the working principles of Patch2Self [135]. This method incorporates a two-step process: (A) self-supervised training, and (B) prediction. Firstly, 3D patches ($p \times p \times p$ neighborhood of voxel k) are extracted from n volumes of an input 4D dataset X ($l \times w \times h \times n$), and one volume is held out for denoising (target volume). Each patch (p -neighborhood of each voxel) from the $n-1$ volumes is flattened and concatenated into a feature vector of length $p^3 \times n$. Feature vectors are stacked into a matrix of size $m \times (p^3 \times n)$, which is used for the prediction of the center voxel in the corresponding patch of the target volume. This way, a linear regressor ($\hat{\Phi}$) for denoising one 3D volume of the 4D diffusion series is trained. Next, the $n-1$ volumes are fed into the regressor, and the prediction represents a denoised version of the target volume. *Right:* Effect of Patch2Self denoising on both diffusion series of the selected patient dataset. Removing stochastic noisy signal, the underlying brain tissue is well-preserved.

5.4.3 Gibbs ringing correction

In MR image reconstruction, inverse Fourier transformation (FT) is used to convert the k-space signal in the frequency domain into the spatial domain. Theoretically, an infinite number of sine waves with varying frequencies, amplitudes and phases would be required for Fourier series to represent discontinuity. However, images are acquired with a finite number of k-space samples, and approximated by using relatively few harmonics in their Fourier representation. Consequently, diffusion-weighted images may exhibit Gibbs ringing (a.k.a. truncation or spectral leakage) artifacts manifested by multiple fine lines parallel to sharp tissue interfaces. These ripple-like patterns are most conspicuous on non-diffusion weighted b_0 volumes. Provided that the signal intensity of an image object gradually changes across multiple voxels, truncation errors are minimal. Conversely, high-contrast interfaces with directly adjacent structures may be obscured by edge enhancement, widening or checkerboard-like patterns (see Figure 5.16). Intensity oscillations have been reported to tremendously affect the quantitative analysis of dMRI data and the quality of derived parametric maps (e.g. radial diffusivity) [136].

Besides k-space prefiltering prior to image reconstruction, the most widely adopted postprocessing suppression method for Gibbs oscillations has been spatial smoothing with an

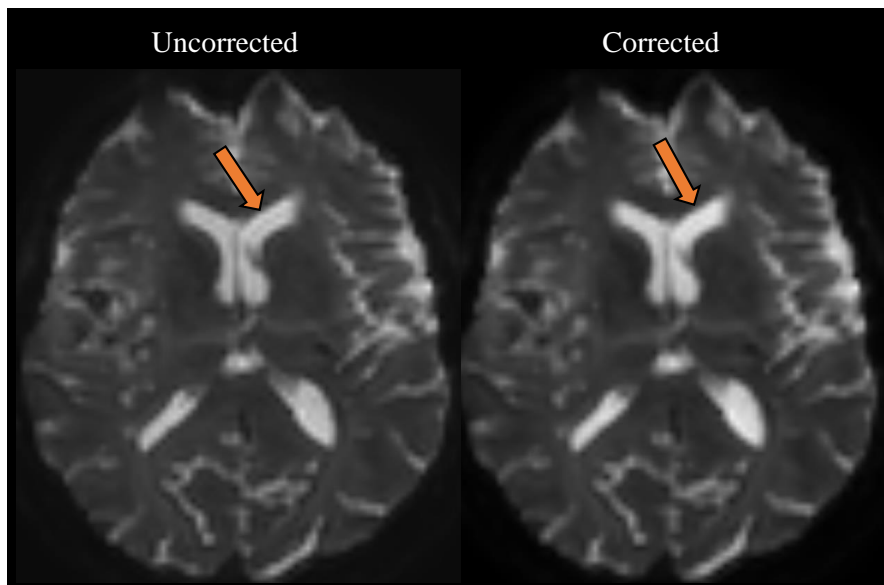


Figure 5.16: Example of Gibbs ringing (*left*) on a b_0 image manifested by rapid intensity fluctuations in the periventricular areas (*arrows*), and the effect of suppression (*right*) in the selected patient dataset.

isotropic smoothing kernel. Nevertheless, spatial smoothing increases blurring in the images, and magnifies partial volume effects that may hinder fiber tracking. In FT4Onco, truncation artifacts are removed by a method of local subvoxel shifts implemented in the MRtrix toolbox [137]. Gibbs ringing correction through subvoxel shifting exploits the idea that using a finite number of k-space samples leads to image reconstruction on a discrete MRI sampling grid, where the Gibbs ringing intensity depends on the precise location of high-contrast edges relative to that grid. In reconstructed MR images, local determination of optimal subvoxel shifts for neighboring pixels at sharp edges can thus suppress these oscillations. This method is designed to run on images acquired with full k-space coverage without additional prefiltering, and should be strictly applied before any interpolation by other processing steps.

As a design choice, the integration of Gibbs ringing correction into FT4Onco assumes that there are always some intensity oscillations present in dMRI data. While ringing artifacts are not detectable automatically and require visual inspection in advance, strict use of this method may cause some image blurring. Nevertheless, the cumulative effect of blurring on fiber tracking performance was not investigated in this work.

5.4.4 Motion correction with outlier detection

Common DTI acquisition schemes based on single-shot echo planar imaging (SSH-EPI) enable recording DWI data in 5–10 minutes, depending on resolution and employment of acceleration techniques (e.g. simultaneous multi-slice imaging). HARDI datasets are generally collected in several acquisitions within ca. 20 minutes. These durations are relatively long compared to anatomical scanning, and brain MRI data corruption with subject motion (from

fidgety movements to short head displacement as a result of normal breathing) is typically inevitable, particularly in case of less MRI compliant pediatric or neonatal cohorts.

The first approaches addressing volume-level motion artifacts aimed at defining a rigid transformation for each volume that best approximates head motion during an MR scan. As a solution, volumes were interpolated into the subject reference frame. However, diffusion MRI data are typically collected in stacks of slices, and subject motion may therefore not only occur between different volumes, but also between slices of individual volumes across series.

The effects of subject motion can be differentiated according to when they appear during the SSH-EPI sequence: inter-shot² motion yields undersampled image regions due to slice scattering, while intra-shot³ motion gives rise to slice dropouts through linear shifts, and these slices must be treated as outliers in further realignment steps. Moreover, subject motion also induces rotation of diffusion gradient directions spanning the scattered slices, which demands a q -space data representation to be fitted to all diffusion encoding b -shells and directions.

FT4Onco incorporates a model-free slice-to-volume motion correction framework representing the diffusion signal based on spherical harmonics and radial decomposition (SHARD) to realign scattered slices both within and across b -shells [138]. Owing to the orientation dependence of the dMRI contrast, SHARD is a suitable data-driven diffusion signal representation as a linear combination of orthogonal components linking the spherical harmonics in each b -shell with a radial singular value decomposition (SVD). Given a SHARD basis rank r , the image to be reconstructed is linearly represented as a 4D image of SHARD coefficients, which are encoded in a vector \vec{x} . A forward model then enables the prediction of the expected diffusion contrast across scattered slices, and the inverse problem lies in optimizing the target vector \vec{x} to maximize similarity between acquired dMRI data and the prediction.

Briefly summarized in Figure 5.17, the SHARD motion correction algorithm integrates a relatively complex iterative process, where each epoch (iteration) consists of a reconstruction (optimizing SHARD representation according to the latest motion estimate), rank reduction (low-rank approximation via SVD), slice registration (updating motion parameters for a given vector \vec{x}), and outlier reweighting (removing damaged slices from reconstruction). The process of motion correction is initialized with all parameters set to 0 (no motion) and equal weights for all slices. The entire motion correction process typically consists of six epochs, two of which perform volume-level registration, the next three slice-to-volume registration, and the last one is a refinement of the reconstruction output with final motion parameters. Eventually, the SH coefficients from a 5D image of multi-shell spherical harmonics functions are mapped to the corresponding dMRI shells along specified directions based on the gradient table to create a 4D amplitude image (final series).

Configuring parameters for the SHARD-based motion correction, the SH basis order per shell for reconstruction (ℓ_{\max}), reduced SHARD basis rank for registration ($r_{\ell_{\max}}$), and two regularization parameters for reconstruction (λ – isotropic Laplacian convolution filter, and ζ – a derivative filter for stabilizing convolution along the slice profile) are defined (see Table 5.3). Regularization serves to stabilize noise amplification and interpolation when solving the inverse problem, and to minimize computational costs. Given that the SHARD method is relatively novel, all parameters for the selected multi-shell patient dataset were optimized by

²occurring between two readout gradients that fill k -space with frequency-encoded data

³occurring while a readout gradient is turned on

empirical testing. An optimal setup of parameters for SHARD reconstruction also facilitates motion correction in DTI data with few b -values and a low number of volumes.

As another input to the SHARD motion correction algorithm, the multiband acquisition factor needs to be specified to correct for intra-shot motion. The term “multiband” refers to the simultaneous excitation of multiple slices during image acquisition, often denoted as MB2, MB3, MB4, etc., which results in acquired signal as a combination of signals from all slices. Separate images are calculated using SENSE (parallel imaging with sensitivity encoding) unfolding algorithms, enabling scan time reduction with minimal loss in SNR. The use of no multiband acquisition is designated as MB1.

Variable	Multi-shell DTI (Klinikum rdl Munich)	Multi-shell HARDI (UH Leuven)	dHCP neonatal (KC London)
b -shells	0/1000 s/mm ²	0/1200/2500 s/mm ²	0/400/1000/2600 s/mm ²
volumes	1/32	5/128/125	20/64/88/128
MB	2	3	4
ℓ_{\max}	0, 4	0, 2, 6	0, 4, 6, 8
$r\ell_{\max}$	2, 0	4, 2, 0	4, 2, 0
λ	0.001	0.005	0.003
ζ	0.01	0.001	0.003

Table 5.3: Parametric setup for slice-to-volume motion correction on different diffusion MRI series. Default values were defined on the motion correction of multi-shell HARDI dHCP (developing Human Connectome Project) neonatal MRI series, for which the SHARD method was originally designed. Abbreviations: rdl = rechts der Isar, UH = University Hospital, KC = King’s College.

To perform efficient motion correction, the SHARD framework is also designed to suppress static EPI distortions, for which a B_0 field map and a PE (phase encoding) table need to be available in a dataset. However, the SHARD method assumes that EPI distortion is invariant in the subject reference frame. Moreover, an automatic estimation of the B_0 field maps is not integrated, and these slices may not always be acquired in scanning sessions. Although these distortion field maps can be generated by FSL topup or the Synb0-DISCO tool [139], a registration-based approach (described later in this section) is adopted for EPI distortion correction of dMRI data in FT4Onco.

Besides subject motion and static EPI distortion correction, the SHARD framework also performs slice outlier detection, where slices with intensity dropout or other artifacts are rejected based on a log-normal mixture model (outlier classification by a two-class Gaussian mixture model of the log-root-mean-squared error). SHARD-based outlier detection is designed to suppress slices with complete or partial signal dropout. However, spin-induced and physiological pulsation effects may introduce outliers more locally, and are not considered in this framework.

The SHARD motion correction algorithm is implemented in the MRtrix toolset with individually compiled libraries for reconstruction, registration, and outlier reweighting. Despite the SHARD method being primarily designed for robust motion correction in severely motion-corrupted multi-shell dMRI scans in neonatal imaging, it can be applied on adult dMRI data with comparable efficiency.

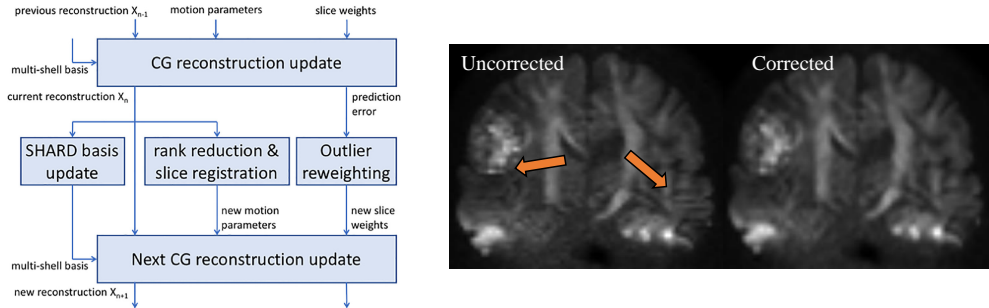


Figure 5.17: *Left:* Schematic overview of a single iteration in the motion correction framework. Before the conjugate gradient (CG, a fast iterative numerical method for solving linear systems of equations) updates the reconstruction, and outputs residuals between data and prediction, the multi-shell SHARD basis, motion parameters, and slice outlier weights are updated based on residuals from the previous reconstruction. *Right:* Effect of SHARD motion correction in the selected patient dMRI series. This subject was rather compliant, which is why significant motion traces are hard to find in the dataset.

5.4.5 B_1 inhomogeneity correction

The analysis of diffusion MRI data is often confounded by the presence of intensity nonuniformities referred to as bias, B_1 (radiofrequency) inhomogeneity or gain field. Bias field typically arises from the image acquisition process itself or due to specific dielectric properties of the imaged object. These artifacts are hardly noticeable to human observers, and are manifested by a smooth spatial variation of intensities across slices, which may highly degrade the performance of automated techniques, such as registration of diffusion data with anatomical underlays or diffusion metric estimation for tractography.

Numerous suppression methods for intensity inhomogeneity correction have been proposed and are well summarized in existing reviews [140]. As such, bias field correction methods are classified into two groups, namely prospective and retrospective methods. Prospective approaches deal with imperfections in the image acquisition process, while retrospective methods can deal both with scanner-induced and anatomy-related bias field artifacts, and focus on the physical properties of the imaged anatomy (magnetic permeability, position, shape, etc.). Retrospective methods are further divided into filtering based, surface fitting based, segmentation based, and histogram based methods.

For brain dMRI data, FT4Onco exploits the well-known implementation of histogram based nonparametric nonuniform normalization (N3), specifically its enhanced version named N4 with B -spline approximation and multi-resolution optimization [141]. Figure 5.18 shows an example of applying the N4 bias field correction on multi-shell data. Each iteration of the N4 algorithm maximizes the high frequency content of the intensity distribution of a given slice to calculate the bias field. Corrected images are computed successively by using the results of the preceding iteration. The N4 method is provided by ANTs through the Insight Toolkit (N4ITK), and is integrated in the MRtrix toolset.

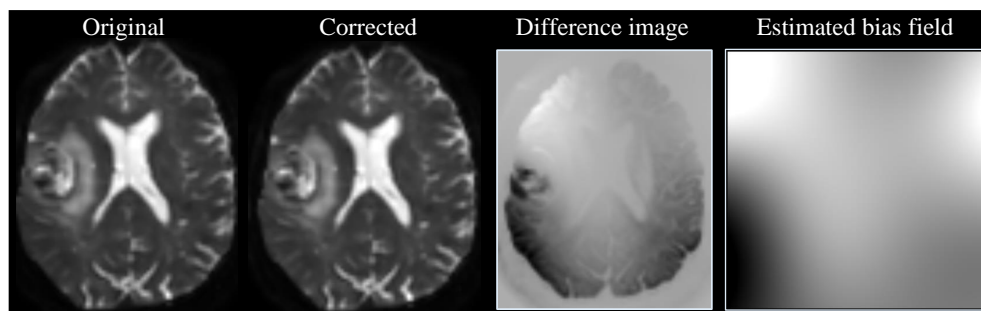


Figure 5.18: Suppression of intensity inhomogeneities on the selected patient dataset. *From left to right:* a slice of the motion-corrected b_0 volume without bias field correction; corrected image with removed shading in the lower left image portion; intensity difference between the original and corrected images; estimated bias field map showing an intensity dropout (dark segments) in the corresponding image areas.

5.4.6 DMRI-T1 co-registration, brain extraction, distortion correction

The registration of dMRI series with T1-weighted data is a challenging endeavor owing to large image contrast differences, and the susceptibility of DWI data both to affine/linear eddy current misalignments and non-linear EPI field distortions. Eddy current artifacts are caused by gradient-intensive isotropic diffusion waveforms during image acquisition, and realignment can be conducted by a constrained affine registration as part of motion correction. However, FT4Onco does not provide any correction for eddy current artifacts as these misalignments are assumed to be corrected by image reconstruction algorithms at Philips scanners.

Spatially nonlinear geometric distortions caused by EPI sensitivity to static magnetic field inhomogeneities along the phase encoding direction can be spotted at air-tissue interfaces and are clearly evident in ventral portions of the frontal and temporal lobes including areas near the sphenoid sinus and brainstem. The severity of these effects increases at higher main magnetic field strengths. The most common approaches to mitigate these issues include distortion correction of all DWI volumes before co-registration or using nonlinear registration transforms to warp anatomical images to the DWI space, both of which possess some drawbacks. Correcting individual dMRI volumes in a series via affine registration of individual DWIs to a non-diffusion weighted image (b_0) does not account for nonlinear geometric distortions, and is computationally expensive in case of HARDI data containing hundreds of volumes. Direct affine registration of anatomical images into the diffusion image space may result in poor or highly variable overlaps [142].

In general, EPI distortion correction strategies can be broadly categorized into two classes: image registration or B_0 field mapping (requires estimated B_0 -inhomogeneity maps from two scans with opposite phase encoding direction). These field maps are also referred to as “blip-up” (primary phase encoding) and “blip-down” (reverse phase encoding) image pairs. The majority of the diffusion-weighted volumes are acquired with the primary phase encoding direction. An MRI acquisition with the reverse phase encoding direction yields an image that is applied to unwarp any distortions present in the primary phase-encoded data. Investigations of best DWI-T1 registration practices have proposed that EPI distortion correction with field mapping should be performed prior to co-registration. However, an accurate estimation of these B_0 maps may be arduous, and regions of severe signal pile-up cannot be properly corrected for.

As a result of omitting FSL neuroimage analysis tools in FT4Onco, another framework had to be designed to account for susceptibility-induced geometric distortions, and to align diffusion and anatomical MR images in the same space. The following registration scheme was designed (Figure 5.19), making use of a combination of algorithms provided by the MRtrix and ANTs(Py) packages:

1. Registration of the T2 volume to the T1 image space using rigid alignment (rotation and translation) with linear interpolation, and mutual information as optimization metric
2. Registration of the mean b_0 volume to the T2-weighted volume (in T1 space) using symmetric normalization with rigid and affine transformation (SyNRA) with mutual information as similarity metric, and linear interpolation
3. Extraction of a T1 image mask and application of transforms from step (2) to this T1 image mask with multi-label interpolation and the registered mean b_0 volume as reference

Registration-based EPI distortion correction enables the alignment of DWIs with the T1 space, which is a necessary step to generate anatomically plausible fiber tracking output. Although areas outside of the intracranial cavity exert very low intensities on DW volumes, mask-aided skull stripping ensures that diffusion orientation distribution maps are computed only within the brain itself up to cortical regions. As described in the next section, only tensor-derived metric maps and FOD maps for CSD tractography are co-registered, capitalizing on the b_0 -T2 transformation and the T1 image mask in the DWI space. Importantly, the mapping of diffusion parametric maps to the T1 space also involves the reorientation of the original b -matrix in the gradient table [143].

The proposed strategy for b_0 -T2 registration-based EPI distortion correction and DWI-T1 co-registration leads to a significant acceleration of the processing pipeline given that skull stripping, realignment, and geometric distortion correction of the entire DWI series is avoided. As an inherent limitation, it should be considered that registration-based EPI distortion correction does not perfectly account for nonlinear magnetic susceptibility distortions in distant brain regions.

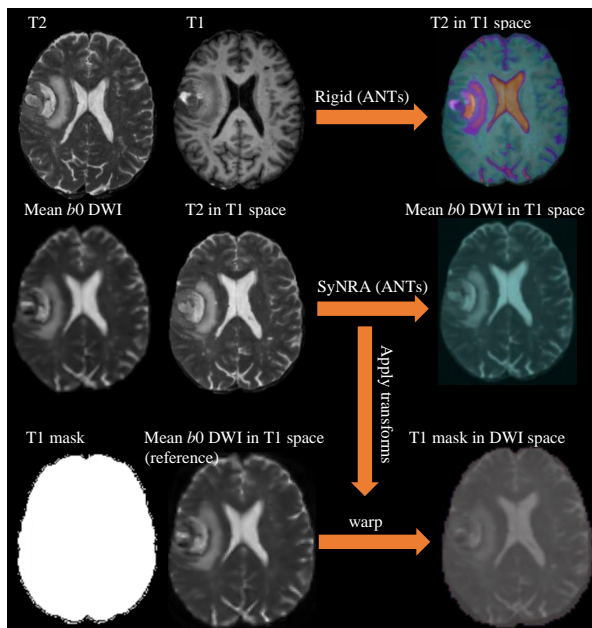


Figure 5.19: Framework for registration-based EPI distortion correction using T2 and average b_0 DWI volumes. Available transforms from the DWI-T1 registration are later applied for mapping diffusion FODs and other diffusion-derived metric volumes to the T1 image space.

5.5 Tractography chain

The previous two sections gave a methodological overview of the main downstream tasks performed on anatomical and diffusion MRI data as a preparation for fiber tracking inference. Employing probabilistic streamlines tractography with the CSD algorithm, the pipeline continues by computing the diffusion orientation density function from the DWI series, followed by voxel-wise principal fiber orientation estimation via WM FOD mapping. This section also explains how fiber bundles are reconstructed using recently published virtual dissection algorithms for streamlines segmentation in whole brain tractograms. Moreover, an adopted filtering approach to suppress false positives in final bundle reconstructions prior to visualization is presented. All algorithms are distributed in open-source packages (MRtrix, DIPY), and their specification can be found in Appendix A Table 4.

5.5.1 Response function estimation

In order to perform spherical deconvolution (SD) on DWI data (see Sections 2.3.4 and 2.4.3 for more background information), deriving the so-called tissue response function (TRF, a.k.a. basis function) is a compulsory step. A TRF models the expected signal in a voxel containing a single, coherently oriented fascicle, and serves as a kernel for the deconvolution algorithm. In case of multi-tissue spherical deconvolution, the TRF is computed for the GM and CSF signals as well. To improve anatomical contrast and the computation of TRFs as well as fiber

orientation distribution, it is recommended that bias field corrected dMRI data be upsampled to an isotropic voxel size of 1.3 mm unless the data resolution was higher during acquisition. In FT4Onco, changing the resolution of DW images is skipped as upsampling causes image processing times to elongate due to a significant increase of data size and required RAM allocation.

To estimate TRFs, FT4Onco incorporates an unsupervised approach fortified by MRtrix contributors, where the diffusion signal is averaged from a set of empirically determined single-fiber (SF) voxels. It should be noted that data-driven TRF estimation is nontrivial, and while multiple algorithms for different scenarios exist in MRtrix, only one algorithm, known as *dhollander* [144, 145], was selected for this pipeline intending to perform a multi-tissue CSD analysis on multi-*b*-value data.

The *dhollander* algorithm was implemented to compute TRFs for single-fiber white matter (SFWM), GM, and CSF signals based solely on the DWI data as input. An additional advantage lies in its ability to deal with TRF estimation in the presence of large hyperintense WM lesions [146]. Originally called *tourner*, this method was first designed only for the single-shell single-tissue scenario using only the highest *b*-value in a dataset [147]. Later, this approach was extended into the *dhollander* form, the working principle of which is exemplified in Figure 5.20. Here, the algorithm optimizes the segmented WM voxels across the entire angular domain in all *b*-shells. This optimization leads to an improved 3-tissue CSD fit to most datasets. Once a single fiber mask (an optimal voxel set) for all tissue types has been determined, a DTI or CSD fit is used to estimate the direction of underlying fibers per voxel. Rotating the diffusion gradient *b*-matrix, the algorithm then determines which fiber orientations are rotationally symmetric with the *z*-axis, and combines all signals to produce a single TRF per tissue.

5.5.2 Estimation of fiber orientation distribution

In streamlines tractography, CSD has been superior to tensor-based fiber orientation estimation from dMRI data by virtue of the ability to overcome crossing fiber limitations (resolving principal fiber orientation in voxels containing partial volume fractions from two or more distinct fiber populations) inherent in the diffusion tensor model. Using the estimated basis functions as a kernel, CSD performs a deconvolution operation (explained in Figure 2.14) to extract fiber orientation density functions (fODF) from the dMRI signal measured within each voxel.

In FT4Onco, tissue-specific ODF maps are generated by the multi-shell multi-tissue CSD (MSMT-CSD) algorithm from MRtrix that makes use of the unique *b*-value dependency of each tissue compartment (WM/GM/CSF) to obtain more precise fiber orientation information extracted from the TRFs. Unlike in SSFT-CSD (single-shell, single-tissue CSD), MSMT-CSD not only greatly improves the fODF estimates, but it can also better suppress spurious FOD peaks, which positively affects the coherence of fODFs in adjacent voxels, both in terms of peak amplitude and fiber orientation. Consequently, tractography benefits from the improved fODF estimates in less noisy tractograms near the WM-GM interfaces, and in a better recognition of tissue boundaries using fODF amplitudes as a stopping criterion to avoid tracking in the CSF or isotropic GM regions [148]. The MSMT-CSD algorithm uses the DWI series corrected for artifacts and bias field, the individual tissue TRFs, and yields

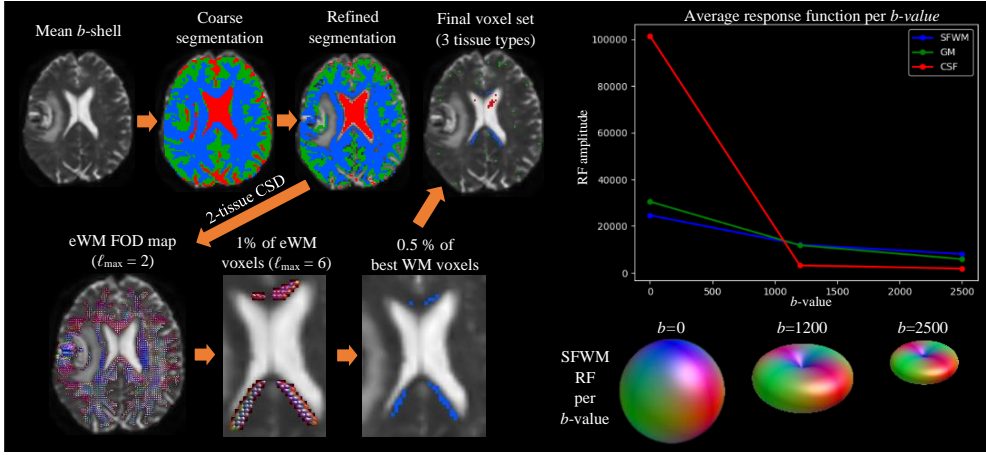


Figure 5.20: *Left:* A simplified schematic showing the process of response function estimation for three tissue types. In the beginning, a brain mask is extracted (not shown), and an averaged image for each b -shell is composed. For every b -value, a crude, fully automated data-driven segmentation of WM (blue), GM (green) and CSF (red) voxels is performed using two metrics: fractional anisotropy (FA), and a signal decay metric (SDM). The WM is initially separated from the rest by a low FA threshold (0.2), and other voxels belonging to GM and CSF regions are split using optimal SDM thresholds [144]. Next, all segmentations are refined by discarding multi-tissue partial volume voxels and removing SDM outliers. The final set of WM voxels is estimated via an artificially defined “extreme” WM response function (eWM) in zonal spherical harmonics (ZSH) – see [145] for details. In this process, a 2-tissue CSD using the eWM response and the CSF response from the data is conducted, which yields an eWM FOD map. Normalizing the resulting FODs by the sum of WM and CSF responses yields the WM tissue signal fraction ODFs. The eWM metric is obtained from the maximum peak amplitude of each ODF, and is computed with ZSH $\ell_{\max} = 2$. Eventually, only the best 1 % of all SFWM voxels are selected to compute the eWM response in these voxels with ZSH $\ell_{\max} = 6$, and 0.5 % of this subselection are accepted. GM voxels closest to the median SDM, and CSF voxels with the highest SDM values are selected in the final voxel set for GM and CSF respectively. *Right:* Relationship (signal decay) between the amplitude of the average response function per tissue type and the b -value, and spherical harmonics surface plots of the anisotropic SFWM TRF reflecting the preferential direction of diffusion along the WM tracts in the voxels.

the ODFs for each tissue compartment, typically full FODs for anisotropic WM, and single scalars for isotropic GM and CSF.

To utilize the full potential of the MSMT-CSD approach, it should be applied on HARDI data with b -values ranging between 2500–3000 s/mm² with minimally three unique b -values to estimate the ODFs in three tissue compartments. However, if a dataset contains only two unique b -values, MSMT-CSD will instead estimate two tissue compartments, e.g. WM and GM, where GM and CSF TRFs are very similar. The output WM FODs then undergo distortion correction through a nonlinear registration into the T1 image space (using inverse transformations obtained from the b_0 -T2 co-registration), and a corresponding FOD reorientation (Figure 5.21).

Finally, the undistorted WM FOD image is corrected for bias field and global intensity differences using the multi-tissue informed log-domain intensity normalization [149]. Intensity normalization is performed by optimizing the voxel-wise sum of all tissue compartments towards a constant value, under constraints of spatial smoothness. This algorithm also accounts for outliers by rejecting tissue areas with extremely high or low combined signal contributions (deep in the brain and along edges).

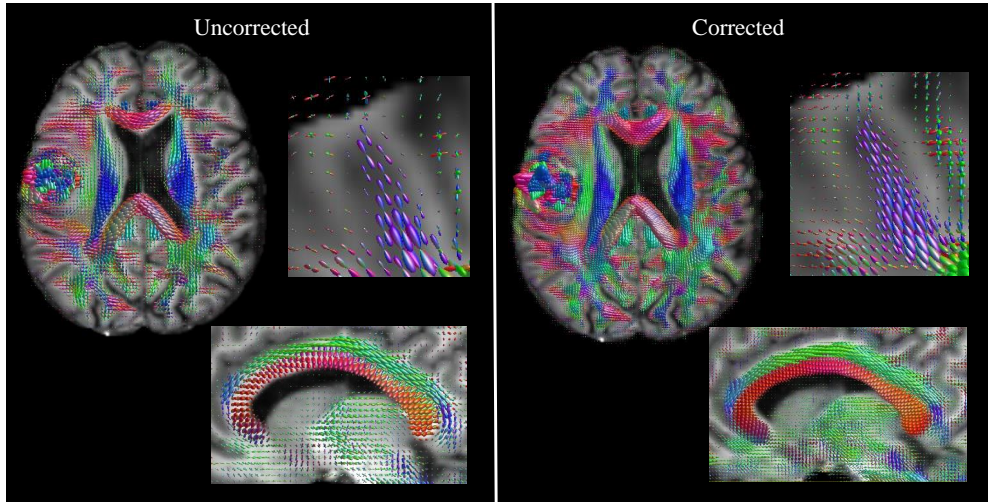


Figure 5.21: Visual comparison of generated FOD maps (full axial slice, sagittal view of the corpus callosum, and a zoomed coronal aspect of the WM-GM interface in a cortical area). *Left:* before registration-based susceptibility distortion correction and FOD reorientation; *right:* after applying EPI distortion correction with FOD reorientation. Color-coding represents the estimated fiber orientations as defined by convention (red – left-right; green – anterior-posterior; blue – superior-inferior). Note the improvement in fiber orientation density in the zoomed cortical termination area. The correction for residual intensity inhomogeneities is crucial for the later quantitative analysis of fiber densities.

5.5.3 Whole brain tractography

Having estimated the orientation distribution of WM fibers from the subject DWI data, the FT4Onco pipeline continues with probabilistic multi-fiber tractography restricted to the segmented WM mask based on the anatomical T1 image. Probabilistic algorithms take into consideration data noisiness, and crossing fiber regions, thereby overpowering deterministic streamlines fiber tracking methods. For details on the differences between deterministic and probabilistic streamlines tractography approaches, readers are referred to Section 2.4.

Streamlines tracking in FT4Onco is conducted using the iFOD2 method in the *tckgen* algorithm (MRtrix), which reconstructs streamlines based on second-order integration over the WM FODs represented in the SH basis [123]. This algorithm steps along streamline paths in short curved arcs of a fixed length (step size), tangential to the current direction of tracking at a particular point in space. Sampling a probability density function (PDF), the most probable candidate path is determined by the highest joint probability of all shortest steps leading to that path. A streamline is more likely to follow a path whenever the FOD amplitudes, sampled using linear interpolation from the eight nearest neighbors, along that path are large. This strategy reduces the overshoot (veering off course) of highly curved bundles and improves tracking through crossing fiber regions. It is recommended that a step size similar to the voxel size be set in order to minimize the delineation of unrealistic tracks.

As an input, *tckgen* seeds from the normalized WM FOD image within the provided anatomical tracking mask in DWI space. Several inclusion and exclusion criteria are defined. Streamline tracking is restricted to WM areas including the edematous zone obtained from brain tumor segmentation to ensure that pathological fiber infiltration is detected. Other tumor

segmentation labels are combined into one mask, which is used as an exclusive ROI together with the CSF-filled ventricles. The output whole brain tractogram is visualized in Figure 5.22.

To determine appropriate seed points, the algorithm needs to be provided with an explicit seeding mechanism and a source ROI, be it a set of image coordinates, a tissue boundary mask or an FOD image. In FT4Onco, the dynamic seeding approach is employed enabling the selection of seed points from the WM FOD image using the SIFT2 model (spherical deconvolution informed filtering of tractograms) that dynamically compensates for the seeding-related bias by preferentially selecting seeding areas with a low streamline density [150]. While it is impossible to guarantee that all voxels within the inclusive WM mask will be used for seeding, dynamic seeding gradually compares the tractogram to the image data throughout the reconstruction process to identify appropriate seeds and maintain a homogeneous seeding frequency.

Both the whole brain tractogram density and subsequently derived bundle representations are heavily dependent on the parametric setup of tracking algorithms. The parametric setup for WBT in multi-shell dMRI data is summarized in Table 5.4. The analysis of reconstructed bundle sensitivity to varying parameter values in whole brain tractography is reported in Section 6.3.

Parameter	Definition	Multi-shell HARDI	Default
l_{\min}	minimum track length [mm]	20	$5 \times \text{voxel size}$
l_{\max}	maximum track length [mm]	280	$100 \times \text{voxel size}$
angle θ	change in underlying fiber orientation between the start and end points of each tracking step	45	45
cutoff	FOD amplitude for terminating tracks	0.1	0.1
n_{samples}	number of FOD samples to take per step	4	4
power	raising the FOD by the inverse of the n_{samples} to mitigate the dependency of path segment probability on n_{samples}	$1.0 / n_{\text{samples}}$	$1.0 / n_{\text{samples}}$
step size	length of each track increment [mm]	$0.5 \times \text{voxel size}$	$0.5 \times \text{voxel size}$
seeds	number of seeds that the algorithm will attempt to track from	$1000 \times \text{select}$	$1000 \times \text{select}$
select	number of streamlines to be selected by <i>tckgen</i> , after all selection criteria have been applied (i.e. inclusion/exclusion ROIs, l_{\min} , l_{\max} , etc.)	10 000 000	5 000

Table 5.4: An overview of the most crucial whole brain fiber tracking parameters that affect the quality of reconstructed bundles. Included is the parametric setup for multi-shell dMRI data (selected dataset for the demonstration of image processing output in this chapter) with default values from the MRtrix documentation. Default values are applied for each parameter when not otherwise specified in the FT4Onco configuration file.

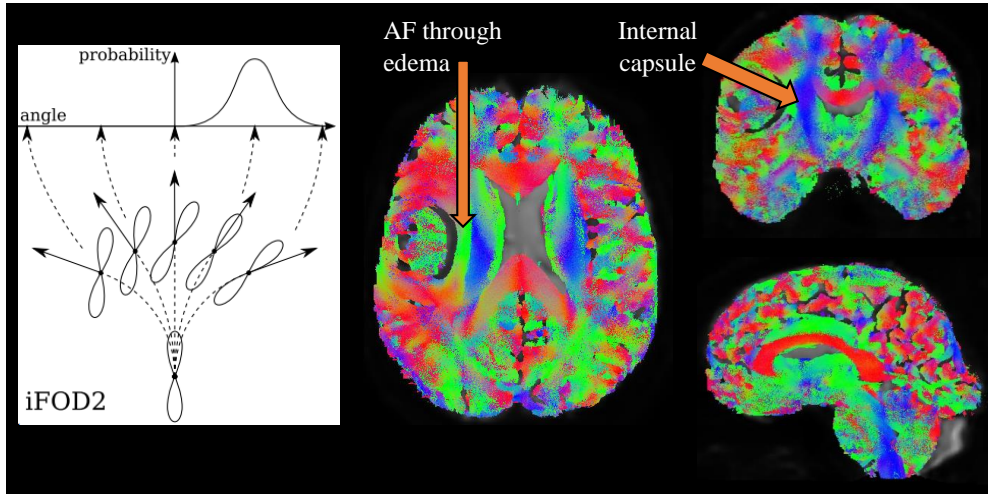


Figure 5.22: Three-plane view of the generated whole brain tractogram with the *tckgen* algorithm. Streamlines propagating close to the excluded ROI with contrast-enhancing tumor area, visible on the axial and coronal slices, prove the capability of the probabilistic iFOD2 method to reveal fiber propagation through edema (AF), and in areas with crossing fibers (e.g. in the internal capsule). Color-coding represents the estimated fiber orientations as defined by convention (red – left-right; green – anterior-posterior; blue – superior-inferior). The schematic shows the working principle of iFOD2. The FOD at one point is sketched at the bottom with a number of FODs at the next candidate points. Out of the charted curves, the path with the highest joint probability represents the most likely track direction.

5.5.4 Bundle recognition

Once a whole brain tractogram has been produced, the next step involves streamline segmentation (virtual dissection) to segment WM fascicles of interest, and remove all streamlines disagreeing with bundles' anatomical definition. State-of-the-art bundle segmentation methods are typically guided by rigorous anatomical priors in bundle reconstruction. The two most widely adopted types of bundle dissection approaches include methods using cortical region labels (typically obtained from brain segmentation) as inclusion/exclusion ROIs (connectivity-based methods), and fiber bundle recognition with bundle-specific shape models averaged from large-scale white matter connectome atlases (streamlines-based methods). In FT4Onco-v0.1, the anatomically constrained framework (ACT, MRtrix) was used in the initial stage of pipeline development, and was collectively evaluated as suboptimal in reports from clinical users (details in Section 6.2). Hence, in FT4Onco-final, the virtual dissection of targeted nerve fiber bundles from whole brain tractograms relies on bundle models available from the HCP842 tractography atlas [39] that are provided to the algorithm as shape priors with additional distance measures and thresholds.

Automatic bundle reconstruction in FT4Onco is realized via the RecoBundles (stands for *recognition of bundles*) algorithm implemented in DIPY [151]. The main advantage of RecoBundles over ACT is the robustness to pathological brains with neoplastic lesions and the ability to recognize bundle deformation or reduction in size along the entire bundle profile. This method first performs a global streamline-based registration (SLR) of the whole brain tractogram into a model atlas space (MNI space here). To further accelerate the global SLR

and bundle recognition processes, the subject's whole brain tractogram is $5 \times$ downsampled⁴. In the segmentation process, RecoBundles uses the QuickBundles method for streamline clustering and simplification of complex tractograms [86]. Instead of analyzing individual streamlines, the computation is accelerated by calculating centroids of individual bundles and working with distance metrics. The extent of the dissected bundle can be regulated by several key parameters and distance metrics explained in Table 5.5. Local and far pruning operations are performed on the tractogram to deprive the recognized bundle of irrelevant streamlines. After bundle recognition has been finished, dissected streamlines are registered back to the subject space. The entire RecoBundles process operates with multiple data formats: TCK (MRtrix), TRK (DIPY format with geometry information contained in its own header), and VTK (streamline visualization format).

Parameter	Multi-shell HARDI	Recommendation
model clustering threshold	0.5	0.01 – 3.0
reduction threshold	20	15 – 30
reduction distance	MDF	MDF
pruning threshold	10	8 – 12
pruning distance	MDF	MDF (default)
local SLR	True	True
SLR metric	asymmetric	asymmetric (default)

Table 5.5: Overview of bundle recognition parameters used to segment targeted bundles. All values are in millimeters. All thresholds were empirically tested and determined as optimal for this particular multi-shell patient dataset. The larger the value of the model clustering threshold, the fewer centroids of the model bundle are calculated. Reduction threshold enables reducing the search space for finding suitable candidate streamlines in the neighboring region of the model bundle (registered to the centroid-determined subject bundle with local SLR). The search distance is calculated with the MDF (minimum average direct-flip) distance function. A pruning threshold is applied together with a pruning distance metric to discard streamlines that are further from the model bundle than this threshold. If local SLR is executed, asymmetric registration is done to align the model bundle with the neighboring area. In FT4Onco, RecoBundles subsequently also performs a refinement step, where the reduction and pruning thresholds are reduced by 5 and 4 mm, respectively, yielding the final reconstructed bundle.

5.5.5 Spurious fiber filtering

Spurious streamlines, often seen in bundle reconstructions produced by probabilistic tracking methods, cause both recognized and refined bundles to look overly noisy. Determining which particular fibers in resulting reconstructions do not correspond to the underlying neuroanatomical configuration in the subject's data is ultimately impossible unless one compares individual streamlines with fascicles obtained from a post-mortem brain dissection. Therefore, an automated approach has to be established to at least remove streamlines that are obviously isolated or poorly aligned with the bundle core.

In FT4Onco, pathway alignment with its neighboring environment is measured with fiber-to-bundle coherence (FBC, included in DIPY), which is a quantitative measure of fiber spuriousness suitable for further pruning of bundles generated with RecoBundles [152]. In this method, bundles are regarded as a set of oriented points with a tangent adjacent to each of them.

⁴Downsampling factor was selected by empirical performance and memory consumption testing.

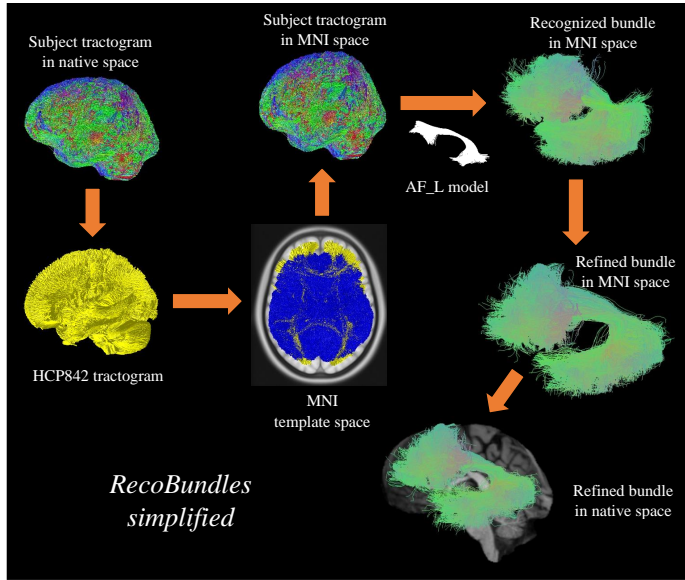


Figure 5.23: A simplified diagram of the underlying bundle recognition process in RecoBundles. The first step is to perform a global affine co-registration of the subject’s whole brain tractogram with the HCP842 tractogram, roughly aligned with the MNI T1 template. Next, streamline centroids are computed, anatomical models are locally co-registered with centroids, and distance metrics with specified parameters are applied to recognize bundles in the common space. Following a shape refinement step, output bundles are transformed back to the native (subject) space.

Every tangent is thought to contribute to the track density, and is considered to follow a Dirac δ -distribution (unit impulse). Bundle “clean-up” is achieved by first estimating the density of a contour enhancement kernel (see Table 5.6 for parametric setup) along each element of a pathway after lifting the bundle into the non-flat 5D domain (3D space with position and orientation). To obtain local FBC (LFBC), the kernel density estimator (sum over all locally aligned kernels) is convolved with the δ -distribution. A global fiber measure, the relative FBC (RFBC), is then calculated as the minimum of the moving average LFBC along a given fiber. Mathematical techniques for the kernel computation and estimation of LFBC are explained in [153].

When interpreting refined and FBC thresholded bundles, it is essential to understand that the RecoBundles-driven refinement step, where groups of streamlines within the search space are removed from the bundle tractograms after applying more stringent pruning and reduction thresholds, should not be perceived as an optimal method for filtering incoherent fibers. In this regard, the mathematical foundation of FBC provides a much more sophisticated and less abrupt way to remove spurious fibers while preserving the initial shape definition. The effect of varying FBC parameters on the quality of output bundles was not investigated in this work.

The removal of spurious fibers from reconstructed WM bundles is the last step in the fully automated virtual dissection process on the whole brain connectome. The next section describes how all neurosurgically relevant outputs of the FT4Onco pipeline are visualized, and how informative features (tumor-tract relationships, fiber tracking uncertainty) are derived.

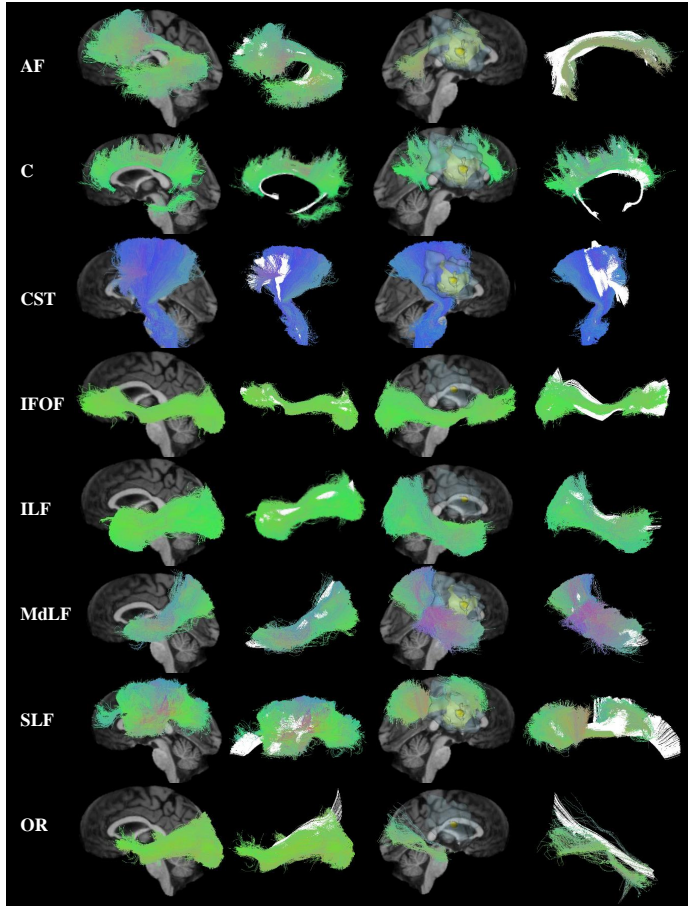


Figure 5.24: Visualization of bundle reconstructions produced with RecoBundles in both hemispheres, and a comparison of the final refined bundles with the model atlas bundles (white) provided by the HCP842 tractography atlas. Note that these fascicle representations are generated as a result of the WM dissection parameter setup described above. Abbreviations of these selected tracts are explained in Table 2.1.

Parameter	Definition	Multi-shell HARDI
D_{33}	$D_{33} > 0$; coefficient for the spatial diffusion of the contour enhancement kernel along the principal axis, determines the kernel width	1.0
D_{44}	$D_{44} > 0$; coefficient for the angular diffusion of the contour enhancement kernel; the quotient $\frac{D_{44}}{D_{33}}$ models fiber bending	0.02
t	$t \geq 0$; diffusion time of the contour enhancement process (similar to a Brownian motion process)	1
τ	RFBC threshold representing how many streamlines are classified as spurious	0.2

Table 5.6: An overview of the parametric setup for the contour enhancement kernel, and the number of fibers to be removed after FBC thresholding. If $\tau = 0.2$, then 20 % of fibers with low coherence are removed from the bundle. The coefficient values were set according to exemplary experiments in [153].

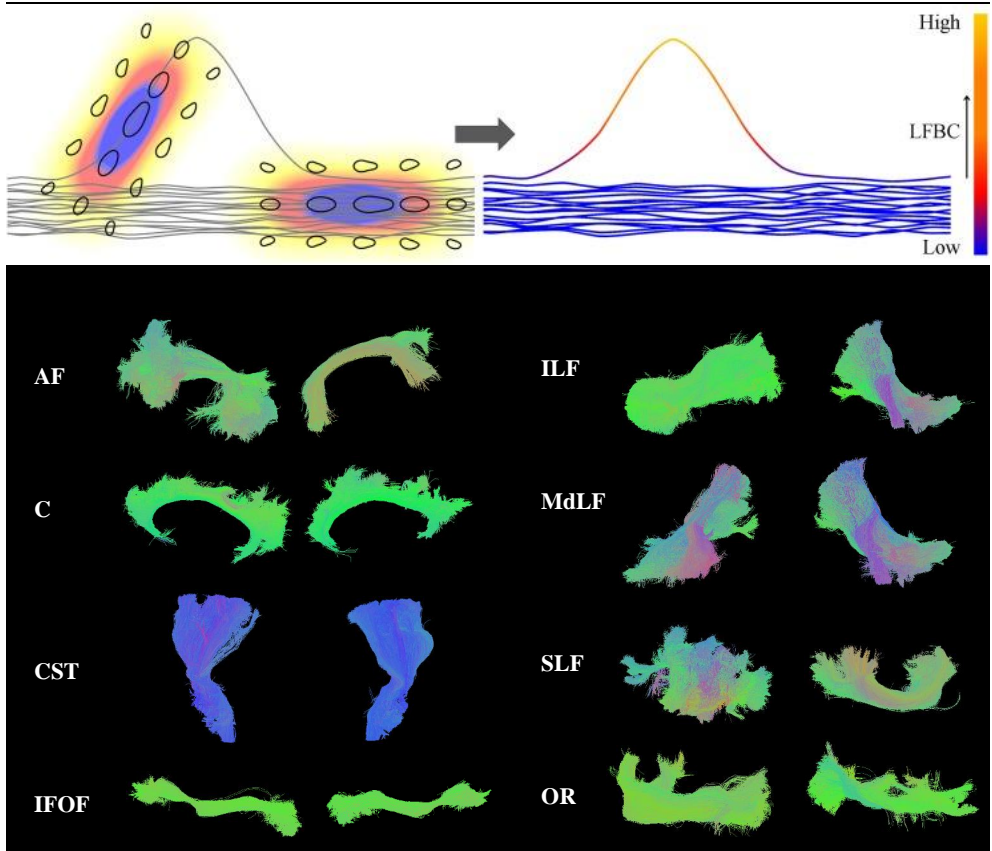


Figure 5.25: *Top:* A figure demonstrating the propagation of the contour enhancement kernel. On the left side, the contribution of two pathway elements to the overall kernel density estimator are shown. On the right, the local FBC, color-coded for each fiber, is obtained by evaluating the kernel density estimator along the fibers. In this case, one spurious fiber was detected as it deviates from the orientation and position of other fibers. As a result, this fiber has a low LFBC value. Figure adopted from [153]. *Bottom:* Bundle representations in both hemispheres after spurious fiber removal by FBC ($\tau = 0.2$). Note that these output bundles originate from filtering spurious streamlines in the recognized (not refined) bundles generated with the previous tractography step.

5.6 Visualization & viewing

Equivalent with UNs 3, 6, 7, and 9 in Table 4.1, the visualization of fiber tracking output should enable selective viewing of reconstructed bundles with geometrically aligned anatomical underlays, and provide informative features to reveal tumor mass effect (bundle displacement) or edematous infiltration zones, through which fibers may propagate. To aid interpretation, bundles should be deprived of spurious fibers generated as a result of using probabilistic methods, and fiber tracking uncertainty should be indicated along bundle profiles. This section explains how these features have been computed and their visualization implemented.

5.6.1 Formatting image processing output

FT4Onco produces various types of image processing output, however, only selected data files are presented to the users. For the inspection of WM bundles on anatomical overlays, the T1 and FLAIR images are used in common space. While the anatomical underlays remain in the NIfTI format along the entire pipeline, reconstructed bundles and segmented tumor labels are by design converted to VTK polydata to create 3D representations [154]. Bundle conversion from TCK to VTK demands a geometrical rotation and flipping to match the coordinate system of the reference underlays. Besides affine matching, individual streamlines are formatted as directionally encoded VTK polylines. The following VTK functionalities (available from the VTK library in Python) are used:

- ▶ *vtkPolyDataReader()* – reads the unaligned tractogram with VTK polylines (converted to VTK using MRtrix’s *tckconvert* functionality)
- ▶ *vtkUnsignedCharArray()* – sets RGB values into tuples of three elements to assign color to mesh points
- ▶ *vtkTransform()* – gets NIfTI image affine transform
- ▶ *vtkTransformPolyDataFilter()* – sets NIfTI image affine transform
- ▶ *vtkPolyDataWriter()* – saves the reoriented output

Akin to the modification of bundle geometry, the tumor labels need to be first converted from NIfTI to VTK meshes, and rotated to match the geometry of the T1 image space. Tumor meshes are colored in light blue (edema), yellow (contrast-enhancing portion), purple (necrosis), and brown (non-enhancing tumor). The following VTK functionalities are used:

- ▶ *vtkNIFTIImageReader()* – reads tumor segmentation labels in NIfTI
- ▶ *vtkDiscreteMarchingCubes()* – generates 3D mesh models representing the boundaries between adjacent voxels
- ▶ *vtkUnsignedCharArray()* – sets RGB values and opacity into tuples of four elements to assign color to mesh points
- ▶ *vtkWindowedSincPolyDataFilter()* – smooths each 3D surface model, and provides further features for surface editing
- ▶ *vtkTransformPolyDataFilter()* – sets NIfTI image affine transform
- ▶ *vtkPolyDataWriter()* – saves the reoriented output mesh

5.6.2 Tumor-tract relationships

In medical visualization, the conjunction between fibers and tumors is indicative of lesion-induced displacement, edematous infiltration or fiber destruction, see Figure 5.26. Nevertheless, to prevent overinterpretation, it is crucial to understand the influence of individual image processing steps that affect the degree of alignment precision with real underlying neuroanatomy. Using simple matrix multiplication and the *target* algorithm integrated in DIPY, tumor-tract relationships are shown as regions with the common cross-section of bundle polylines and tumor meshes.

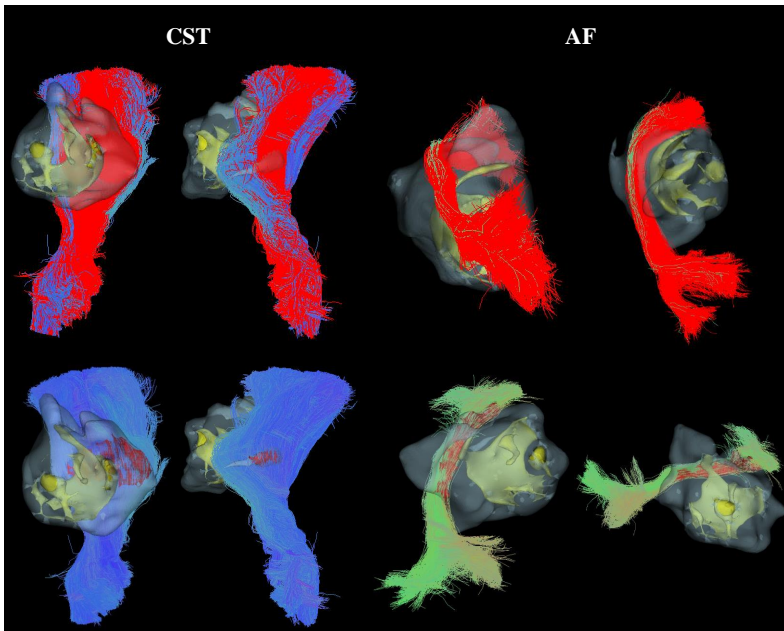


Figure 5.26: Various aspects of the right CST and AF (both FBC thresholded). Streamlines affected by edematous infiltration are shown in the top row and are colored in red. The bottom row highlights the extent of the infiltrated area in red. These pathological findings were confirmed by neurosurgeons during tumor resection. No further infiltration of other reconstructed bundles was detected in this patient case.

5.6.3 Visualization of fiber tracking uncertainty

As described in the upper sections, probabilistic streamlines tractography generates a number of spurious fiber bundles that can be classified as false positives when comparing bundle reconstructions to intraoperative observations. By definition, fiber tracking uncertainty arises from ignoring the true fiber tracking outcome, i.e. the difference between reconstructed bundles and the underlying WM anatomy, and has miscellaneous sources. Probabilistic tracking algorithms derive a voxel-wise distribution of fiber orientations based on noise estimation. Besides noise, examples of uncertainty sources include MR scanner settings, magnetic distortions, partial volume effects, diffusion modeling errors or elements of fiber tracking algorithms (numerical integration, interpolation, stopping criteria, seeding strategies, etc.).

Apart from estimating the fiber orientation distribution, CSD has been widely used to obtain apparent fiber density (AFD) [64], which can essentially infer the intra-axonal signal fraction along multiple fiber pathways, thereby providing information on microstructural axonal integrity, and indicating areas with a higher number of crossing fibers. AFD maps are obtained with MRtrix tools by first segmenting continuous FODs on the WM FOD maps to produce fixels. A fixel represents a single fiber population in a voxel, i.e. the smallest discrete element of a fiber bundle. Then, the fixel-based sparse-data image is converted to scalar data by computing the mean value across all fixels within each voxel.

The quantification of fiber tracking uncertainty in FT4Onco is facilitated by computing the AFD and FA evolution along bundle profiles [155] to provide insights into bundle integrity and support the possible visual revelation of edematous infiltration or bundle displacement. For demonstration, the infiltrated right arcuate fasciculus in the selected patient dataset is used as an example in Figure 5.27. A decrease in AFD may indicate to the users that the specific bundle segment is affected by edema, hence increasing the uncertainty of bundle propagation across this area. Similarly, lower FA values may be indicative of areas with complex fiber architectures and crossing fibers, thereby decreasing the degree of certainty about bundle presence in this particular brain area. Though not implemented in this work, the calculated AFD/FA bundle profiles can be overlaid on individual reconstructed bundles to simplify the localization of uncertainty along all bundle segments. Note that this way of indicating tractography uncertainty does not account for the inherent inaccuracy of the actual tracking algorithm (probabilistic CSD).

FT4Onco uses MRtrix tools to compute DTI/HARDI metrics, and DIPY's Python libraries for bundle tractometry. To demonstrate fiber tracking uncertainty by showing AFD/FA values along each fascicle, the automated fiber quantification (AFQ) framework was applied [156]. AFQ firstly computes bundle centroids using the MDF metric [86], and then subsamples these centroids to an arbitrarily chosen number of equidistant points N . Secondly, every streamline of the processed bundle is assigned to its closest centroid point. Since some bundle streamlines may still diverge significantly from other streamlines (even after FBC thresholding), the contribution of each streamline to the bundle profile is determined by the distance of each streamline from the mean bundle trajectory at each point. Moreover, streamlines are reoriented so that each streamline of the bundle points in the same direction. Correct orientation is achieved by creating standard streamlines from centroids of bundle atlas models. Thirdly, N averaged values along the pathway are extracted from the volumetric image data (AFD/FA

maps), which are projected to the subsampled bundle. Finally, each voxel is Gaussian-weighted by its relative geodesic distance to the closest centroid point, and these weights are subsequently used for the calculation of the bundle profile of interest.



Figure 5.27: Visualization of fiber tracking uncertainty using bundle feature (AFD, FA) profiles. Each feature is resampled to 100 points representing 100 segments of the whole bundle. This graph reveals the evolution of bundle measures along the right arcuate fasciculus, which is affected by GBM-induced infiltration. Both bundle measures range between 0 and 1, zero indicating the highest uncertainty, and 1 representing the lowest uncertainty of fiber presence.

5.6.4 Selective viewing

Designing FT4Onco as a command-line tool for clinical research, a graphical user interface (GUI) was identified as a non-functional requirement. Without a GUI, the entire pipeline would merely consist of a set of image processing steps without possibilities for selective viewing of individual results in an interactive environment. While UI development was unnecessary in the first conceptual architecture with ISD, the existence of a user interface later became somewhat logical as there is no particular means how physicians view the outcomes once image processing has terminated. There is a plethora of open-source medical visualization tools: from compiled libraries such as *mrview* in MRtrix, *horizon* in DIPY, up to standalone software tools like TrackVis, DSI Studio, or 3D Slicer. Nevertheless, it may be preferred by users to avoid the tedious installation and configuration of bulky software from third-party distributions, let alone outcome reformatting to match the geometry in these tools.

Moreover, FT4Onco itself does not support a fully automated data preselection and pipeline configuration. Specific configuration files need to be adjusted before the pipeline is launched. For these reasons, a novel multi-feature GUI (Figure 5.28) with an interactive layout was designed. This user interface was written entirely in Python using the *tkinter* Python library that interfaces the *Tk* GUI programming toolkit. The GUI is equipped with the following features:

- ▶ option menus for parametric setup, pipeline configuration, and the modular selection of image processing steps
- ▶ user hints in hover-over mode at every button
- ▶ drop-down lists for the selection of desired fiber bundles to be reconstructed
- ▶ an integrated Linux terminal with file explorer capabilities
- ▶ picture viewer for the visualization of various file formats (PNG, JPEG, TIFF, etc.)
- ▶ VTK-based Philips Omniview fiber tracking viewer for selective 3D viewing of reconstructed bundles with anatomical images
- ▶ third-party Aliza Medical Imaging DICOM viewer for the inspection of DICOM data and NIfTI volumes; this tool can be connected to patient archiving systems

This chapter provided a comprehensive overview of both system, and software architectures, including explanations of the fundamental principles for all functional constituents of the FT4Onco pipeline. The next chapter reports FT4Onco verification, clinical evaluation of FT4Onco-v0.1 (the first ISD-integrated release) and presents observations collected from a bundle reconstruction sensitivity analysis.

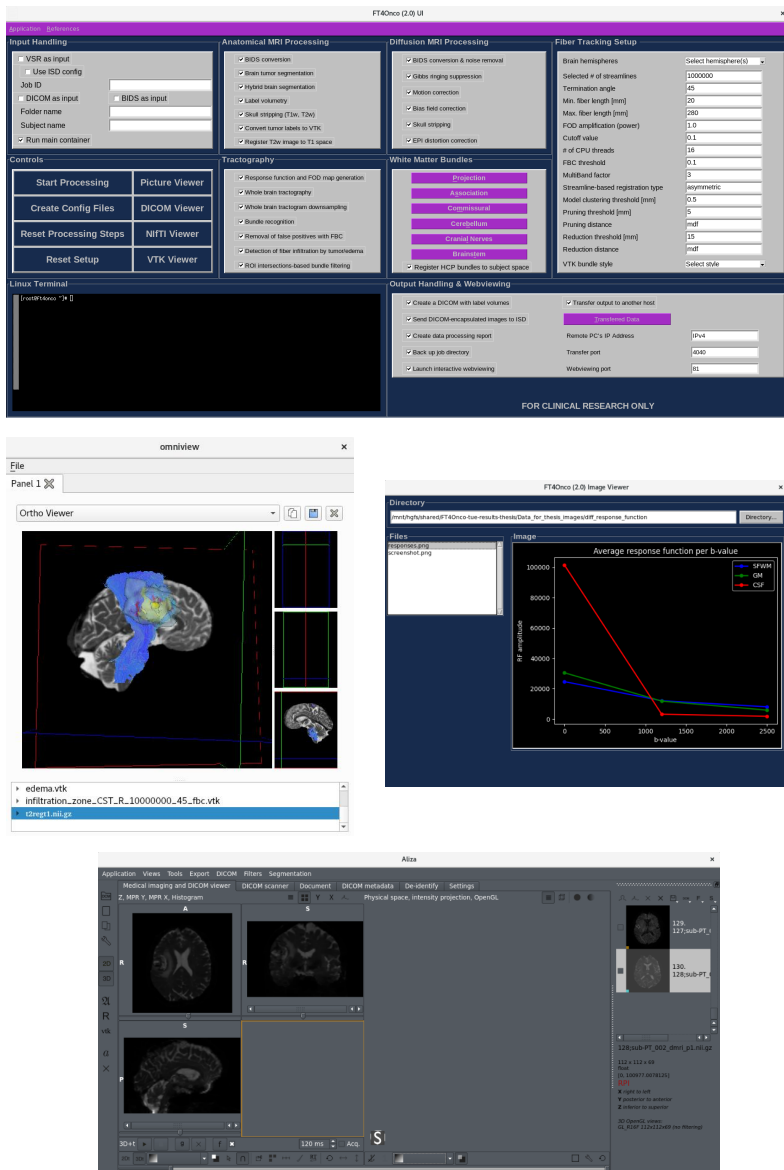


Figure 5.28: Screenshots of the FT4Onco GUI layout (*top*) with the interactive VTK-based Philips Omniview (*middle left*), picture viewer (*middle right*), and the Aliza Medical Imaging software for DICOM and NIfTI inspection (*bottom*). It should be noted that the layout of the FT4Onco GUI serves two main purposes, namely the pipeline configuration and data inspection in clinical research, and it does not intend to provide a single button to automate the entire workflow.

6 Verification, evaluation & sensitivity analysis

This chapter reports software verification to confirm whether the developed demonstrator conforms to defined functional requirements, and qualitative clinical evaluation to assess fiber tracking performance on selected patient datasets. The experimental design and outcomes of evaluation are described, where medical doctors visually inspected fiber tracking output and judged the feasibility of neurosurgery planning based on observed representations of bundles and pathology. The last section demonstrates bundle reconstruction sensitivity to the varying initialization of fiber tracking parameters.

6.1 Software verification

Standard verification guidelines for software as a medical device (regulated by FDA 21 CFR 820.30 and ISO 13485) define verification as confirmation that the design output meets the design input requirements. Software verification aims at determining whether the developed solution conforms to its functional requirements and related specifications. Depending on the preferred feature to be verified, the verification process may comprise memory leak tests, stress tests, exploratory tests, code reviews or usability tests, amongst others. The verification of FT4Onco was performed by scrutinizing the output of individual image processing steps at three levels:

- *Unit testing* to verify the design implementation for a single software element (i.e. image processing step) or a subgroup of processing steps in the pipeline
- *Integration testing* to verify if sets of image processing steps (for anatomical MRI data, diffusion MRI data, and fiber tracking) perform correctly when separated from the rest of the system
- *System testing* to verify the entire integration of all sets of image processing steps and whether they meet specified requirements

Unit testing involved a set of automated unit tests on clinical datasets from two centers (Table 6.1) in a test environment that was configured in accordance with the minimum hardware requirements for FT4Onco, see Table 5.2.

Data	Klinikum rDI Munich	UH Leuven
Diffusion MRI	multi-shell DTI, 33 volumes $b = 0/1000 \text{ s/mm}^3$ (2 iso)	multi-shell HARDI, 258 volumes $b = 0/1200/2500 \text{ s/mm}^3$ (2 iso)
Anatomical MRI	T1 (0.75 iso) T2 (0.35 x 0.35 x 4.4) T1C (0.75 iso) FLAIR (0.71 iso)	T1 (0.9 iso) T2 (0.5 iso) T1C (0.9 iso) FLAIR (1 iso)

Table 6.1: Datasets used in the verification process. Brackets contain voxel size of each volume/series in millimeters; iso = isotropic voxel size. A patient informed consent was signed, and MERC (Medical Ethics Review Committee) approval granted prior to obtaining these data. Abbreviations: rDI = rechts der Isar, UH = University Hospital.

For each functional requirement, multiple tests were launched and, where needed, image processing parameters systematically optimized (value ranges were found in literature) to reach desired outcomes. The acceptability of image processing output was determined according to defined acceptance criteria in the form of unambiguous statements, each with a clear pass/fail result. In the event of suboptimal performance of an image processing step, a substitution of the underlying functionality was found and unit testing was repeated. Verification outcomes are summarized in Table 6.2. Unit testing was followed by *integration testing*, where datasets were applied on a subgroup of concatenated image processing steps. Finally, the entire processing chain underwent *system testing* to optimize the order of image processing steps, troubleshoot glitches along the pipeline, and mitigate them by bug fixing or code rewriting. System testing also helped verify the compatibility of image processing output between pairs of consecutive image processing steps. Outcomes of all tests helped arrive at conclusions whether all functional requirements have been fulfilled or if substitutions had to be found for functionalities where verification had failed.

FT4Onco verification revealed several limitations, listed in Tab 6.2. These known anomalies nevertheless do not hamper the primary goal of fully automated image processing, and repeatable outcome generation across all verified levels. It can therefore be concluded that all functional requirements have been satisfied, and FT4Onco was built in the correct way.

6.2 Clinical evaluation

During development, the FT4Onco pipeline was evaluated in-house through unit testing on clinical datasets from collaborating clinical centers (University Hospital in Leuven, Klinikum rechts der Isar in Munich). The first architectural concept of FT4Onco (a fully automated plugin embedded in ISD, details in Section 5.1.1) underwent clinical evaluation with end-users (medical physicians) at Klinikum rechts der Isar in Munich (Germany). Invited neuroradiologists and neurosurgeons were trained to understand the architecture of FT4Onco, and assess the quality of image processing output as well as the overall usability of FT4Onco in their daily presurgical workflow. Spreadsheets were filled out by six users, who were asked to manually interact with the application interface on ISD, and evaluate data analysis outcomes.

Collected observations from this user evaluation were subsequently applied to significantly refactor the entire image processing pipeline, which eventually gave birth to the existing concept described in Section 5.1.2. Instead of performing a second evaluation, the enhanced version, reflecting this user evaluation, was applied in the final cross-validation experiment described in Chapter 7. This section summarizes the evaluation setup, explains relevant considerations, and reports both quantitative and qualitative results. A version number, namely *v0.1*, is attached to FT4Onco to differentiate between the evaluated demonstrator (FT4Onco-v0.1) and final software (FT4Onco-final)¹.

¹Version differentiation is solely applicable to the thesis section describing clinical evaluation. In all other chapters, “FT4Onco” designates the final version.

Functional requirement	Verified functionalities	Acceptance criteria	Known limitations
Whole-tumor segmentation	Glioblastoma segmentation	Lesion(s) are detected and labels are created	If the imaging field of view is too large, extracerebral regions may be identified as edema.
Lesion compartment classification	Glioblastoma segmentation	All tumor compartments (necrosis, edema, CE, non-CE) are detected	N/A
Whole brain segmentation	Hybrid brain segmentation	Hemispheres, subcortical structures, ventricles and CSF areas are segmented	WM structures in lesion-affected areas are wrongly classified.
Cortical parcellation	Hybrid brain segmentation	Cortical areas are parcellated into lobes and gyri	GM structures in lesion-affected areas are wrongly classified.
Whole brain white matter tractography	Diffusion data quality inspection Denoising Gibbs ringing correction Motion correction with outlier detection B_1 inhomogeneity correction TRF estimation FOD estimation Streamlines WBT	Whole brain tractogram with defined number of streamlines	Gibbs ringing correction and motion correction may introduce some blurring to the data. Average duration of whole brain tractography for tested HARDI datasets on CPU-driven systems amounts to several hours due to the <i>tkgen</i> algorithm.
Advanced probabilistic tracking with more sophisticated diffusion models beyond tensor	Probabilistic multi-shell multi-tissue CSD	Tracking through edema and crossing fiber regions yields anatomically plausible results	Low angular resolution data are not suitable for probabilistic CSD tracking.
Segmentation of fiber bundles connecting eloquent areas Filtration of false positive streamlines	Bundle recognition and refinement, spurious fiber filtering	Selected bundles are segmented from whole brain tractograms	In dMRI data with a single non- b_0 series and low number of volumes, some bundles may fail to be reconstructed.
Detection of fiber tract displacement or edematous infiltration	T1 and T2 brain extraction T2 and T1 co-registration b_0 and T2 co-registration EPI distortion correction Detection of tumor-tract relationships	Labels representing overlaps between tracts and tumors in distortion-corrected image space	N/A
Indication of tracking uncertainty along bundle profiles	Automatic bundle quantification	Calculated FA, ADC and AFD profiles along each reconstructed bundle	N/A
Fully automated and orchestrated data flow with optimized conversion among multiple formats Export of outcomes in common data formats	Input data format inspection DICOM to BIDS conversion GBS and HBS label combination Tumor label and bundle conversion into VTK Output file reorganization to BIDS	Tractography output is converted to VTK with correct geometry of all tumor labels and underlays	Input data selection and output viewing need to be done manually by users.
Informative color-coded 3D visualization of reconstructed bundles with tumor labels and segmented anatomical underlays	VTK visualization scripts Philips Omniview viewer	3D tumor labels, color-coded fiber bundles according to fiber orientation, tracking uncertainty (graphically shown bundle profiles)	Information on tracking uncertainty is not integrated in visualization and is stored in separate PNG files.
Support for datasets coming from different sites, MRI scanners, and acquisition protocols	Entire pipeline	New datasets are processed with expected outcomes	The current pipeline only enables processing of clinically acquired data with two distinct imaging protocols.

Table 6.2: Verification table summarizing acceptance criteria (expected output) and known limitations of individual functionalities for functional requirements defined earlier in Table 4.1. Technical specifications of each functionality are defined in Appendix A and not repeated here. Acceptance criteria were visually evaluated by two observers, and compared with outcomes in literature. For visual evidence that all functional requirements have been fulfilled, see outputs from all image processing steps in Sections 5.3, 5.4, and 5.5.

6.2.1 Assumptions for successful evaluation

The evaluation of FT4Onco-v0.1 consisted of its on-site installation, pre-evaluation testing, collection of pertinent data, appraisal of collected data according to specified acceptance criteria, image processing, and construction of a clinical evaluation report. Various (sometimes unpredictable) technical issues typically occur on premise despite having successfully verified a software application in an in-house development environment. Possible violations to the fully automated nature of the presented workflow were anticipated owing to access restrictions to the computation servers, slow network connectivity, or other unforeseeable IT problems. Moreover, the viewing of data processing outcomes had to be performed separately on another device since no permission was granted to install the interactive fiber tracking viewer (Philips

Omniview, see Section 5.6.4) on the hospital's PACS computers. Based on these assumptions, an evaluation plan was outlined as follows:

1. On premise, the Philips IntelliSpace Discovery research platform, the computation node service, and a remote computing Linux server are set up and configured.
2. On the neuroradiology PACS server, a total of ten suitable LGG/HGG MRI patient datasets, acquired with the latest glioma MR imaging protocol, are collected.
3. All ten patient datasets are processed with FT4Onco-v0.1 to reconstruct bundles of interest (AF, CST, OR).
4. At least 5 medical doctors specialized in neurosurgery or neuroradiology evaluate the overall software design, image processing speed, and output quality.
5. Suggestions for further improvement of the clinical research application are documented.

6.2.2 MRI data selection

Diffusion and anatomical MRI data were collected in line with the department's research study protocol (Neuroonkologisches Register, approved by the MERC act No. 340/16 S), and a patient informed consent (Aufklärung für Studienteilnehmer und Einwilligungserklärung) was obtained from all patients. A total of 42 patient datasets were exported from the hospital's PACS server and transferred to ISD via the clinic's experimentally developed DICOM data transfer mechanism (Teleradiologie). During data migration, no anonymization was performed because the receiving ISD platform was located on the same network of the same hospital. Anonymization was applied prior to image processing, where both anatomical and diffusion volumes were skull-stripped and converted to the BIDS NIfTI format.

All MRI data were acquired using a standard MR scanning protocol for neuro-oncological imaging. To achieve faster image acquisition, nonuniform distribution of diffusion gradients is often employed (see Section 5.4.1). Uniform distribution is essential to avoid the underestimation of diffusion orientations in datasets, which enables more accurate determination of principal voxel-wise nerve fiber propagation. Switching off the Philips-proprietary scan-accelerating feature *gradient overplus* enabled the acquisition of diffusion series with evenly distributed gradient orientations. Each diffusion series was inspected for diffusion gradient distribution using an auxiliary ISD plugin to discard unsuitable datasets.

Out of the 42 collected datasets, ten patient cases (Table 6.3) were selected by local neuroradiologists according to the following selection criteria:

- Patient diagnosis must be one of the following: LGG or HGG tumors, ideally with surrounding edema.
- Datasets must comprise an EPI-dMRI series, a T1, T2, T1C, and a FLAIR volume.
- All diffusion series must be acquired shell-wise with uniformly distributed diffusion gradient directions.
- Tumors must be located in diverse brain regions and multi-focal lesions are accepted.

Appraised datasets included diffusion MRI scans (33 volumes, $b = 0/1000 \text{ s/mm}^3$, isotropic voxel size of 2 mm), and four 3D anatomical contrasts. Information on tumor characteristics (type and location) was extracted from the PACS system. Lesion sizes and shapes significantly vary across patients, and are not tracked in the diagnostic patient register. Tumor grading followed the latest official WHO recommendations for brain tumor classification.

Patient	Lesion type	Location
PT01	LGG with high-grade portions (II-III)	Left insular to temporopolar regions
PT02	HGG WHO IV	Right frontal lobe, cingulate gyrus
PT03	Bifrontal GBM with massive edema	Frontal lobe, ischemia at the genu of corpus callosum
PT04	GBM, IDH wild type	Right occipital lobe
PT05	Multi-focal GBM	Primary portion of the parietal lobe, also temporally in both hemispheres
PT06	GBM with massive edema	Left frontal anterior part of precentral gyrus
PT07	Multi-focal glioma	Right frontal lobe
PT08	GBM	Right and left temporopolar region
PT09	Glioma	Right hippocampal region
PT10	GBM	Left insular region

Table 6.3: Selected datasets for clinical evaluation.

6.2.3 Hardware setup and pipeline configuration

All ten patient datasets were processed with FT4Onco-v0.1, which was installed on the hospital's hardware (Table 6.4). This software version already incorporated the majority of processes for diffusion and anatomical MRI data which are also integrated in the final release (see Chapter 5). Clinical evaluation was conducted midway through the development time, which is why FT4Onco-v0.1 was composed of a number of functionalities that were later either removed or substituted in FT4Onco-final.

System info	CN server	ISD server
Type	desktop computer	virtual machine
Operating system	Ubuntu 20.04.1 LTS 64-bit	Windows Server 2016 64-bit
Processor	8x Intel Xeon W-2223 CPU, 3.60 GHz	2x Intel Xeon CPU E5-2643 v3, 3.40 GHz
RAM	32 GB	32 GB

Table 6.4: Hardware configuration at the hospital department during evaluation.

Compared to FT4Onco-final, the first major difference in FT4Onco-v0.1 was the use of a dMRI noise correction method, which is based on the MP-PCA algorithm available from MRtrix. Moreover, FT4Onco-v0.1 tractography employed anatomically constrained fiber tracking (ACT) based on MRtrix. A methodological explanation of ACT is provided in Section 2.4.5, and not repeated here. Akin to the RecoBundles approach used in FT4Onco-final, brain

tissue segmentation, diffusion image distortion correction, and the dMRI-T1 co-registration are prerequisites for a successful application of the ACT framework. In fact, image co-registration is the most crucial step since the output bundle quality is highly determined by the accuracy of alignment between provided anatomical ROIs and FOD maps.

When integrating the ACT framework to FT4Onco-v0.1 prior to the clinical evaluation, the ACT approach was tested on other datasets from Klinikum rechts der Isar in Munich (Germany) with unsatisfactory results, where streamlines did not terminate in the cortex, and were incompletely tracked. Therefore, in FT4Onco-v0.1, the ACT setup was modified such that anatomical ROIs were used for virtual dissection from a prefiltered whole brain tractogram, thereby driving bundle reconstruction strictly by inclusive criteria (bundle-specific ROIs). The following two paragraphs explain the FT4Onco-v0.1 tractography framework.

Applying the described modifications to the ACT approach, whole brain tractography was first performed with the iFOD2 algorithm and the MSMT-CSD tracking model (Table 6.5). Generated whole brain tractograms were refined by spherical-deconvolution informed filtering of tractograms (SIFT2) to improve the quantitative nature of streamlines reconstruction [150]. SIFT essentially compensates for bias reduction (underfitting and overfitting) in reconstructed bundles, and improves their biological plausibility. Tractogram filtering is achieved by mapping streamline densities back to the underlying diffusion signal (FOD lobe integrals), which exploits the SD property that the FOD magnitude is proportional to the DW signal in a particular orientation, which is conversely proportional to the tissue volume in each voxel. To counterbalance streamline over-representation in bundles, the SIFT2 algorithm calculates voxel-wise weights in fixel (fiber bundle element) space. Additionally, a 4D five-tissue-type (5TT) image was created, where the fourth dimension comprises five masks: cortical GM, subcortical GM, bihemispheric WM, CSF, and pathological tissue. The 5TT series is composed by concatenating the 3D brain segmentation output masks, and added to the SIFT2 algorithm to constrain the fixel-streamlines comparison model. After counting the weighting factors for each streamline, the tractogram was corrected by assigning a weight to each streamline such that the weighted contribution of all streamlines to the spherical deconvolution diffusion model matches the FOD lobe integrals of the diffusion data as accurately as possible.

Whole brain tractogram filtering was followed by selective bihemispheric anatomically constrained dissection of three bundles of fibers: AF, CST, and OR. Bundle reconstruction was achieved by the *tckedit* algorithm from MRtrix, where an empirically determined minimum streamline weight was specified, and inclusive/exclusive ROIs were given as constraints. Table 6.5 lists the dissection parameters and ROIs for each bundle of interest. Given that whole brain tractography was performed by dynamic seeding from the normalized WM FOD image, and not restrained to the WM areas, dissected bundles contained many spurious streamlines. To suppress false positives in output bundles, a filtering strategy developed by [119] was adopted. In this approach, each bundle of interest is first mapped to a high-resolution 3D track density image (TDI) based on a co-registered T1 template mask. The median value of the produced TDI volume is then multiplied by an empirically set constant, and the resulting value is used to threshold the TDI intensity. In addition, the TDI is filtered with a connected-component filter and dilated. Next, the ANTsX toolkit is applied to flatten the filtered TDI volume by 10 % of its maximum value, and threshold it with a 3D K-means clustering algorithm at a distance of 10. The final TDI volume is then thresholded once again at a minimum value of 2, and multiplied by the sum of all inclusive ROI masks for each bundle.

WBT parameters		Bundle	Inclusive ROIs	Exclusive ROIs
l_{\min}	40 mm	AF	pars opercularis, pars triangularis, superior temporal g., supramarginal g.	putamens, paracentral g., postcentral g., precentral g., middle temporal g., parahippocampal g., insulae, superior frontal g., transverse temporal g., superior parietal g., lateral occipital g., thalami, corpus callosum, brainstem, pons
l_{\max}	280 mm			
angle θ	22.5			
cutoff	0.1			
n_{samples}	4			
power	$1.0 / n_{\text{samples}}$	CST	paracentral g., postcentral g., precentral g., brainstem, pons	amygdalae, corpus callosum, contralateral cerebral WM
step size	$0.5 \times \text{voxel size}$			
seeds	1000 \times select	OR	pericalcarine cortex, lateral occipital g., thalamus	isthmus of cingulate g., contralateral thalamus, bilateral nn. caudatus and accumbens, ventricles, contralateral cerebral and cerebellar WM, corpus callosum, brainstem, pons
select	1 000 000			
seeding	dynamic from WM FOD map			
exclusive ROIs	tumor without edema, ventricles			

Table 6.5: *Left table:* Fiber tracking setup for whole brain tractography in FT4Onco-v0.1. *Right table:* Inclusive and exclusive ROIs for bundle dissection. Abbreviations: gyrus (g.), nuclei (nn.). All anatomical ROIs were segmented with the Philips-proprietary hybrid brain segmentation tool.

Eventually, the MRtrix *tckedit* algorithm applies this refined TDI volume together with all inclusive and exclusive ROIs to remove spurious fibers from bundle tractograms.

6.2.4 Experimental design

Reconstructed bundles were visualized and viewed for inspection as 3D T1 image overlays in Philips Omniview. A total of five neuroradiologists and one neurosurgeon participated in the clinical evaluation (it was impossible to recruit more participants due to COVID-19 pandemic-related staff shortages, and a tight clinical schedule). During approximately 45-minute meetings in person, clinicians were introduced to the TRABIT project, and presented with a demo of FT4Onco-v0.1 as well as the fiber tracking viewer (Figure 6.1).

Next, a training document with step-by-step instructions was given to the participants, while they took control over the application and experienced its use. Patient cases were selected randomly for inspection to prove robustness of the application on the department's data. Eventually, physicians were asked to do a visual quality assessment by answering a questionnaire consisting of sections shown in Appendix C Table 7. The main goal of the evaluation sheet was to collect information in the following areas of interest:

- Clinicians' background, prior experience with fiber tracking, and use of clinical research applications for tractography
- ISD plugin user interface (intuitiveness, data selection from databases, plugin execution, missing features)

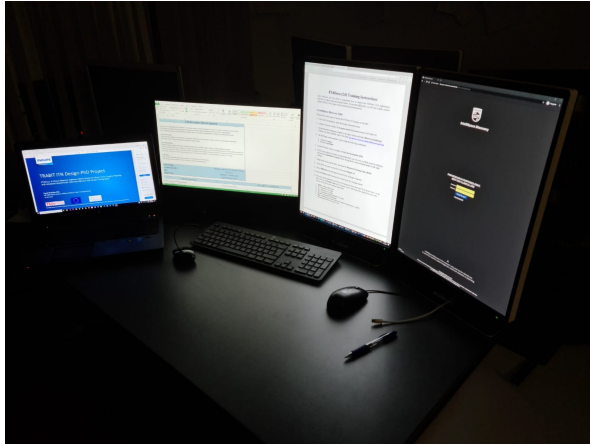


Figure 6.1: Experimental setup for evaluation. The image shows a PACS workstation at the neuroradiology department with remotely controlled FT4Onco-v0.1. *From left to right:* introductory presentation about TRABIT, evaluation spreadsheet, instructions for use, ISD user interface.

- ▶ Performance of both ISD and FT4Onco-v0.1 (interaction speed, data loading speed, bundle/brain tissue segmentation accuracy, viewing speed, data processing duration)
- ▶ Visualization and viewing of data processing results (output informativeness, representativeness of underlying neuroanatomy, artifacts, geometrical alignment of overlays, viewer interactivity, missing functionalities in viewer, tumor-tract relationships, feasibility to plan surgery)
- ▶ Overall impression (suggestions for improvement, adoption in clinical research/practice, clinical value)

The evaluation questionnaire contained mixed types of questions: dichotomous questions (answered *yes* or *no*), single-select multiple-choice questions, ordinal-scale rating questions (excellent–5, good–4, moderate–3, fair–2, poor–1), and one open-ended question to enable sharing elaborated suggestions for improvement. Clinicians’ background was evaluated by self-assessment of their skill proficiency levels (beginner, elementary, intermediate, advanced, proficient).

6.2.5 Evaluation outcomes

Image processing was successful in all ten patient cases (see Figure 6.2). Participants’ education background and their self-assessment of experience in diffusion MRI tractography are reported in Table 6.6. Average scores from the visual qualitative assessment of FT4Onco-v0.1 are listed in Table 6.7.

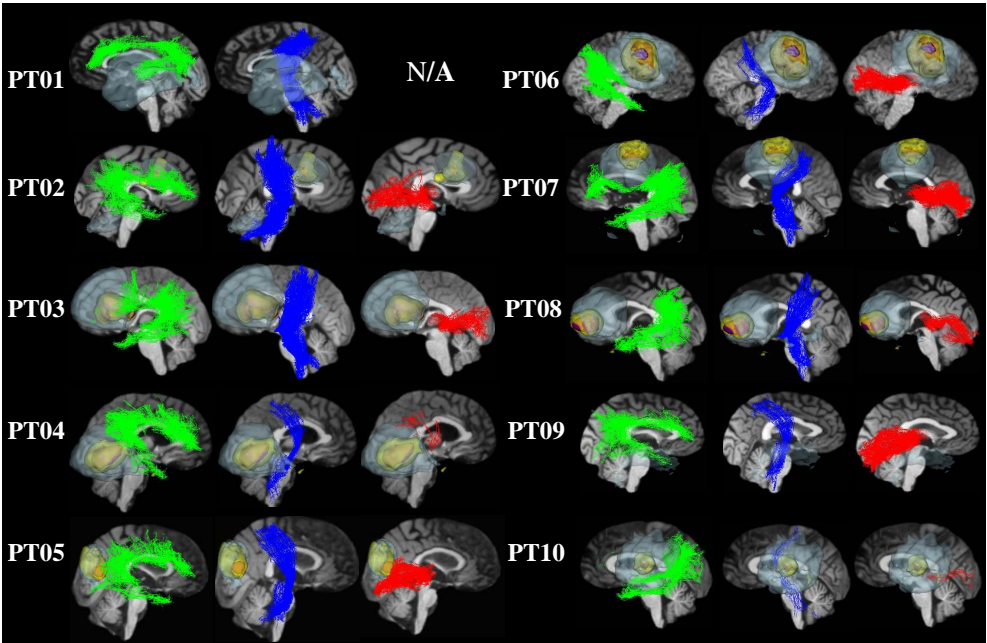


Figure 6.2: Bundle reconstructions (AF–green, CST–blue, and OR–red) produced by FT4Onco-v0.1. In patient case PT01, tracking of the right OR failed and is therefore unavailable for viewing. All tumors contain a necrosis except for cases PT01 and PT09, where only large edema with small contrast-enhancing portions are present.

Clinicians’ self-assessment	
Educational background	medicine (6)
Specialty	functional and oncological neurosurgery (1), neuroradiology (5)
Surgical planning platform	Brainlab iPlan (6)
Involvement in surgery planning	yes (1), no (5)
Knowledge of dMRI data analysis	intermediate (4), advanced (2)
Knowledge of dMRI-based tractography	elementary (1), intermediate (2), advanced (3)

Table 6.6: Self-assessment of the interviewed clinical personnel with respect to their background and experience with tractography.

In the last section of the questionnaire, clinicians shared their overall impression of the fiber tracking application and complementary comments to substantiate their chosen rankings. All participants reported to be willing to start using FT4Onco-final once made available, and they also mentioned recognizing high clinical value of the tool, especially for diagnosis determination in tumor board meetings or the selection of adequate neurosurgical treatment approaches. Clinicians mostly appreciated the use of advanced fiber tracking models to enable tracking through crossing fiber regions, and to reveal tumor-tract relationships.

Group	Features	Scores	μ_{ft}	μ_{group}
ISD plugin UI	Data selection from database	4-3-5-3-5-5	4.17	4.17
	Plugin layout clarity	4-3-5-5-3-5	4.17	
Performance	Responsiveness	3-4-5-2-3-4	3.5	3.38
	Data loading speed	4-3-2-1-2-1	2.17	
	Segmentation accuracy	4-4-3-5-4-4	4.0	
	Viewing speed	4-4-5-3-2-5	3.83	
Visualization Viewing	Amount of informative content	4-4-5-4-4-4	4.17	3.83
	Bundle-neuroanatomy similarity (compared to DICOM images)	3-0-5-5-4-4	3.5	
	Geometrical alignment of overlays	4-4-5-4-4-4	4.17	
	Viewer interactivity	3-4-4-3-3-3	3.33	
	Feasibility to plan neurosurgery	3-4-5-4-4-4	4.0	

Table 6.7: Average scores obtained from the qualitative evaluation of FT4Onco-v0.1 as an ISD plugin. μ_{ft} denotes the mean score for a particular feature, and μ_{group} for the entire set. Based on the group averages, performance and visualization were assessed as slightly better than moderate.

Referring to the presented system architecture, software version, and its data processing outcomes, various ideas for improvement were suggested in the following areas:

- **Workflow:** The ISD plugin UI was easy to understand. The need for manual dragging and dropping of imaging series into active view was confusing. An automatic data preselection, configuration of the active view in the ISD platform's ROS as well as automatic input parameter filling for the plugin was desired. Physicians unanimously agreed that the FT4Onco-v0.1 plugin should be integrated into the PACS system. Though suggested, integration into the MR scanner console would only be acceptable if more automated, ideally with a dictionary for the preselection of appropriate MR sequences.
- **Data processing speed:** The average data processing duration amounted to 1 h 55 min, which was considered fast enough for daily clinical workflow. However, since planning is often only performed shortly before surgery, neurosurgeons would have to plan more in advance. The ISD platform's responsiveness was rated as slow, especially when loading imaging data into active view in ROS. FT4Onco-v0.1 should ideally support GPU-driven image processing.
- **Visualization:** In the viewer, produced fascicles should be modifiable (e.g. by sliders to adjust the threshold for spurious fiber filtering). It was stated that while neuroscientists are interested in fiber connections to the cortex, surgeons want to see thin fibers with minimum false positives. Reconstructed bundles contained thick, densely intertwined fibers, which is why possible artifacts or misalignments could not be assessed. Visual clutter led to difficulties in determining tumor-tract relationships.
- **Viewing UI:** Ideally, the viewer would offer buttons for switching among viewing planes (axial, coronal, sagittal) and selective overlays. Fiber bundles should be more transparent and surface fibers should be removed to reveal tumor infiltration and its depth. Interactive tools for closer tumor-tract distance measurements would be preferred. Available anatomical underlays should offer to choose between FLAIR and T1 volumes.

- **Multimodality fusion – a site-specific requirement:** Fiber tracking outcomes should be integrable into the intraoperative workflow, e.g. by loading them into Brainlab’s neuronavigation platforms. Potentially, other sources of functional information (TMS, fMRI) should be available for viewing to increase the anatomical plausibility and confidence of observed results. In the operating room, preoperative and intraoperative MR images should be fused to provide real-time updates on the extent of resection.

Figures 6.3 and 6.4 show barplots of bundle features (number of streamlines and average streamline length) for all reconstructed fascicles. Although FT4Onco-v0.1 tractography succeeded in all patient cases except for the optic radiation in patient PT01, visual inspection of the reconstructed bundles shows striking evidence that bundles contain intercepted fibers, which tend to be very short despite the use of spherical deconvolution informed filtering that is supposed to remove them. Moreover, anatomical constraints in the form of inclusive and exclusive ROIs provided to the ACT-based fiber filtering approach do not seem to sufficiently restrict the track integration process, and cortical terminations are missing. Hence, many false positive bundles are still present in the tractograms, which leads to a visual clutter.

In view of these observations, development continued after the clinical evaluation with the aim to exploit acquired findings with user feedback in further improvement of the designed software. The major differences in functionalities between FT4Onco-v0.1 and FT4Onco-final are summarized in Table 6.8. The majority of suggestions for improvements from the clinical evaluation of the first version (FT4Onco-v0.1) matched with initially identified, but not yet fully realized user requirements. Therefore, the development of the second version (FT4Onco-final) focused on implementing these still needed improvements.

6.2.6 Clinical implications

Results obtained from the user assessment of FT4Onco-v0.1 confirmed the feasibility to perform multi-tissue CSD tractography in multi-shell datasets with low resolution and inadequate SNR (b -values: 0/1000 s/mm², 33 volumes), where the benefits of applying the CSD model cannot be fully reaped due to the limited orientational information along a low number of diffusion gradient directions. Distinguishing multiple tissue types using MSMT-CSD in single-shell data with a single b_0 volume (like in this evaluation) has been proven valid by MRtrix contributors [157], rendering this approach highly suitable for FT4Onco.

The average scores from the qualitative evaluation of FT4Onco-v0.1 (4.17/5 for plugin user interface; 3.38/5 for overall performance, and 3.83/5 for visualization and viewing) emphasized that there was a high potential for the adoption of this tool in clinical research once improved and released, which was congruent with clinicians’ statements.

Quantitative bundle analysis across all six reconstructed tracts by calculating the average fiber length (Figure 6.3) in each dataset indicated a consistent length of streamlines for the left and right AF, namely 52.91 ± 5.07 mm and 53.61 ± 3.97 mm. Higher variability was observed in bundles representing the left and right CST (107.65 ± 27.34 mm, 101.59 ± 25.39 mm) and OR (61.79 ± 27.25 mm, 63.04 ± 24.44 mm) bundles respectively. Track density quantification (Figure 6.4) using number of streamlines per bundle as a measure revealed dense representations of bundles for the left and right AF (559.1 ± 56.57 , 586 ± 60.57) and CST (336.6 ± 109.79 , 277.8 ± 108.28), and a low fiber density of the optic radiations (181 ± 103.61 , 187 ± 103.4). High variability in average streamline length across the CST and OR bundles,

and reduced bundle density of the OR could be explained by three major factors: tumor effects (in many cases shown in Figure 6.2, lesions caused large tract displacements due to massive edema), sparsely populated whole brain tractograms, and the under-representation of WM fibers in the underlying datasets with low spatial and angular resolution.

Although dedicated primarily to glioblastoma segmentation, this evaluation further demonstrates that the brain and multi-compartment tumor segmentation functionalities in FT4Onco can be applied to tractography in data with a broader spectrum of neoplastic lesions (LGGs, HGGs, multi-focal tumors, mixed-type gliomas).

FT4Onco-final was eventually technically cross-validated in Chapter 7 by quantitative comparisons of its fiber bundle reconstructions in oncological datasets with outputs generated by another image processing chain, regularly used at University Hospital in Leuven (Belgium), and with the HCP842 tractography atlas models.

Functionality	FT4Onco-v0.1	FT4Onco-final
Anatomical processes		
Tumor segmentation	Philips tool (DeepMedic+SPM)	Philips tool (DeepMedic+SPM)
Brain segmentation	Philips tool (HBS)	Philips tool (HBS)
Diffusion processes		
Denoising	MRtrix (MP-PCA)	DIPY (Patch2Self)
Gibbs ringing correction	MRtrix (local subvoxel shifts)	MRtrix (local subvoxel shifts)
Motion correction with outlier detection	MRtrix (SHARD-recon)	MRtrix (SHARD-recon)
Eddy current correction	MRtrix (SHARD-recon)	MRtrix (SHARD-recon)
EPI distortion correction	MRtrix, ANTsPy, ANTsX (registration-based EPI distortion correction with T2 MRI)	MRtrix, ANTsPy, ANTsX (registration-based EPI distortion correction with T2 MRI)
B_1 inhomogeneity correction	MRtrix, ANTsPy (N4ITK)	MRtrix, ANTsPy (N4ITK)
Tractography processes		
TRF estimation	MRtrix (dhollander)	MRtrix (dhollander)
FOD estimation	MRtrix (MSMT-CSD)	MRtrix (MSMT-CSD)
Whole brain tractography	seeding from a whole brain WM mask (MRtrix) with probabilistic iFOD2	dynamic seeding from WM FOD map, probabilistic iFOD2
Bundle dissection	region-informed with brain segmentation labels and cortical parcellations (ACT framework, MRtrix)	recognition of bundles with HCP842 atlas bundle priors (RecoBundles, DIPY)
Spurious fiber filtering	SIFT2 and TDI thresholding (MRtrix)	FBC thresholding (DIPY)

Table 6.8: Core differences (in yellow) between the FT4Onco-v0.1 and FT4Onco-final image processing pipelines.

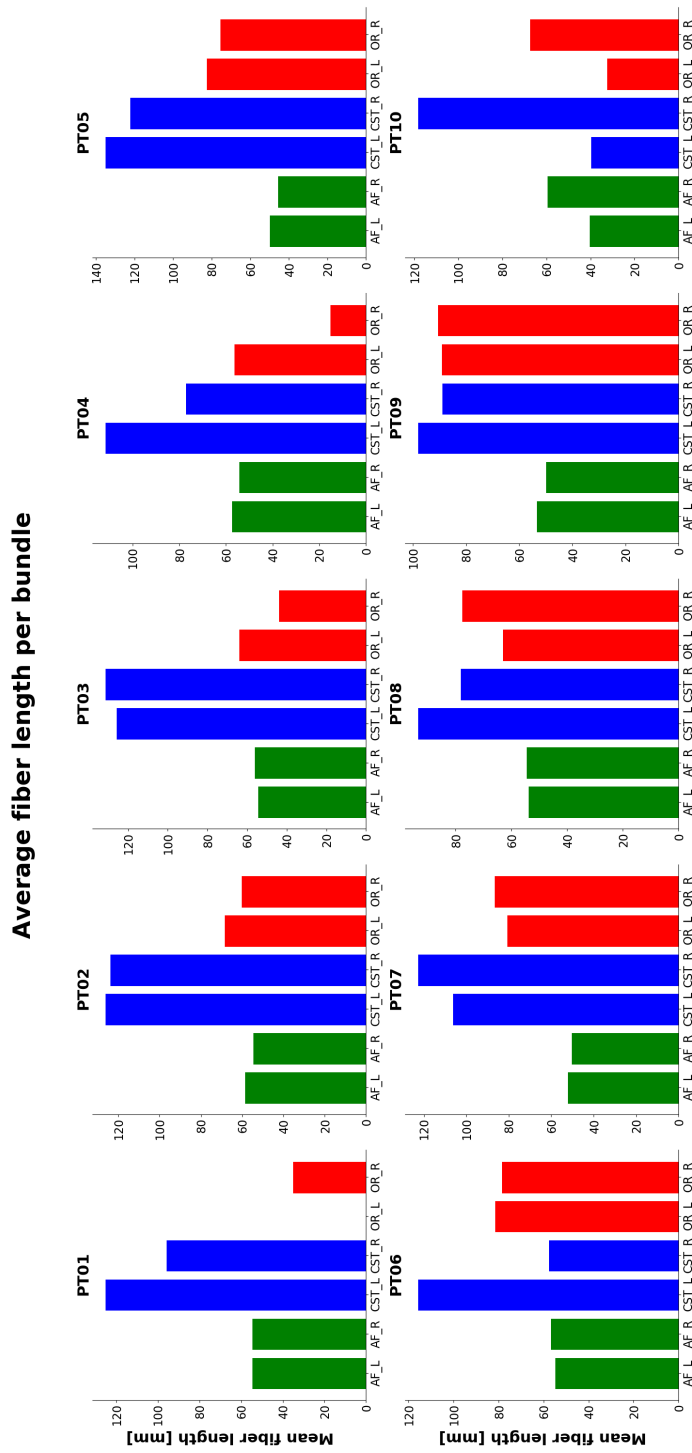


Figure 6.3: FT4Onco-v0.1: Average path length of the reconstructed bundles for all 10 patient datasets.

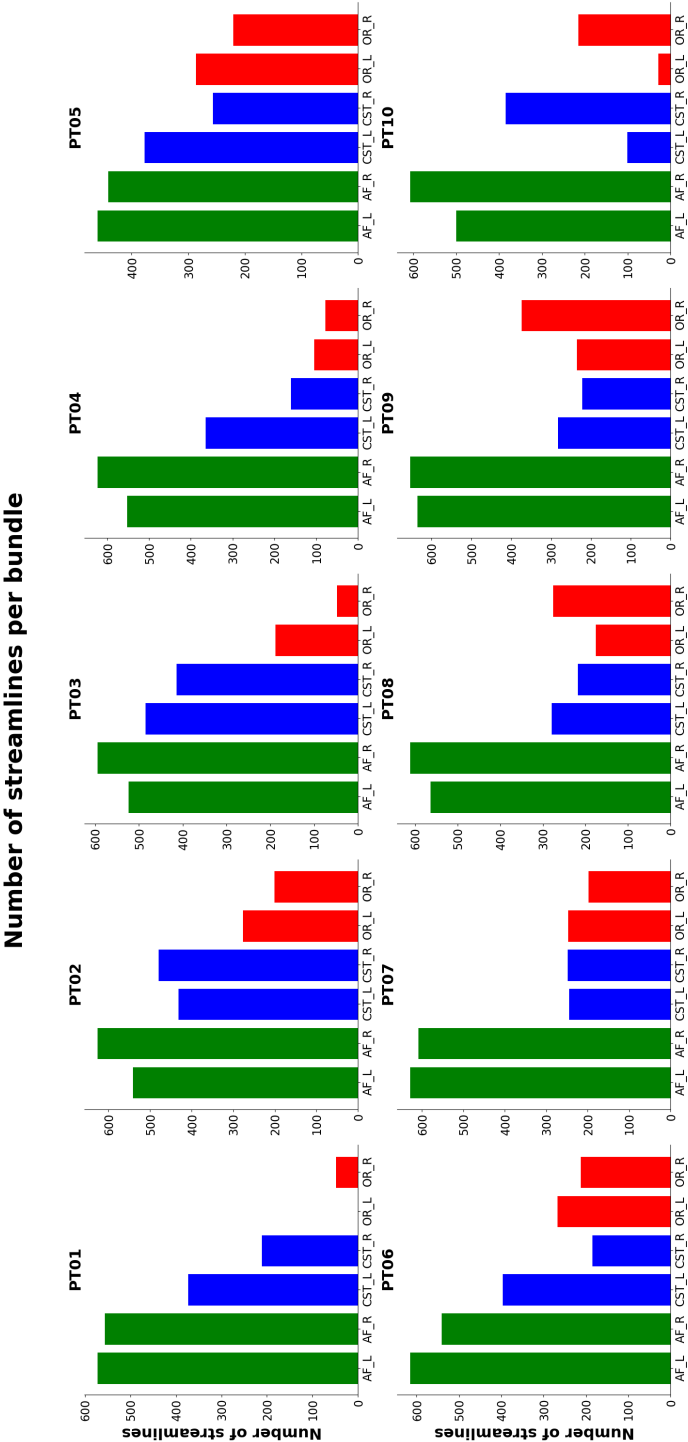


Figure 6.4: FT4Onco-v0.1: Number of streamlines per reconstructed bundle for all 10 patient datasets.

6.3 Sensitivity analysis

Diffusion MRI tractography algorithms are typically configurable with a broad spectrum of tracking parameters to constrain whole brain connectome reproduction to anatomically plausible ranges. Owing to the absence of ground truth in single-subject tractography, an optimal combination of tracking parameters that would produce an “ideal tractogram” simply cannot be found. In every tractography pipeline, there is a consistent sensitivity and specificity tradeoff (higher sensitivity meaning lower specificity and vice versa) through all models and parameters, which are often specified based on previous experience or empirical testing, thereby inducing user bias. According to the collected clinical user statements [107, 108, 111], little or no effort is typically put into measuring the effect of varying thresholds on bundle-specific features, leading to the under- or overestimation of tractography results. Visual insights into bundle reconstruction quality across a range of threshold combinations were collected in previous work [158].

FT4Onco’s whole brain tractograms are generated with the integrated MRtrix *tckgen* tool that can be tuned with an array of attributes (see Table 5.4). To quantitatively investigate the differences in bundle reconstructions as a function of varying input criteria for whole brain tractography, a sensitivity analysis was performed. Some tracking parameters have an easily conceivable impact on the appearance of output tractograms, such as the minimum streamline length or number of selected streamlines. On the contrary, there are tracking criteria that may significantly affect bundle features at subvoxel level, especially those located near infiltrating tumors due to complex fiber crossing. The two most commonly used stopping criteria in tensor-based algorithms are the anisotropy threshold (tracking terminates if the FA value of a tensor field drops below a given value) and angular threshold (change in underlying fiber orientation between the start and end points of each tracking step). In CSD tractography, tracking termination is usually governed by an FOD amplitude threshold, where a candidate path is given a probability of zero if the amplitude along the FOD lobe’s tangent falls below a certain value.

In FT4Onco sensitivity analysis, varying initialization of the angular threshold, FOD amplitude, and step size (length of each tracking increment in mm) was analyzed to observe the change effects on three features of the arcuate fasciculus bundle: mean streamline length, number of fibers in bundle, and bundle volume. The setup of RecoBundles and FBC thresholding were kept the same as presented in Section 5.5, and reconstructions were created bihemispherically. For each changing parameter threshold, all other parameter values remained unchanged. Sensitivity analysis was performed on the example multi-shell dataset (described in Figure 5.7) with a tractogram density of 2 mill. streamlines. Sensitivity was calculated by dividing the percentage change in examined parameter thresholds by the percentage change in the output of associated features. Percentage changes in mean streamline length, number of fibers in bundle, and bundle volume are summarized in Table 6.9.

AF right (GBM-affected)				
Parameter	Value	Feature		
		Mean streamline length [%]	Number of streamlines [%]	Bundle volume [%]
Angular threshold	30 (↓ 33 %)	↓ 6.16	↑ 70.39	↓ 20.94
	45	164.44 mm	233	2979.13 mm³
	60 (↑ 33 %)	↓ 8.08	↓ 67.38	↓ 49.34
FOD amplitude	0.05 (↓ 50 %)	↑ 8.19	↑ 65.55	↑ 172.39
	0.1	153.05 mm	238	1751.01 mm³
	0.2 (↑ 100 %)	↓ 6.67	↑ 372.29	↓ 13.17
Step size coeff.	0.3 (↓ 40 %)	↑ 2.97	↓ 65.81	↓ 53.17
	0.5	150.08 mm	620	2458.44 mm³
	0.7 (↑ 40 %)	↑ 1.20	↑ 46.29	↑ 19.93
AF left				
Parameter	Value	Feature		
		Mean streamline length [%]	Number of streamlines [%]	Bundle volume [%]
Angular threshold	30 (↓ 33 %)	↓ 1.57	↑ 22.01	↑ 16.97
	45	153.9 mm	2989	6472.36 mm³
	60 (↑ 33 %)	↓ 1.66	↓ 12.41	↓ 26.44
FOD amplitude	0.05 (↓ 50 %)	↑ 1.42	↓ 31.25	↑ 3.93
	0.1	154 mm	2752	5929.7 mm³
	0.2 (↑ 100 %)	↓ 3.42	↑ 81.36	↓ 1.82
Step size coeff.	0.3 (↓ 40 %)	↑ 1.68	↓ 55.69	↓ 22.86
	0.5	152.03 mm	2986	6342.74 mm³
	0.7 (↑ 40 %)	↑ 1.32	↑ 63.36	↓ 3.05

Table 6.9: *Upper:* Outcomes of sensitivity analysis for the selected features of the right tumor-affected arcuate fasciculus. Note the almost quadruple increase in number of streamlines after raising the FOD amplitude threshold twice. *Lower:* Outcomes of sensitivity analysis for selected features of the left normal arcuate fasciculus. Parameter value ranges were selected by empirical testing. Step size is obtained by the multiplication of unidimensional voxel size by a coefficient. Reference values for the computation of feature change are highlighted in yellow. ↓ = percentage decrease, ↑ = percentage increase. Outcomes in this table prove that determining the optimal parametric setup is not trivial, and would require a more extensive sensitivity analysis.

It is essential to note that in this sensitivity analysis, the presented final bundle representations are influenced by the overall effects of all steps after bundle recognition, i.e. including FBC thresholding, which further change individual bundle features due to the removal of spurious trajectories (fibers ranked as incoherent with the bundle core in the FBC output). Given the fully automated nature of FT4Onco-based processing, the inspection of quantitative features in bundles directly after dissection and before FBC thresholding would be insufficient as users only see output bundles after the convergence of all processing steps.

The visual illustration of bundle reconstruction sensitivity to changes in input parameter thresholds is demonstrated in Figures 6.5, 6.6, and 6.7. The representation of both reconstructed bundles in this sensitivity analysis, the right and left arcuate fasciculi, shows large volumetric differences, which are expected due to various lesion effects. In the processed GBM patient

case, the right AF was neurosurgically confirmed to be infiltrated by the adjacent GBM-induced vasogenic edema that may additionally cause axonal loss or fiber disruptions. These lesion-WM effects introduce inaccuracies in WM orientation estimates based on the diffusion-weighted signal due to a local decrease in anisotropy, thereby ensuing premature tracking terminations and false negative (missed) pathways [159].

Decreasing the angular threshold by 33% led to a significant increase of the number of streamlines ($\uparrow 70.39\%$ and $\uparrow 22.01\%$), and raising the FOD amplitude generated notably more streamlines in the tumor-affected bundle ($\uparrow 372.39\%$). Both of these observations are mathematically explicable since decreasing the angular threshold and increasing the FOD amplitude causes the fiber tracking algorithm to follow more spurious traces. Bundle volume was mostly affected by lowering the FOD amplitude ($\uparrow 172.39\%$). Varying step size seems to only have a marginal impact on all bundle features.

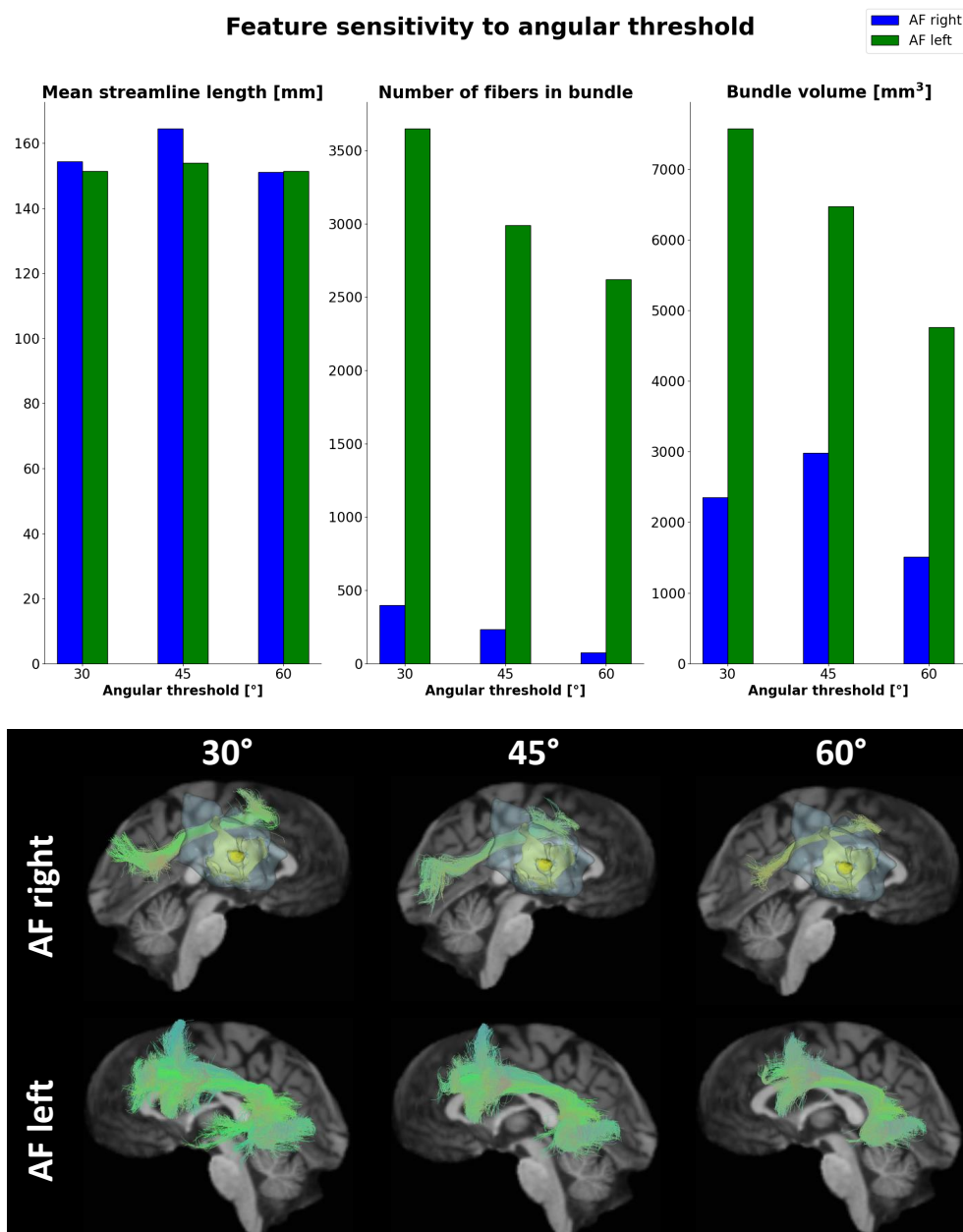


Figure 6.5: Demonstration of bundle feature sensitivity to varying angular threshold. *Upper:* Bar charts reporting changes in assessed bundle features. *Lower:* Left and right AF bundles color-coded according to fiber orientation (red – left-right; green – anterior-posterior; blue – superior-inferior) with edema (opaque blue) and the contrast-enhancing tumor portion (yellow) overlaid on T1 images.

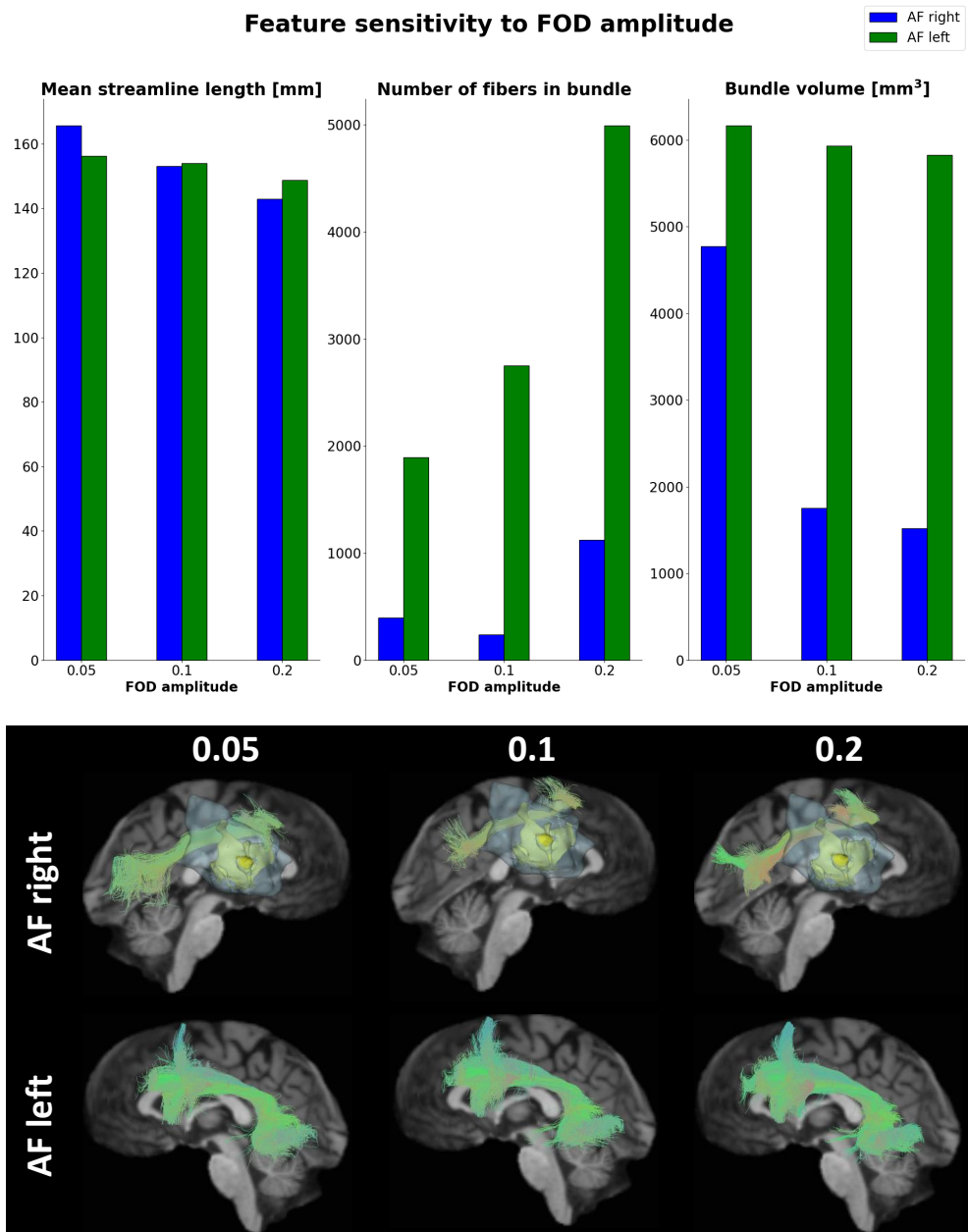


Figure 6.6: Demonstration of bundle feature sensitivity to varying FOD amplitude. *Upper:* Bar charts reporting changes in assessed bundle features. *Lower:* Left and right AF bundles color-coded according to fiber orientation (red – left-right; green – anterior-posterior; blue – superior-inferior) with edema (opaque blue) and the contrast-enhancing tumor portion (yellow) overlaid on T1 images.

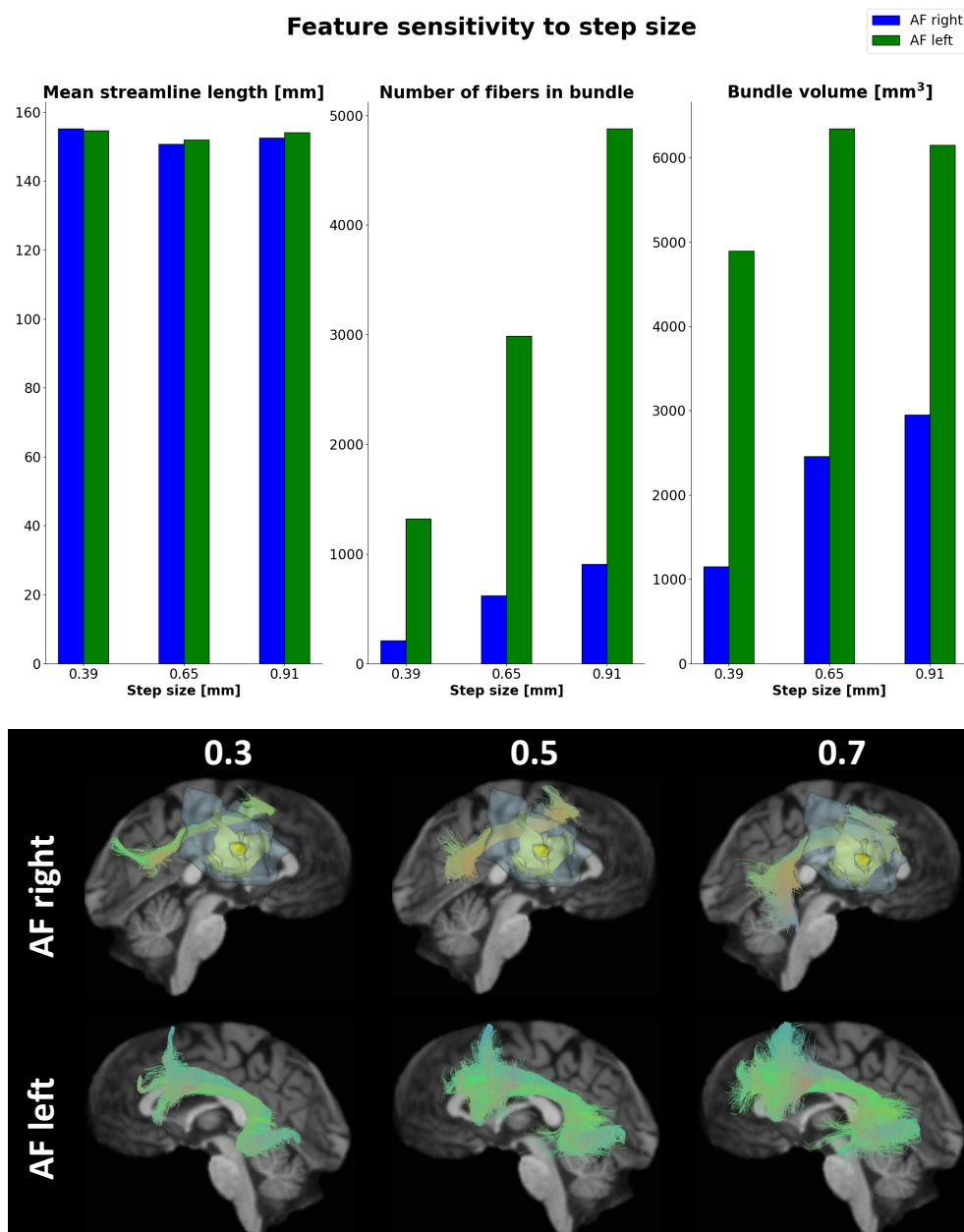


Figure 6.7: Demonstration of bundle feature sensitivity to varying step size. *Upper:* Bar charts reporting changes in assessed bundle features. *Lower:* Left and right AF bundles color-coded according to fiber orientation (red – left-right; green – anterior-posterior; blue – superior-inferior) with edema (opaque blue) and the contrast-enhancing tumor portion (yellow) overlaid on T1 images.

7 Technical cross-validation

In this chapter, the purpose is to assess the neuroanatomical plausibility of FT4Onco-derived nerve fiber bundle representations. Such assessment cannot be accomplished by in vivo validation owing to the lack of ground-truth reference and validation standards. Because of these limitations, the anatomical fidelity of FT4Onco-reconstructed fascicles was judged through a technical cross-validation with another clinically utilized software and tractography atlas models, which enabled the identification of the strengths and limitations of FT4Onco, and gauged its suitability for clinical (research) practice. Cross-validation was performed on the final release (FT4Onco-final, for simplicity hereinafter called FT4Onco).

7.1 Hurdles in tractography validation

Human brain anatomy is extremely complicated and consists of various richly intertwined networks. It has been proven that tractography can reconstruct known WM anatomy by showing valid pathways, shapes and positions, and it may serve as a predictor of the presence or absence of axonal connections. However, from data acquisition through various stages of image processing, bundle reconstructions are created under numerous assumptions carrying uncertainties that may decrease the feasibility of tractography to faithfully represent the true axonal pathways in the brain. For humanly and ethical reasons, brain nerve fiber dissection (as a potentially ideal ground truth) is typically impossible. Moreover, there is no optimal combination of image acquisition, processing or tractography parameters [160], which means that a “sufficient quality” of tractography output is determined on an ad hoc basis. Ultimately, there are a number of confounding biases and obstacles that need to be overcome: path-length biases, issues with fibers propagating to the cortex, regions with crossing fibers or correction for free extracellular water in edema.

Every step in the diffusion image acquisition, image processing and tractography pipeline accumulates variability and/or ambiguity, which have to be carefully considered when judging final results. The most prominent affecting factors are enumerated in Table 7.1. Tractography outcomes should ideally be validated at the following levels:

- ▶ *axonal level*: volume fractions of tissue microstructure, location and trajectory of individual streamlines
- ▶ *axon distribution level*: estimation of fiber orientation distributions representing the geometry of axons in each voxel
- ▶ *fiber bundle level*: location, existence and connections of streamline bundles
- ▶ *whole brain coverage*: derived properties of the human connectome

To illustrate the complexity of finding the most suitable *preoperative* fiber tracking validation approach, validation methods can be divided into four different groups [114]: numerical simulations, physical phantoms, anatomical model systems, and empirical validation methods. Besides differences in their areas of use, these validation methods have their advantages and drawbacks. Numerical simulations together with physical phantoms share the asset of

DWI acquisition	Local reconstructions	Fiber tracking	Interpretation
Image resolution	Image processing steps	Seeding strategy	Atlas choice
Scanner quality	b -value	Stopping criteria	Thresholding
SNR	Number of diffusion directions in data	Step size	Dissection approach
Distortions & artifacts	Intravoxel fiber geometry	Spatial priors	Bundle definition
Motion effects	Reconstruction algorithm	Fiber filtering	Quantification
		Number of streamlines	Subject inference
		Propagation method	

Table 7.1: Major contributors to ambiguity and variability in dMRI tractography. Moving across columns from left to right, fiber tracking variability is cumulatively induced along the data processing pipeline. Eventual inference is therefore subject to the validation of all preceding steps including image acquisition, reconstruction strategies, fiber tracking, and interpretation metrics.

being well-characterized and largely modifiable, but these approaches oversimplify the tissue microstructure. Anatomical model systems achieve high performance in representing the true complexity of tissue microstructure, but they are cumbersome to characterize. Finally, empirical validation helps establish reproducibility and assess variation differences across repeated runs, scanners, sites, etc. However, this approach is ultimately problematic due to its observational nature, and lack of gold standards.

Further existing tractography validation techniques include histological myelin-stained postmortem dissections [161], which cannot be adopted in vivo as their name suggests, or axonal tracing with manganese-enhanced MR imaging [162], which is only used in animal studies due to toxicity concerns. Overall, there is no unified consensus on how to validate the output of dMRI-based fiber tracking in clinical research (regardless of custom site-specific agreement protocols). Intraoperatively, the by far most widely used method to validate the anatomical location of tracked fiber bundles is electrophysiological direct electrical stimulation (DES) [163], where neurosurgeons can perturb the function of WM tracts.

The most important question in tractography validation is how to quantify agreement that observed fiber orientation [164], bundle reconstructions [165], or connectome networks [166] represent the true anatomical structures in a subject’s brain. There are miscellaneous measures used for agreement quantification, yet each of them bears some limitations.

7.2 Experimental setup

FT4Onco validation addressed performance in the reconstruction of 8 selected fiber tracts (introduced in Table 2.1). It was conducted in the form of a quantitative cross-validation between (1) FT4Onco-generated bundles and output produced by the BIDS-CSD pipeline integrated into the KUL NeuroImaging Suite (KUL_NIS), and (2) FT4Onco-generated bundles and HCP842 atlas models, which were used as anatomical priors in RecoBundles dissection (Section 5.5.4). In both cross-validation experiments, outcomes of the reference source were considered a “silver standard”, against which comparisons of FT4Onco bundle dissections were made.

The reasons for choosing particularly the BIDS-CSD pipeline from the KUL_NIS software package as a reference in cross-validation are manifold. Firstly, in parallel with FT4Onco development, the BIDS-CSD pipeline (Figure 5.4) that had initially laid the

foundation for FT4Onco was restructured and optimized to become a well-established image processing tool in brain tumor resection planning at the Department of Imaging and Pathology, Translational MRI, University Hospital in Leuven (Belgium). Secondly, KUL_NIS exemplified the most comprehensive, freely available toolkit for oncological neurosurgery planning, and was composed of state-of-the-art open-source neuroimaging packages. Finally, the cross-validation setup and outcomes were consulted with the developers of KUL_NIS, who also created reference bundle reconstructions according to a mutually agreed cross-validation protocol (Table 7.2).

The primary cross-validation aim was to investigate similarities between bundle reconstructions obtained with the two pipelines (KUL_NIS and FT4Onco). Bundle dissection similarity and dissimilarity can be quantitatively assessed either voxel-wise or streamline-wise. The latter is more applicable when directly comparing different dissection methods, where bundles are segmented from the same set of underlying streamlines. This condition was violated in FT4Onco cross-validation since each pipeline dissected bundles from different whole brain tractograms. Hence, only the following voxel-wise measures of spatial overlap were employed:

- **Weighted Dice similarity coefficient** [155]: a measure of spatial similarity between two WM fascicles (reconstructed bundle \mathcal{X} and reference bundle \mathcal{Y}), ranging between 0 and 1, with 0 meaning no similarity and 1 meaning full agreement:

$$\text{DSC} = \frac{\sum_{v'} \mathcal{X}_{v'} + \sum_{v'} \mathcal{Y}_{v'}}{\sum_v \mathcal{X}_v + \sum_v \mathcal{Y}_v} \{ \text{DSC} \in \mathbb{R} \mid 0 < \text{DSC} < 1 \},$$

where v designates the index of a voxel containing a fraction of streamlines from any of the two bundles, and v' stands for voxels located within the intersection of \mathcal{X} and \mathcal{Y} . As opposed to the standard Dice coefficient [167] that greatly penalizes for spurious streamlines far from the bundle core, the weighted Dice metric is weighted by streamline density, accounting for the number of streamlines in each voxel. As bundles typically contain more streamlines at their core than in the periphery, the weighted DSC gives more significance to densely populated areas. Note that there is no explicit weighting factor in the formula.

- **Bundle overlap** [118]: a volumetric measure of voxels that contain the reference volume and are traversed by at least one streamline; determines how well tractography is able to describe the volume occupied by the reference bundle:

$$\text{BOL} = \frac{|\mathcal{X} \cap \mathcal{Y}|}{|\mathcal{Y}|},$$

- **Bundle overreach** [118]: a volumetric measure of voxels containing streamlines that are outside of the reference volume divided by the total number of voxels within the reference bundle:

$$\text{BOR} = \frac{|\mathcal{X} \setminus \mathcal{Y}|}{|\mathcal{Y}|},$$

where \setminus denotes the relative complement operator.

- **Bundle adjacency** [86]: a measure of the average distance of disagreement between two bundles in voxel coordinates:

$$BA = \frac{BOR(\mathcal{X}, \mathcal{Y}) + BOR(\mathcal{Y}, \mathcal{X})}{2} \text{ [mm]}$$

These metrics were chosen because FT4Onco's tracking approach in fact represents a segmentation task in 3D space. The same metrics were used to quantitatively assess the correspondence of FT4Onco bundles with the HCP atlas models. For each set of comparisons, validation hypotheses were formulated, and confirmed or rejected with reference to the following statements:

- H1: There is at least a 90% similarity between bundle reconstructions from FT4Onco and KUL_NIS as measured by the average weighted DSC. The average volumetric BOL across all bundles is not smaller than 90%, the mean BOR is not greater than 50%, and bundles are in a maximum disagreement of 1 mm as measured by BA.
- H2: There is at least a 90% similarity between bundle reconstructions from FT4Onco and HCP842 atlas model bundles as measured by the average weighted DSC. The average volumetric BOL across all bundles is not smaller than 90%, the mean BOR is not greater than 50%, and bundles are in a maximum disagreement of 1 mm as measured by BA.

Patient datasets (Table 7.3) used in the cross-validation setup were different from data applied to pipeline development and optimization. The image processing parameter setup was consistent in both pipelines (whole brain tractograms were created with the probabilistic iFOD2 algorithm, min./max. streamline length of 20/280 mm, and 10 mill. selected streamlines. Details on the values of other tracking parameters are listed in Table 5.4 and not repeated here.

Item	Realization
Image data	Four HGG multi-shell dMRI datasets, each with 258 volumes, $b = 0/1200/2500 \text{ s/mm}^3$ (2 mm iso), and four anatomical scans: T1 (0.9 mm iso), T2 (0.5 mm iso), T1C (0.9 mm iso), and FLAIR (1 mm iso)
Reference outcome	Reconstructed bundles from KUL_NIS and model bundles from the HCP842 tractography atlas
Desired outcome	Reconstructions of 8 bundles (AF, C, CST, MdLF, ILF, IFOF, SLF, OR) bihemispherically
Persons involved	1 clinical neuroradiologist, 1 study leader
Performance measures	Graphical comparison of bundle profiles, and volumetric quantification of bundle similarity
Results analysis	Bundle profiles for FA and AFD; weighted Dice coefficient, bundle overreach, bundle overlap, bundle adjacency

Table 7.2: Experimental setup in cross-validation.

Patient	Tumor type	Location
PT01	GBM WHO grade IV	right frontoparietal region
PT02	GBM WHO grade IV	right frontal lobe
PT03	GBM WHO grade IV	right frontoparietal region
PT04	GBM WHO grade IV	left temporoparietal region

Table 7.3: Selected datasets in cross-validation.

7.3 Non-negligible pipeline differences

As stated above, tractography uncertainty and outcome variability increases with differences between consecutive image processing steps along the pipeline. Hence, the correspondence between outputs from two conceptually and methodologically differing image processing chains underlies multiple assumptions, e.g. comparable performance in imaging artifact suppression, distortion correction or spatial alignment of overlays. Table 7.4 lists the most crucial image processing steps and their functionalities across both pipelines.

Functionality	FT4Onc	KUL_NIS
T1 processes		
Denoising	×	adaptive non-local means (FS, ANTsX)
B_1 inhomogeneity correction	×	N4ITK (FS recon-all)
Brain segmentation & parcellation	HBS (Philips)	VBG [168] (FastSurfer [169], FS), MSBP [170]
Tumor segmentation	GBS (Philips)	semi-automated image classification workflow with CNN (ITK-SNAP) [120]
Resampling	mrresample (MRtrix)	mrresample (MRtrix)
Brain extraction	MNI template-based (ANTsX)	neural network enabled (HD-BET) [171]
Registration on DWI	SyNRA (ANTsPy)	Affine and SyN (ANTsX)
DWI processes		
Denoising	Patch2Self (DIPY)	MP-PCA (MRtrix)
Gibbs ringing correction	dwidegibbs (MRtrix)	dwidegibbs (MRtrix)
EPI distortion correction	registration-based EPI distortion correction with T2 and b_0	FSL topup with B_0 field maps, Synb0-DISCO [172]
Eddy current correction	SHARD-recon (MRtrix)	FSL eddy
b -matrix reorientation	MRtrix, ANTsX	FSL topup
Motion correction	SHARD-recon (MRtrix)	FSL eddy
b_0 image extraction	dwiextract (MRtrix)	dwiextract (MRtrix)
Brain extraction	T1 mask based (MRtrix, ANTsX)	BET (ANTsX)
B_1 inhomogeneity correction	N4ITK (MRtrix)	N4ITK (MRtrix)
Tractography		
TRF estimation	dhollander (MRtrix)	dhollander (MRtrix)
FOD estimation	MSMT-CSD (MRtrix)	MSMT-CSD (MRtrix)
Whole brain tractography	iFOD2 (MRtrix)	iFOD2 (MRtrix)
Bundle dissection	RecoBundles (DIPY) with HCP842 atlas models	FastSurfer, FS, MSBP, and anatomical atlas VOIs [173]
Spurious fiber filtering	FBC thresholding (DIPY)	SIFT2 (MRtrix), SCILpy, DIPY

Table 7.4: Differences (highlighted in yellow) in functionalities between the KUL_NIS and FT4Onc pipelines employed in cross-validation. These differences must be considered when interpreting cross-validation outcomes. The table contains bibliographical references to software tools previously unreferenced in this work. Abbreviations and version numbers in FT4Onc: HBS = Hybrid Brain Segmentation, GBS = Glioblastoma Segmentation (DeepMedic 0.7.3, SPM 12), MRtrix (v3.0.1 for SHARD-recon, otherwise v3.0.2), DIPY = Diffusion Imaging in Python (v1.4.1), SCILpy = Sherbrooke Connectivity Imaging Lab Python tools (v1.1.0), ANTsX (v0.2.0), ANTsPy (v2.3.1). Abbreviations and version numbers in KUL_NIS: ITK-SNAP (v3.8.0), VBG = Virtual Brain Grafting, FS = FreeSurfer (v6.0), FastSurfer (v1.1.1), MSBP = MultiScale Brain Parcellator (v1.1.1), FSL (v6.0) Synb0-DISCO = Synthesized b_0 for diffusion distortion correction (v3.0), DIPY (v1.3.0), MRtrix (v3.0.2), ANTsX (v2.4.1), HD-BET = Heidelberg Brain Extraction Tool, SCILpy (v1.1.0).

7.4 Bundle comparison and analysis

Technical cross-validation aimed to compare the reconstructions of selected brain fascicles, introduced earlier in Table 2.1. All bundle metrics were calculated with SCILpy tools [174]. Among many functions, these tractography analysis scripts enable quantifying various bundle features and generating pairwise agreement statistics between bundles of different origin in the same image space.

Between-bundle profile comparisons for FA (Figure 7.1) and AFD (Figure 7.2) were calculated and visualized via the AFQ (automated fiber quantification) framework available from DIPY, where each bundle is subsampled to 100 equidistant parts along its centroid streamline. Details on bundle profile computation are explained in Section 5.6.3. To enable shape and volume comparisons among bundles from heterogeneous sources, model bundles were registered from MNI space to subject space using SLR [151], while KUL_NIS reconstructions were kept aligned to the T1 volume processed with the KUL_NIS pipeline.

Computed values for weighted Dice scores, bundle overreach, overlap and adjacency are tabulated in Appendix D. Voxel-wise bundle comparisons between FT4Onco/KUL_NIS, and FT4Onco/HCP842 atlas are graphically reported in Figure 7.3, and a visual demonstration of the comparison among all four patient reconstructions of the arcuate fasciculus is illustrated in Figure 7.4. The magnitude of bundle similarity to silver standards was assessed by weighted Dice scores.

Addressing FT4Onco's bundle reconstruction accuracy, the relationship between bundle overreach and overlap can be translated into the quantification of sensitivity and specificity. With respect to silver standards, high overlap (= high sensitivity) indicates that tractography succeeded in recovering true positive connections, while high overreach (= low specificity) shows that tractography reconstructed many false positive connections. To assess the link between the BOL and BOR per compared bundle pairs, the Pearson product-moment correlation coefficient was computed [175]. In this cross-validation experiment, the Pearson correlation coefficient (ρ) enables finding direct association between the probability of reconstructing a greater portion of the silver-standard bundle (BOL), and producing artifactual trajectories (BOR) [5]. Its values are interpreted as follows:

- +1 = complete positive correlation
- +0.8 = strong positive correlation
- +0.6 = moderate positive correlation
- 0 = no correlation whatsoever
- 0.6 = moderate negative correlation
- 0.8 = strong negative correlation
- 1 = complete negative correlation

In the sensitivity-specificity correlation analysis, bundle overreach and overlap are expressed in percentages instead of cubic millimeters. This analysis of cross-validation outcomes also involved computing the mean (μ) and standard deviation (σ) for all voxel-wise comparison measures. These results can be found in Table 7.5 along with Pearson correlation coefficients ($\rho_{\{BOL, BOR\}}$) for each compared set of bundle reconstructions.

7.5 Cross-validation outcomes

The spatial overlap comparison between bundles obtained from two methodologically distinct image processing pipelines must be interpreted with care. Different algorithms process imaging data in different ways, increasing the cumulative influence on fiber tracking output beyond uncertainties already present in each pipeline. As visually presented in Figure 7.4, these differences are, amongst others, attributed to the impossibility to capture and select the exact same streamlines in the tractography processes, different approaches to the correction of susceptibility-induced distortions, and geometrical misalignments originating from divergent dMRI-T1 co-registration methods.

Qualitative comparisons between FT4Onco and KUL_NIS using bundle profiles of FA and AFD convey significant global similarities in the majority of pairwise comparisons. Closer inspection of compared FA and AFD bundle profiles (Figures 7.1 and 7.2) reveals the highest joint correspondence in the left cingulum of PT01, the left inferior longitudinal fasciculus of PT02, the right inferior longitudinal fasciculus of PT03, and the right corticospinal tract of PT04. Absence of graphs for the right arcuate and right superior longitudinal fasciculi of PT02 was explained by a neuroradiologist to possibly stem from left-hemispheric language dominance in this patient.

Addressing the initially defined hypotheses for each set of comparisons, quantitative cross-validation outcomes (listed in Table 7.5 and visualized in Figure 7.3) enable the formulation of the following conclusive statements:

- Ad H1: The highest similarity between bundle reconstructions from FT4Onco and KUL_NIS reached 0.59 (± 0.21) as measured by the average weighted DSC. The highest average volumetric BOL was 24.13 % (± 8.67), the lowest average BOR was 200.5 % (± 144.84), and bundles were in a minimum disagreement of 2.78 mm (± 1.28) as measured by BA.
- Ad H2: The highest similarity between bundle reconstructions from FT4Onco and HCP842 atlas model bundles reached 0.42 (± 0.17) as measured by the average weighted DSC. The highest average volumetric BOL was 14.73 % (± 6.27), the lowest average BOR was 380.2 % (± 244.28), and bundles were in a minimum disagreement of 2.68 mm (± 1.00) as measured by BA.

Although the average weighted DSC similarity between FT4Onco and KUL_NIS reached more than 50 %, other conditions for all of the voxel-wise volumetric correspondence measures were not satisfied, which is why both formulated hypotheses have to be rejected. While it would be challenging to increase bundle similarity between FT4Onco and KUL_NIS given the vast differences in the processing pipelines, the similarity between FT4Onco output and HCP842 atlas models can be improved by iterative refinement and optimization of dissection thresholds for bundle reduction and pruning in the RecoBundles algorithm.

Metric	PT01	PT02	PT03	PT04
FT4Onco vs. KUL_NIS ($\mu \pm \sigma$)				
DSC	0.52 ± 0.23	0.52 ± 0.23	0.59 ± 0.21	0.41 ± 0.25
BOL [%]	21.13 ± 9.89	20 ± 9.42	24.13 ± 8.67	16.75 ± 11.74
BOR [%]	746.38 ± 2103.81	233.54 ± 181.14	200.5 ± 144.84	376.67 ± 366.75
BA [mm]	3.31 ± 2.37	3.58 ± 2.51	2.78 ± 1.28	3.55 ± 3.35
$\rho_{\{BOL, BOR\}}$	-0.59	-0.84	-0.86	-0.68
FT4Onco vs. HCP842 ($\mu \pm \sigma$)				
DSC	0.36 ± 0.16	0.37 ± 0.16	0.35 ± 0.19	0.42 ± 0.17
BOL [%]	13.94 ± 6.82	14.56 ± 6.22	14.06 ± 8.00	14.73 ± 6.27
BOR [%]	614.69 ± 1132.03	361.38 ± 189.01	468.69 ± 372.71	380.2 ± 244.28
BA [mm]	3.39 ± 1.68	2.78 ± 0.75	3.33 ± 1.63	2.68 ± 1.00
$\rho_{\{BOL, BOR\}}$	-0.6	-0.93	-0.86	-0.93

Table 7.5: Mean and standard deviation for all volumetric comparison measures across all patient datasets. The highest DSC, highest BOL, lowest BOR and lowest BA are highlighted in green. The representation by these particular statistical measures corresponds to comparable reports in literature [5].

The correlation analysis clearly indicated a moderate to complete negative correlation (ranging between $\rho = -0.59$ and $\rho = -0.93$), which means there is no direct link between the probability of reconstructing a greater portion of the silver-standard bundle (BOL) and generating false positive fibers (BOR) in any of the computed pairwise comparisons.

Outcomes of this cross-validation substantiate the difficulties in developing optimal tractography validation strategies, identification of high-quality gold standards, and missing consensus how to interpret quantitative metrics. The following and last chapter of this thesis discusses whether all identified unmet user requirements have been met through the designed software, describes possible improvements in terms of architecture, outcome reproducibility and future development, and summarizes the relevance of FT4Onco in clinical research.

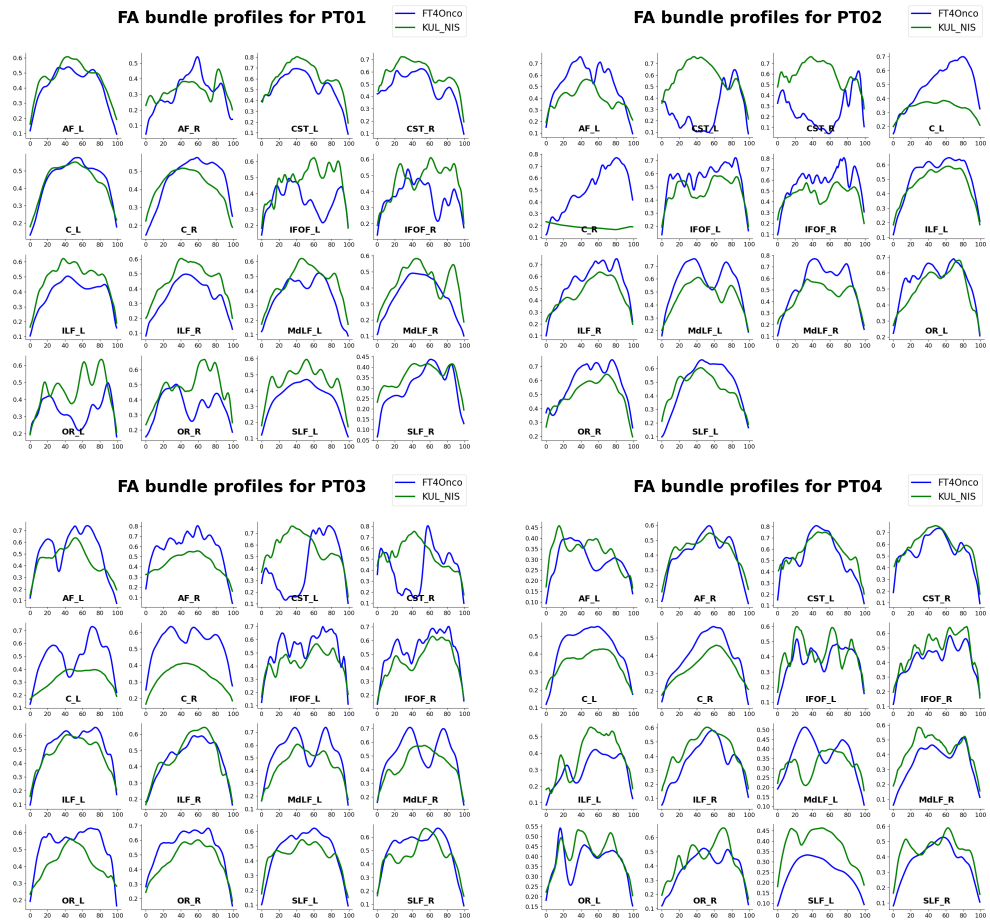


Figure 7.1: Comparison of bundle profiles for the evolution of fractional anisotropy (values on the y-axes) along each bundle subsampled to 100 segments (x-axes). For patient PT02, the right arcuate fasciculus and the right superior longitudinal fasciculus are missing from the datasets since these bundles were not reconstructed by the KUL_NIS pipeline. Details on bundle profile computation are explained in Section 5.6.3.

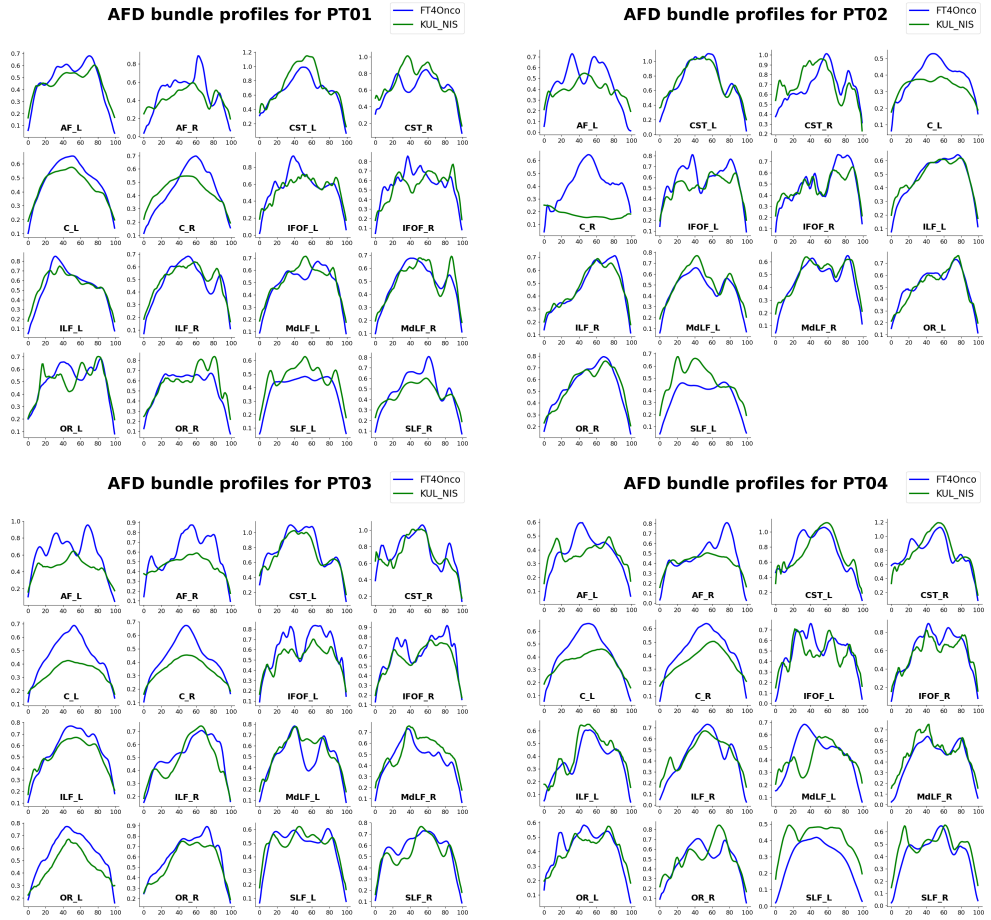


Figure 7.2: Comparison of bundle profiles for the evolution of apparent fiber density (values on the y-axes) along each bundle subsampled to 100 segments (x-axes). For patient PT02, the right arcuate fasciculus and the right superior longitudinal fasciculus are missing from the datasets since these bundles were not reconstructed by the KUL_NIS pipeline. Details on bundle profile computation are explained in Section 5.6.3.

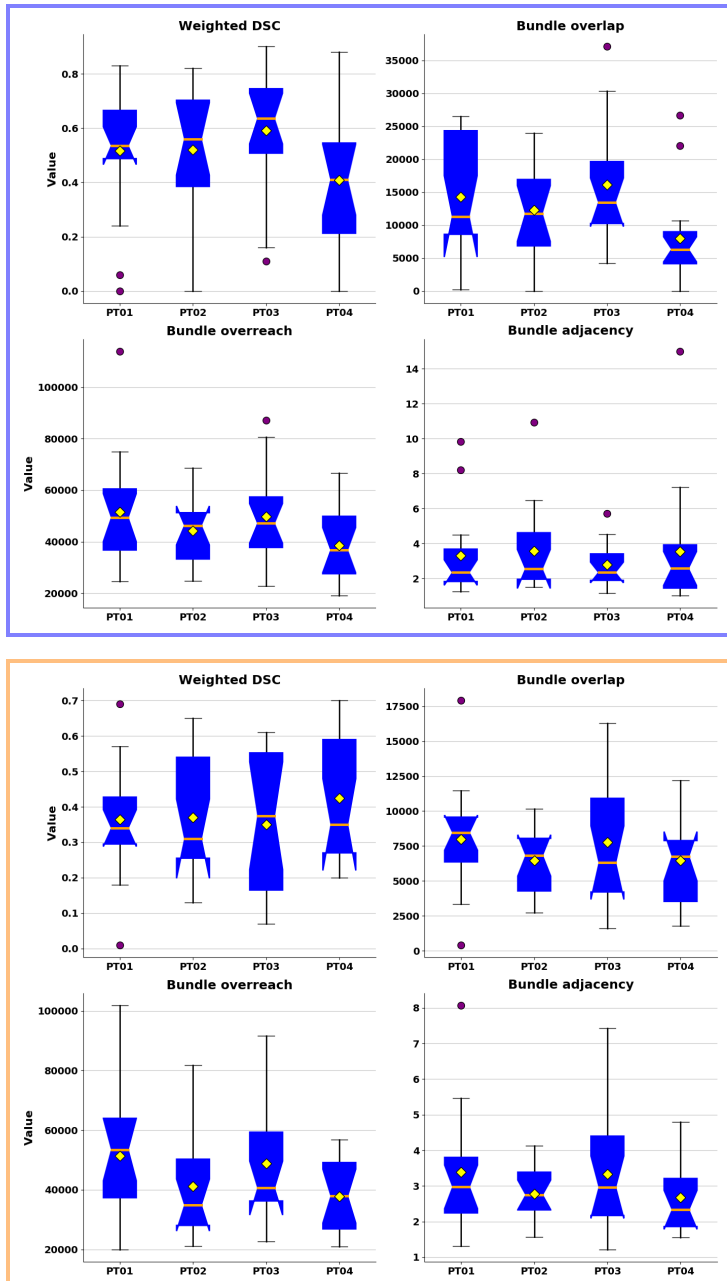


Figure 7.3: Boxplots showing the distribution of values (DSC, BOL, BOR, BA) for voxel-wise comparisons of FT4Onco output with KUL_NIS bundles (*blue-framed image*), and the HCP842 atlas models (*orange-framed image*) in all four patient datasets. Mean values are represented by yellow diamonds, median is shown with orange lines, and outliers are indicated with purple circles. Comparison intervals for individual measures are supported by blue boxes notched around the median values.


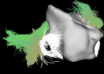




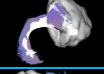




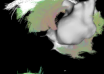

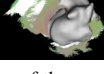

Patient	Comparison	AF left	DSC	BA [mm]	AF right	DSC	BA [mm]
PT01	FT4Onco vs. KUL_NIS		0.64	2.28		0.0	9.84
	FT4Onco vs. HCP842		0.39	2.22		0.3	2.53
PT02	FT4Onco vs. KUL_NIS		0.15	5.14	N/A	N/A	N/A
	FT4Onco vs. HCP842		0.65	1.6		0.27	2.82
PT03	FT4Onco vs. KUL_NIS		0.11	4.51		0.16	5.72
	FT4Onco vs. HCP842		0.61	1.21		0.56	1.53
PT04	FT4Onco vs. KUL_NIS		0.34	3.79		0.51	2.44
	FT4Onco vs. HCP842		0.54	1.93		0.52	1.67

Figure 7.4: Visual demonstration of the cross-validation experiment showing the final weighted Dice coefficients and bundle adjacency values for the reconstructions of arcuate fasciculi across all four patient datasets in the T1 image space. For all cases, the AF bundle was affected by the GBM mass in one hemisphere. These pathological findings and location of the GBM lesion were neurosurgically confirmed. Green-blue-colored bundles represent FT4Onco reconstructions, compared to outputs of KUL_NIS and atlas model bundles, which are colored in white. Grey meshes represent the whole tumor volume.

8 Discussion, recommendations & conclusions

This dissertation presented the conceptualization, requirement-driven design, implementation, integration, clinical evaluation, and technical cross-validation of a novel fiber tracking software for brain tumor resection planning in clinical research. In the beginning, five overarching aims were defined:

- ▶ Identify unmet needs in the presurgical workflow of oncological neurosurgery by interviewing neuroradiologists and neurosurgeons.
- ▶ Optimize (accelerate and automate) the preoperative workflow of diffusion and anatomical MRI data processing on routine clinical data.
- ▶ Improve the quality and accuracy of dMRI-based tractography output using the CSD model, and probabilistic tractography algorithms to overcome DTI-FACT limitations.
- ▶ Represent fiber tracts and tumors in a more informative three-dimensional multiparametric fashion via indication of fiber tracking confidence and relationships between tumor and healthy tissue.
- ▶ Deploy the finalized application at clinical sites to evaluate and validate its output quality and performance with potential end-users.

The discussion below focuses on the accomplishment of individual thesis aims by retrospectively considering design outcomes and suggesting improvements in terms of architecture, workflow as well as further evaluation and validation. The forthcoming sections also describe future outlooks as the field of diffusion MRI-based tractography evolves, and possibilities to utilize FT4Onco as an extensible piece of software in other clinical areas beyond oncological neurosurgery.

8.1 User needs fulfillment

In the preceding seven chapters, all stages of both the descending and ascending parts of the V-model were addressed, which now enables drawing conclusions whether all identified unmet user needs have been satisfied through the explained design choices. This section discusses the last ascending block of the V-model, namely acceptance testing, where arguments are given if user needs were or were not fulfilled by the FT4Onco design.

UN1: *Localize brain tumor and classify all its microenvironments (compartments)*

Brain tumor classification is performed with the Philips-proprietary GBS tool (Section 5.3.2), which is capable of determining all lesion compartments (contrast-enhancing portion, necrosis, surrounding edema) based on anatomical T1, T2, FLAIR and contrast-enhanced T1-weighted images. As demonstrated in Section 6.2, this tool can be applied seamlessly to segment both low-grade and high-grade gliomas, although it is primarily dedicated to the multi-compartment segmentation of GBMs.

UN2: *Localize brain anatomy (cortical structures, white matter fibers, subcortical structures)*

The Philips-proprietary HBS tool (Section 5.3.1) enables the localization of cortical GM areas through deep learning classification with the DKT atlas, and identification of WM, CSF, and SC regions through model-based segmentation. The delineation of surgically relevant nerve fiber bundles connecting eloquent cortical and subcortical regions is possible through atlas-aided bundle dissection via RecoBundles (Section 5.5.4).

UN3: *Recognize tumor mass effect and edematous infiltration of fiber tracts*

The visualization of safe resection margins by means of the DIPY-enabled detection of cross-section areas of streamlines with tumor masks in the common T1 image space yields information on tumor-induced bundle displacement, zones of edematous infiltration or destruction due to necrosis. Users should nonetheless note that the integrated method for detecting tumor-tract relationships is solely *indicative* of possible relationships between the pathology and surrounding tissue, and needs to be validated intraoperatively.

UN4: *Mitigate problems with MRI data formatting and conversion*

Data formatting and conversion is fully automated throughout the entire pipeline, enriched by diffusion MR image quality control, and organized to conform to the BIDS format. Between pairs of image processing steps, the output of the first step is adequately converted to meet the input format requirements for the next consecutive process in the pipeline. In the pursuit of robustness, an additional future step would be to integrate the so-called BIDS Validator to check whether the structure of image processing files adheres to BIDS.

UN5: *Create a fully automated and computationally efficient solution*

FT4Onco constitutes a sequential chain of image processing and analysis steps, all of which are automated and tested on datasets from the two mentioned clinical sites. There is no need for active data manipulation or recruitment of tech-savvy assistants to supervise the pipeline. As explained earlier in Figure 5.6, FT4Onco by design does not support automated data pre-selection, parameter configuration, and transfer of processing outcomes to a viewing platform. When run on a previously untested dataset (acquired with different MRI acquisition protocols), configuration files need to be modified and optimal parameters have to be found. Parametric adjustments are especially required for the diffusion MRI motion correction step, whole brain tractography, thresholds in RecoBundles, and FBC thresholding. Viewing needs to be performed manually either with the presented Philips-proprietary VTK-based viewer, or any viewer of choice supporting VTK-formatted data.

The computational efficiency of the pipeline is globally dependent on two major factors: the available hardware configuration of the system, on which FT4Onco is running, and the parametric setup including the number of bundles in reconstruction. In the clinical evaluation of FT4Onco-v0.1 with medical doctors, data processing duration was considered of secondary importance because surgery planning was rarely performed on the same day as MR imaging. Because of these factors, there are no firm claims reported on the speed of FT4Onco-based

image processing, and the impact of parametric setup on the overall image processing duration was not investigated in this work.

A qualitative inspection of the tractography output during development nevertheless suggested that the image processing duration be directly proportional to the changing initialization of tracking parameters in the pipeline. The most significant factors determining image processing duration seem to be the number of selected streamlines in whole brain tractography, and the RecoBundles dissection being performed on the whole brain tractogram instead of a streamline subset. Provided that the minimum hardware requirements are met, Table 8.1 lists the duration of all major processing steps for datasets from the two partner clinics.

Processing step	Multi-shell HARDI	Multi-shell DTI
Hybrid brain segmentation	00:03:06	00:05:18
Brain tumor segmentation	00:09:06	00:11:14
Anatomical segmentation label rearrangement	00:01:04	00:02:07
T1 and T2 brain extraction	00:00:47	00:00:33
Diffusion data quality check	00:01:29	00:00:12
Denoising	00:35:31	00:00:55
Gibbs ringing correction	00:00:21	00:00:03
Motion correction with outlier detection	00:12:58	00:02:46
B_1 inhomogeneity correction	00:01:07	00:00:24
Registration-based EPI distortion correction	00:00:35	00:00:38
Response function and FOD estimation	00:00:45	00:00:57
Whole brain tractography	09:02:02	00:19:07
Bundle recognition (AF, CST, OR)	03:57:01	00:19:12
Spurious fiber filtering (AF, CST, OR)	01:56:40	00:09:17
Detection of tumor-tract relationships	00:00:53	00:00:21
Calculation of bundle profiles for tracking uncertainty	00:04:58	00:01:06
Total duration	16:08:23	01:14:10

Table 8.1: Comparison of CPU-based pipeline duration (formatted as HH:MM:SS) on clinical multi-shell data. Related data conversion and formatting times are included in each duration. Clinically less acceptable durations are highlighted in red. Tractography in HARDI and DTI datasets was performed at 10 mill. and 1 mill. selected streamlines, respectively. Selected bundles (AF, CST, OR) were reconstructed bihemispherically.

UN6: *Generate fiber tracking results that can be easily interpreted in the intraoperative workflow*

The transfer of bundle reconstructions into the intraoperative workflow, and their interpretation during neurosurgery remains a nontrivial topic. The current solution is strictly provided as a means for planning tumor resection preoperatively, and its integration into neuronavigation systems was out of scope. Segmented and co-registered representations of brain anatomy and pathology offer anatomical guidance to determine where functionally crucial neuronal networks can be expected during surgery. Lesion-induced functional deficits and brain network disruptions may already be anticipated to some extent by scrutinizing tumor-tract relationships

in visualizations. To support data handling in the operating room, FT4Onco tractography outcomes are formatted as VTK polylines, and are independent of any specific viewing platform. Hence, bundle reconstructions may serve as a useful input for multi-modal image fusion, e.g. with intraoperative MRI or ultrasound data if a suitable functional module is added to FT4Onco.

UN7: *Visualize all tissue types and bundles in a 3D fashion with options for selective viewing*

FT4Onco facilitates the visualization of anatomical underlays with geometrically aligned 3D fiber bundles in any VTK-compatible viewer of choice. By default, bundles are color-coded by convention according to the spatial orientation of their fibers. Brain tumors are stored as VTK meshes with opaque shades to unveil tumor compartments otherwise obscured by the outermost edema. Bundle displacement or infiltration are indicated with highlighted areas of cross-sections in the T1 image space. Reconstructed bundles, tumor meshes, and anatomical underlays can be viewed selectively.

UN8: *Use more advanced fiber tracking methods that can resolve crossing fibers and propagation through edema*

The application of the probabilistic CSD algorithm enables the reconstruction of bundles in regions densely populated with crossing fibers. For instance, the CSD model is capable of determining the primary fiber orientation in the centrum semiovale area, where fibers from the CST, SLF, and interhemispheric callosal fibers are known to meet and cross. Moreover, bundle dissection using RecoBundles with HCP842 anatomical models and FBC thresholding enables the reconstruction of bundles in a shape-directed manner, and capturing the predicted core of each fascicle after removing short or incoherent fibers from the tractograms. The CSD algorithm seems to also be capable of detecting fibers that propagate through edema around tumors, which helps identify infiltration effects. Users should however keep in mind that tracking with the probabilistic CSD algorithm available from MRtrix does not directly compensate for extracellular free water diffusion in peritumoral areas. Therefore, the tracing of WM pathways through edematous zones is still limited, leading to possible under-representation of eloquent fibers. On the contrary, as reported in initial interviews, denser bundle representations around tumors make it more difficult for neurosurgeons to decide whether or not to apply resection techniques in these areas [107].

UN9: *Indicate uncertainty in the presence of peritumoral bundles to aid result interpretation*

Fiber tracking uncertainty is estimated by computing bundle profiles for FA and AFD, explained in Section 5.6.3. A decrease in AFD may indicate to the users that the specific bundle segment is affected by edema, hence increasing the uncertainty of bundle propagation across this area. Similarly, lower FA values may be indicative of areas with complex fiber architectures and crossing fibers, thereby decreasing the degree of certainty that a bundle is present in this particular location.

UN10: *Create a robust solution for datasets from different centers, scanners, and acquisition protocols*

Designing a dMRI tractography pipeline capable of processing MRI data from various sources is by no means straightforward. Creating a *robust* fiber tracking application entails numerous hurdles that need to be overcome: adjusting to varying data representations and data structures, fine-tuning of image processing parameters, ensuring robustness against previously unknown MRI data acquisition protocols, and extensive verification on new datasets. FT4Onco addressed the automation and acceleration of the image processing workflow for surgery planning in two partner clinics. Therefore, the pipeline was tailored to accept MRI data acquired with two distinct image acquisition protocols. Extending the input data portfolio for FT4Onco is a matter of future development.

8.2 Architecture and site-specific workflow optimization

The software architecture of FT4Onco as a standalone command-line application was particularly governed by the aim to optimize (automate and accelerate) MRI data processing, and address the labor-intensive workflow in daily clinical practice.

Firstly, while a fully automated application was designed and realized, there is large room for improvement in the orchestration of functional elements and pipeline composition. Currently, functionalities are distributed across several Docker images, which are sequentially instantiated as image processing continues. Higher technical efficiency of the pipeline is achievable, amongst others, by integrating the whole chain into one virtual machine (e.g. a single Docker/Singularity image) or the orchestration of containers via multi-threading or parallel image processing. Significant performance enhancement could also be achieved by deploying FT4Onco in a high-performance computing environment or a cloud service. These improvements could eventually simplify the on-premise installation of FT4Onco and users may benefit from such optimizations when aiming for simultaneous multi-subject tractography.

Secondly, FT4Onco currently supports the automatic conversion of DICOM input to BIDS-NIfTI, which is the most demanded conversion method for clinical research purposes. In order to prospectively adhere to the BIDS format and fulfil its specification, the aforementioned BIDS Validator should be added to the pipeline. Moreover, DICOM images should be accessible by FT4Onco through a DICOM data sharing mechanism coupled to the hospital patient archiving systems (e.g. PACS). Tractography outcomes can be visualized with any viewer of preference provided that the tool supports the visualization of VTK- and NIfTI-formatted data. The viewer presented in Figure 5.28 is constrained in functionality and intended solely for research and development. For utilization in clinical practice, FT4Onco output would have to be stored as DICOM and merged with original patient data in the hospital archiving systems. Should a dedicated viewer be utilized within the internal hospital network, then more interactive features would have to be added, some of which were mentioned by medical experts during the clinical evaluation of FT4Onco-v0.1: sliders for bundle thresholding, windowing, transparency adjustments, etc. The visualization of reconstructed bundles in 3D space should offer more quantitative features, such as overlays of bundle profiles (FA, AFD).

Thirdly, from the product transformation viewpoint, there are many non-functional requirements, the fulfillment of which was not targeted in this thesis. To attain the properties

of a full-fledged workflow-enhancing application, FT4Onco should be tested more thoroughly on usability requirements (ease of use, internationalization, etc.); performance requirements (runtime, reliability, etc.); maintainability and support requirements; and finally, security and compliance requirements to ensure safe installation and use within the hospital network. For quality assurance reasons, FT4Onco should be marketed together with a recommended MR examination protocol, e.g. a 10–15-minute acquisition scheme including techniques (parallel MRI, simultaneous multi-slice, multi-band or partial Fourier) for faster acquisition of isotropic anatomical images, multi-*b*-value dMRI with 60+ directions (to ensure robustness to crossing fibers), and potentially also resting-state blood-oxygen level dependent (BOLD) fMRI data. Furthermore, an example configuration file should be packaged together with the software, mentioning acceptable interval ranges for all parameters that affect the quality of fiber tracking results.

Eventually, FT4Onco should be extended to enable integrating functional information from rs-fMRI or TMS. Neuronavigation system vendors should incorporate a HARDI tractography suite by default, and enable advanced visualization with automatic data fusion from various modalities. Intraoperative visualization should also provide options to closely scrutinize edema-obscured tracks, peritumoral safety zones, and cortical/subcortical bundle terminations.

In general, the translation of advanced fiber tracking tools to clinical practice, including FT4Onco, can be supported by educated tractographers (personnel specialized in fiber tracking) who spread awareness of the capabilities of these solutions. To persuade medical experts, tractographers need to learn neuroanatomy, focus on the validation of (novel) techniques, work with neurosurgeons to educate them on methodological limitations, and prepare lightweight online tutorials.

Despite their notoriously known busy schedule, neurosurgeons should be more encouraged to integrate fiber tracking technology in their routine, and actively supply tractographers and vendors with qualitative feedback to drive standardization in the field. Neurosurgeons should ideally supervise tractographers and enrich the fiber tracking process by their anatomical knowledge. Most importantly, to avoid the underuse of tractography in surgery planning, surgeons must understand that bundle reconstructions cannot be thought of as a precise in vivo representation of WM bundles, but as a modeled estimation of large tracts in the brain.

8.3 Repeatability, replicability, reproducibility, reliability & robustness

Successive computational trials conducted with a piece of software can be compared via descriptive terminology that defines the degree of trustworthiness and ambiguity in produced output based on involved operators, study setup, measurement conditions, applied methods, and input data. This lexicon comprises three sometimes confused terms, namely “repeatability”, “replicability”, and “reproducibility” [176]. Whether an image processing pipeline must be repeatable, replicable or reproducible depends on what is acceptable in clinical practice.

As a minimum non-functional requirement, *repeatability* of FT4Onco-based fiber tracking is achieved when the same team arrives at similar results and conclusions by running the pipeline under exactly the same conditions in several experiments. *Replicability* of a processing pipeline means that if launched twice by an independent team with the same input data, parameters, and experimental setup, it will produce concordant outcomes that do not vary beyond an agreed limit. Assuming flexible precision requirements in this work, the final version of FT4Onco enables generating repeatable and replicable output.

Tractography *reproducibility* has been broadly investigated both qualitatively and quantitatively in numerous studies [5, 24, 81, 114, 177], and remains an open problem. A processing pipeline is reproducible if it can be run in multiple trials by independent teams in a different experimental setup including data from different MR scanners and produce comparable outcomes. The most critical image processing steps decreasing the level of reproducibility in tractography are brain extraction, the dMRI-T1 co-registration, and random seeding. Reproducibility also entails guaranteeing no change in pipeline output quality as a result of changing software packages, dependencies, seeding strategies or algorithmic parameters.

The next characteristic of a fiber tracking software refers to *reliability*, that is how accurate the anatomical representation is and how well it describes a brain's WM organization. Fiber tracking reliability is strongly dependent on how dMRI data are acquired and processed since bundle dissections are impacted by different vendors and MR scanners, different choices of image resolution, diffusion directions and gradient sensitizations [178]. As summarized in Chapter 7, numerous uncertainties (imaging artifacts, chosen diffusion model, tracking parameters, etc.) cumulatively penalize the fiber tracking process. The reliability of FT4Onco can be assessed in algorithmic, biological and clinical terms.

Algorithmically reliable tractography methods (e.g. tensor-based deterministic approach) may not necessarily be biologically reliable, albeit highly reproducible. Based on the technical cross-validation outcomes, FT4Onco is algorithmically reliable in a sense that selected bundles can be reconstructed in the majority of cases. Nevertheless, their biological reliability (or plausibility) cannot be assessed through indirect validation methods. Eventually, the clinical applicability of FT4Onco needs yet to be addressed by employing postsurgical functional measures, where the reliability of performing surgery based on FT4Onco bundle segmentations is evaluated with respect to e.g. functional loss [179]. Although FT4Onco facilitates the selection of adequate neurosurgical approaches, intraoperative brain shift decreases the estimated localization of segmented bundles. Future investigation of FT4Onco reliability should consider the quantification of tracking variability through clinical datasets from various centers world-wide, and conduct studies that validate bundle reconstructions functionally with intraoperative DES.

Finally, as already described above, the next FT4Onco improvement should focus on *robustness*, i.e. the ability of the pipeline to continue performing sufficiently well despite abnormalities in the input imaging series. In the pursuit of robustness to new data, the pipeline should be adjusted to the latest dMRI acquisition schemes. Consequently, there is currently no guarantee that FT4Onco will reliably process a dataset acquired with a novel, previously unknown MR imaging protocol or image acquisition schemes from other vendors than Philips (e.g. Siemens or GE).

8.4 Future development of FT4Onco

There is a plethora of software features that were not addressed in this work due to intentionally imposed restrictions on the design extent. Future development of FT4Onco should focus on several critical topics mentioned in this section.

Firstly, there is absolutely no consensus on what an optimal dMRI processing pipeline should look like. Due to the increasing variety of clinical datasets, the combination of tools from different software packages into an optimized pipeline becomes tremendously challenging. Each and every package commonly reads, interprets and writes different data in inconsistent ways, which has a huge impact on the estimation of spherical harmonics components, handling coordinate spaces, scaling factors, etc. FT4Onco should become a flexible neuroimage analysis tool for tractography in oncological data, continuously reflecting and incorporating the latest scientific updates in available open-source frameworks. Though the current version of FT4Onco comprises state-of-the-art neuroimage processing tools, this release will have most likely become outdated within a year's time, which is why version control should be introduced in subsequent development.

Secondly, automatic quality control should be implemented to monitor and report data formats and metadata (e.g. acquisition parameters), the unprocessed data (e.g. SNR) and processed data (e.g. noise estimates). This tractography software feature is crucial but very often neglected because it can be time-consuming and not straightforward. An improved integration of dMRI acquisition, reconstruction, processing, and fiber tracking may affect the current order of steps in the pipeline, and even make some steps redundant in the future.

Thirdly, the refactoring of FT4Onco should concentrate on the sensitivity-specificity tradeoff, which closely relates to further parametric optimization of the whole pipeline. Model-driven bundle dissection should be enhanced by utilizing information from a combination of sources, such as other tractography atlases, involving microstructural information, or adding machine-learning models that are able to better replicate the bundle structure. Cortical track terminations should be refined by combining model-based bundle dissection with start/end ROIs, again subsegmented from various cortical parcellation and white matter atlases. Next, the single-subject processing pipeline should incorporate algorithms to suppress currently unaddressed imaging artifacts, which were considered small culprits in FT4Onco, but should be corrected when aiming for microstructural and statistical (group) analyses:

- ▶ *signal drift* [180] (gradual signal intensity fluctuations within a single dMRI acquisition over time)
- ▶ *noise distribution bias* [181] (signal bias propagating in all diffusion-derived measures)
- ▶ *EPI Nyquist ghosts* [182] (aliasing artifact occurring in EPI sequences using zig-zag k -space trajectory, caused by eddy current induced phase shifts between alternate k -space lines)
- ▶ *gradient deviations* [183] (gradient nonlinearities and gradient gain miscalibration)
- ▶ *signal dropouts* [184] (strong diffusion gradients causing patient table vibrations and consequential MR echo shifts in k -space)

In addition, more attention should be paid to fiber tracking in peritumoral areas, especially in the presence of lesion-induced edema. In FT4Onco, diffusion modeling in peritumoral areas remains a limitation as there is currently no compensation for extracellular water diffusion

confounding the estimation of principal fiber orientation in edematous zones. Besides fiber propagation through edema, FT4Onco should also be able to detect fibers propagating through parts of the tumor core.

The quality of FT4Onco output can further be advanced by incorporating machine learning algorithms along the entire image collection and processing workflow. In particular, DL methods may (1) enable faster HARDI data acquisition and reconstruction at the scanner, (2) generate super-resolution datasets, (3) further accelerate image processing, (4) significantly improve the accuracy of segmentation and registration tasks in the pipeline, or (5) increase performance in image restoration (artifact detection, artifact removal, image synthesis, distortion correction and quality monitoring). Nevertheless, caution should be exercised when drawing inference based on DL-driven fiber tracking results due to the prohibitive black-box nature of DL methods [100].

Finally, the FT4Onco pipeline may also be extended in functionality to facilitate population-based neuroimaging studies, tractography in healthy subject datasets, or it can be branched to support microstructural analysis in other clinical contexts, such as investigating WM fiber integrity in neurodegenerative diseases.

8.5 Concluding remarks

Summarizing the clinical relevance, advanced dMRI-based tractography enables inspecting the relationships between lesions and adjacent structures, and visualizing macroscopic bundle displacement or discontinuities in WM tracts near tumors. It may also help neurosurgeons find the best surgical route, select a surgical approach, and detect terminal boundaries of resection. Accurate preoperative planning facilitates greater safe resection and less functional deterioration due to damage to peritumoral WM fascicles. Considering all technical limitations of advanced tractography techniques, the spatial concordance between anatomy and function needs to be confirmed intraoperatively, pairing fiber tracking outcomes with functional mapping by awake DES. This combination leads to faster intraoperative identification of eloquent WM fibers, greater extent of lesion resection, and eventually higher ability to objectivize postoperative functional deficits.

This dissertation addressed the topic of the clinical translation of advanced dMRI-based tractography to optimize preoperative workflow for the resection of primary glial brain tumors that are particularly hard to resect due to their aggressive, infiltrative and recurrent nature. The majority of commercial tractography software tools are dominated by the use of the tensor model and the outdated DTI-FACT algorithm, originally introduced approximately 24 years ago. Owing to the known limitations of this methodology and the missing integration of advanced techniques in vendor solutions, there remains a pressing need for moving beyond tensor-based tractography. The herein designed clinical research prototype, FT4Onco, simplifies neurosurgery planning by:

- ▶ fully automating and accelerating MRI data processing and fiber tracking analysis
- ▶ optimizing parametric setup for tractography in routinely acquired MRI data
- ▶ utilizing advanced probabilistic algorithms with the CSD model to overcome the crossing fibers problem
- ▶ providing 3D visualizations that indicate surgical risk areas and fiber tracking uncertainty

In general, to adopt advanced dMRI tractography techniques in brain tumor surgery workflow, both clinicians, researchers, and vendors must collaboratively bridge the gap between research and practice. Expert consortia involving neuroanatomists and tractographers should be established to pursue the goal of tractography standardization. The performance of different in-house fiber tracking pipelines used in neurosurgery departments should be quantitatively analyzed and compared e.g. through already existent international tractography challenges. Similarly, there remains a future need for improvements in the technical efficiency and usability of FT4Onco to encourage clinicians to apply it in their surgery planning routines. Further FT4Onco evaluation on heterogeneous patient data as well as validation of tractographical reconstructions against expert bundle delineations or outcomes from intraoperative functional mapping may herald great potential for this prototype to be widely accepted in the neurosurgical realm.

Appendices

The following sections provide supplementary material for related chapters.

A Technical specification of FT4Onco

Hybrid brain segmentation	
Distribution	Philips proprietary
Version	N/A
Algorithm	voxel-wise 3D F-Net based full brain segmentation and shape-constrained model-based subcortical segmentation
Data formats	NIfTI
License	Philips Research Hamburg, Germany
Brain tumor segmentation	
Distribution	Philips proprietary
Version	DeepMedic 0.7.3, SPM 12
Algorithm	3D U-Net based GBM classification with bias field correction, mask extraction, co-registration, normalization, and resampling
Data formats	NIfTI
License	Philips ICAP Aachen, Germany
T1 and T2 brain extraction	
Distribution	ANTsPy
Version	0.2.0
Algorithm	ants.registration, ants.apply_transforms
Data formats	NIfTI
License	Apache License 2.0

Table 2: Software packages, algorithms, versions, and licenses used in FT4Onco anatomical data processing.

Diffusion data quality inspection	
Distribution	MRtrix
Version	3.0.2
Algorithm	dwigradcheck
Data formats	NIfTI, MIF
License	Mozilla Public License 2.0
Denoising	
Distribution	DIPY
Version	1.4.1
Algorithm	Patch2Self
Data formats	NIfTI
License	BSD License
Gibbs ringing correction	
Distribution	MRtrix
Version	3.0.2
Algorithm	mrdegibbs
Data formats	NIfTI, MIF
License	Mozilla Public License 2.0
Motion correction with outlier detection	
Distribution	MRtrix
Version	3.0.1
Algorithm	SHARD (dwimotioncorrect, mssh2amp)
Data formats	NIfTI, MIF
License	Mozilla Public License 2.0
B ₁ inhomogeneity correction	
Distribution	MRtrix
Version	3.0.2
Algorithm	N4ITK
Data formats	NIfTI, MIF
License	Mozilla Public License 2.0
DMRI-T1 co-registration, brain extraction, distortion correction	
Distribution	MRtrix, ANTsPy, ANTsX
Version	3.0.2 (MRtrix), 0.2.0 (ANTsPy), 2.3.1 (ANTsX)
Algorithm	SyNRA (ANTsPy), ConvertTransformFile (ANTsX), warpinit (MRtrix), antsApplyTransforms (ANTsX), warpcorrect (MRtrix), mrtransform (MRtrix), dwiextract (MRtrix)
Data formats	NIfTI, MIF
License	Apache License 2.0 (ANTs), Mozilla Public License 2.0 (MRtrix)

Table 3: Software packages, algorithms, versions, and licenses used in FT4Onco diffusion data processing.

Response function estimation	
Distribution	MRtrix
Version	3.0.2
Algorithm	dwi2response dhollander
Data formats	NIfTI, MIF
License	Mozilla Public License 2.0
Estimation of fiber orientation distribution	
Distribution	MRtrix
Version	3.0.2
Algorithm	dwi2fod msmt_csd
Data formats	NIfTI, MIF
License	Mozilla Public License 2.0
Normalization of FODs	
Distribution	MRtrix
Version	3.0.2
Algorithm	mtnormalise
Data formats	NIfTI, MIF
License	Mozilla Public License 2.0
Whole brain tractography	
Distribution	MRtrix
Version	3.0.2
Algorithm	tckgen, tckresample
Data formats	NIfTI, MIF
License	Mozilla Public License 2.0
Bundle recognition	
Distribution	DIPY
Version	1.4.1
Algorithm	RecoBundles
Data formats	NIfTI, TCK, TRK
License	BSD License
Spurious fiber filtering	
Distribution	DIPY
Version	1.4.1
Algorithm	FBC thresholding
Data formats	NIfTI, TCK, TRK
License	BSD License
Uncertainty and tumor-tract relationships computation	
Distribution	SCILpy, DIPY
Version	1.1.0 (SCILpy), 1.4.1 (DIPY)
Algorithm	<i>scil_evaluate_bundles_pairwise_agreement.py</i> , AFQ, QuickBundles
Data formats	NIfTI, TCK, TRK
License	BSD License

Table 4: Software packages, algorithms, versions, and licenses used in the FT4Onco tractography chain.

B Functionality comparison across pipelines

Functionality	Tractoflow	BIDS-CSD Leuven
T1 processes		
Denoising	DIPY	FreeSurfer (for T1) ANTsX (for VBG)
B_1 inhomogeneity correction	ANTsX	FreeSurfer
Brain segmentation & parcellation	FSL	FreeSurfer
Tumor segmentation	×	ITKSnap
Resampling	SCILpy	MRtrix
Brain extraction	ANTsX	FreeSurfer
Registration on DWI	ANTsX	ANTsX
DWI processes		
Denoising	MRtrix	MRtrix
Gibbs ringing correction	MRtrix	MRtrix
EPI distortion correction	FSL	FSL
Eddy current correction	FSL	MRtrix, FSL
Motion correction	FSL	FSL
b_0 image extraction	DIPY	MRtrix
Brain extraction	FSL	ANTsX
B_1 inhomogeneity correction	ANTsX	ANTsX
Tractography		
TRF estimation	DIPY	MRtrix
FOD estimation	DIPY	MRtrix
Whole brain tractography	DIPY	MRtrix
Bundle dissection	DIPY	MRtrix
Spurious fiber filtering	DIPY	MRtrix

Table 5: Comparison of clinical research software packages integrated in the Tractoflow and BIDS-CSD pipelines. Crosses represent unavailable functionalities.

Functionality	Tractoflow	BIDS-CSD Leuven
T1 processes		
Denosing	non-local means with Rician correction	adaptive non-local means
B_1 inhomogeneity correction	N4ITK	recon-all (N4ITK)
Brain segmentation & parcellation	FAST	ASEG
Tumor segmentation	×	semi-automated image classification workflow with CNN
Resampling	reslicing method	mrresample
Brain extraction	T1 template-based	ANTsX
Registration on DWI	SyN	Affine and SyN
DWI processes		
Denosing	MP-PCA	MP-PCA
Gibbs ringing correction	local subvoxel shifts	local subvoxel shifts
EPI distortion correction	topup with field maps	topup with field maps
Eddy current correction	eddy	eddy
Motion correction	eddy	eddy
b_0 image extraction	SCILpy	dwiextract
Brain extraction	FSL BET	ANTsX BET
B_1 inhomogeneity correction	N4ITK	N4ITK
Tractography		
TRF estimation	SCILpy	dhollander
FOD estimation	SCILpy	MSMT-CSD
Whole brain tractography	SCILpy	iFOD2
Bundle dissection	SCILpy	ACT
Spurious fiber filtering	SCILpy	SIFT2 with voxel-wise filtering of bundles based on TDI

Table 6: Comparison of methods from respective software packages listed in Table 5. Crosses represent unavailable functionalities.

C Clinical evaluation questionnaire

Table 7 lists questions with rating scales that were answered by neurosurgeons and neuroradiologists during evaluation sessions.

ISD plugin user interface	
Is it easy to understand the layout? If not, why?	yes, no
How do you rate the button reaction speed?	poor, fair, moderate, good, excellent
How do you rate data selection from the patient database for viewing?	poor, fair, moderate, good, excellent
Is it easy to find the desired plugin? If not, why?	yes, no
Is the plugin description (after hovering over input parameter names) clear? If not, what is missing/unclear?	yes, no
Which features are you missing in the plugin UI? Please describe.	all images in drop-down list, automatic adjustment of plugin window length, automatic input parameter filling, all anatomical images in view by default, other—please specify
Performance	
How do you rate the overall performance of interaction?	poor, fair, moderate, good, excellent
Is the number of pop-up notifications sufficient (if anything fails)?	yes, no
How do you rate the data loading speed after opening the Research Oncology Suite?	poor, fair, moderate, good, excellent
How do you rate data selection from the patient database?	poor, fair, moderate, good, excellent
How do you rate the accuracy of the lesion segmentation?	poor, fair, moderate, good, excellent
How do you assess the representativeness of shown fiber tracts compared with what you observe in the original DICOM MR images?	poor, fair, moderate, good, excellent
How do you rate the time efficiency of viewing results?	poor, fair, moderate, good, excellent
Data processing has taken 1 h 55 min per case on average. Is it a clinically acceptable duration? If not, what would be the ideal duration?	yes, no
Visualization and viewing	
Do you have experience with clinical decision-making based on 3D tractography visualization as produced by FT4Onco-v0.1?	yes, no
How do you rate the informativeness of the overall visualization?	poor, fair, moderate, good, excellent
How do you rate the interactivity of the viewer?	poor, fair, moderate, good, excellent
Which interactive controls are you missing in the viewer?	sliders for viewing planes, sliders for transparency of objects, buttons for selective overlays, switch on/off values, probing window, other—please specify
Do you see any artifacts in the shown visualizations?	yes, no
How do you rate the geometrical alignment of tracts and lesion labels with the T1 underlay?	poor, fair, moderate, good, excellent
How would you rate the reliability of visualized fiber tracts with respect to commonly perceived subject's neuroanatomy?	poor, fair, moderate, good, excellent
Which tumor-tract relationships can you derive from what you see?	bundle displacement, edematous infiltration, fiber destruction
How would you rate the feasibility to plan surgery based on shown visualizations?	poor, fair, moderate, good, excellent
Overall impression	
What is the main (set of) improvement(s) needed for you to use this tool, i.e. where do you perceive the largest area for improvement?	visualization, ISD plugin user interface, data processing speed, workflow, other—please specify
Would you start using the FT4Onco-final plugin once widely available? If not, why?	yes, no
Would you recommend this tool to your clinical peers once widely available? If not, why?	yes, no
Do you recognize clinical value in this prototype application for your center? If yes, please clarify in which aspect(s).	yes, no
Do you have any suggestions for further improvement (other than already mentioned)?	yes, no
Final comments or remarks?	open statement

Table 7: Evaluation questionnaire.

D Technical cross-validation results

Tables 8 and 9 provide an overview of values generated during technical cross-validation. Bundle overlap and overreach are expressed volumetrically in voxel coordinates.

PT01					PT02			
Bundle	Weighted DSC	BOL [mm ³]	BOR [mm ³]	BA [mm]	Weighted DSC	BOL [mm ³]	BOR [mm ³]	BA [mm]
AF_L	0.64	15154.9	53694.67	2.28	0.15	2783.6	44300.3	5.14
AF_R	0	169.17	29134.41	9.84	N/A	N/A	N/A	N/A
CST_L	0.83	26137.71	47275.04	1.77	0.82	23964.87	46897.16	2.05
CST_R	0.71	25439.06	45143.95	1.38	0.76	23347.52	46602.76	2.39
C_L	0.65	12481.16	28670.85	1.26	0.63	6393.27	29578.21	2.77
C_R	0.73	7687.3	24516.32	1.88	0	0	25814.75	10.94
IFOB_L	0.51	9051.64	41099.28	3	0.57	13577.46	52470.95	3.76
IFOB_R	0.42	9260.35	51409.8	4.51	0.55	9943.62	45851.39	6.46
ILF_L	0.64	26476.04	68074.04	1.4	0.68	21994.16	68577.15	1.5
ILF_R	0.06	4712.56	74849.59	8.2	0.51	15097.78	59231.11	1.85
MdLF_L	0.24	10156.73	61142.5	4.24	0.74	17004.78	46007.37	2.15
MdLF_R	0.53	16743.34	60276.89	2.34	0.46	16679.62	55168.86	1.92
OR_L	0.54	8902.24	34747.75	2.33	0.36	4413.77	27009.92	2.69
OR_R	0.51	7370.93	37410.51	3.26	0.71	8961.56	24654.73	1.59
SLF_L	0.51	24243.89	113934.21	3.49	0.35	8188.22	47639.74	4.9
SLF_R	0.73	24586.62	53268.46	1.84	N/A	N/A	N/A	N/A
PT03					PT04			
Bundle	Weighted DSC	BOL [mm ³]	BOR [mm ³]	BA [mm]	Weighted DSC	BOL [mm ³]	BOR [mm ³]	BA [mm]
AF_L	0.11	5575.99	57069.27	4.51	0.34	3576.72	30061.55	3.79
AF_R	0.16	4202.86	50287.13	5.72	0.51	7283.05	33572.35	2.44
CST_L	0.9	25726.87	33223.03	1.15	0.88	22079.85	28062.28	1.01
CST_R	0.76	21928.25	46057.9	1.97	0.84	26702.34	39888.73	1.45
C_L	0.74	10380.82	41472.77	2.23	0.59	6285.62	24615.19	1.91
C_R	0.73	9534.98	22752.13	1.29	0.67	6659.11	22600.54	1.43
IFOB_L	0.66	12553.66	42588.84	4.52	0.3	4308.32	28194.1	1.34
IFOB_R	0.81	18533.89	48167.02	3.17	0.53	9141.72	42685.51	1.61
ILF_L	0.77	30322.99	70075.51	1.42	0.22	3620.66	54454.84	2.7
ILF_R	0.43	18878.82	58277.62	1.73	0.19	5160.75	48637.18	7.22
MdLF_L	0.55	14372.77	52244.65	3.27	0	8.79	25979.52	15
MdLF_R	0.5	10484.08	37353.39	2.45	0.1	1729.04	53532.1	3.18
OR_L	0.61	10187.49	32041.04	1.94	0.48	5079.46	19008.44	1.29
OR_R	0.51	10255.6	37869.69	3.14	0.16	6351.53	43674.16	4.54
SLF_L	0.52	18331.77	80601.33	3.81	0.23	8935.2	66705.31	4.31
SLF_R	0.71	37091.95	87122.03	2.11	0.48	10659.84	55324.85	3.57

Table 8: Comparison values between bundle reconstructions from FT4Onco and KUL_NIS.

PT01					PT02			
Bundle	Weighted DSC	BOL [mm ³]	BOR [mm ³]	BA [mm]	Weighted DSC	BOL [mm ³]	BOR [mm ³]	BA [mm]
AF_L	0.39	10587.34	56087.21	2.22	0.65	10156.73	30580.04	1.6
AF_R	0.3	3354.82	19893.83	2.53	0.27	3139.51	21183.47	2.82
CST_L	0.31	7094.11	63651.48	5.46	0.27	9363.61	50974.79	2.96
CST_R	0.39	10218.25	57673.44	3.61	0.35	8425.49	50005.91	3.74
C_L	0.54	8943.99	29312.37	1.46	0.57	7926.78	30290.04	1.87
C_R	0.69	9352.63	22629.1	1.31	0.58	7276.46	23578.2	2.33
IFOF_L	0.57	7366.54	30487.77	2.02	0.53	7522.53	29391.46	1.57
IFOF_R	0.57	11466.14	43135.89	3.04	0.61	5896.75	24753.6	2.38
ILF_L	0.33	8625.42	78685.55	2.56	0.13	6577.82	81787.71	4.13
ILF_R	0.18	7322.6	64800.51	3.74	0.19	7080.93	73228.2	3.62
MdLF_L	0.28	4174.3	52224.88	3.7	0.21	3045.04	48839.31	2.68
MdLF_R	0.3	8284.89	64886.19	2.91	0.27	6052.73	59059.75	3.06
OR_L	0.23	3660.2	39605.32	3.99	0.39	3409.74	27003.32	2.38
OR_R	0.01	424.02	40934.5	8.07	0.26	2748.45	28389.63	2.32
SLF_L	0.39	17903.35	101795.79	2.25	0.41	9991.96	39143.95	3.31
SLF_R	0.35	9269.14	54698.7	5.33	0.24	4578.54	39394.4	3.63
PT03					PT04			
Bundle	Weighted DSC	BOL [mm ³]	BOR [mm ³]	BA [mm]	Weighted DSC	BOL [mm ³]	BOR [mm ³]	BA [mm]
AF_L	0.61	14864.9	37665.36	1.21	0.54	6768.96	28099.63	1.93
AF_R	0.56	8669.36	30351.55	1.53	0.52	7595.03	29989.05	1.67
CST_L	0.55	14750.66	43966.36	2.3	0.2	3260.35	37860.9	3.8
CST_R	0.18	4514.83	56069.63	7.43	0.35	8186.02	48452.63	3.26
C_L	0.52	9636.04	43456.66	1.73	0.61	7403.89	25625.81	1.81
C_R	0.56	6019.78	29191.54	2.53	0.7	7050.17	23499.11	1.56
IFOF_L	0.58	6593.2	22692.81	1.78	0.57	6533.88	28536.83	1.91
IFOF_R	0.38	7722.45	36786.56	3.17	0.65	11534.25	43140.29	1.68
ILF_L	0.11	5173.93	91520.42	5.63	0.25	5044.31	56085.01	4.31
ILF_R	0.12	4760.9	68977.01	4.58	Failed	Failed	Failed	Failed
MdLF_L	0.07	1612.6	48254.9	4.55	0.25	1788.36	20959.38	2.33
MdLF_R	0.3	3310.88	34908.13	2.76	0.29	3816.19	51576.77	3.16
OR_L	0.19	2985.72	37436.88	3.34	0.31	2616.63	21800.83	2.89
OR_R	0.1	2370.56	36678.91	4.35	0.2	2258.52	44436.52	4.8
SLF_L	0.39	14968.16	72000.08	4.03	0.31	12184.56	56746.31	1.98
SLF_R	0.37	16292.95	90103.36	2.41	0.62	11125.61	49784.02	3.04

Table 9: Comparison values between bundle reconstructions from FT4Onco and the HCP842 atlas.

List of publications

- [1] Daniel Krahulec, Ahmed Radwan, Jan Kirschke, Stefan Sunaert, Kim van de Ven, Maarten Versluis, and Marcel Breeuwer. Tumor-Tract Relationships Detected by Novel Clinical Research Application with Tractography for Neurosurgical Planning. Abstract from 59th ASNR Virtual Annual Meeting (May 22–26, 2021). ASNR21 Proceedings, p. 696–697.
- [2] Daniel Krahulec, Ahmed Radwan, Stefan Sunaert, Maarten Versluis, Kim van de Ven, and Marcel Breeuwer. Minimizing false streamlines in anatomically constrained tractography for neurosurgery guidance in patients with brain neoplasms. Abstract and poster from ISMRM and SMRT Virtual Conference and Exhibition (August 8–14, 2020). Proceedings No. 1738.
- [3] Andrey Zhylyka, Nico Sollmann, Alberto De Luca, Daniel Krahulec, Marcel Breeuwer, Alexander Leemans, and Josien Pluim. Multi-level fiber tracking: evaluation on clinical data. Abstract and poster from ISMRM and SMRT Virtual Conference and Exhibition (August 8–14, 2020). Proceedings No. 1746.
- [4] Daniel Krahulec, Frank Thiele, Ahmed Radwan, Fabian Wenzel, Stefan Sunaert, Maarten Versluis, Kim van de Ven, and Marcel Breeuwer. A clinical research software prototype with diffusion MRI tractography for glioma surgery planning. Abstract and software demonstration from 26th OHBM Annual Virtual Meeting (June 23 – July 3, 2020).
- [5] Daniel Krahulec, Ahmed Radwan, Stefan Sunaert, Maarten Versluis, Kim van de Ven, and Marcel Breeuwer. A clinical research demonstrator with diffusion MRI-based tractography and minimization of false positives for brain tumor surgery. Abstract and poster from 12th ISMRM Benelux Chapter Meeting (January 24, 2020) in Koninklijke Burgers' Zoo, Arnhem, The Netherlands.
- [6] Daniel Krahulec, Frank Thiele, Fabian Wenzel, Maarten Versluis, Kim van de Ven, and Marcel Breeuwer. Platform for Enhanced Diffusion MRI Data Processing Pipeline to Guide Tumor Neurosurgery. Software exhibit from 36th Annual Scientific Meeting Congress of the European Society for Magnetic Resonance in Medicine and Biology (October 3–5, 2019) in Rotterdam, The Netherlands.

Acknowledgements

This dissertation reports clinical research-oriented design activities between 2018 and 2022, conducted at Philips Healthcare, Dept. of MR R&D Clinical Science, Philips Research, and scientific learnings collected from Eindhoven University of Technology, Dept. of Biomedical Engineering, Medical Image Analysis group. The outcome, FT4Onco, was eventually adopted by Philips Research to be transformed into a modular clinical research application and applied for the demonstration of image quality on innovative Philips MR scanners. Hopefully, FT4Onco will one day become an indispensable tool in the workflow of neurosurgery planning.

Hereby, I would like to collectively express my sincere gratitude to all members of the Philips Healthcare and Philips Research teams who actively participated in countless sessions organized to steer my design thinking, provided me with comfortable work conditions, invaluable training, and encouraged me to bring this work to a successful end. I am extremely thankful for the opportunity to explore multiple areas: project management, applied research, workflow optimization, software design and development, efficient programming, prototyping, customer needs analysis, and foundations of hospital IT.

My biggest thanks belong to my supervisors, Marcel Breeuwer and Josien Pluim, namely for your thorough supervision, brisk and smart brainstorming throughout all our sessions, and immense help whenever seemingly insurmountable problems arose. I was always in awe of your extensive experience. But for you two, I would have never succeeded in finalization, and you literally lit up the darkness every time I would begin to succumb to it or my persistence would start to wither away. Marcel, thank you for spending all lunch breaks with me and for all the enjoyable conversations off work.

Liesbeth Geerts and Paul Folkers, thank you for negotiating project-related financial issues with the higher management, allowing me to travel to various conferences, educational courses and congress meetings, speeding up internal processes to arrange necessary equipment, for thought-provoking meetings, and for your informative bird's-eye view that always helped me avoid doing what was meaningless.

Kim van de Ven and Maarten Versluis, without your everlasting smile, grin, and jokes whenever we bumped into each other in the corridors, the work environment at Philips Best would be lame. Not only once did you make my day, perhaps without realizing it. Practicing my Dutch with you was always an honor. Your good mood, insightful contributions, assistance in customer meetings, and positive attitude helped boost my motivation.

My enthusiastic external collaborators, Ahmed Radwan and Willem Huijbers, you two have shown me how to navigate in the field of diffusion MRI, and neuroimage processing. You were and will stay an inspiration to me, for your hard-working demeanor influenced me in pursuing this endeavor. Moreover, I want to show my appreciation to Jan Kirschke, without whom my evaluation experiments in Munich would have failed.

Frank Thiele and Alexander Fischer, thank you both for your unfailing forbearance whenever I demanded prompt responses from you due to time constraints. I really appreciated your time to listen when I first presented the coarse and vaguely outlined concept of my solution to you as a complete newbie in industrial design. I am grateful to you for including me in your tight schedule at your premise in Aachen as a trainee on the Philips IntelliSpace Discovery research platform.

Fabian Wenzel and Arne Ewald, amongst many things, I am particularly appreciative of you accompanying me in our visualization and viewing hackathon, where I was able to gain incredible amounts of experience. Without your assistance and fruitful ideas, no user interface would have been created.

Finally, I want to thank my dearest family in the Czech Republic and my great friends, who would always raise my spirits when my motivation levels dropped. The challenges along my PhD journey were intensified by the COVID-19 pandemic that caused unforeseen delays, extensions, and uncertainties that veiled my mind. Throughout all ups and downs, I was lucky to share my emotions and receive moral support from the closest ones to my heart: my mother, my grandparents, Lukáš, Honza, Toni, and Beata, thank you for everything. My high five also goes to all TRABIT peers for their support and encouragement they have given me during the PhD track.

Daniel Krahulec
February 1st, 2023

Curriculum Vitae



Daniel Krahulec was born on July 12th, 1993 in Ostrava-Vítkovice in the Czech Republic. After finishing the Language Grammar School of Pavel Tigrid in 2012, he studied for a Bachelor's degree in Biomedical Engineering at VŠB – Technical University of Ostrava, where he focused on methods for artifact suppression in clinical MRI. In 2014, he joined an Erasmus exchange program at Tampere University of Technology in Finland. Inspired by Finland's outstanding education system, Daniel continued to pursue a Master's degree in Human Neuroscience and -technology at Aalto University in Espoo, where he graduated *Cum Laude*. His

Master thesis dealt with the optimization of proprioceptive stimulation during routine and ultra-fast functional MRI. This project aimed at developing a rehabilitation protocol for patients with cerebral palsy, and was carried out under the supervision of Prof. Harri Piitulainen in cooperation with Prof. Fa-Hsuan Lin from National Taiwan University.

Upon an unexpectedly received invitation from Prof. Lauri Parkkonen in December 2017, Daniel applied for the position of an Early Stage Researcher within the TRABIT network. In February 2018, he was admitted as a PhD candidate at Eindhoven University of Technology and hired as a Marie Curie Fellow at Philips Healthcare in Best, The Netherlands, financed via the EU's Horizon 2020 grant. His main research consisted of the design and realization of a novel clinical research software prototype for diffusion MRI tractography in neurosurgery planning, the results of which are reported in this design thesis. In this project, Daniel closely collaborated with clinicians during externships at Klinikum rechts der Isar in Munich (Germany), and University Hospital in Leuven (Belgium).

In July 2022, Daniel was employed as an Advanced R&D Project Engineer in the SnkeOS GmbH division of Brainlab AG in Munich, Germany, where he is now engaged in the entire development lifecycle for medical image processing algorithms to drive the digital transformation in healthcare.

Bibliography

- [1] David N. Louis, Arie Perry, Guido Reifenberger, et al. The 2016 World Health Organization Classification of Tumors of the Central Nervous System: a summary. *Acta Neuropathologica*, 131(6):803–820, June 2016. ISSN 1432-0533. doi: 10.1007/s00401-016-1545-1.
- [2] Michael Iv, Byung C. Yoon, Jeremy J. Heit, et al. Current Clinical State of Advanced Magnetic Resonance Imaging for Brain Tumor Diagnosis and Follow Up. *Seminars in Roentgenology*, 53(1):45–61, January 2018. ISSN 1558-4658. doi: 10.1053/fj.ro.2017.11.005.
- [3] Nancy Ann Oberheim Bush, Susan M. Chang, and Mitchel S. Berger. Current and future strategies for treatment of glioma. *Neurosurgical Review*, 40(1):1–14, January 2017. ISSN 1437-2320. doi: 10.1007/s10143-016-0709-8.
- [4] Woo Suk Tae, Byung Joo Ham, Sung Bom Pyun, et al. Current Clinical Applications of Diffusion-Tensor Imaging in Neurological Disorders. *Journal of Clinical Neurology (Seoul, Korea)*, 14(2):129–140, April 2018. ISSN 1738-6586. doi: 10.3988/jcn.2018.14.2.129.
- [5] Klaus H. Maier-Hein, Peter F. Neher, Jean-Christophe Houde, et al. The challenge of mapping the human connectome based on diffusion tractography. *Nature Communications*, 8(1):1349, November 2017. ISSN 2041-1723. doi: 10.1038/s41467-017-01285-x.
- [6] Ben Jeurissen, Maxime Descoteaux, Susumu Mori, and Alexander Leemans. Diffusion MRI fiber tractography of the brain. *NMR in biomedicine*, 32(4):e3785, April 2019. ISSN 1099-1492. doi: 10.1002/nbm.3785.
- [7] S. Mori, B. J. Crain, V. P. Chacko, and P. C. van Zijl. Three-dimensional tracking of axonal projections in the brain by magnetic resonance imaging. *Annals of Neurology*, 45(2):265–269, February 1999. ISSN 0364-5134. doi: 10.1002/1531-8249(199902)45:2<265::aid-ana21>3.0.co;2-3.
- [8] Shawna Farquharson, J.-Donald Tournier, Fernando Calamante, et al. White matter fiber tractography: why we need to move beyond DTI. *Journal of Neurosurgery*, 118(6):1367–1377, June 2013. ISSN 1933-0693. doi: 10.3171/2013.2.JNS121294.
- [9] Jacques-Donald Tournier, Susumu Mori, and Alexander Leemans. Diffusion tensor imaging and beyond. *Magnetic Resonance in Medicine*, 65(6):1532–1556, June 2011. ISSN 1522-2594. doi: 10.1002/mrm.22924.
- [10] Ben Jeurissen, Alexander Leemans, Jacques-Donald Tournier, et al. Investigating the prevalence of complex fiber configurations in white matter tissue with diffusion magnetic resonance imaging. *Hum Brain Mapp*, 34(11):2747–2766, May 2012. ISSN 1065-9471. doi: 10.1002/hbm.22099. URL <https://www.ncbi.nlm.nih.gov/pmc/articles/PMC6870534/>.
- [11] Stamatis N. Sotiropoulos and Andrew Zalesky. Building connectomes using diffusion MRI: why, how and but. *NMR in biomedicine*, 32(4):e3752, April 2019. ISSN 1099-1492. doi: 10.1002/nbm.3752.
- [12] Dong-Hoon Lee, Ji Won Park, Sung-Hee Park, and Cheolpyo Hong. Have You Ever Seen the Impact of Crossing Fiber in DTI? Demonstration of the Corticospinal Tract Pathway. *PLoS One*, 10(7):e0112045, 2015. ISSN 1932-6203. doi: 10.1371/journal.pone.0112045.
- [13] Manabu Kinoshita, Kei Yamada, Naoya Hashimoto, et al. Fiber-tracking does not accurately estimate size of fiber bundle in pathological condition: initial neurosurgical experience using neuronavigation and subcortical white matter stimulation. *NeuroImage*, 25(2):424–429, April 2005. ISSN 1053-8119. doi: 10.1016/j.neuroimage.2004.07.076.
- [14] Walid I. Essayed, Fan Zhang, Prashin Unadkat, et al. White matter tractography for neurosurgical planning: A topography-based review of the current state of the art. *NeuroImage. Clinical*, 15:659–672, 2017. ISSN 2213-1582. doi: 10.1016/j.nicl.2017.06.011.
- [15] Joseph Yuan-Mou Yang, Chun-Hung Yeh, Cyril Poupon, and Fernando Calamante. Diffusion MRI tractography for neurosurgery: the basics, current state, technical reliability and challenges. *Phys Med Biol*, 66(15), July 2021. ISSN 1361-6560. doi: 10.1088/1361-6560/ac0d90.
- [16] Masashi KINOSHITA, Katsuyoshi MIYASHITA, Taishi TSUTSUI, et al. Critical Neural Networks in Awake Surgery for Gliomas. *Neurol Med Chir (Tokyo)*, 56(11):674–686, November 2016. ISSN 0470-8105. doi: 10.2176/nmc.ra.2016-0069. URL <https://www.ncbi.nlm.nih.gov/pmc/articles/PMC5221778/>.
- [17] Sebastian M. Toescu, Patrick W. Hales, Martin M. Tisdall, et al. Neurosurgical applications of tractography in the UK. *Br J Neurosurg*, 35(4):424–429, August 2021. ISSN 1360-046X. doi: 10.1080/02688697.2020.1849542.
- [18] J.-Donald Tournier, Fernando Calamante, David G. Gadian, and Alan Connelly. Direct estimation of the fiber orientation density function from diffusion-weighted MRI data using spherical deconvolution. *NeuroImage*, 23(3):1176–1185, November 2004. ISSN 1053-8119. doi: 10.1016/j.neuroimage.2004.07.037.
- [19] J.-Donald Tournier, Fernando Calamante, and Alan Connelly. Robust determination of the fibre orientation distribution in diffusion MRI: non-negativity constrained super-resolved spherical deconvolution. *NeuroImage*, 35(4):1459–1472, May 2007. ISSN 1053-8119. doi: 10.1016/j.neuroimage.2007.02.016.
- [20] Maxime Descoteaux. High Angular Resolution Diffusion Imaging (HARDI). In *Wiley Encyclopedia of Electrical and Electronics Engineering*, pages 1–25. American Cancer Society, 2015. ISBN 978-0-471-34608-1. URL <https://onlinelibrary.wiley.com/doi/abs/10.1002/047134608X.W8258>.
- [21] E. Mormina, M. Longo, A. Arrigo, et al. MRI Tractography of Corticospinal Tract and Arcuate Fasciculus in High-Grade Gliomas Performed by Constrained Spherical Deconvolution: Qualitative and Quantitative Analysis. *AJNR. American journal of neuroradiology*, 36(10):1853–1858, October 2015. ISSN 1936-959X. doi: 10.3174/ajnr.A4368.
- [22] Jeremy C. Lim, Pramit M. Phal, Patricia M. Desmond, et al. Probabilistic MRI tractography of the optic radiation using constrained spherical deconvolution: a feasibility study. *PLoS One*, 10(3):e0118948, 2015. ISSN 1932-6203. doi: 10.1371/journal.pone.0118948.
- [23] Enricomaria Mormina, Alessandro Arrigo, Alessandro Calamuneri, et al. Optic radiations evaluation in patients affected by high-grade gliomas: a side-by-side constrained spherical deconvolution and diffusion tensor imaging study. *Neuroradiology*, 58(11):1067–1075, November 2016. ISSN 1432-1920. doi: 10.1007/s00234-016-1732-8.
- [24] Guillaume Theaud, Jean-Christophe Houde, Arnaud Boré, et al. TractoFlow: A robust, efficient and reproducible diffusion MRI pipeline leveraging Nextflow & Singularity. *NeuroImage*, 218:116889, September 2020. ISSN 1053-8119. doi: 10.1016/j.neuroimage.2020.116889. URL <https://www.sciencedirect.com/science/article/pii/S105381192030375X>.
- [25] Christian Bucanac. The V-Model, January 1999. URL www.bucanac.com/documents/The_V-Model.pdf.
- [26] Roger S. Pressman. *Software engineering : a practitioner's approach*. McGraw-Hill Higher Education, 7th edition, March 2009. ISBN 978-0-07-126782-3.
- [27] Karim ReFaey, Gabriella C. Quinones, William Clifton, et al. The Eye of Horus: The Connection Between Art, Medicine, and Mythology in Ancient Egypt. *Cureus*, 11(5):e4731, May 2019. ISSN 2168-8184. doi: 10.7759/cureus.4731.
- [28] Estomih Mtui, Gregory Gruener, Peter Dockery, and M. J. T. Fitzgerald. *Fitzgerald's Clinical Neuroanatomy and Neuroscience*. Elsevier, 8th edition, September 2020. ISBN 978-0-7020-7909-2.
- [29] Zhi-gang Min, Chen Niu, Netra Rana, et al. Differentiation of pure vasogenic edema and tumor-infiltrated edema in patients with peritumoral edema by analyzing the relationship of axial and radial diffusivities on 3.0T MRI. *Clin Neurol Neurosurg*, 115(8):1366–1370, August 2013. ISSN 1872-6968. doi: 10.1016/j.clineuro.2012.12.031.
- [30] Natalie L. Voets, Andreas Bartsch, and Puneet Plaha. Brain white matter fibre tracts: a review of functional neuro-oncological relevance. *Journal of Neurology, Neurosurgery & Psychiatry*, 88(12):1017–1025, December 2017. ISSN 0022-3050, 1468-330X. doi: 10.1136/jnnp-2017-316170. URL <https://jnnp.bmj.com/content/88/12/1017>.

- [31] M. V. Ivanova, A. Zhong, A. Turken, et al. Functional Contributions of the Arcuate Fasciculus to Language Processing. *Frontiers in Human Neuroscience*, 15:349, 2021. ISSN 1662-5161. doi: 10.3389/fnhum.2021.672665. URL <https://www.frontiersin.org/article/10.3389/fnhum.2021.672665>.
- [32] Emma J. Bubb, Claudia Metzler-Baddeley, and John P. Aggleton. The cingulum bundle: Anatomy, function, and dysfunction. *Neuroscience and Biobehavioral Reviews*, 92:104–127, September 2018. ISSN 1873-7528. doi: 10.1016/j.neubiorev.2018.05.008.
- [33] Qais AbuHasan and Sunil Munakomi. Neuroanatomy, Pyramidal Tract. In *StatPearls*. StatPearls Publishing, Treasure Island (FL), 2021. URL <http://www.ncbi.nlm.nih.gov/books/NBK545314/>.
- [34] Yupeng Wu, Dandan Sun, Yong Wang, and Yibao Wang. Sub-components and Connectivity of the Inferior Fronto-Occipital Fasciculus Revealed by Diffusion Spectrum Imaging Fiber Tracking. *Frontiers in Neuroanatomy*, 10:88, September 2016. ISSN 1662-5129. doi: 10.3389/fnana.2016.00088. URL <https://www.ncbi.nlm.nih.gov/pmc/articles/PMC5033953/>.
- [35] Guillaume Herbet, Ilyess Zemmoura, and Hugues Duffau. Functional Anatomy of the Inferior Longitudinal Fasciculus: From Historical Reports to Current Hypotheses. *Frontiers in Neuroanatomy*, 12:77, 2018. ISSN 1662-5129. doi: 10.3389/fnana.2018.00077. URL <https://www.frontiersin.org/article/10.3389/fnana.2018.00077>.
- [36] Francesco Latini, Gianluca Trevisi, Markus Fahlström, et al. New Insights Into the Anatomy, Connectivity and Clinical Implications of the Middle Longitudinal Fasciculus. *Frontiers in Neuroanatomy*, 14:106, 2021. ISSN 1662-5129. doi: 10.3389/fnana.2020.610324. URL <https://www.frontiersin.org/article/10.3389/fnana.2020.610324>.
- [37] Riho Nakajima, Masashi Kinoshita, Harumichi Shinohara, and Mitutoshi Nakada. The superior longitudinal fascicle: reconsidering the fronto-parietal neural network based on anatomy and function. *Brain Imaging and Behavior*, 14(6):2817–2830, December 2020. ISSN 1931-7565. doi: 10.1007/s11682-019-00187-4. URL <https://doi.org/10.1007/s11682-019-00187-4>.
- [38] Michael Dayan, Monica Munoz, Sebastian Jentschke, et al. Optic radiation structure and anatomy in the normally developing brain determined using diffusion MRI and tractography. *Brain Structure & Function*, 220(1):291–306, 2015. ISSN 1863-2653. doi: 10.1007/s00429-013-0655-y. URL <https://www.ncbi.nlm.nih.gov/pmc/articles/PMC4286633/>.
- [39] Fang-Cheng Yeh, Sandip Panesar, David Fernandes, et al. Population-averaged atlas of the macroscale human structural connectome and its network topology. *NeuroImage*, 178:57–68, September 2018. ISSN 1095-9572. doi: 10.1016/j.neuroimage.2018.05.027.
- [40] Derek R. Johnson, Julie B. Guerin, Caterina Giannini, et al. 2016 Updates to the WHO Brain Tumor Classification System: What the Radiologist Needs to Know. *Radiographics: A Review Publication of the Radiological Society of North America, Inc.*, 37(7):2164–2180, December 2017. ISSN 1527-1323. doi: 10.1148/rj.2017170037.
- [41] Otto Rapalino, Tracy Batchelor, and R. Gilberto González. Chapter 14 - Intra-axial brain tumors. In Joseph C. Masdeu and R. Gilberto González, editors, *Handbook of Clinical Neurology*, volume 135 of *Neuroimaging Part I*, pages 253–274. Elsevier, January 2016. doi: 10.1016/B978-0-444-53485-9.00014-3. URL <http://www.sciencedirect.com/science/article/pii/B9780444534859000143>.
- [42] Otto Rapalino and James G. Smirniotopoulos. Chapter 15 - Extra-axial brain tumors. In Joseph C. Masdeu and R. Gilberto González, editors, *Handbook of Clinical Neurology*, volume 135 of *Neuroimaging Part I*, pages 275–291. Elsevier, January 2016. doi: 10.1016/B978-0-444-53485-9.00015-5. URL <http://www.sciencedirect.com/science/article/pii/B9780444534859000155>.
- [43] Marc S. Greenberg. *Handbook of Neurosurgery*. Thieme, 9th edition, October 2019. ISBN 978-1-68420-137-2.
- [44] David Schiff. Low-grade Gliomas. *Continuum (Minneapolis, Minn.)*, 23(6, Neuro-oncology):1564–1579, December 2017. ISSN 1538-6899. doi: 10.1212/CON.0000000000000537.
- [45] Lakshmi Nayak and David A. Reardon. High-grade Gliomas. *Continuum (Minneapolis, Minn.)*, 23(6, Neuro-oncology):1548–1563, December 2017. ISSN 1538-6899. doi: 10.1212/CON.0000000000000554.
- [46] Daria Krivosheya, Sujit S. Prabhu, Jeffrey S. Weinberg, and Raymond Sawaya. Technical principles in glioma surgery and preoperative considerations. *Journal of Neuro-Oncology*, 130(2):243–252, November 2016. ISSN 1573-7373. doi: 10.1007/s11060-016-2171-4.
- [47] Gaurav Shukla, Gregory S. Alexander, Spyridon Bakas, et al. Advanced magnetic resonance imaging in glioblastoma: a review. *Chinese Clinical Oncology*, 6(4):40, August 2017. ISSN 2304-3873. doi: 10.21037/cco.2017.06.28.
- [48] Gayle R. Salama, Linda A. Heier, Praneil Patel, et al. Diffusion Weighted/Tensor Imaging, Functional MRI and Perfusion Weighted Imaging in Glioblastoma-Foundations and Future. *Frontiers in Neurology*, 8:660, 2017. ISSN 1664-2295. doi: 10.3389/fneur.2017.00660.
- [49] Chase H. Foster, Peter J. Morone, and Aaron Cohen-Gadol. Awake craniotomy in glioma surgery: is it necessary? *Journal of Neurosurgical Sciences*, 63(2):162–178, April 2019. ISSN 1827-1855. doi: 10.23736/S0390-5616.18.04590-3.
- [50] Matthew M. Grabowski, Pablo F. Recinos, Amy S. Nowacki, et al. Residual tumor volume versus extent of resection: predictors of survival after surgery for glioblastoma. *Journal of Neurosurgery*, 121(5):1115–1123, November 2014. ISSN 1933-0693. doi: 10.3171/2014.7.JNS132449.
- [51] Qian Han, Hengpo Liang, Peng Cheng, et al. Gross Total vs. Subtotal Resection on Survival Outcomes in Elderly Patients With High-Grade Glioma: A Systematic Review and Meta-Analysis. *Frontiers in Oncology*, 10, 2020. ISSN 2234-943X. doi: 10.3389/fonc.2020.00151. URL <https://www.frontiersin.org/articles/10.3389/fonc.2020.00151/full>.
- [52] Shawn L. Hervey-Jumper and Mitchel S. Berger. Maximizing safe resection of low- and high-grade glioma. *Journal of Neuro-Oncology*, 130(2):269–282, November 2016. ISSN 1573-7373. doi: 10.1007/s11060-016-2110-4.
- [53] Siming Bayer, Andreas Maier, Martin Ostermeier, and Rebecca Fahrh. Intraoperative Imaging Modalities and Compensation for Brain Shift in Tumor Resection Surgery. *International Journal of Biomedical Imaging*, 2017:6028645, 2017. ISSN 1687-4188. doi: 10.1155/2017/6028645.
- [54] Alonso Garcia-Ruiz, Pablo Naval-Baudin, Marta Ligerio, et al. Precise enhancement quantification in post-operative MRI as an indicator of residual tumor impact is associated with survival in patients with glioblastoma. *Scientific Reports*, 11, January 2021. ISSN 2045-2322. doi: 10.1038/s41598-020-79829-3. URL <https://www.ncbi.nlm.nih.gov/pmc/articles/PMC7804103/>.
- [55] Donald W. McRobbie, Elizabeth A. Moore, Martin J. Graves, and Martin R. Prince. *MRI from Picture to Proton*. Cambridge University Press, Cambridge, 3 edition, 2017. ISBN 978-1-107-64323-9. doi: 10.1017/9781107706958. URL <https://www.cambridge.org/core/books/mri-from-picture-to-proton/83CFA27533607FC2F45EFC48C0FC628B>.
- [56] Derek K. Jones. *Diffusion MRI: Theory, Methods, and Applications*. Oxford University Press, November 2010. ISBN 978-0-19-996514-4. URL <https://oxfordmedicine.com/view/10.1093/med/9780195369779.001.0001/med-9780195369779>.
- [57] A. Einstein. Über die von der molekularkinetischen Theorie der Wärme geforderte Bewegung von in ruhenden Flüssigkeiten suspendierten Teilchen. *Annalen der Physik*, 322(8):549–560, 1905. ISSN 1521-3889. doi: <https://doi.org/10.1002/andp.19053220806>. URL <https://onlinelibrary.wiley.com/doi/abs/10.1002/andp.19053220806>.
- [58] Denis Le Bihan. Diffusion MRI: what water tells us about the brain. *EMBO molecular medicine*, 6(5):569–573, May 2014. ISSN 1757-4684. doi: 10.1002/emmm.201404055.
- [59] Heidi Johansen-Berg and Timothy E. J. Behrens. *Diffusion MRI: From Quantitative Measurement to In vivo Neuroanatomy*. Academic Press, November 2013. ISBN 978-0-12-405509-4.
- [60] David C. Van Essen, Stephen M. Smith, Deanna M. Barch, et al. The WU-Minn Human Connectome Project: An Overview. *NeuroImage*, 80:62–79, October 2013. ISSN 1053-8119. doi: 10.1016/j.neuroimage.2013.05.041. URL <https://www.ncbi.nlm.nih.gov/pmc/articles/PMC3724347/>.
- [61] Yaniv Assaf, Heidi Johansen-Berg, and Michel Thiebaut de Schotten. The role of diffusion MRI in neuroscience. *NMR in biomedicine*, 32(4):e3762, April 2019. ISSN 1099-1492. doi: 10.1002/nbm.3762.

- [62] AD Elster. Diffusion tensor, October 2021. URL <http://mriquestions.com/diffusion-tensor.html>. Publication Title: Questions and Answers ?in MRI.
- [63] Lawrence R. Frank. Characterization of anisotropy in high angular resolution diffusion-weighted MRI. *Magnetic Resonance in Medicine*, 47(6):1083–1099, June 2002. ISSN 0740-3194. doi: 10.1002/mrm.10156.
- [64] David Raffelt, J.-Donald Tournier, Stephen Rose, et al. Apparent Fibre Density: a novel measure for the analysis of diffusion-weighted magnetic resonance images. *NeuroImage*, 59(4):3976–3994, February 2012. ISSN 1095-9572. doi: 10.1016/j.neuroimage.2011.10.045.
- [65] Till W. Riffert, Jan Schreiber, Alfred Anwander, and Thomas R. Knösche. Beyond fractional anisotropy: extraction of bundle-specific structural metrics from crossing fiber models. *NeuroImage*, 100:176–191, October 2014. ISSN 1095-9572. doi: 10.1016/j.neuroimage.2014.06.015.
- [66] Flavio Dell’Acqua, Andrew Simmons, Steven C.R. Williams, and Marco Catani. Can spherical deconvolution provide more information than fiber orientations? Hindrance modulated orientational anisotropy, a true-tract specific index to characterize white matter diffusion. *Human Brain Mapping*, 34(10):2464–2483, April 2012. ISSN 1065-9471. doi: 10.1002/hbm.22080. URL <https://www.ncbi.nlm.nih.gov/pmc/articles/PMC6870506/>.
- [67] M. D. King, J. Houseman, S. A. Roussel, et al. q-Space imaging of the brain. *Magnetic Resonance in Medicine*, 32(6):707–713, December 1994. ISSN 0740-3194. doi: 10.1002/mrm.1910320605.
- [68] Lin Tian, Hao Yan, and Dai Zhang. [Diffusion spectrum magnetic resonance imaging]. *Beijing Da Xue Xue Bao. Yi Xue Ban = Journal of Peking University. Health Sciences*, 41(6):716–720, December 2009. ISSN 1671-167X.
- [69] David S. Tuch, Timothy G. Reese, Mette R. Wiegell, et al. High angular resolution diffusion imaging reveals intravoxel white matter fiber heterogeneity. *Magnetic Resonance in Medicine*, 48(4):577–582, October 2002. ISSN 0740-3194. doi: 10.1002/mrm.10268.
- [70] Tax, CMW, Viergever, Max A., Leemans, Alexander, and University Utrecht. *Less Confusion in Diffusion MRI*. PhD Thesis, Utrecht University, September 2016. URL <https://dspace.library.uu.nl/handle/1874/337377>.
- [71] P. J. Basser, S. Pajevic, C. Pierpaoli, et al. In vivo fiber tractography using DT-MRI data. *Magnetic Resonance in Medicine*, 44(4):625–632, October 2000. ISSN 0740-3194. doi: 10.1002/1522-2594(200010)44:4<625::aid-mrm17>3.0.co;2-o.
- [72] T. E. J. Behrens, M. W. Woolrich, M. Jenkinson, et al. Characterization and propagation of uncertainty in diffusion-weighted MR imaging. *Magnetic Resonance in Medicine*, 50(5):1077–1088, November 2003. ISSN 0740-3194. doi: 10.1002/mrm.10609.
- [73] J.-Donald Tournier, Fernando Calamante, David G. Gadian, and Alan Connelly. Diffusion-weighted magnetic resonance imaging fibre tracking using a front evolution algorithm. *NeuroImage*, 20(1):276–288, September 2003. ISSN 1053-8119. doi: 10.1016/s1053-8119(03)00236-2.
- [74] S. Jbabdi, M. W. Woolrich, J. L. R. Andersson, and T. E. J. Behrens. A Bayesian framework for global tractography. *NeuroImage*, 37(1):116–129, August 2007. ISSN 1053-8119. doi: 10.1016/j.neuroimage.2007.04.039. URL <https://www.sciencedirect.com/science/article/pii/S1053811907003503>.
- [75] Geoffrey J. M. Parker, Hamied A. Haroon, and Claudia A. M. Wheeler-Kingshott. A framework for a streamline-based probabilistic index of connectivity (PICO) using a structural interpretation of MRI diffusion measurements. *Journal of magnetic resonance imaging: JMIR*, 18(2):242–254, August 2003. ISSN 1053-1807. doi: 10.1002/jmri.10350.
- [76] Mariana Lazar and Andrew L. Alexander. Bootstrap white matter tractography (BOOT-TRAC). *NeuroImage*, 24(2):524–532, January 2005. ISSN 1053-8119. doi: 10.1016/j.neuroimage.2004.08.050.
- [77] P. Mukherjee, J. I. Berman, S. W. Chung, et al. Diffusion tensor MR imaging and fiber tractography: theoretic underpinnings. *AJNR. American journal of neuroradiology*, 29(4):632–641, April 2008. ISSN 1936-959X. doi: 10.3174/ajnr.A1051.
- [78] Susumu Mori and Peter C. M. van Zijl. Fiber tracking: principles and strategies – a technical review. *NMR in Biomedicine*, 15(7-8):468–480, 2002. ISSN 1099-1492. doi: 10.1002/nbm.781. URL <https://onlinelibrary.wiley.com/doi/abs/10.1002/nbm.781>.
- [79] J.-F. Mangin, P. Fillard, Y. Cointepas, et al. Toward global tractography. *NeuroImage*, 80:290–296, October 2013. ISSN 1095-9572. doi: 10.1016/j.neuroimage.2013.04.009.
- [80] Daan Christiaens, Marco Reisert, Thijs Dhollander, et al. Global tractography of multi-shell diffusion-weighted imaging data using a multi-tissue model. *NeuroImage*, 123:89–101, December 2015. ISSN 1095-9572. doi: 10.1016/j.neuroimage.2015.08.008.
- [81] Setsu Wakana, Arvind Caprihan, Martina M. Panzenboeck, et al. Reproducibility of quantitative tractography methods applied to cerebral white matter. *NeuroImage*, 36(3):630–644, July 2007. ISSN 1053-8119. doi: 10.1016/j.neuroimage.2007.02.049.
- [82] Robert E. Smith, Jacques-Donald Tournier, Fernando Calamante, and Alan Connelly. Anatomically-constrained tractography: improved diffusion MRI streamlines tractography through effective use of anatomical information. *NeuroImage*, 62(3):1924–1938, September 2012. ISSN 1095-9572. doi: 10.1016/j.neuroimage.2012.06.005.
- [83] Gaolang Gong, Yong He, Luis Concha, et al. Mapping anatomical connectivity patterns of human cerebral cortex using in vivo diffusion tensor imaging tractography. *Cerebral Cortex (New York, N.Y.: 1991)*, 19(3):524–536, March 2009. ISSN 1460-2199. doi: 10.1093/cercor/bhn102.
- [84] Yajing Zhang, Jiangyang Zhang, Kenichi Oishi, et al. Atlas-Guided Tract Reconstruction for Automated and Comprehensive Examination of the White Matter Anatomy. *NeuroImage*, 52(4):1289–1301, October 2010. ISSN 1053-8119. doi: 10.1016/j.neuroimage.2010.05.049. URL <https://www.ncbi.nlm.nih.gov/pmc/articles/PMC2910162/>.
- [85] Fang-Cheng Yeh and Wen-Yih Isaac Tseng. NTU-90: a high angular resolution brain atlas constructed by q-space diffeomorphic reconstruction. *NeuroImage*, 58(1):91–99, September 2011. ISSN 1095-9572. doi: 10.1016/j.neuroimage.2011.06.021.
- [86] Eleftherios Garyfallidis, Matthew Brett, Marta Morgado Correia, et al. QuickBundles, a Method for Tractography Simplification. *Frontiers in Neuroscience*, 6:175, December 2012. ISSN 1662-4548. doi: 10.3389/fnins.2012.00175. URL <https://www.ncbi.nlm.nih.gov/pmc/articles/PMC3518823/>.
- [87] Jakob Wasserthal, Peter F. Neher, Dusan Hirjak, and Klaus H. Maier-Hein. Combined tract segmentation and orientation mapping for bundle-specific tractography. *Medical Image Analysis*, 58:101559, December 2019. ISSN 1361-8423. doi: 10.1016/j.media.2019.101559.
- [88] Benjamin Ades-Aron, Jelle Veraart, Peter Kochunov, et al. Evaluation of the accuracy and precision of the Diffusion parameter ESTimation with Gibbs and Noise Removal pipeline. *NeuroImage*, 183:532–543, December 2018. ISSN 1053-8119. doi: 10.1016/j.neuroimage.2018.07.066. URL <https://www.ncbi.nlm.nih.gov/pmc/articles/PMC6371781/>.
- [89] Leon Y. Cai, Qi Yang, Colin B. Hansen, et al. PreQual: An automated pipeline for integrated preprocessing and quality assurance of diffusion weighted MRI images. *Magn Reson Med*, 86(1):456–470, July 2021. ISSN 1522-2594. doi: 10.1002/mrm.28678.
- [90] Johannes Köster and Sven Rahmann. Snakemake—a scalable bioinformatics workflow engine. *Bioinformatics*, 28(19):2520–2522, October 2012. ISSN 1367-4803. doi: 10.1093/bioinformatics/bts480. URL <https://doi.org/10.1093/bioinformatics/bts480>.
- [91] Krzysztof J. Gorgolewski, Tibor Auer, Vince D. Calhoun, et al. The brain imaging data structure, a format for organizing and describing outputs of neuroimaging experiments. *Scientific Data*, 3:160044, June 2016. ISSN 2052-4463. doi: 10.1038/sdata.2016.44.
- [92] Paolo Di Tommaso, Maria Chatzou, Evan W. Floden, et al. Nextflow enables reproducible computational workflows. *Nature Biotechnology*, 35(4):316–319, April 2017. ISSN 1546-1696. doi: 10.1038/nbt.3820.
- [93] Gregory M. Kurtzer, Vanessa Sochat, and Michael W. Bauer. Singularity: Scientific containers for mobility of compute. *PloS One*, 12(5):e0177459, 2017. ISSN 1932-6203. doi: 10.1371/journal.pone.0177459.
- [94] Matthew Cieslak, Philip A. Cook, Xiaosong He, et al. QSPREP: an integrative platform for preprocessing and reconstructing diffusion MRI data. *Nat Methods*, 18(7):775–778, July 2021. ISSN 1548-7105. doi: 10.1038/s41592-021-01185-5. URL <https://www.nature.com/articles/s41592-021-01185-5>. Number: 7 Publisher: Nature Publishing Group.

- [95] B. A. Wandell, A. Rokem, L. M. Perry, et al. Data management to support reproducible research, 2015. URL <https://arxiv.org/abs/1502.06900>.
- [96] Jacky T. Yeung, Hugh M. Taylor, Isabella M. Young, et al. Unexpected hubness: a proof-of-concept study of the human connectome using pagerank centrality and implications for intracerebral neurosurgery. *J Neurooncol*, 151(2):249–256, January 2021. ISSN 1573-7373. doi: 10.1007/s11060-020-03659-6. URL <https://doi.org/10.1007/s11060-020-03659-6>.
- [97] Paolo Avesani, Brent McPherson, Soichi Hayashi, et al. The open diffusion data derivatives, brain data upcycling via integrated publishing of derivatives and reproducible open cloud services. *Sci Data*, 6(1): 69, May 2019. ISSN 2052-4463. doi: 10.1038/s41597-019-0073-y.
- [98] J.-Donald Tournier, Robert Smith, David Raffelt, et al. MRtrix3: A fast, flexible and open software framework for medical image processing and visualisation. *NeuroImage*, 202:116137, November 2019. ISSN 1095-9572. doi: 10.1016/j.neuroimage.2019.116137.
- [99] Eleftherios Garyfallidis, Matthew Brett, Bagrat Amirbekian, et al. Dipy, a library for the analysis of diffusion MRI data. *Frontiers in Neuroinformatics*, 8:8, 2014. ISSN 1662-5196. doi: 10.3389/fninf.2014.00008.
- [100] Chantal M. W. Tax, Matteo Bastiani, Jelle Veraart, et al. What's new and what's next in diffusion MRI preprocessing. *NeuroImage*, 249: 118830, April 2022. ISSN 1095-9572. doi: 10.1016/j.neuroimage.2021.118830.
- [101] José M. Soares, Paulo Marques, Victor Alves, and Nuno Sousa. A hitchhiker's guide to diffusion tensor imaging. *Front Neurosci*, 7:31, 2013. ISSN 1662-4548. doi: 10.3389/fnins.2013.00031.
- [102] Pinar Celtikci, David T. Fernandes-Cabral, Fang-Cheng Yeh, et al. Generalized q-sampling imaging fiber tractography reveals displacement and infiltration of fiber tracts in low-grade gliomas. *Neuroradiology*, 60(3):267–280, March 2018. ISSN 1432-1920. doi: 10.1007/s00234-018-1985-5.
- [103] Emrah Celtikci, Pinar Celtikci, David Tiago Fernandes-Cabral, et al. High-Definition Fiber Tractography in Evaluation and Surgical Planning of Thalamopoduncular Pilocytic Astrocytomas in Pediatric Population: Case Series and Review of Literature. *World Neurosurgery*, 98:463–469, February 2017. ISSN 1878-8769. doi: 10.1016/j.wneu.2016.11.061.
- [104] Tamara Ius, Luca Turella, Giada Pualetto, et al. Quantitative Diffusion Tensor Imaging Analysis of Low-Grade Gliomas: From Preclinical Application to Patient Care. *World Neurosurgery*, 97:333–343, January 2017. ISSN 1878-8769. doi: 10.1016/j.wneu.2016.10.006.
- [105] Lauren J. O'Donnell and Ofer Pasternak. Does diffusion MRI tell us anything about the white matter? An overview of methods and pitfalls. *Schizophrenia Research*, 161(1):133–141, January 2015. ISSN 1573-2509. doi: 10.1016/j.schres.2014.09.007.
- [106] Ahmed Radwan, Stefan Snaet, and Thomas Decramer. Private communication with dr. Thomas Decramer (neurosurgeon), dr. Ahmed Radwan (neuroradiologist), and prof. dr. Stefan Snaet (neuroradiologist). Technical report, University Hospital in Leuven, Leuven, Belgium, 2018.
- [107] Ekje Bos and A.J.P.E. Vincent. Private communication with dr. Ekje Bos (neurosurgeon) and prof. dr. A.J.P.E. Vincent (neurosurgeon). Technical report, Erasmus MC Rotterdam, Rotterdam in The Netherlands, 2018.
- [108] Philip C. de Witt Hamer and Niels Verburg. Private communication with prof. dr. Philip de Witt Hamer (neurosurgeon) and dr. Niels Verburg (neurosurgeon). Technical report, VU University Medical Center, Amsterdam, The Netherlands, 2018.
- [109] Geert-Jan Rutten. Private communication with prof. dr. Geert-Jan Rutten (neurosurgeon). Technical report, Elisabeth-TweeSteden Ziekenhuis, Tilburg, The Netherlands, 2018.
- [110] Charles Mellerio and Johan Pallud. Private communication with dr. Charles Mellerio (neuroradiologist) and dr. Johan Pallud (neurosurgeon). Technical report, Sainte-Anne Hospital, Paris, France, 2018.
- [111] Elna-Marie Larsson and Francesco Latini. Private communication with dr. Elna-Marie Larsson (neuroradiologist) and dr. Francesco Latini (neurosurgeon). Technical report, Uppsala University, Akademiska Sjukhuset, Uppsala, Sweden, 2018.
- [112] Jan S. Kirschke and Chiara Negwer. Private communication with prof. dr. Jan Kirschke (neuroradiologist) and dr. Chiara Negwer (neurosurgeon). Technical report, Klinikum rechts der Isar der TUM, Munich, Germany, 2018.
- [113] Alberto Bizzi. Private communication with dr. Alberto Bizzi (neuroradiologist). Technical report, Carlo Besta Neurological Institute, Milan, Italy, 2018.
- [114] Kurt G. Schilling, Alessandro Daducci, Klaus Maier-Hein, et al. Challenges in diffusion MRI tractography - Lessons learned from international benchmark competitions. *Magnetic Resonance Imaging*, 57:194–209, April 2019. ISSN 1873-5894. doi: 10.1016/j.mri.2018.11.014.
- [115] Leif Olteidal. Private communication with dr. Leif Olteidal (neuroradiologist). Technical report, Haukeland University Hospital, Bergen, Norway, 2018.
- [116] Dirk Merkel. Docker: lightweight linux containers for consistent development and deployment. *Linux journal*, 2014(239):2, 2014.
- [117] Roy Thomas Fielding. *Architectural styles and the design of network-based software architectures*. Dissertation, University of California, Irvine, 2000.
- [118] Kurt G. Schilling, Vishwesh Nath, Colin Hansen, et al. Limits to anatomical accuracy of diffusion tractography using modern approaches. *NeuroImage*, 185:1–11, January 2019. ISSN 1053-8119. doi: 10.1016/j.neuroimage.2018.10.029. URL <https://www.sciencedirect.com/science/article/pii/S1053811918319888>.
- [119] Ahmed Radwan, Jeroen Blommaert, Silvia Kovacs, et al. A BIDS compliant automated CSD fiber tracking pipeline for presurgical white matter mapping, October 2019.
- [120] Paul A. Yushkevich, Joseph Piven, Heather Cody Hazlett, et al. User-guided 3D active contour segmentation of anatomical structures: significantly improved efficiency and reliability. *NeuroImage*, 31(3): 1116–1128, July 2006. ISSN 1053-8119. doi: 10.1016/j.neuroimage.2006.01.015.
- [121] Bruce Fischl. FreeSurfer. *NeuroImage*, 62(2):774–781, August 2012. ISSN 1095-9572. doi: 10.1016/j.neuroimage.2012.01.021.
- [122] Mark Jenkinson, Christian F. Beckmann, Timothy E. J. Behrens, et al. FSL. *NeuroImage*, 62(2):782–790, August 2012. ISSN 1095-9572. doi: 10.1016/j.neuroimage.2011.09.015.
- [123] Jacques-Donald Tournier, F. Calamante, and Alan Connelly. Improved probabilistic streamlines tractography by 2nd order integration over fibre orientation distributions. *Proc. Intl. Soc. Mag. Reson. Med. (ISMRM)*, 18, January 2010.
- [124] Sjoerd B. Vos, Chantal M. W. Tax, Peter R. Luijten, et al. The importance of correcting for signal drift in diffusion MRI. *Magnetic Resonance in Medicine*, 77(1):285–299, 2017. ISSN 1522-2594. doi: 10.1002/mrm.26124. URL <https://onlinelibrary.wiley.com/doi/abs/10.1002/mrm.26124>.
- [125] Fabian Wenzel, Carsten Meyer, Thomas Stehle, et al. Rapid fully automatic segmentation of subcortical brain structures by shape-constrained surface adaptation. *Medical Image Analysis*, 46:146–161, May 2018. ISSN 1361-8423. doi: 10.1016/j.media.2018.03.001.
- [126] Samuel Deslauniers-Gauthier, Drew Parker, François Rheault, et al. Edema-Informed Anatomically Constrained Particle Filter Tractography. In Alejandro F. Frangi, Julia A. Schnabel, Christos Davatzikos, et al., editors, *Medical Image Computing and Computer Assisted Intervention - MICCAI 2018 - 21st International Conference, Granada, Spain, September 16-20, 2018, Proceedings, Part III*, volume 11072 of *Lecture Notes in Computer Science*, pages 375–382. Springer, 2018. URL https://doi.org/10.1007/978-3-030-00931-1_43.
- [127] Michael Perkuhn, Pantelis Stavrinou, Frank Thiele, et al. Clinical Evaluation of a Multiparametric Deep Learning Model for Glioblastoma Segmentation Using Heterogeneous Magnetic Resonance Imaging Data From Clinical Routine. *Investigative Radiology*, 53(11):647–654, November 2018. ISSN 0020-9996. doi: 10.1097/RLI.0000000000000484. URL https://journals.lww.com/investigativeradiology/Fulltext/2018/11000/Clinical_Evaluation_of_a_Multiparametric_Deep.2.aspx.
- [128] Konstantinos Kamnitsas, Christian Ledig, Virginia F. J. Newcombe, et al. Efficient multi-scale 3D CNN with fully connected CRF for accurate brain lesion segmentation. *Medical Image Analysis*, 36:61–78, February 2017. ISSN 1361-8423. doi: 10.1016/j.media.2016.10.004.

- [129] Brian B. Avants, Nicholas J. Tustison, Gang Song, et al. A Reproducible Evaluation of ANTs Similarity Metric Performance in Brain Image Registration. *NeuroImage*, 54(3):2033–2044, February 2011. ISSN 1053-8119. doi: 10.1016/j.neuroimage.2010.09.025. URL <https://www.ncbi.nlm.nih.gov/pmc/articles/PMC3065962/>.
- [130] John Mazziotta, Arthur Toga, Alan Evans, et al. A Four-Dimensional Probabilistic Atlas of the Human Brain. *Journal of the American Medical Informatics Association : JAMIA*, 8(5):401–430, 2001. ISSN 1067-5027. URL <https://www.ncbi.nlm.nih.gov/pmc/articles/PMC131040/>.
- [131] Suyash P. Awate and Ross T. Whitaker. Feature-preserving MRI denoising: a nonparametric empirical Bayes approach. *IEEE transactions on medical imaging*, 26(9):1242–1255, September 2007. ISSN 0278-0062. doi: 10.1109/TMI.2007.900319.
- [132] P. Coupe, P. Yger, S. Prima, et al. An optimized blockwise nonlocal means denoising filter for 3-D magnetic resonance images. *IEEE transactions on medical imaging*, 27(4):425–441, April 2008. ISSN 1558-254X. doi: 10.1109/TMI.2007.906087.
- [133] Antonio Tristán-Vega and Santiago Aja-Fernández. DWI filtering using joint information for DTI and HARDI. *Medical Image Analysis*, 14(2):205–218, April 2010. ISSN 1361-8423. doi: 10.1016/j.media.2009.11.001.
- [134] Jelle Veraart, Dmitry S. Novikov, Daan Christiaens, et al. Denoising of diffusion MRI using random matrix theory. *NeuroImage*, 142:394–406, November 2016. ISSN 1095-9572. doi: 10.1016/j.neuroimage.2016.08.016.
- [135] Shreyas Fadnavis, Joshua Batson, and Eleftherios Garyfallidis. Patch2Self: Denoising Diffusion MRI with Self-Supervised Learning. *arXiv:2011.01355 [cs, q-bio]*, November 2020. URL <http://arxiv.org/abs/2011.01355>.
- [136] Jelle Veraart, Els Fieremans, Ileana O. Jolescu, et al. Gibbs Ringing in Diffusion MRI. *Magnetic resonance in medicine*, 76(1):301–314, July 2016. ISSN 0740-3194. doi: 10.1002/mrm.25866. URL <https://www.ncbi.nlm.nih.gov/pmc/articles/PMC4915073/>.
- [137] Elias Kellner, Bibek Dhital, Valerij G. Kiselev, and Marco Reisert. Gibbs-ringing artifact removal based on local subvoxel-shifts. *Magnetic Resonance in Medicine*, 76(5):1574–1581, November 2016. ISSN 1522-2594. doi: 10.1002/mrm.26054.
- [138] Daan Christiaens, Lucilio Cordero-Grande, Maximilian Pietsch, et al. Scattered slice SHARD reconstruction for motion correction in multi-shell diffusion MRI. *NeuroImage*, 225:117437, January 2021. ISSN 1095-9572. doi: 10.1016/j.neuroimage.2020.117437.
- [139] Kurt G. Schilling, Justin Blaber, Colin Hansen, et al. Distortion correction of diffusion weighted MRI without reverse phase-encoding scans or field-maps. *PLOS ONE*, 15(7):e0236418, July 2020. ISSN 1932-6203. doi: 10.1371/journal.pone.0236418. URL <https://journals.plos.org/plosone/article?id=10.1371/journal.pone.0236418>.
- [140] Shuang Song, Yuanjie Zheng, and Yunlong He. A review of Methods for Bias Correction in Medical Images. *Biomedical Engineering Review*, 1(1), 2017. ISSN 2375-9151. doi: 10.18103/bme.v3i1.1550. URL <https://esmed.org/MRA/bme/article/view/1550>.
- [141] Nicholas J. Tustison, Brian B. Avants, Philip A. Cook, et al. N4ITK: improved N3 bias correction. *IEEE transactions on medical imaging*, 29(6):1310–1320, June 2010. ISSN 1558-254X. doi: 10.1109/TMI.2010.2046908.
- [142] David Qixiang Chen, Flavio Dell’Acqua, Ariel Rokem, et al. Diffusion Weighted Image Co-registration: Investigation of Best Practices. Technical report, bioRxiv, December 2019. URL <https://www.biorxiv.org/content/10.1101/864108v2>.
- [143] Alexander Leemans and Derek K. Jones. The B-matrix must be rotated when correcting for subject motion in DTI data. *Magnetic Resonance in Medicine*, 61(6):1336–1349, 2009. ISSN 1522-2594. doi: 10.1002/mrm.21890. URL <https://onlinelibrary.wiley.com/doi/abs/10.1002/mrm.21890>.
- [144] Thijs Dhollander, David Raffelt, and Alan Connelly. Unsupervised 3-tissue response function estimation from single-shell or multi-shell diffusion MR data without a co-registered T1 image. In *ISMRM Workshop on Breaking the Barriers of Diffusion MRI*, volume 5. ISMRM, September 2016.
- [145] Thijs Dhollander, Remika Mito, David Raffelt, and Alan Connelly. Improved white matter response function estimation for 3-tissue constrained spherical deconvolution. In *27th International Society of Magnetic Resonance in Medicine*, volume 27 of 555, Montréal, Québec, Canada, May 2019. ISMRM.
- [146] Remika Mito, David Raffelt, Thijs Dhollander, et al. Fibre-specific white matter reductions in Alzheimer’s disease and mild cognitive impairment. *Brain*, 141(3):888–902, January 2018. ISSN 0006-8950. doi: 10.1093/brain/awx355. URL <https://doi.org/10.1093/brain/awx355>.
- [147] J.-Donald Tournier, Fernando Calamante, and Alan Connelly. Determination of the appropriate b value and number of gradient directions for high-angular-resolution diffusion-weighted imaging. *NMR in biomedicine*, 26(12):1775–1786, December 2013. ISSN 1099-1492. doi: 10.1002/nbm.3017.
- [148] Ben Jeurissen, Jacques-Donald Tournier, Thijs Dhollander, et al. Multi-tissue constrained spherical deconvolution for improved analysis of multi-shell diffusion MRI data. *NeuroImage*, 103:411–426, December 2014. ISSN 1095-9572. doi: 10.1016/j.neuroimage.2014.07.061.
- [149] T Dhollander, R Tabbara, J Rosnarho-Tornstrand, et al. Multi-tissue log-domain intensity and inhomogeneity normalisation for quantitative apparent fibre density. *29th Proceedings of International Society of Magnetic Resonance in Medicine*, page 2472, 2021.
- [150] Robert E. Smith, Jacques-Donald Tournier, Fernando Calamante, and Alan Connelly. SIFT2: Enabling dense quantitative assessment of brain white matter connectivity using streamlines tractography. *NeuroImage*, 119:338–351, October 2015. ISSN 1095-9572. doi: 10.1016/j.neuroimage.2015.06.092.
- [151] Eleftherios Garyfallidis, Marc-Alexandre Côté, Francois Rheault, et al. Recognition of white matter bundles using local and global streamline-based registration and clustering. *NeuroImage*, 170:283–295, April 2018. ISSN 1095-9572. doi: 10.1016/j.neuroimage.2017.07.015.
- [152] S. P. L. Meesters, G. R. Sanguinetti, E. Garyfallidis, et al. Cleaning output of tractography via fiber to bundle coherence, a new open source implementation. In *22nd Annual Meeting of the Organization for Human Brain Mapping*, Geneva, Switzerland, June 2016. URL <http://www.humanbrainmapping.org/i4a/pages/index.cfm?pageID=3662>.
- [153] J. M. Portegies, R. H. J. Fick, G. R. Sanguinetti, et al. Improving Fiber Alignment in HARDI by Combining Contextual PDE Flow with Constrained Spherical Deconvolution. *PloS One*, 10(10):e0138122, 2015. ISSN 1932-6203. doi: 10.1371/journal.pone.0138122.
- [154] Will Schroeder, Ken Martin, and Bill Lorensen. *The Visualization Toolkit—An Object-Oriented Approach To 3D Graphics*. Kitware, Inc., fourth edition, 2006.
- [155] Martin Cousineau, Pierre-Marc Jodoin, Eleftherios Garyfallidis, et al. A test-retest study on Parkinson’s PPMI dataset yields statistically significant white matter fascicles. *NeuroImage: Clinical*, 16:222–233, 2017. ISSN 2213-1582. doi: <https://doi.org/10.1016/j.nicl.2017.07.020>. URL <https://www.sciencedirect.com/science/article/pii/S2213158217301869>.
- [156] Jason D. Yeatman, Robert F. Dougherty, Nathaniel J. Myall, et al. Tract Profiles of White Matter Properties: Automating Fiber-Tract Quantification. *PLOS ONE*, 7(11):e49790, November 2012. ISSN 1932-6203. doi: 10.1371/journal.pone.0049790. URL <https://journals.plos.org/plosone/article?id=10.1371/journal.pone.0049790>. Publisher: Public Library of Science.
- [157] Thijs Dhollander and Alan Connelly. A novel iterative approach to reap the benefits of multi-tissue CSD from just single-shell (+b=0) diffusion MRI data. In *24th International Society of Magnetic Resonance in Medicine*, May 2016.
- [158] Ralph Brechenhein, Bram Platel, Anna Vilanova, and Bart ter Haar Romeny. Parameter sensitivity visualization for DTI fiber tracking. *IEEE Trans Vis Comput Graph*, 15(6):1441–1448, December 2009. ISSN 1077-2626. doi: 10.1109/TVCG.2009.170.
- [159] Delphine Leclercq, Christine Delmaire, Nicolas Menjot de Champfleury, et al. Diffusion tractography: methods, validation and applications in patients with neurosurgical lesions. *Neurosurg Clin N Am*, 22(2):253–268, ix, April 2011. ISSN 1558-1349. doi: 10.1016/j.nec.2010.11.004.

- [160] Karen S. Ambrosen, Simon F. Eskildsen, Max Hinne, et al. Validation of structural brain connectivity networks: The impact of scanning parameters. *NeuroImage*, 204:116207, January 2020. ISSN 1095-9572. doi: 10.1016/j.neuroimage.2019.116207.
- [161] Arne Seehaus, Alard Roebroeck, Matteo Bastiani, et al. Histological validation of high-resolution DTI in human post mortem tissue. *Front Neuroanat*, 9:98, 2015. ISSN 1662-5129. doi: 10.3389/fnana.2015.00098.
- [162] Axel Sandvig, Ioanna Sandvig, Martin Berry, et al. Axonal tracing of the normal and regenerating visual pathway of mouse, rat, frog, and fish using manganese-enhanced MRI (MEMRI). *J Magn Reson Imaging*, 34(3):670–675, September 2011. ISSN 1522-2586. doi: 10.1002/jmri.22631.
- [163] Davy Charles Vanderweyen, Guillaume Theaud, Jasmeen Sidhu, et al. The role of diffusion tractography in refining glial tumor resection. *Brain Struct Funct*, 225(4):1413–1436, May 2020. ISSN 1863-2661. doi: 10.1007/s00429-020-02056-z.
- [164] Kurt G. Schilling, Vaibhav Janve, Yurui Gao, et al. Histological validation of diffusion MRI fiber orientation distributions and dispersion. *NeuroImage*, 165:200–221, January 2018. ISSN 1095-9572. doi: 10.1016/j.neuroimage.2017.10.046.
- [165] Francois Rheault, Alessandro De Benedictis, Alessandro Daducci, et al. Tractostorm: The what, why, and how of tractography dissection reproducibility. *Human Brain Mapping*, 41(7):1859–1874, May 2020. ISSN 1097-0193. doi: 10.1002/hbm.24917.
- [166] Kelly Shen, Gleb Bezgin, Michael Schirner, et al. A macaque connectome for large-scale network simulations in TheVirtualBrain. *Scientific Data*, 6(1):123, July 2019. ISSN 2052-4463. doi: 10.1038/s41597-019-0129-z.
- [167] Lee R. Dice. Measures of the Amount of Ecologic Association Between Species. *Ecology*, 26(3):297–302, 1945. ISSN 1939-9170. doi: 10.2307/1932409. URL <https://onlinelibrary.wiley.com/doi/abs/10.2307/1932409>. eprint: <https://onlinelibrary.wiley.com/doi/pdf/10.2307/1932409>.
- [168] Ahmed M. Radwan, Louise Emsell, Jeroen Blommaert, et al. Virtual brain grafting: Enabling whole brain parcellation in the presence of large lesions. *NeuroImage*, 229:117731, 2021. ISSN 1053-8119. doi: <https://doi.org/10.1016/j.neuroimage.2021.117731>. URL <https://www.sciencedirect.com/science/article/pii/S1053811921000082>.
- [169] Leonie Henschel, Sailesh Conjeti, Santiago Estrada, et al. FastSurfer - A fast and accurate deep learning based neuroimaging pipeline. *NeuroImage*, 219:117012, October 2020. ISSN 1053-8119. doi: 10.1016/j.neuroimage.2020.117012. URL <https://www.sciencedirect.com/science/article/pii/S1053811920304985>.
- [170] Sébastien Tourbier, Yasser Aleman-Gomez, Alessandra Griffa, et al. sebastientourbier/multiscalebrainparcellator: Multi-Scale Brain Parcellator v1.1.1, October 2019. URL <https://zenodo.org/record/3627097>.
- [171] Fabian Isensee, Marianne Schell, Irada Pfueger, et al. Automated brain extraction of multisequence MRI using artificial neural networks. *Human Brain Mapping*, 40(17):4952–4964, 2019. ISSN 1097-0193. doi: 10.1002/hbm.24750. URL <https://onlinelibrary.wiley.com/doi/abs/10.1002/hbm.24750>. eprint: <https://onlinelibrary.wiley.com/doi/pdf/10.1002/hbm.24750>.
- [172] Kurt G. Schilling, Justin Blaber, Yuankai Huo, et al. Synthesized b0 for diffusion distortion correction (Synb0-DisCo). *Magn Reson Imaging*, 64:62–70, December 2019. ISSN 1873-5894. doi: 10.1016/j.mri.2019.05.008.
- [173] Ahmed M. Radwan, Stefan Sanaert, Kurt Schilling, et al. An atlas of white matter anatomy, its variability, and reproducibility based on constrained spherical deconvolution of diffusion MRI. *NeuroImage*, 254:119029, July 2022. ISSN 1095-9572. doi: 10.1016/j.neuroimage.2022.119029.
- [174] Arnaud Bore, François Rheault, Guillaume Theaud, and Antoine Théberge. The Sherbrooke Connectivity Imaging Lab (SCIL) Python dMRI processing toolbox, 2021. URL <https://scilpy.readthedocs.io/en/latest/scripts/modules.html#>.
- [175] Jacob Benesty, Jingdong Chen, Yiteng Huang, and Israel Cohen. Pearson correlation coefficient. In *Noise reduction in speech processing*, pages 37–40. Springer, 2009.
- [176] Hans E. Plesser. Reproducibility vs. Replicability: A Brief History of a Confused Terminology. *Front Neuroinform*, 11:76, 2017. ISSN 1662-5196. doi: 10.3389/fninf.2017.00076.
- [177] Alessandro Daducci, Erick Jorge Canales-Rodríguez, Maxime Descoteaux, et al. Quantitative comparison of reconstruction methods for intra-voxel fiber recovery from diffusion MRI. *IEEE Trans Med Imaging*, 33(2):384–399, February 2014. ISSN 1558-254X. doi: 10.1109/TMI.2013.2285500.
- [178] Kurt G. Schilling, Chantal M. W. Tax, Francois Rheault, et al. Fiber tractography bundle segmentation depends on scanner effects, vendor effects, acquisition resolution, diffusion sampling scheme, diffusion sensitization, and bundle segmentation workflow. *NeuroImage*, 242:118451, 2021. ISSN 1053-8119. doi: <https://doi.org/10.1016/j.neuroimage.2021.118451>. URL <https://www.sciencedirect.com/science/article/pii/S1053811921007254>.
- [179] John L. Ulmer, Andrew P. Klein, Wade M. Mueller, et al. Preoperative Diffusion Tensor Imaging: Improving Neurosurgical Outcomes in Brain Tumor Patients. *Neuroimaging Clinics of North America*, 24(4):599–617, 2014. ISSN 1052-5149. doi: <https://doi.org/10.1016/j.nic.2014.08.002>. URL <https://www.sciencedirect.com/science/article/pii/S105251491400080X>.
- [180] Colin B. Hansen, Vishwesh Nath, Allison E. Hainline, et al. Characterization and correlation of signal drift in diffusion weighted MRI. *Magnetic Resonance Imaging*, 57:133–142, April 2019. ISSN 0730-725X. doi: 10.1016/j.mri.2018.11.009. URL <https://www.sciencedirect.com/science/article/pii/S0730725X18302546>.
- [181] Cornelius Eichner, Stephen F. Cauley, Julien Cohen-Adad, et al. Real diffusion-weighted MRI enabling true signal averaging and increased diffusion contrast. *NeuroImage*, 122:373–384, November 2015. ISSN 1095-9572. doi: 10.1016/j.neuroimage.2015.07.074.
- [182] D. A. Porter, F. Calamante, D. G. Gadian, and A. Connelly. The effect of residual Nyquist ghost in quantitative echo-planar diffusion imaging. *Magn Reson Med*, 42(2):385–392, August 1999. ISSN 0740-3194. doi: 10.1002/(sici)1522-2594(199908)42:2<385::aid-mrm21>3.0.co;2-j.
- [183] Hamed Y. Mesri, Szabolcs David, Max A. Viergever, and Alexander Leemans. The adverse effect of gradient nonlinearities on diffusion MRI: From voxels to group studies. *NeuroImage*, 205:116127, January 2020. ISSN 1095-9572. doi: 10.1016/j.neuroimage.2019.116127.
- [184] Siawoosh Mohammadi, Zoltan Nagy, Chloe Hutton, et al. Correction of vibration artifacts in DTI using phase-encoding reversal (COVIPER). *Magnetic Resonance in Medicine*, 68(3):882–889, 2012. ISSN 1522-2594. doi: 10.1002/mrm.23308. URL <https://onlinelibrary.wiley.com/doi/abs/10.1002/mrm.23308>. eprint: <https://onlinelibrary.wiley.com/doi/pdf/10.1002/mrm.23308>.